Florian Frank Schweinberger

Catalysis with Supported Size-selected Pt Clusters

Fundamental UHV and Applied Ambient Experiments

Springer Theses

Recognizing Outstanding Ph.D. Research

Aims and Scope

The series "Springer Theses" brings together a selection of the very best Ph.D. theses from around the world and across the physical sciences. Nominated and endorsed by two recognized specialists, each published volume has been selected for its scientific excellence and the high impact of its contents for the pertinent field of research. For greater accessibility to non-specialists, the published versions include an extended introduction, as well as a foreword by the student's supervisor explaining the special relevance of the work for the field. As a whole, the series will provide a valuable resource both for newcomers to the research fields described, and for other scientists seeking detailed background information on special questions. Finally, it provides an accredited documentation of the valuable contributions made by today's younger generation of scientists.

Theses are accepted into the series by invited nomination only and must fulfill all of the following criteria

- They must be written in good English.
- The topic should fall within the confines of Chemistry, Physics, Earth Sciences, Engineering and related interdisciplinary fields such as Materials, Nanoscience, Chemical Engineering, Complex Systems and Biophysics.
- The work reported in the thesis must represent a significant scientific advance.
- If the thesis includes previously published material, permission to reproduce this must be gained from the respective copyright holder.
- They must have been examined and passed during the 12 months prior to nomination.
- Each thesis should include a foreword by the supervisor outlining the significance of its content.
- The theses should have a clearly defined structure including an introduction accessible to scientists not expert in that particular field.

Florian Frank Schweinberger

Catalysis with Supported Size-selected Pt Clusters

Fundamental UHV and Applied Ambient Experiments

Doctoral Thesis accepted by
the Technische Universität München, Germany

🐎 Springer

Author
Dr. Florian Frank Schweinberger
Catalysis Research Center
Technische Universität München
Garching
Germany

Supervisor
Prof. Ueli Heiz
Department of Chemistry,
  Catalysis Research Center
Technische Universität München
Garching
Germany

Printed on acid-free paper

Parts of this Thesis have been Published in the Following Journal Articles:

Schweinberger, F.F.; Beer, M.J; Döblinger, M.; Ridge, C.J.; Crampton, A.S.; Wolff, C.; Jäckel, F.; Feldmann, J.; Tschurl, M.; Heiz, U. 2013, *J. Am. Chem. Soc.* 135 (36): 13262. doi: 10.1021/ja406070q

Beer, M.J.; Schweinberger, F.F.; Döblinger, M.; Sanwald, K.E.; Wolff, C.; Breimeier, J.; Crampton, A.S.; Ridge, C.J.; Tschurl, M.; Heiz, U.; Jäckel, F.; Feldmann, J. 2012, *Nano. Lett.* 12 (11): 5903. doi: 10.1021/nl3033069

Schweinberger, F.F.; Crampton, A.S.; Zimmermann, T.; Kwon, G.; Ridge, C.J.; Günther, S.; Heiz, U. 2013, *Surf. Sci.* 609: 18. doi: 10.1016/j.susc.2012.09.005

Spirkl, F.S.; Kunz, S.; Schweinberger, F.F.; Farnbacher, A.; Schröter, R.; Heiz, U. 2012, *Rev. Sci. Instr.* 83: 013144. doi: 10.1063/1.3677648

Kunz, S.; Hartl, K.; Nesselberger, M.; Schweinberger, F.F.; Kwon, G.; Hanzlik, M.; Mayrhofer, K. J.J.; Heiz, U.; Arenz, M. 2010, PCCP 12: 10288. doi: 10.1039/c0cp00288g

Don't waste time,

or time will waste you

— Muse

For Lisa

Supervisor's Foreword

Studying the influence of the precise size of the catalytically active species on reactivity is of major interest in catalytic research but is still extremely demanding. There are few examples carried out in the UHV showing that a catalytic process can indeed be tuned by the precise number of atoms in the catalyst. Under more realistic conditions, e.g. ambient pressure or liquid environment, such investigations are almost completely missing. Florian Schweinberger tackled in his doctoral thesis *Catalysis with Supported Size-Selected Platinum Clusters*: *Fundamental UHV and Applied Ambient Experiments* both topics and presents results both from UHV and ambient studies. His work has been exceptionally well received and the doctoral thesis is particularly well written.

From the wealth of the obtained results, I would like to highlight just a few. One research topic was the building of a UPS/MIES spectroscopic setup for the investigation of the electronic structure of model catalysts at UHV conditions. He succeeded to develop a state-of-the-art experiment with superior sensitivity and measured the molecular state of adsorbed TCE on a variety of surfaces. From these data, he could describe the bonding behavior of the molecule to the surface; furthermore, he studied the interaction of TCE with size-selected platinum clusters and described the corresponding bonding behavior. These results formed the basis for further studies on the interaction of ethene with platinum clusters and ongoing studies on the hydrogenation of olefins in the UHV.

A further highlight is the investigation of the water splitting reaction on size-selected platinum clusters on CdS nanorods that he performed in a collaborative effort between the Technische Universität München and the Ludwig-Maximilian-Universität München. He prepared the metal-cluster-semiconductor photocatalysts in the UHV and measured the H_2 evolution in liquid water upon radiation of visible light. He observed that just about 40 platinum clusters on a single CdS nanorod are enough for reaching maximal reactivity. This important finding will contribute to minimize the amount of precious platinum in industrial photocatalysts. Furthermore, he discovered distinct size effects with Pt_{46} to be the most active catalyst for the H_2 evolution reaction. For the rationalization of this surprising size effects, he could formulate a simple model where the position of the cluster's LUMO with respect to the lower edge of the conduction band of the semiconductor and the H^+/H_2 electrochemical potential is key for the photochemical reaction rate.

These impressive results are underlaid by a thorough characterization by means of high resolution STEM and XPS, showing that the photocatalysts do indeed consist of size-selected clusters and are surprisingly stable in aqueous solution.

Overall, the doctoral thesis that Florian presents is not only interesting for all of those who want to perform similar experiments but also because of the superb scientific insights.

Munich, April 2013   Prof. Ueli Heiz

Acknowledgments

Rötzer, Jakob Riedel, and Kai Sanwald, as well as the bachelor students Hannes Stecher, Philip Weber, and Sophie Jürgens. The fact that all of you stayed longer (both on a daily and monthly basis) than one would usually expect, showed me that you must have enjoyed it as much as I did.

Beside the students, this work would surely not have been possible without the numerous collaborators. Together with Dr. Frank Jäckel, Jochen F., Christian Wolff, and Dr. Maxi Berr at the LMU we have created a very productive ambient cluster collaboration. In particular with Maxi it was a pleasure to work with, as I have met no other Ph.D. student, who understood to optimize toward a maximum of scientific output. The achieved TEM results were a prerequisite for most of the experiments and thus I am thankful for all the hours spend. I acknowledge Dr. Markus Döblinger for the clear STEM images, Dr. Marianne Hanzlik for often a-la-minute measurement, as well as the team at DTU CEN—Dr. Thomas Hansen, Dr. Jakob Wagner, and most of all Davide Deiana. The people at the CINF at DTU, I thank for allowing me to visit them, more than once, to get the μ-reactor cluster project running against all odds. Thank you Dr. Jakob Olsen, Dr. Robert Jensen, Jakob Riedel, and Prof. Ib Chorkendorff for your hospitality, time, and coffee. In particular, I thank Ib for the interest and support for my ambitious projects. In Sweden, at Chalmers I acknowledge Prof. Christoph Langhammer and Kristina Wettergren, with whom we try the probably most difficult combination of our clusters with his plasmon technique. Despite that results often set us back, I am happy that we never gave up. Previously at TUM and now at Copenhagen University—the starting point of clusters at ambient conditions was initiated by Prof. Matthias Arenz, Dr. Karl J. J. Mayrhofer, Dr. Katrin Schlögl, and continued by Markus Nesselberger and Dr. Melanie Roefzaad. All of you I thank for the productive collaboration and the good times I was able to spend in Copenhagen with you.

My canadian connections—Prof. Louise Vandelac, Prof. Claude Emond, Prof. Rene Roy, and Dr. Yoann Chabre I thank for welcoming me any time in Montreal and the insights into different topics. Many of the collaborations, ideas, and scientific input I got from being a member and attending the meetings of the 'European Graduate School of Sustainable Energy Technology'. I would like to thank Prof. Hans Niemandsverdriet, Prof. Ib Chorkendorff, and Prof. Johannes Lercher for opening such a powerful platform to Ph.D. students.

Besides the Grad school, I want to thank Prof. Hubert Gasteiger and Dr. Andreas Markmann for showing me new perspectives. Big thanks to the TUM GS team, the Graduate Council and the people at the FGC Chemistry, foremost Dr. Markus Drees, for the distraction and the opportunities of the TUM GS.

The members of the Heiz Group I thank for the last years in such a familiar atmosphere, that makes our kind of work much more enjoyable. In particular I need to thank Josef Kiermaier, who as a 'long term member' as I am one, helped me to get through this roller coaster like Ph.D. time. Also I thank my friends: Max Hoffmann, Klaus Wutz, Konrad Hindelang, as well as my flatmate Stephan Janssen.

I am further indebted to my family for their endless support. Thanks to my siblings Markus, Nicole, and to my parents Ilse and Georg for offering me all the possibilities, supporting my choices, and believing in me. Last I want to thank Lisa—I am in deep gratitude for your support, love, and companionship.

Contents

Nomenclature

bcc	Body centered cubic
C_S	Spherical aberration coefficient
E_F	Fermi energy
E_g	Band gap
E_{kin}	Kinetic Energy
fcc	Face centered cubic, also cubic close-packed (ccp)
LN_2	Liquid nitrogen—boiling point at 77 K (-196 °C)
Pt_n	'Unselected' Pt cluster of size n or n > x, with (x + 1) as the smallest possible size (number of atoms)
Pt_x	Size-selected Pt cluster of size x (number of atoms)
AD	Auger deexcitation
ADF	Annular dark field
ADF	Area distribution function
AES	Auger electron spectroscopy
AN	Auger neutralization
BF	Bright field
CB	Conduction band
CFS	Constant Final State
CIS	Constant Initial State
CTF	Contrast transfer function
DF	Dark field
DOS	Density of States
EES	Electron emission spectroscopies (i.e. AES, XPS, UPS, MIES)
ESCA	Electron spectroscopy for chemical analysis, acronym for XPS
ETEM	Environmental transmission electron microscopy
HAADF	High-angle annular dark field
IRRAS	Infrared reflective adsorption spectroscopy
JDOS	Joint Density of States
LH	Langmuir-Hinshelwood (mechanism)
LSPR	Localized surface plasmonic resonance
MBD	Molecular beam doser

MIES	Metastable impact electron spectroscopy
MO	Molecular orbital
NR	Nanorod
PIES	Penning ionization electron spectroscopy
pMBRS	Pulsed molecular beam reactive scattering
PSD	Particle size distribution
QMS	Quadrupol mass spectrometer
R.f.	Radio frequency
RDS	Rate determining step
RFA	Retarding field analysis
RT	Resonant transfer
RTD	Resistant temperature detector
SDOS	Surface Density of States
STEM	Scanning transmission electron microscopy
TCE	Trichloroethene (also trichloroethylene)
TEA	Triethanolamine
TEM	Transmission electron microscopy
TPD	Temperature programmed desorption
TPR	Temperature programmed reaction
UHV	Ultra high vacuum
UPS	Ultraviolet photoelectron spectroscopy
VB	Valence band
WF	Work function
XPS	X-ray photoelectron spectroscopy
A	Ampère, SI base unit for the physical quantity of electric current I
K	Kelvin, SI base unit for the physical quantity of thermodynamic temperature T (293.15 K = 20 °C)
kg	Kilogram, SI base unit for the physical quantity of mass M
m	Meter, SI base unit for the physical quantity of length l
mol	Mole, SI base unit for the physical quantity of amount of substance n
s	Second, SI base unit for the physical quantity of time t
%ML	Percentage of a mono layer, unit for cluster coverage based on the amount of surface atoms for a MgO(100) surface with a surface atom density of 2.25×10^{15} atoms/cm^2
e/nm^2	Cluster coverage defined by measured cluster charges per surface area
H$_2$/h	Hydrogen evolution per hour
m/SA	Molecule (e.g. adsorbate) per surface atom (related to the density of surface atoms of the single crystal)
m/z	Mass to charge ratio—separation principle for the QMS
e	Elementary charge—defined by proton charge as 1.602×10^{-19}C
ML	Mono layer first single, closely packed layer
$ML\ QE$	Monolayer quantum efficiency

QE	Quantum efficiency
SA	Surface atom(s)
u	Atomic mass unit (amu)—1 u equals to one-twelfth of the mass of an atom of carbon (C^{12}). It is equal to approximately 1.66×10^{-27} kg
Z	Atomic number

Chapter 1
Introduction

1.1 Motivation for Cluster Catalysis and State of Research

The phenomenon of **catalysis**, the acceleration (of the rate) of a chemical reaction by means of a (catalyst) material through an energetically favorable mechanism, is a concept known for almost 200 years. The technological revolution in the last century would not have been possible without catalysis and nowadays approximately 85–90 % of the products of the chemical industry are made using catalytic processes, making a world without catalysis hard to imagine [1]. In the future, catalysis is expected to play a key role in helping to overcome major challenges of society, for example the ever growing demand for energy, by the use of alternative and sustainable energy sources [2]. **Heterogeneous catalysis**, as one of the sub-disciplines in catalysis, is considered to be a part of the solution. Here, catalyst materials allow one to carry out reactions at lower pressures and temperatures or under thermodynamic more ideal conditions at the interface of a solid. Most often these heterogeneous materials consist of the catalytic reactive metal, i.e. *Pt* dispersed in the form of particles on an inert support material [3].

A common approach to study heterogeneous catalyst materials is by means of **surface science** techniques, in particular spectroscopy [4]. These techniques allow one to characterize and investigate surfaces and interfaces (routinely) and improved their understanding significantly [5, 6]. However, the techniques of surface science are mainly restricted to UHV pressure conditions, thus are in general only applicable under 'ideal' conditions far from real catalyst environments. Further, for application of i.e. spectroscopy, usually model systems with reduced complexity and trying to mimic real catalysts are used in order to understand catalytic phenomena [7]. In the early days of surface science these systems were predominantly single crystal surfaces [8], that evolved into supported particles [9, 10], which still often lack the complexity of real catalyst materials.

A particularly sophisticated and advanced model systems are **supported, size-selected metal clusters**, with a precision of designing a catalyst atom by atom [11]. The first experiments of synthesizing such well defined agglomerates in the gas phase

were reported in the early 1980s' [12–16] and revealed particular properties for each cluster size. Using these well defined particles as heterogeneous catalyst materials was made possible only with significant development of the experimental means [17, 18].

The use of supported, size-selected clusters as model systems has a number of advantages and peculiarities compared to other preparation methods, i.e. PVD (Physical Vapor Deposition) [19, 20] that motivate their use despite extreme experimental effort. Most important, the deposition of clusters formed in the gas phase allows for unprecedented control of size. The application of a QMS, size selection down to a single atom is achieved. Simultaneously, the **coverage can be controlled precisely and independently of the size**. High control on both parameters, allows to prepare reproducible catalyst materials, a prerequisite for systematic studies [7]. Further, the size selection allows to use integral surface science techniques to probe an ensemble of clusters without loosing the information on the cluster size, thus allowing one to study parameters as a function of size. From a more fundamental point of view, small mono disperse clusters make it possible to investigate the '**non-scalable size regime**'. In this size regime, many material properties can no longer be extrapolated from those observed for bulk catalytic systems or particles in the so called 'scalable size regime' [11]. Clusters in the non-scalable size regime with up to ∼100 atoms are strongly influenced and dominated by electronic quantum size effects, in the case of supported clusters also by charging, cluster support interaction, geometry, oxidation state, etc.. These observations (in the non-scalable regime) give rise to a third dimension of the periodic table, in which not only the number of electrons per atom (sorted in periods and group), but also the number of atoms determines the chemical and physical properties [21]. Thus, for the reactivity and selectivity of small clusters 'each atom counts' and consequently this dependency on the cluster size can be exploited towards designing new catalyst materials [22].

Investigating the reactivity of supported size-selected metal clusters in order to contribute to the understanding of heterogeneous catalysis on a molecular level is the focus of interest in the '**nanocat**' lab. To work out the origin of size effects [23] and 'structure insensitivity' [24] of heterogeneous catalysts, different systems and techniques have been successfully applied [20, 25–29]. Major milestones were the investigation of *Pt*, *Au*, *Pd* clusters towards their reactivity in the *CO* oxidation reaction [30–35] and the *acetylene* cyclotrimerization [24, 31, 36, 37] on *Pd* clusters. Further, in the last years successful experiments with clusters under ambient conditions have been performed [20, 38–40] and showed the possibility to use clusters for application to more realistic problems in heterogeneous catalysis.

In conclusion, the use of supported clusters as well defined model systems have fostered the understanding of heterogeneous catalyst materials on a fundamental level. They have a high potential to contribute to answering major questions in this field in the future and possibly help to design more efficient catalyst materials.

1.2 Open Challenges and Scopes of this Work

Despite the mentioned successes, there are still plenty of challenges to face. Upon others, open questions are the electronic structure, reactivity and behavior towards more complex molecules/reactions and under realistic conditions. Within the scope of this thesis, using (exclusively) *Pt* clusters, under well defined (UHV) and applied (ambient) reaction conditions (see Fig. 1.1) different issues are tackled.

In **UHV** the electronic structure of cluster and cluster adsorbate complexes, as well as the reactivity of more complex molecules are investigated. Up to date only little is known of the **electronic structure** of supported size-selected clusters, however, is considered as a key towards the understanding of adsorption and surface reactivity in general (see Sect. 2.2). Of particular interest is the valence electronic structure, as it defines the reactivity with respect to reactants. A better understanding of the electronic structure of the clusters and/or the change of the molecular orbital (MO) structure upon adsorption, has the prospect to later manipulate cluster materials towards matching the energetic levels of the reactants and/or substrate for optimum activation and reactivity. To this end, an experimental approach, using two surface sensitive electron emission spectroscopies (EES), is chosen. Further, previous experiments under UHV conditions were mainly focused on the *CO* oxidation. In order to learn more about the reactivity of clusters, more complex molecules, in particular, the **adsorption** and **reactivity** of olefines (*TCE* and *ethene*) is studied.

With respect to experiments under **ambient conditions**, the previous approach [20] of cluster transfer for *ex situ* studies (see Sect. 2.3) is followed up, however with size-selected clusters. As a first step, **characterization** of the prepared materials is performed. Further, for reactivity studies a knowledge on the **stability** under reactive conditions is a prerequisite and thus the clusters are tested towards their temperature stability. Last, the **reactivity** of cluster catalysts is probed under different conditions, towards two different reactions. Various 'new' experimental means are applied to probe and analyze (*Pt*) clusters and serve as a perspective for future testing and application of cluster based materials.
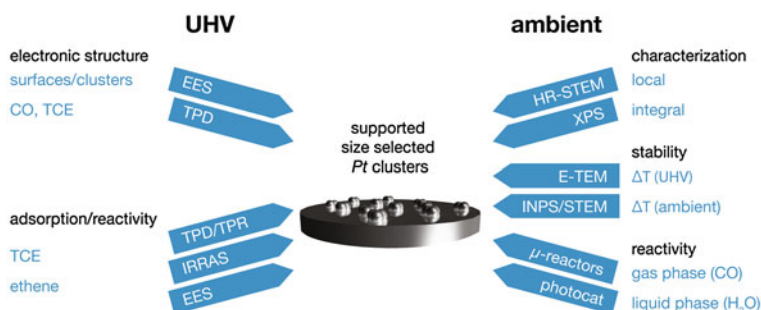
Fig. 1.1 Schematic sketch of the thesis approach to further the understanding of *Pt* cluster catalyst materials under UHV (*left*) and ambient (*right*) conditions. The main focus points are depicted in *black*, the studied systems/aims in *blue* and the techniques with the *arrows*

As a **long term goal**, the results of both UHV and ambient experiments are supposed to contribute to bridge the well known 'pressure gap' in surface science (Sect. 2.3.1), for the particular case of clusters. Thus, both vacuum and applied experiments need to be combined to gain an insight to which extent cluster results under UHV conditions can be extrapolated towards 'real' materials and conditions applied in industry. The work presented is hereby intended to contribute to foster the understanding on both the fundamental and the applied level and aims to further the use of cluster based model catalysts, with prospect for improving catalyst materials in general.

1.3 Approach, Concept and Collaborations

The particular approaches, concepts and collaborations chosen in this work to fulfill the scope of this thesis are stated in the following and summarized in a sketch in Fig. 1.1.

For the vacuum section, all cluster experiments were carried out *in situ*, i.e. under **UHV** conditions and repeated on single crystal surfaces under the exact same measurement conditions, thus allowing for the best possible comparability (also to literature with slightly different experimental conditions). To cope with the necessary high surface sensitivity when probing the electronic structure of cluster and adsorbates, the absolute surface sensitive technique MIES in combination with the more conventional UPS was used. To interpret the obtained spectroscopic results better a new data treatment for MIES/UPS data was designed and applied to quantify the adsorption studies (Sect. 2.2.2). Further standard surface science techniques: TPD/TPR, IRRAS and AES were used for the adsorption and reactivity measurements on new reactions and molecules.

In order to prepare cluster materials more efficiently, with higher reproducibly and also on insulating materials the sample deposition system has been improved (Sect. 3.3.1). The performed *ex situ* experiments under **ambient** conditions are inspired by the requirements for a successful 'real' catalyst depicted in Fig. 1.2. These requirements constitute a good measure to test the applicability of (mono disperse) cluster materials as model systems under more realistic environments. Experiments in all three main categories were conducted in order to elucidate the capabilities of cluster catalysts. A thorough characterization to confirm the high precision of cluster materials (reproducibility) also after transfer to ambient conditions, is performed by means of STEM (local information) and using XPS (integral).

Further, the stability using ETEM and INPS/TEM with respect to temperature (and pressure), as well as the reactivity (μ-reactors and photo catalysis) under applied conditions were probed with different methods. The aspects of regeneration and mechanical stability as well as selectivity were not explicitly addressed.

As probing low surface area catalyst materials such as clusters is a nontrivial task, it requires, as under UHV, highly sensitive and sophisticated methods. A variety of different and complementary **collaborations** were initiated as a part of this thesis, to profit from their expertise in the study of (cluster) materials under ambient conditions.
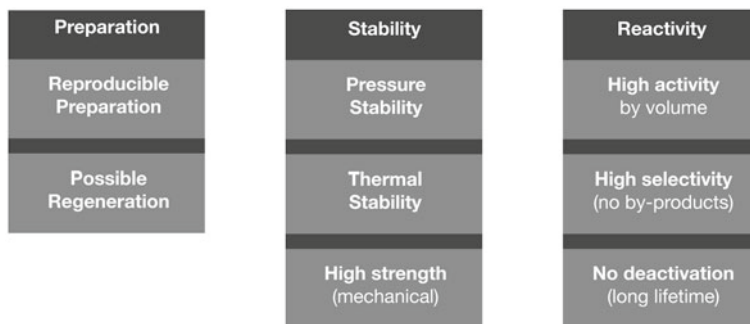
Fig. 1.2 Requirements for successful, applied catalysts, divided into three groups: preparation, stability and reactivity. The graph is based on the argumentation by Niemantsverdriet in [41]

Some of the techniques are corroborating each other and thus help to gain a more complete picture. The cluster deposition was performed at TUM, before, during and after the measurement close contact was held with all collaboration partners. Further, the results were discussed and interpreted in a joint work. All partners for the ambient experiments are briefly introduced in the following.

TEM measurements (Sects. 5.1.1 and 5.2.1) for local characterization were performed at three different locations: TUM (Fachgebiet Elektronenmikroskopie, Dr. Hanzlik), LMU (Chair of Physical Chemistry II, Dr. Döblinger) and DTU/CEN (Dr. Hansen, Dr. Wagner and D. Deiana). Post detection data treatment for characterization of the micrographs has exclusively been performed at TUM using a new data treatment (Sect. 3.3.2). **INPS** sample chips (Sect. 5.2.2) were produced and measured at Chalmers University (Prof. Langhammer and K. Wettergren); corresponding TEM images taken at DTU/CEN and treated at TUM. The μ**-reactors** (Sect. 5.3) were prepared and measured at DTU/CINF (Prof. Chorkendorff, Dr. Jensen and J. Riedel); preliminary measurements were performed during visits at the DTU. **Photocatalysis** samples (Sect. 5.4) were prepared and measured in collaboration with LMU (Chair of Photonics and Optoelectronics—Dr. Jäckel, Prof. Feldmann, Dr. Berr).

1.4 Choice of Systems

As **catalyst material**, *Platinum* is used for all (both ambient and UHV) experiments in this thesis. *Pt* represents one of the most important elements used in catalysis, due to its outstanding (catalytic) reactivity (see Sect. 2.2.1) for a large variety of reactions [3] and thus has wide application in both industry and academia. Of course, in the light of the argumentation for possible comparison of experiments in UHV and *ex situ* also the same catalyst material is necessary.

As particle **support** in the UHV for all experiments, clusters were deposited onto *MgO*, a well studied inert metal oxide [26, 27]. For ambient experiments similar inert supports, i.e. SiO_2, Si_3N_4 or amorphous *carbon* were used. It is planned and

currently ongoing work to use similar supports for UHV and ambient experiments in the future, with *silicate* as a common support material.

Beside the interest to probe supported size-selected clusters under different conditions and with the general challenges as introduced above, the use of cluster based materials in this work is motivated by a variety of individual scientific questions. The motivation for the particular choice of the different systems and reactions studied are briefly presented, a literature survey covering some theoretical and mechanistic details is subject of a later section (Sect. 2.1).

CO as probe molecule and the **catalytic oxidation of *CO*** is chosen as benchmark reaction for comparison of reactivity in both UHV and ambient experiments. It is one of the best studied reactions in catalysis [42–45]. Most data from cluster reactivity in UHV is available for the *CO* oxidation reaction and the electronic structure of *CO* is well understood. Thus, investigating the *CO* oxidation in the ambient experiments, is preferential, with prospect of comparison to the results in the UHV. Further, clusters might contribute to clarify the ongoing discussion on the structure insensitivity of the *CO* oxidation on supported particles [46].

The study of the ubiquitous ground-water pollutant **trichloroethene** (*TCE*) [47] is motivated by developing an alternative for the degradation of this health hazard. Due to its chemical inertness, current *TCE* degradation methods are inefficient and energy intensive. Promising alternative approaches reported so far, include photocatalytic conversion of *TCE* (gasphase [48] and supported [49]) and the use of small noble metal particles to catalyze the conversion [50, 51]. Yet, more efficient catalysts are desirable, however require a more fundamental knowledge of the activation of *TCE* towards degradation. Up to date, mainly theoretical approaches are reported [52–54] and only few experimental works are known [54, 55]. To this end, in order to elucidate the capabilities of clusters and investigate the underlying mechanisms for (possible) *TCE* conversion, adsorption studies in UHV on surfaces and *Pt* clusters are performed.

As a second example for hydrocarbon activation and reactivity, ***ethene* hydrogenation** is investigated. The study of olefines is of high industrial relevance, for example in the process of refining, where crude oil is separated and treated in order to give applicable products like fuel and raw materials for petrochemical use [56]. In this context, the hydrogenation of hydrocarbons (including *ethene*) is a main reaction and occurs in large scales, usually on metal oxide supported *Pt* or *Re* particles [57]. Particularly, *Pt* is known to be a good hydrogenation catalyst [5] and consequently a logical choice for use towards the activation and conversion of olefines. As the *CO* oxidation, the hydrogenation of *ethene* (especially on *Pt*) has been subject to countless publications [58–64], fostered by its industrial relevance. Up to date, important mechanistic details (intermediate species, avoiding deactivation, etc.) are still not solved. Mono disperse *Pt* clusters might shed light on some of the open questions, and are therefore investigated along with a *Pt* (111) surface, by different experimental means in UHV.

Under ambient conditions the **photocatalytic *water* splitting** reaction is studied, with focus on the *hydrogen* evolution. Motivated by the necessity of the introduction of renewable sources of energy [2, 65] *hydrogen* is considered to play an impor-

tant role in the future mix of sustainable energies [66, 67]. In order to generate *hydrogen*, the photocatalytic water splitting reaction (Sect. 2.1.3) is a promising approach to contribute to future hydrogen fuel production [68]. In particular semi-conductor materials, decorated with noble metals have proven to have suitable optical properties [69] and chemical stability [70] along with considerably high reactivity towards *hydrogen* evolution. However, up to now the composition of the cluster catalyst materials [71–73] were not well defined and thus circumvented a systematic study of such materials. To this end, a new hybrid photocatalyst material with size-selected clusters was synthesized and its performance towards *hydrogen* production studied as a function of cluster coverage and size.

1.5 Thesis Outline

A graphical overview of the chapters and sections in this thesis is summarized in the roadmap in Fig. 1.3. As the thesis is divided into two major parts, corresponding to the UHV and ambient experiments performed, these parts are reflected in various chapters.

In a **literature survey** and **theory chapter**, the three studied catalytic reactions (*CO* oxidation, *ethene* hydrogenation and *water* splitting) are presented. A short introduction into the electronic structure of model systems is given, explaining the relation between adsorption and electronic structure and presenting some consider-ations and models utilized. With respect to the UHV experiments, EES of supported clusters and adsorbate species and the data treatment and interpretation for EES results is given. As a last part, the motivation for ambient experiments of model catalyst and a small section dealing with the stability of catalyst is presented.

The **experimental chapter** consists of three parts, covering first the cluster syn-thesis (formation, mass selection and deposition). In a second part, the UHV setup and the procedures for experiments followed by a short introduction to each of the used techniques along with some experimental details is given. Third, the approach for catalyst preparation and transfer and the used techniques for ambient experiments are presented, including explanations of the methods.

The first results part is dedicated to studies under **UHV** conditions and begins with the determination of the sensitivity of the MIES/UPS setup. Next, the measurements of the electronic structure of two different cluster sizes is presented. The capabilities of the setup are further elucidated, using *CO* as probe molecule and its adsorption properties probed on $Pt(111)$. Last and most important, the adsorption properties and reactivity of the olefins TCE and *ethene* are studied as a function of coverage on surfaces and also on supported Pt clusters by means of EES, TPD/TPR as well as IRRAS and AES.

The second results part, dealing with **ambient** cluster catalysis is divided into three sections. First, the outcome of the characterization of the cluster catalysts (STEM/XPS) is shown. Second, first results on the stability (ETEM/INPS) are pre-sented. Last, two examples for reactivity of size-selected clusters are presented. As an

example for gasphase catalysis, results of *CO* oxidation in μ-reactors are discussed. In liquid phase, a new hybrid cluster photocatalyst material is systematically tested for photocatalytic *water* splitting.

Based on the results of the previous sections a **summary and conclusion** is presented. Further, a short **outlook** is given, with respect to ongoing experiments and future work.

The **appendix** contains further (experimental) details on the UHV and ambient part. Additionally, gas phase photoelectron spectra of the studied molecules are included.

1.6 Thesis Roadmap
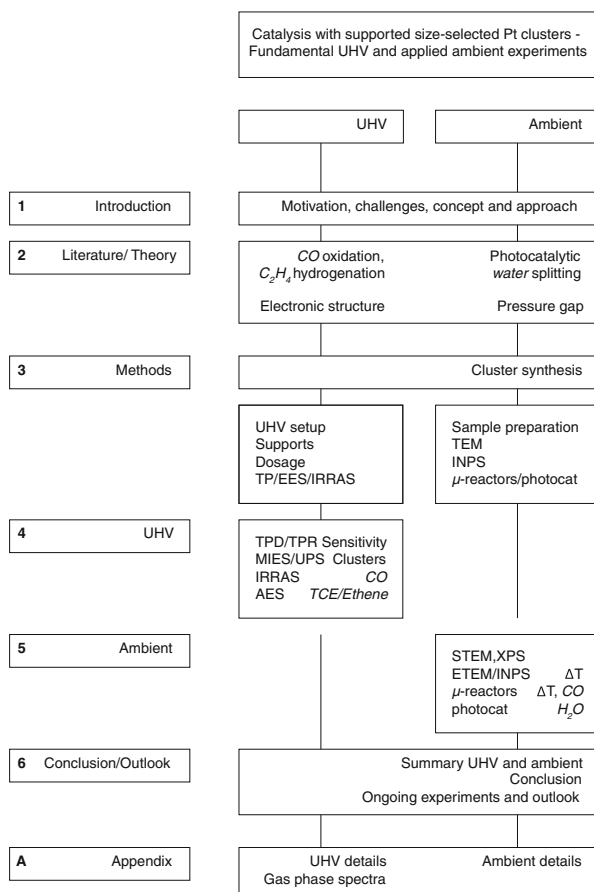
Fig. 1.3 Thesis road-map: Chapters are listed on the *left*; their content is pictured on the *right*, with distinguishing between UHV and ambient parts. Chapters 4 and 5 list the major techniques utilized (*left*) and the systems studied (*right*)

References

1. Chorkendorff, I., & Niemantsverdriet, J. W. (2007). *Concepts of modern catalysis and kinetics* (2nd ed.). Weinheim: Wiley-VCH.
2. Dincer, I. (2000). *Renewable Sustainable Energy Reviews*, *4*, 157.
3. Ertl, G., Knözinger, H., Schüth, F., Weitkamp, J. (2008). *Handbook of heterogeneous catalysis* (2nd ed.). Weinheim: Wiley-VCH.
4. Ertl, G. (1980). *Pure and Applied Chemistry*, *52*, 2051.
5. Somorjai, G. (1994). *Introduction to surface chemistry and catalysis* (Vol. 2). Weinheim: Wiley-Interscience.
6. Somorjai, G., & Park, J. (2007). *Catalysis Letters*, *115*, 87.
7. Boudart, M. (2000). *Topics in Catalysis*, *13*, 147.
8. Ertl, G., Küppers, J. (1974). *Low energy electrons and surface chemistry; monographs in modern chemistry* (Vol. 1). Weinheim: Verlag Chemie.
9. Henry, C. R. (1998). *Surface Science Reports*, *31*, 231.
10. Freund, H. (2008). *Topics in Catalysis*, *48*, 137.
11. Heiz, U., Landman, U., & Henry, C. R. (2008). In U. Heiz & U. Landman (Eds.), *Nanocatalysis*. Berlin: Springer.
12. Schumacher, E., Blatter, F., Frey, M., Heiz, U., Roethlisberger, U., Schaer, M., et al. (1988). *Chimia*, *42*, 357.
13. Herrmann, A., Schumacher, E., & Wöste, L. J. (1978). *Journal of Chemical Physics*, *68*, 2327.
14. Dietz, T. G., Duncan, M. A., Powers, D. E., & Smalley, R. E. J. (1981). *Journal of Chemical Physics*, *74*, 6511.
15. Knight, W. D., Clemenger, K., de Heer, W. A., Saunders, W. A., Chou, M. Y., & Cohen, M. L. (1984). *Physical Review Letters*, *52*, 2141.
16. Fayet, P., Granzer, F., Hegenbart, G., Moisar, E., Pischel, B., & Wöste, L. (1985). *Physical Review Letters*, *55*, 3002.
17. Heiz, U., Vanolli, F., Trento, L., & Schneider, W.-D. (1986). *Review of Scientific Instruments*, *1997*, 68.
18. Heiz, U., Vayloyan, A., & Schumacher, E. (1997). *Review of Scientific Instruments*, *68*, 3718.
19. McClure, S. M., & Goodman, D. W. (2011). *Topics in Catalysis*, *54*, 349.
20. Kunz, S. (2010). Ph.D. thesis, Technische Universität München.
21. Arenz, M., Gilb, S., & Heiz, U. (2007). In D. Woodruff (Ed.), *In the chemical physics of solid surfaces* (Vol. 12, p. 1). Amsterdam: Elsevier.
22. Schlögl, R., & Abd Hamid, S. B. (2004). *Angewandte Chemie (International ed. in English)*, *43*, 1628.
23. Bond, G. (1985). *Surface Science*, *156*, 966.
24. Abbet, S., Sanchez, A., Heiz, U., Schneider, W.-D., Ferrari, A., Pacchioni, G., et al. (2000). *Surface Science*, *454*, 984.
25. Vanolli, F. (1997). Ph.D. thesis, Unversité de Lausanne.
26. Sanchez, A. (2000). Ph.D. thesis, Unversité de Lausanne.
27. Abbet, S. (2001). Ph.D. thesis, Unversité de Lausanne.
28. Wörz, A. (2005). Ph.D. thesis, Universität Ulm.
29. Röttgen, M. A. (2007). Ph.D. thesis, Technische Universität München.
30. Heiz, U., Sanchez, A., Abbet, S., & Schneider, W.-D. J. (1999). *Journal of the American Chemical Society*, *121*, 3214.
31. Abbet, S., Sanchez, A., Heiz, U., Schneider, W., Ferrari, A. M., Pacchioni, G., et al. (2000). *Journal of the American Chemical Society*, *122*, 3453.
32. Heiz, U., Sanchez, A., Abbet, S., & Schneider, W. D. (2000). *Journal of the Chemical Physics*, *262*, 189.
33. Sanchez, A., Abbet, S., Heiz, U., Schneider, W.-D., Häkkinen, H., Barnett, R. N., et al. (1999). *Journal of Physical Chemistry A*, *103*, 9573.
34. Röttgen, M. A., Abbet, S., Judai, K., Antonietti, J.-M., Wörz, A. S., Arenz, M., et al. (2007). *Journal of the American Chemical Society*, *129*, 9635.

35. Kunz, S., Schweinberger, F. F., Habibpour, V., Röttgen, M., Harding, C., Arenz, M., et al. (2010). *Journal of Physical Chemistry C*, *114*, 1651.
36. Ferrari, A. M., Rösch, N., Heiz, U., Giordano, L., Abbet, S., Sanchez, A., et al. (2000). *Journal of Physical Chemistry B*, *104*, 10612.
37. Ferrari, A. M., Heiz, U., Giordano, L., Pacchioni, G., & Abbet, S. J. (2002). *Journal of Physical Chemistry B*, *106*, 3173.
38. Kunz, S., Hartl, K., Nesselberger, M., Schweinberger, F. F., Kwon, G., Hanzlik, M., et al. (2010). *PCCP*, *12*, 10288.
39. Hartl, K., Nesselberger, M., Mayrhofer, K. J., Kunz, S., Schweinberger, F. F., Kwon, G., et al. (2010). *Electrochimica Acta*, *56*, 810.
40. Schlögl, K. (2011). Ph.D. thesis, Technische Universität München.
41. Niemantsverdriet, J. W. (2007). *Spectroscopy in catalysis: An introduction* (3rd ed.). Weinheim: Wiley-VCH.
42. Engel, T., & Ertl, G. (1979). In D. D. Eley, H. Pines, & P. B. Weez (Eds.) *Advances in catalysis* (Vol. 28, p. 1). New York: Academic Press.
43. Libuda, J., Meusel, I., Hoffmann, J., Hartmann, J., Piccolo, L., Henry, C. R., et al. (2001). *Journal of Chemical Physics*, *114*, 4669.
44. Meusel, I., Hoffmann, J., Hartmann, J., Libuda, J., & Freund, H. J. J. (2001). *Physical Chemistry B*, *105*, 3567.
45. Herzing, A., Kiely, C., Carley, A., Landon, P., & Hutchings, G. (2008). *Science*, *321*, 1331.
46. Allian, A. D., Takanabe, K., Fujdala, K. L., Hao, X., Truex, T. J., Cai, J., et al. (2011). *Journal of the American Chemical Society*, *133*, 4498.
47. Russell, H., Matthews, J., & Sewell, G. (1992). *TCE removal from contaminated soil and ground water*; EPA ground water issue EPA/540/S-92/002; United States Environmental Protection Agency. Robert S. Kerr Environmental Research Laboratory Ada, Oklahoma: USA
48. Nimlos, M. R., Jacoby, W. A., Blake, D. M., & Milne, T. A. (1993). *Environment Science & Technology*, *27*, 732.
49. Fan, J., & Yates, J. J. J. (1996). *Journal of the American Chemical Society*, *118*, 4686.
50. Schüth, C., Disser, S., Schüth, F., & Reinhard, M. (2000). *Applied Catalysis B: Environmental*, *28*, 147.
51. Barrabes, N., Cornado, D., Foettinger, K., Dafinov, A., Llorca, J., Medina, F., et al. (2009). *Journal of Catalysis*, *263*, 239.
52. Barbosa, L. A. M. M., & Sautet, P. (2002). *Journal of Catalysis*, *207*, 127.
53. Barbosa, L. A. M. M., Loffreda, D., & Sautet, P. (2002). *Langmuir*, *18*, 2625.
54. Jugnet, Y., Bertolini, J. C., Barbosa, L. A. M. M., & Sautet, P. (2002). *Surface Science*, *505*, 153.
55. Cassuto, A., Hugenschmidt, M., Parent, P., Laffon, C., & Tourillon, H. (1994). *Surface Science*, *310*, 390.
56. Gary, J. H., Handwerk, G. E., & Kaiser, M. J. (2007). *Petroleum refining: Technology and economics* (0005th ed.). Boca Raton: CRC Press Inc.
57. Ciapetta, F. G., & Wallace, D. N. (1972). *Catalysis Reviews—Science and Engineering*, *5*, 67.
58. Farkas, A., & Farkas, L. J. (1938). *Journal of the American Chemical Society*, *60*, 22.
59. Demuth, J. E., & Eastman, D. E. (1974). *Physical Review Letters*, *32*, 1123.
60. Fischer, T., & Kelemen, S. (1977). *Surface Science*, *69*, 485.
61. Zaera, F., & Somorjai, G. A. J. (1984). *Journal of the American Chemical Society*, *106*, 2288.
62. Zaera, F. (1996). *Langmuir*, *12*, 88.
63. Öfner, H., & Zaera, F. J. (1997). *Journal of Physical Chemistry B*, *101*, 396.
64. Öfner, H., & Zaera, F. J. (2002). *Journal of the American Chemical Society*, *124*, 10982.
65. Lewis, N. S., & Nocera, D. G. (2006). *PNAS*, *103*, 15729.
66. Züttel, A., Borgschulte, A., & Schlapbach, L. (2008). *Hydrogen as a future energy carrier*. Weinheim: Wiley-VCH.
67. Langhammer, C. (2009). Ph.D. thesis, Chalmers University of Technology.
68. Zhu, J., & Zäch, M. (2009). *Current Opinion in Colloid & Interface Science*, *14*, 260.
69. Maeda, K., & Domen, K. J. (2007). *Journal of Physical Chemistry C*, *111*, 7851.

70. Sathish, M., & Viswanath, R. (2007). *Catalysis Today*, *129*, 421.
71. Berr, M., Vaneski, A., Susha, A., Rodrigues-Fernandez, J., Döblinger, M., Jäckel, F., et al. (2010). *Applied Physics Letters*, *97*, 093108.
72. Vaneski, A., Susha, A. S., Rodríguez-Fernández, J., Berr, M., Jäckel, F., Feldmann, J., et al. (2011). *Advanced Functional Materials*, *21*, 1547.
73. Berr, M. J., Vaneski, A., Mauser, C., Fischbach, S., Susha, A. S., & Rogach, A. L. et al. (2011). *Small*, *8*, 291–297.

Part I
Background and Methods

Chapter 2
Literature Survey and Theory

This part is split into three sub sections. First a brief introduction, covering the studied reactions and their mechanisms is presented. Second, the fundamentals of the electronic structure of model systems and adsorbed species, with a focus on electron emission spectroscopy (EES) are discussed. Last, the motivation for studying catalyst model systems under ambient pressure conditions is introduced, followed by a brief description of thermal stability under applied conditions.

2.1 Chosen Catalytic Reactions

The following sections deals with the reactions studied within this work. For UHV and ambient experiments *CO* oxidation, for UHV *ethene* hydrogenation and for ambient conditions photocatalytic *water* splitting is introduced. As these model reactions are extensively studied in surface science only a brief overview is given. Further, the survey is limited to findings on *Pt* surfaces and *Pt* nanoparticles, in the case of photocatalysis, to semiconductor based systems (i.e. *CdS*).

2.1.1 CO Oxidation

The conversion of *CO* and O_2 into CO_2 in the gas phase has a free enthalpy of –283 kJ/mol and is therefore thermodynamically favored [1, 2]. However, in order to initiate this reaction, the activation energy for the dissociation of O_2 has to be overcome, lowered e.g. by a heterogeneous catalyst. The reaction occurs on *Pt* (and other group VIII metals) surfaces via a **Langmuir-Hinshelwood** (LH) **mechanism** [3–8] with the following steps[1] (Eqs. 2.1–2.4, ∗ represent surface adsorption sites).

---

[1] Also a low temperature mechanism based on molecular *oxygen* [9, 10] and additional pathways for different surface sites (steps and terraces) [11] are known.

$$O_2 + 2* \rightleftharpoons 2O* \tag{2.1}$$

$$CO + * \rightleftharpoons CO* \tag{2.2}$$

$$CO*+O* \rightleftharpoons CO_2*+* \quad (RDS) \tag{2.3}$$

$$CO_2* \rightleftharpoons CO_2 + * \tag{2.4}$$

$$2CO + O_2 \rightleftharpoons 2CO_2 \quad (sum) \tag{2.5}$$
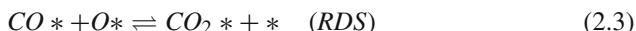
Despite this simple mechanism a few particularities of the reaction need to be mentioned. It is necessary for the *CO* and the O_2 molecule first to be strongly adsorbed (chemisorbed) before reaction takes place [1], a coverage dependent step. Pre-adsorbed *CO* inhibits dissociative *oxygen* chemisorption (a necessary prerequisite for the reaction to happen), whereas a pre-adsorbed *oxygen* layer affects the sticking probability for *CO* only slightly [12]. This phenomenon is commonly known as **'CO poisoning'** and needs to be taken into account for experimental considerations. Based on these observations the two key factors influencing the reactivity of a catalyst towards *CO* oxidation are given: First, the chemisorption of *CO* and second, the dissociative adsorption of *oxygen* [13].

Supported **Pt clusters**[2] on $MgO(100)$ showed a change in reactivity towards *CO* oxidation atom by atom [15, 16]. Based on TPR and IRRAS results different reaction pathways were assigned [2, 15, 17]. The reactivity as a function of size was also correlated to the corresponding level of the center of the *d*-band [18–21] for each size and thus the efficiency of breaking the *oxygen* double bond [17, 22]. Recent results in a similar size range support the correlation between electronic structure and reactivity [23, 24], additionally stressing the influence of the shape of the catalyst particle. For bigger particles, the different adsorption sites observed for *CO* responsible for the different TPR peaks, were successfully assigned, by comparing it with stepped surfaces [25].

The observed behavior of changing reactivity atom by atom, is particularly intriguing since the *CO* oxidation reaction is one of the classic examples of **structure insensitivity**. This means, its turnover rate is essentially independent of metal dispersion, even though the structure and coordinative unsaturation of exposed metal atoms are known to differ among clusters of different size [7, 26]. However, several examples for insensitivity are known [27] (and herein) for very small sizes and is correlated to the higher binding strength of *CO* on step sites present on these small particles, which contain a higher fraction of *CO* bound to step sites.

Recently the *CO* oxidation reaction on supported *Pt* particles (of different sizes) was studied under **applied conditions** (elevated pressures and temperatures, as well as steady-state conditions) and by means of different techniques. Monitoring changes in plasmon frequency (INPS, Sect. 5.2.2) the reaction as a function of the mole fraction (at ambient pressures) was measured on *Pt* catalysts (2–20 nm size) on SiO_2 and proved to be able to detect *CO* poisoning [28], comparable to UHV results. Similar sized catalysts were investigated under near atmospheric pressures (in a

---

[2] Previously Pt_x ($x = 1, 2, 3$) on SiO_2 had shown different *CO* adsorption/desorption properties in TPD measurements already [14], however no *CO* oxidation had been studied at that point.

reaction cell) and supported by UHV characterization. TOF and activation energies were extracted and the results were extrapolated to single crystal data, suggesting no size effects in 2–3 nm particles [27, 29]. Catalysts synthesized by colloidal methods and tested in flow reactors, at elevated temperatures, support these findings [7, 30] and the assumption of structure insensitivity. *CO* oxidation on cluster materials produced with atomic size control were recently investigated at elevated pressures and revealed size dependent reactivity which was correlated to a change in particle shape and electronic structure [31]. Lastly, larger nanoparticles (3–9 nm) in μ-reactors showed oscillation behavior for the reaction [32], similar to observations known from Ertl et al. [33].

Measuring the reactivity in these studies, steady-state reaction conditions are present and the change in reactivity as a function of temperature is probed. While running the reaction the temperature is increased, at a certain temperature a sudden increase in turnover is observed and this known as **light off** phenomenon. This behavior is explained by the earlier introduced *CO* poisoning effect. In the low temperature range *CO* has a much higher sticking coefficient than *oxygen* and thus the *CO* molecules occupy all free sites on the catalyst as soon as exposed to the reactant mixture and consequently prevents the catalytic conversion. With increasing temperature the residence time of the *CO* gets shorter and eventually *oxygen* can bind and subsequently react to CO_2—due to stoichiometry each *oxygen* molecule reacts with two *CO* and thus leaves two free surface sites after desorption. In a cascade reaction all available adsorbed *CO* molecules react off and give rise to a sudden increase in CO_2 production. Decreasing the temperature a hysteresis is found, because when cooling the sample, free sites are still available and sustain the conversion down to temperatures below the ignition temperature of the light off [30, 32].

In conclusion, the *CO* oxidation mechanism on *Pt*, and other *d*-metals is well understood and serves as a benchmark reaction to characterize reactivity. However, with respect to behavior for supported metal particles and small clusters under ambient conditions, there is still the need for studies in order to fully understand the role of the size, particularly with respect to the electronic structure.

2.1.2 Ethene Hydrogenation

The decomposition of *ethene* under vacuum has been proven to occur over a family of single crystal surfaces, *Pt*, *Rh*, *Pd*, *Ru* as well as supported *Pt*, *Pd* and *Ni* particles. For *Pt*(111), but also for other *d*-metals, in the absence of *hydrogen*, *ethane* is formed and can be detected when studying thermal desorption of *ethene*, thus the formation of *ethane* occurs via a **self-hydrogenation** [34].

During the thermal decomposition, *hydrogen* is formed on the surface and is able to hydrogenate *ethene* to *ethane*. The rate determining step (RDS) is the $C - H$ bond breaking [35] and the overall reaction is described by the following steps (Eqs. 2.6–2.10).

$$C_2H_4 + * \rightleftharpoons C_2H_4* \tag{2.6}$$

$$C_2H_4* \rightleftharpoons C_2H_3 * + H * \quad (RDS) \tag{2.7}$$

$$2H* \rightleftharpoons H_2 \tag{2.8}$$

$$C_2H_4 * + H* \rightleftharpoons C_2H_5 * + 2* \tag{2.9}$$

$$C_2H_5 * + H* \rightleftharpoons C_2H_6 + 2* \tag{2.10}$$
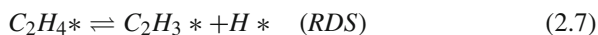
Based on isotope labeling experiments (TPD, IRRAS) [36–39] it was concluded that the catalytic *ethene* **hydrogenation** reaction on surfaces proceeds as a step wise process of *hydrogen* incorporation. This step wise general mechanism is called the **Horiuti-Polanyi** mechanism [40] and is shown in Eqs. 2.11–2.15 [41].[3]

$$H_2 + 2* \rightleftharpoons 2H* \tag{2.11}$$

$$C_2H_4 + * \rightleftharpoons C_2H_4 * \quad (\pi - bonded) \tag{2.12}$$

$$C_2H_4 * + * \rightleftharpoons *C_2H_4 * \quad (di - \sigma\ bonded) \tag{2.13}$$

$$*C_2H_4 * + H* \rightleftharpoons C_2H_5 * + 2 * \quad (RDS) \tag{2.14}$$

$$C_2H_5 * + H* \rightleftharpoons C_2H_6 + 2* \tag{2.15}$$

$$C_2H_4 + H_2 \rightleftharpoons C_2H_6 \quad (sum) \tag{2.16}$$
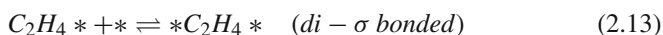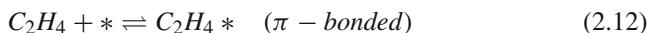
As denoted in the equations, *ethene* forms two types of adsorbates on the surface depending on the temperature [44]. Between 37–45 K, π**-bonded** species (associatively chemisorbed) are formed [45, 46], which upon heating above 52 K begins to form a stronger chemisorbed **di-**σ species [47–49] on $Pt(111)$ sitting in a *fcc* 3-fold hollow site [49]. These species are the kinetically relevant ones and the RDS is the recombination of the reactants, which must overcome the strong $di - \sigma$ species [41]. Above $\sim$250 K[4] *ethylidine* is formed [49, 50] which is a strongly triple-bond carbonaceous surfaces species that forms a strongly adsorbed and difficult to remove over layer on the Pt-surface. Calculations suggest that *ethylidyne* does not directly participate in the reaction mechanism, thus the conversion to *ethane* is likely to proceed via *hydrogen* incorporation [51]. This process increases significantly at higher temperatures [35], but so does the formation of elementary ***carbon*** on the metal surface, at temperatures above 450–500 K. At higher concentrations a graphite layer forms and the organic deposits become immobile, consequently the active sites on the metal are poisoned [34, 35]. At even higher temperatures ($\sim$700 K) *ethene* rapidly forms a monolayer of **graphene**. The formation of *carbon* is structure sensitive

---

[3] The presented mechanism is the simplest proposed hydrogenation mechanism, and also known as competitive Horiuti-Polanyi mechanism, as the reactants *ethene* and *hydrogen* compete for one single class of adsorption sites. In order to explain observations with respect to micro kinetics on heterogeneous catalysts this approach is too simple, however since no kinetic interpretation is done within this thesis, the reader is referred to the literature for a more detailed understanding [42, 43].

[4] At room temperature the hydrogenation reaction of *ethene* is again surface-insensitive because of the size and symmetry of *ethene* [35].

as described above in contrast to the hydrogenation and represents due to catalyst deactivation one of the major problems in industrial processes.

Despite the numerous publications available, two major questions remain (part wise) unanswered [36]. First, the exact mechanism for the formation of *ethylidyne* and its actual role in the catalytic formation of *ethane* and second, a detailed picture of the *ethane* formation including all relevant C_2 moieties.

For the *ethylidyne* species the question arises as to whether it is a simple spectator [52] or does it have a more active role in the hydrogenation of *ethene* [36]. The current opinion is [53], that it does not actively participate in the reaction, however blocks the sites available for *ethene* adsorption [54] or reacts with *hydrogen* and thus indirectly affects the reaction kinetics of hydrogenation [51, 55].

The catalytic hydrogenation probably occurs via the incorporation of *hydrogen* atoms into a weakly adsorbed *ethene*, maybe even on a carbonaceous layer [56]. This *ethene* then forms ethyl moieties and eventually forms *ethane*, released as product form the surface [36, 55, 56]. However, all these processes are competing with the formation of *ethylidyne*. As a consequence of the competitive formation the efficiency of the reaction under vacuum is low and the formation of *ethane* only accounts for a small percentage of the initial amount of *ethene*. For example, measurements found that only 10 % of a saturated *ethene* layer were converted via self-hydrogenation to *ethane* at 283 K [54].

Based on these considerations and experimental evidences a current model for the *ethane* formation on $Pt(111)$ is depicted in Fig. 2.1a, involving both π-bonded and $di - \sigma$ bonded species [49]. The competitive interplay between *ethylidyne* formation and the hydrogenation to form *ethane* [49] is presented as both a reaction scheme and as an energy diagram.

Possible routes to the formation of *ethylidyne* are shown in Fig. 2.1b, despite experimental [34–36, 49, 53, 54, 56–58] and theoretical [44, 51, 59, 60] efforts, the elementary steps involved in the transformation from *ethene* to *ethylidyne* are still debated. Further, the influence of co-adsorbates (i.e. *oxygen*, *CO*) on the reactivity (as a function of coverage) have been studied [39, 53, 57, 61, 62], however are not within scope of this thesis and are not discussed.

Various investigations on *ethene* hydrogenation on **supported (*Pt*) particles** also have been performed [25, 43, 63–66] and the following observations are reported. For the adsorption of *ethene* on *platinum* nanoparticles, the *ethylidyne* species is formed at slightly lower temperatures than 300 K; carbon polymers are already formed at 390–480 K showing no trace of attached *hydrogen* in contrast to single crystals [59]. Hydrogenation studies on *Pt* particles supported on silica (zeolites) indicate a structure insensitive behavior as for $Pt(111)$ [43, 63]. However, for particles supported on SiO_2 and Al_2O_3 with a size below 2 nm a structure sensitivity is observed. For progressively smaller sizes a four times increase in reactivity diminishes below 0.6 nm, until no reactivity was measured [64, 65]. On a more mechanistic level it was mentioned that *ethylidyne* would not be involved in the reaction in the case of supported particles [49, 67] and that in absence of *hydrogen* only the $di - \sigma$ species could be converted to *ethylidyne* [68].
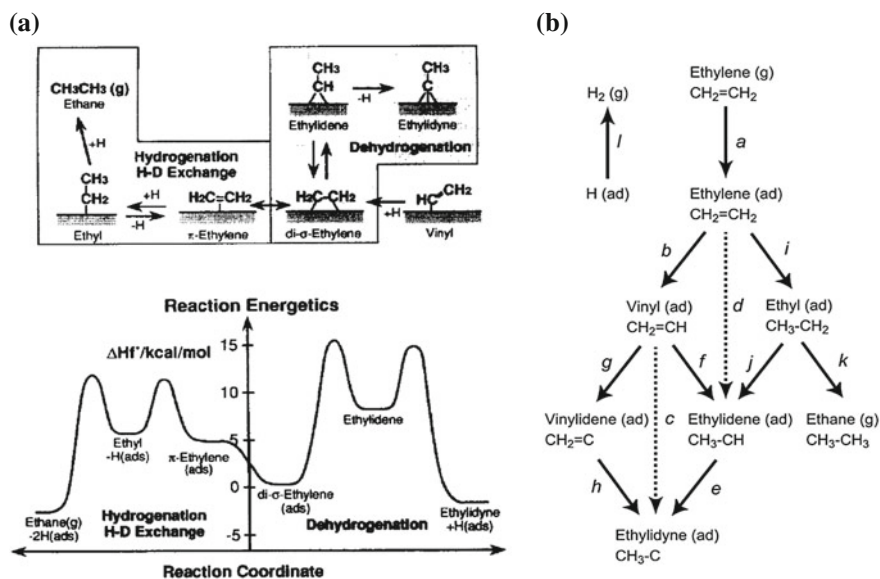
Fig. 2.1 Reaction scheme and energy diagram for the surface chemistry occurring during thermal conversion of *ethene* via hydrogenation on *Pt*(111), (a). The mechanisms shown, for both the conversion of *ethene* to *ethylidyne* (via an *ethylidene* intermediate) and for $H - D$ exchange and hydrogenation reactions (via a common ethyl moiety) [36]. Possible reaction pathways for *ethylidyne* formation over *Pt* group metals at $T > 200$ K, (b), three mechanisms are suggested: mechanism 1 (*a,b,f* and *e*), mechanism 2 (*a,b,g* and *h*) and mechanism 3 (*a,i,j* and *e*) [51]. **a** *Reprinted with permission from* [36]-*Copyright (1996) American Chemical Society*. **b** *Reprinted from* [51], *Copyright (2012), with permission from Elsevier*

In summary, the mechanisms of the catalyzed *ethene* hydrogenation reaction (even on simple model surfaces) is far from being settled. A better control on the reaction, i.e. by means of a well defined catalyst might help to shed light on some of these open questions.

2.1.3 Photocatalytic Water Splitting

Photocatalysis is based on the principle, that through adsorption of photons free charge carriers are generated, which supply catalyzed redox reactions with enough energy to get a reaction going. In the case of *water* splitting, the mechanism of photocatalytic *hydrogen* generation as illustrated in Fig. 2.2a, can be divided into three steps: first absorption of photons by a semiconductor material creating electron/hole-pairs, second migration to the surface or recombination, and third surface reduction/oxidation reactions [69].
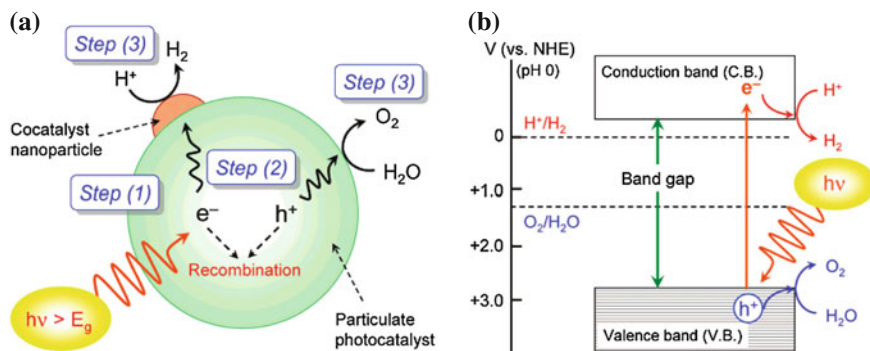
Fig. 2.2 Illustration of the mechanism of photocatalytic *water* splitting and corresponding energy diagram. **a** Process sketch. **b** Energy diagram. The process **a** involves three steps: photon absorption generating electron-hole pairs (step 1), charge-carrier separation (and recombination, step 2) and surface reduction/oxidation reactions (step 3). Schematic energy diagram **b** for exciton mediated *water*-splitting in a semiconductor. A minimum band gap size of 1.23 V versus NHE and suitable band edge positions are prerequisite [70]. *Reprinted with permission from* [70]-*Copyright (2007) American Chemical Society*

A photocatalyst material should adsorb UV-Vis photons efficiently to meet the requirement of using the sunlight as an energy source [69]. This property is determined by the DOS of the underlying semiconductor material. Electronic states in semiconductors, according to the band model, can be described by a valence band (VB) and a conduction band (CB) separated by a band gap (E_g) [71]. Illumination will lead to excitation of electrons from the VB to the CB and generation of empty states (so called 'holes' h^+) at the upper edge of the VB as soon as the photon energy exceeds the band gap ($h\nu > E_g$). Photo generated electrons and holes that subsequently migrate to the surface of the semiconductor without recombination can cause reduction (H_2 formation, $E_{H_2O/H_2} = 0\,V$) and oxidation (O_2 formation, $E_{OH^-/O_2} = 1.23\,V$ or oxidation of a hole scavenger) reactions [69]. The *water* splitting reaction ($2H_2O \rightleftharpoons 2H_2 + O_2$) can be described by the partial equations for reduction (Eq. 2.17) and oxidation (Eq. 2.18) [70].

$$4H_2O + 4e^- \rightleftharpoons 2H_2 + 4OH^- + 4h^+ \quad (red) \tag{2.17}$$

$$4OH^- + 4h^+ \rightleftharpoons O_2 + 2H_2O + 4e^- \quad (ox) \tag{2.18}$$

$$2H_2O \rightleftharpoons 2H_2 + O_2 \quad (sum) \tag{2.19}$$
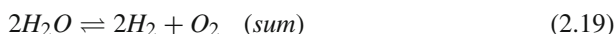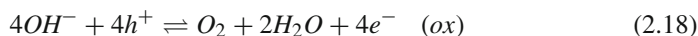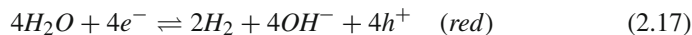
Since for the formation of the O_2 molecule a complex four hole oxidation is necessary (see Eq. 2.18), the oxidation reaction is quite difficult to achieve. In order to still be able to study the reduction reaction (Eq. 2.17) the oxidation step is replaced by the oxidation of a so called **hole scavenger**. The reduction potential of this scavenger lies energetically above the VB; the oxidation usually requires only one or two holes and can therefore be easily achieved. In the experiments within this thesis, ***TEA***

(triethanolamine) as a sacrificial hole scavenger was used. The disadvantage of a scavenger is, that it gets consumed during reaction (*hydrogen* evolution) and thus the reaction is no longer a cyclic process.[5]

In order for H_2 and O_2 formation to occur at the semiconductor surface the CB edge must be more negative than the reduction potential[6] of the H_2O/H_2 redox couple whereas the upper VB edge must be more positive than the oxidation potential of OH^-/O_2 as illustrated in Fig. 2.2b. These requirements for a semiconductor photocatalyst for *hydrogen* generation give rise to a **minimum band gap of** 1.23 eV, corresponding to a wavelength of 1008 nm. Due to losses from over potentials in various steps of the photocatalytic process, suitable band gaps for real photo catalysts lie in the range of 2 eV ($\leq$620 nm) and therefore these systems are in principle capable of utilizing light in the visible range of the solar spectrum [69]. For the discussion of nano structured materials as photo catalysts the above considerations of the general electronic structure of semiconductors are however not quite adequate, since quantum size effects have to be considered. These lead to a distribution of rather individual, discontinuous electronic states and enable the tailoring of the band gap of nanometer size objects by synthetic variation of their composition, shape and dimensions [72, 73].[7]

In the presented case *CdS*, as a prominent example for nano structured II-VI semiconductors, were used since their lower band gaps compared to corresponding oxide materials make them attractive candidates for visible light assisted photocatalytic *hydrogen* generation. The hole scavenger *TEA* protects the *CdS* from anodic photo corrosion (caused by oxidation reactions, i.e. $CdS + 2h^+ \rightarrow Cd^{2+} + S$) by swiftly consuming the holes, preventing any other oxidation reactions [75]. Using **nanorods (NRs)**, the metal sulfide photo catalysts permit short bulk to surface transfer distances for the charge carriers reducing the probability of electron-hole recombination by control of the rod diameter [69]. NRs are particularly advantageous compared to nano particles, because of their high chemical stability. Their large structures, up to hundreds of nanometers, prevent them better from agglomeration or coalescence [74]. Further, concerning noble metal decoration, it has been shown that these structures can serve as a suitable support for the nucleation and growth of noble metal clusters and larger particles from solution [76, 77].

After photon absorption, charge carrier separation and migration is the next crucial step of photocatalytic *hydrogen* generation. For the formation of *hydrogen* the generated electrons need to be transferred to the semiconductor surface or to a catalytic active metal particle. In a similar way holes must be transferred to the surface, in order to catalyze O_2 formation or the oxidation of a hole scavenger. High photocatalytic

---

[5] In terms of energy efficiency this makes the performance less productive; thus in perspective of an applied research the reduction potential and the availability of a scavenger needs to be taken into account.

[6] Redox potentials are given with respect to the normal *hydrogen* electrode (NHE) at $pH = 0$.

[7] For example, it was shown that the band gap size of CdS clusters decreases from about 3.6 to about 2.6 eV (bulk CdS $E_g = 2.4$ eV [74]) when increasing the diameter of the clusters from 10 to 60 Å.

activity can only be obtained when competing processes like trapping by surface defects or photoluminescence by electron/hole recombination can be suppressed to some extent [78].

The use of **noble metal particles** as co-catalysts has proven to greatly enhance the photocatalytic activity for *hydrogen* generation [70, 75, 76, 79]. A comparative study on CdS nanoparticles showed that amongst *Pt*, *Pd* and *Rh* the highest *hydrogen* production rate can be obtained over *Pt* metal[8] loaded *CdS* particles [79]. Thus, *Pt* was chosen as the co-catalyst metal. The metal particles act as an efficient sink for photo generated electrons and thereby catalyze the reduction of *water* to *hydrogen* [81].

In order to improve further the efficiency of the *hydrogen* evolution reaction, it is necessary to fully understand the underlying reaction mechanisms. Understanding and controlling the metal co-catalyst is one way to achieve higher reactivity.

2.2 Electronic Structure and EES

This section is dedicated to the main focus of the UHV experiments in this thesis, the electronic structure of metal surfaces, supported metal clusters and adsorbate interactions. In the light of the idea to tune reactivity by the modification of the catalyst (i.e. size) a brief introduction of adsorption and the electronic structure of the catalyst adsorbate interaction is given.[9] Further, an overview over EES results on metal particles and clusters is presented, followed by a sections about EES of adsorbates and the data treatment for comparison to gas phase spectra, applied in this work.

2.2.1 Adsorption

As mentioned, the way of how gases/adsorbates interact with surfaces is of crucial importance and considered as a key step in heterogeneous catalysis [85]. Consequently, in order to understand the nature of heterogeneous catalyst properties, it is essential to investigate the adsorption behaviour of reactants [35, 86]. A comprehensive understanding of adsorption requires detailed information about the electronic properties of the adsorbate-substrate pair [38], as the electronic structure of a surface is an essential factor determining its chemical reactivity [19]. A few thoughts, considerations and models utilized in this work are briefly mentioned in the following.

---

[8] These findings can also be related to *Pt* being the most active metal in electrochemical *hydrogen* evolution, owing to the ideal chemisorption strength of the adsorbed reaction intermediate H^+ corresponding to the Sabatier principle [80].

[9] An introduction to the underlying fundamental solid state theory can be found in the literature [41, 82–84].

The catalytic reactivity of a material can be described by **Sabatier's principle** [41, 87]. It states, that catalytic reactions proceed best if the interaction between reactant/adsorbate and surface is neither too strong, nor too weak[10]; thus the optimum reactivity is related to the heat of adsorption. Sabatier's principle is reflected in **volcano curves** [88], where the reactivity of different elements towards a particular reaction is plotted as a function of its position in the periodic table, and thus its electron(ic) configuration [87]. As a result of experimental and theoretical observations plotted as volcano curves, often *Pt* turns out to be the optimum catalyst material [89]. This is the reason for the choice of *Pt* in this thesis with respect to *CO* oxidation [1, 20] and for the hydrogenation of *ethene* [21, 35], where *Pt* is known to be ideal. The optimum reactivity of *Pt* (compared to other *d*-metals) is further well described using the popular ***d*-band model** [18–21]. The model describes trends in the interaction between an adsorbate[11] and a *d*-metal surface to be governed by the coupling to the metal *d*-bands [90].

Consequently, the bond strength between catalyst and adsorbate, and thus, whether a metal is reactive or not, can be estimated and manipulated changing i.e. the center or the filling, of the *d*-band. In the case of *Pt*, its aforementioned outstanding reactivity (for oxidation and hydrogenation) can be explained by an optimum position of the metal *d*-band. Thus, an ideal ability of the surface to bond to the adsorbates in the sense of Sabatier's principle, based on considerations on the electronic structure [91]. This model also explains, why molecules adsorb more strongly on under-coordinated sites, such as steps and defects, on surfaces. Since the surface atoms on these sites miss neighbors, they have less overlap and will be narrower, leading to a *d*-band shift and consequently a stronger bonding [92]. Based on this insight, the reactivity of supported clusters[12] with under-coordinated sites, can be explained and exploited to fine tune desired chemisorption bond strength and reactivity [15, 22].

Further, the adsorbate surface interaction can be described on the basis of **molecular orbitals (MO)**. Of course, the interaction involves the whole band structure of the solid, however these simplified MO considerations are sufficient to explain and understand the later experimentally observed adsorbate MOs (see appendix Sect. A.3 for gas phase EES spectra [93]) and their changes in the EES spectra. Briefly, the relevant (outermost) MOs for *CO* and *ethene*/*TCE* activation and chemisorption to a surface are summarized.

The **Blyholder model** [94–96] describes the MO interaction of a *CO* molecule at a transition metal surface. The lone pair of electrons on the *carbon* atom (5σ, HOMO) donates into the metal, forming a σ-bond. The *d*-orbitals of the metal donate electron density into the anti-bonding ($2\pi^*$, LUMO) orbital of *CO* giving rise to a π-bond (back donation). The energetic **shift of the 5σ orbital** is therefore directly related to the strength of the bond formed between *CO* and the surface (lower 5σ

---

[10] I.e., in the case of *CO* oxidation the metal should bind neither to strong for the *CO* to poison the surface, nor to weak to not being able to break the *oxygen* bond.

[11] An atom or molecule in front of a metal surface interacts with all valence states of the surface atoms. For a transition metal, a broad s*p*-band and a narrow *d*-band.

[12] Assuming a cluster with enough atoms, to be considered already metallic.

MO, stronger bond). Thus, the lower the energy level of the MO (i.e. high *BE*), the stronger the chemisorption of the *CO* [97].[13] For olefines, a similar MO, the **Dewar Chatt Dunchanson** model is known. As for *CO*, the *ethene* molecule donates π-electrons of its lone pair (HOMO) into a *d*-metal with the right symmetry and forms a σ-bond. By means of a back donation the *d*-orbitals of the metal donate electron density back into the $\pi*$ orbital (LUMO) of the olefin, weakening the $C = C$ bond, while the metal olefin π-bond gets stronger [98, 99]. The stronger the bond of the molecule to the surface, the lower the energy of the *ethene* HOMO, thus as measure of chemisorption strength the **BE of the *ethene* π_{C-C} is decisive**.

In cases of **substitute groups** on the olefine (i.e. chlorine), the different substitutes of the alkene alter its electronic structure and therefore the energy levels of the MOs. Dependent on the electronegativity of the substitute groups the strength of the $C = C$ bond is influenced [93, 100]. Using **substitute groups** such as halogens, the **strength of the $C=C$ bond is lowered**. Consequently, in the case of i.e. *TCE*, the interaction with the metal for both donation and back-donation gets less and chemisorption is more difficult. Further, the additional substitute groups attached to the olefine render the molecule more **sterically demanding**, complicating a strong chemisorption bond to the metal [101].

2.2.2 EES of Supported Clusters

From an experimental perspective, electron emission spectroscopy is probably the most important and often used technique to investigate the (valence) electronic structure [102]. The following briefly discusses the major results of the last few decades gained by means of EES with respect to clusters (without adsorbates). In contrast to gas phase PES [103, 104], conventional EES of supported clusters yielded little information [22].

For the first EES of supported 'clusters' reported, deposition was performed by **metal evaporation** and thus the experiments suffered form poor cluster size control and increase in size with the deposited amount [102, 105]. However, the evolution of deposited atoms/clusters to bulk properties were observed for *Ag* on *SiO*$_2$ [106], *Pt* and *Pd* on *C* [107] by means of XPS. In the case of silver, bulk features were established at a coverage of 5×10^{15} atoms/cm^2 and were preceded by a shift towards lower binding energy (BE) for increasing coverages in the low BE energy threshold of the EES spectrum by approximately 2.5 eV and the appearance of the spin-orbit split Ag 4*d* peaks. A similar behavior, was observed for *Pt* and *Pd* as a function of coverage. The most prominent feature of the EES however, was the onset

---

[13] The 5σ and 1π orbital are almost energetically degenerate, as a consequence of chemisorption and thus, the extent to which these MOs are joined is another marker of the strength of chemisorption.

of electron density at E_f and a bulk *Pd* behavior at 14×10^{15} atoms/cm^2 [108].[14] The origins of the aforementioned core level shifts were discussed in relation to final and initial state effects and as a function of 'size', based on growth models for the chosen deposition method [105, 109].

Later experiments, promoted through the development of **sophisticated cluster sources**, first 'real' EES data of size-selected *Pt* clusters was obtained and clarified earlier observations [110–112]. Comparing IP of *Pt* atoms and dimers, the support was seen to induce a 1.6–1.8 eV negative shift in IP due to final state screening (explanation see Sect. 2.2.3), suggesting that clusters of this size were not metallic. Also, the valence electronic structure was probed as a function of cluster size, showing the characteristic *Pt* spin-orbit split photoemission peaks. However, the experiments were performed using cluster coverages at which aggregation of the clusters cannot be ruled out and thus contradict observations made for similar systems in gas phase [96]. More recently experiments, present no new insights except, that EES (UPS) of 'size-selected' Ag_{923} and Ag_{25} clusters is achievable while assuring that no agglomeration[15] occurs [113]. Selected *Pt* clusters supported on TiO_2 probed by means of XPS [31], showed size-dependent shifts towards lower BE for increasing size, in agreement with the above literature.

Concerning MIES, only in the last decade and considerably few attempts have been done towards elucidating the electronic structure of supported catalyst materials. On *MgO* the alkali metals *Na* and *Li* have been probed [114] as well as *Ag* [115], deposited via vapor deposition—in either case the metals could hardly be detected and only at high coverages. Further, *Pd* on *MgO* was probed revealing small features at extreme high coverages [116, 117], the authors consider that a reduction in particles size beyond 1 nm will give rise to the change of the interaction process between He* and the adsorbate from AN to AD as soon as the transition from metallic-like to molecular behavior of the cluster takes place.

2.2.3 Photoemission of Adsorbates: Data Treatment

Photoemission experiments have been shown to provide much insight into the electronic structure of the adsorbate/adsorbent interaction [64, 97, 118]. Thus, this section is dealing with the peculiarities and problems of these techniques for the study of adsorbate interaction and approaches used in this thesis. General choices for data treatment are presented and explained, the interpretation is subject of the following section. The considerations are based on the general knowledge on PES/EES, the (experimental) principles are briefly introduced in the Chap. 3 in Sect. 3.2.5.

---

[14] Within this work also *CO* was dosed on the surface and the resulting UP spectrum revealed the expected *CO* MO peaks, which were shifted about +0.5 eV compared to of single crystal data thus indicating a possible cluster induced effect [108].

[15] Using lower coverages additionally characterized by means of STM.
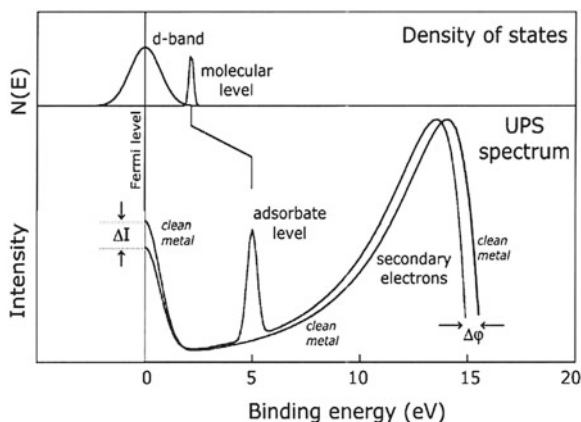
Fig. 2.3 Schematic UPS spectra of adsorbed species on a *d*-metal and the corresponding DOS of the metal and MOs of the adsorbed species [119]. *J.W. Niemantsverdriet: Spectroscopy in Catalysis: An Introduction, page 69. 2007. Copyright Wiley-VCH Verlag GmbH & Co. KGaA. Reproduced with permission*

The general picture of a EES experiment of an adsorbate on a *d*-metal, including the changes to the spectrum, can be seen in Fig. 2.3. The important features are the change $\Delta\phi$ in the work function (WF), attenuation of the *d*-band signal, ΔI, and the presence of adsorbate photoemission peaks. The change in WF can be explained using the jellium model as a simple description. An adsorbed species changes the dipole layer of the surface (depending on the dipole moment of the adsorbate) which is the surface contribution to the WF and this changes its value. The attenuated *d*-band intensity is changed because the adsorbed gas reduces the photo emission of the substrate [119].[16]

With the intention to study the adsorbate-substrate/catalyst interactions the occurrence of adsorbate peaks originating from the corresponding MOs are of paramount interest. In particular, a comparison with gas phase PE spectra of the free molecule can yield information on the MO interaction with a surface, which manifests itself as a shift in the IP of the adsorbate's MO [97, 99, 120, 121]. Further, the changes in the WF of the adsorbent can reveal more information on the nature of the interaction as well as corroborate conclusions reached by studying the shift of IPs.

In gas-phase studies the electron BEs are commonly **referenced to the vacuum level** and plotted on an ionization potential (IP) scale, whereas in the study of solids, E_F provides the experimental reference point on a BE scale (with $E_F = 0$) [101]. Thus, in order to compare gas phase spectra with spectra of adsorbed molecules

---

[16] However, this does not need to be interpreted as an electron flow from the *d*-band into the unoccupied states of the adsorbate.

on a surface, the BE scale of the latter is converted into IP energy scale.[17] For this purpose the WF has to be added to the measured electron BE. It is usual practice to reference with respect to a fixed WF value, either the WF of the clean substrate as recommended by Broughton et al. [122] or by using the WF of the saturated surface as suggested by Kelemen et al. [97, 101]. The practice of using a fixed WF reference point accounts for the fact that usually adsorbate BE (measured with respect to E_F), which belong to non-interacting orbitals, are fixed in energy when increasing the adsorbate coverage; although the WF is coverage dependent [101, 122]. Further details on the argumentation on the so called 'reference level problem' can be found in the literature [123, 124]. For referencing the EE spectra of this work, the WF of the clean metal substrate as indicated in Eq. 2.20 is added, thus following the procedure suggested by Broughton et al.:

$$IP_{solid} = BE_{solid} + \phi_{clean\,surface} \tag{2.20}$$

Furthermore, as seen in the sketch in Fig. 2.3, at high IP energies an increasing amount of **secondary electrons** [86, 119] are present. These electrons have undergone inelastic collisions and additional scattering events while traveling through the specimen and therefore contain no meaningful information about the electronic structure [97, 121]. Unfortunately, these electrons also suppress features from the adsorbed molecule in the spectra. In order to reveal features obscured by these secondaries, it is a common approach to subtract a fit function [125]; for the spectra in this work a polynomial function is fitted to the spectra and subtracted from the original spectrum [126].

A more detailed description of this approach, along with the used peak fitting procedure and details on the parameters, is stated in the appendix in Sect. A.1.5.

2.2.4 Interpretation of BE Shifts of Adsorbates in EES

Comparing gas phase spectra of the free molecules with that of adsorbed ones, two observations are made: loss of rotational fine structure, thus broadening of peaks, and a **shift in energies** on an IP scale. The extent of the energy shift reflects the state of the adsorbed molecule [101, 118]. However these shifts ΔE_B compared to the gas phase values cannot be directly related to chemical properties since they consist of mainly two parts that can be separated in contributions from physical adsorption, called **'relaxation shifts'** ΔE_{RV} and chemical adsorption ΔE_{BOND} (Eq. 2.21) [97, 118].

---

[17] It is noteworth, that this conversion of BE to IP still fails to completely define the adsorbate surface interaction in terms of the molecular orbitals of the adsorbate. In the case of UPS this is largely due to the fact that it is an integral technique and therefore probes a very large number of molecules at once, while at the same time requiring relatively high coverages (1 *ML*) to resolve individual peaks [97]. Only with a local technique at very low coverage, i.e. in the absence of adsorbate-adsorbate interactions which can lead to a 1 eV shift, can the true adsorbate electronic structure be realized.

$$\triangle E_B = \triangle E_{RV} + \triangle E_{BOND} \tag{2.21}$$

For **physisorption**, the valence band peaks belonging to MOs are found to shift towards lower IP compared to the gas phase values. Most of this effect can be accounted for as a **final state** effect, where the electron hole from the emitted electron is screened by surrounding molecules and the surface [97], thereby increasing the KE of the emitted electrons and lowering the IP [99]. This energy shift (ΔE_{RV}) is referred to as '**relaxation energy**' [118, 127] although it also contains a potential energy contribution which depends on the adsorption geometry in front of the surface [123].

For core-level BE the observed relaxation shifts (ΔE_{RC}) are usually bigger, as the presence of valence-electron reservoir in the metal allows the molecular equivalent of outer-shell relaxation, as electron charge is transferred into the molecule's valence orbitals during photoemission. Concerning the size of the molecule, the larger the molecule, the less the observed relaxation shift as the created hole charge tends to be screened already in the molecule itself [118].

In the case of **chemisorption**, the shifts oppose the trend observed and shift to higher BE/IP. The cause is an **initial state** effect, due to the change in the chemistry of the molecule [99], where the **bonding MO is lowered**[18] in energy [128].

The different changes expected in EES along with their energy shifts upon adsorption of a molecule are summarized in Fig. 2.4. The energy level diagram highlights again, that due to the possible convolution of the introduced initial and final state effects, it is difficult, to gain clear chemical information from EES if both physisorption and chemisorption occur [124].

Last, with respect to the differences found in the application of UPS and MIES for probing adsorbates, **symmetry considerations** are necessary. For UPS an additional selection rule based on symmetry needs to be applied, that has a polarization dependency of the light [96, 97]. Thus, the orientation of the adsorbate orbitals and the polarization of the incoming light both play a decisive role in the photoemission of an electron in UPS. Applying Fermi's Golden Rule, the photoemission experiment only detects electrons that lead to a total symmetric dipole transition matrix element and the final state of the photoemission is necessarily gerade. If the incident light is *s*-polarized then it has ungerade symmetry in the emission plane and in order for the transition matrix element to be non-zero, the initial state must also be ungerade. This occurs for *p*-orbitals that are parallel to the surface plane (i.e. 1π or $2\pi^*$ in the case of CO, as it is known to adsorb perpendicular to the surface in many cases). If the incident light is *p*-polarized then it has gerade symmetry and therefore only gerade initial states will photo emit (for CO, 5σ and 4σ).

For MIES, other selection rules apply which are not considered in this thesis. The UPS setup in this work uses unpolarized light, thus contributions of both *s*-and *p*-polarized light can be seen.

---

[18] For the particular case of C_2H_4 chemisorption the important MO to observe is the π_{C-C} MO, a high BE/IP corresponding to a strong bond [99].
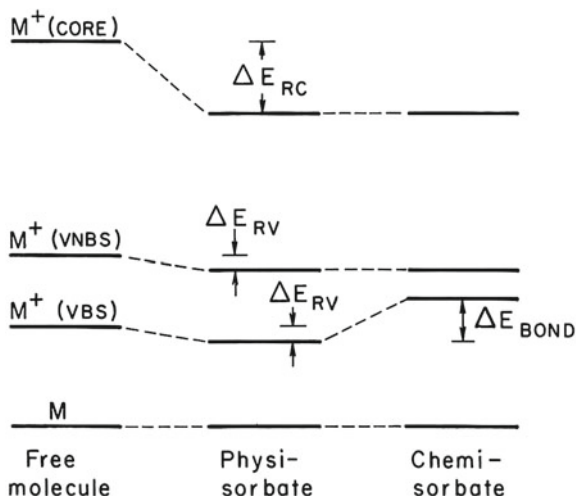
Fig. 2.4 Energy level diagram for EES (on an IP scale) from an adsorbate molecule, showing ground state M, core-hole state $M^+(core)$, as well as hole states $M^+(VBS)$ and $M^+(VNBS)$ of binding and non-binding valence orbitals to the substrate, respectively. Hole-state energies (BE) are lowered (ΔE_{RV}) upon physisorption, because of screening by the substrates (note the bigger relaxation for core holes ΔE_{RC}). Upon chemisorption, the bonding orbital can be identified by an increase ΔE_{BOND} in BE, may however include contributions of ΔE_{RV} [118]

2.3 Model Catalysts Under Ambient and Applied Conditions

In this section the motivation and common approaches for the study of model catalyst materials under ambient conditions is further elucidated. Additionally, in the context of the performed experiments, a short introduction into the stability of supported catalysts is given.

2.3.1 Materials and Pressure Gap

The understanding of surface reactions in general, with respect to catalytic reactions, was predominantly achieved using surface science [64, 86, 129]. Most of these findings, however were obtained on idealized systems and under idealized conditions, mainly on single crystals at low pressure and temperature conditions. The **dilemma of the traditional surface science approach** becomes apparent. Investigations of real catalysts (complex materials), conducted under relevant conditions by $in-situ$ techniques, provide little information on the surface of the catalyst, because the techniques which are surface-sensitive can often only be applied on model surfaces under particular conditions (e.g. vacuum). Further, despite being able to describe a catalytic reaction on a well-defined single crystal of a metal under well defined

and simplified conditions, this becomes tremendously more complicated when the same reaction runs over small catalyst particles on a support in a realistic reactor environment [119].

In this perspective, gaps between catalysis and traditional surface science have been identified in the mid 1980s: the '*pressure gap*' [130], the '*materials gap*' [131] and sometimes the '*complexity gap*'[19] [132]. Bridging these gaps are still important [119] and current issues in catalysis [133].

The first approaches to overcome these gaps were so-called single crystal approaches. The bridge to more realistic conditions was established by simply **extrapolating the results** from UHV/single crystal experiments to industrial conditions [134].[20] Considering the difference of roughly ten orders of magnitude in pressure and simplification of the reaction [131] this is a rather surprising result and does not work, but for a few examples [134, 137].

In order to overcome the **materials gap**, more complex surfaces under UHV conditions are studied. In particular, moving from single crystal surfaces towards metal oxide supported particles with different sizes and complexity. These model catalyst surfaces have significantly contributed to a better understanding [35, 64, 138–143]. Beside these supported particles, prepared in UHV usually by means of deposition by evaporation processes [27], other means of preparing model catalyst surfaces are know, e.g. using lithography [129, 144–146]. Except, for a few examples (as the use of size-selected supported clusters in this work) the prepared model materials often lack **reproducibility**, thus the majority of experiments cannot be reproduced and compared [26]. Furthermore, all these more realistic, model systems also mark only another way point, since the structure and chemical composition of a catalyst in operation will be largely determined by dynamic processes. This is problematic, since static conditions, typically applied in surface science, become increasingly irrelevant with increasing rate and pressure [134].

Therefore, by using these more sophisticated materials, two major strategies towards bridging the **pressure gap** have been pursued. On one hand there is the popular approach of **adapting conventional surface science techniques** to work at **elevated/high pressures for *in-situ* measurements** [24, 27]. This has been successfully achieved for a wide variety of instruments, i.e. STM [53, 147, 148], XPS [137] or (E)TEM [149–151]. Other, (optical) techniques have been readily applied at higher pressures as well, e.g. IRRAS [29, 152], S-SHG [49] or FEM [153]. On the other hand, a current trend in achieving insight at elevated pressures and more realistic conditions is the application of **new characterization methods**, such as micro-reactors [154, 155] or sensing devices, exploiting different physical properties [156–159].

Despite the mentioned efforts being only a rough and only partial overview on the current work on the materials and pressure gap, it is still a way to go until conventional

---

[19] The complexity gap is covering the study of gas and mass transport phenomena, which additionally to materials and pressure gaps need to be considered [132].

[20] The first example was the calculation of the rate of *ammonia* formation under industrial conditions [130, 131], based on well studied single-crystal surface reactions [1, 135, 136].

surface science allows for ultimate insight into the 'work' of an industrial catalyst. Using sophisticated model catalyst systems and a variety of different techniques, this work helps to contribute bridging the gaps.

2.3.2 Stability

With respect to reactivity studies of model catalysts, but also during application in industrial processes of 'real' catalysts, the stability and possible deactivation of a catalyst is a problem of great concern for both [160, 161]. In either case, good knowledge of the stability of the catalyst is a prerequisite for the study of its reactivity, however, often catalyst reactivity is probed [25, 27, 29], with addressing little attention to its stability.

Causes of deactivation are basically three-fold: chemical, mechanical or thermal—hereby six different routes of deactivation of catalyst material are described (some have been introduced before, without further explanation): poisoning (i.e. *CO* on *Pt*), fouling (i.e. coke formation during *ethene* hydrogenation on *Pt*), thermal degradation, vapor compound formation accompanied by transport, vapor-solid and/or solid-solid reactions, and attrition/crushing [162, 163].

Within focus on the ambient part of this work the **thermal deactivation**, and more particular sintering as temperature induced degradation mechanism is studied. Three mechanisms for crystallite growth are known and advanced: crystallite migration, atomic migration and vapor transport. These processes can in general be accelerated by promoters (i.e. *water* vapor, *oxygen*) and are usually irreversible.

Since vapor transport requires very high temperatures it is unlikely to happened in the conducted experiments, the two remaining possible mechanisms of particle growth are: Ostwald ripening (interparticle transport) or particle coalescence and are briefly introduced on an qualitative basis, further information in the literature [149, 164]. Figure 2.5 shows illustrations for the two processes along with theoretical particle size distributions (PSD)—as an initial PSD, the ideal case of a Gaussian distribution is taken (of course this varies with synthesis process). In general, the sintering of small metal particles on an oxide support are driven by a favorable, lower total energy of the particle, due to the loss of surface area and further enhanced by the additional lower surface free energy when uncovering the support surface [41].

The minimization of the surface free energy is the driving force for particle **coalescence** (merging of particles) after **migration** of particles over the surface. The movement of the surface atoms at elevated temperatures induces a Brownian type movement of particles on the surface and eventually two meeting particles coalescent and become one particle. The total number of particles decreases as larger particles are formed on the expense of smaller ones. With respect to the PSD the number of larger particles will rise, while the distribution in general will decrease in size—a particular characteristic is the tail towards larger particles. During **Ostwald ripening** the larger particles grow at the expense of smaller ones, as atoms get detached from

Migration and coalescence   Ostwald ripening
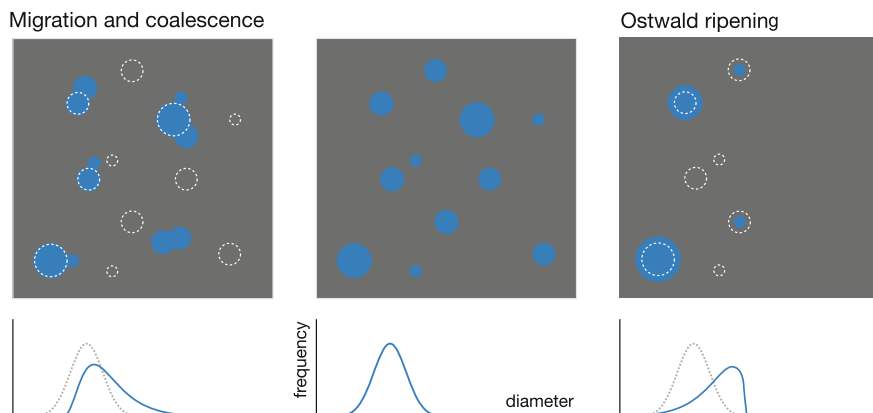
Fig. 2.5 Schematic illustration of Ostwald ripening (*right*) and Migration and coalescence (*left*) sintering processes of particles on surfaces. Below are shown the corresponding, theoretically to expect PSD

the smaller ones and subsequently attached to the bigger particles. When the sintering process is advanced, a decrease in the number of particles is expected, as atoms move to the larger particles and smaller ones 'disappear'. The maximum of the PSD is shifted to higher values with a sharp cut-off; however, the tail of the distribution faces towards smaller particles as a consequence of the continuous supply of smaller particles [149, 165].

The different mechanisms can in general be distinguished by their 'tail' of the PSD, even if this argumentation might be considered part-wise invalid based on experimental observations [166]. Concerning the temperature, when to expect sintering, the correlation with characteristic physical properties is useful [161]. The so-called Tamman and Hüttig temperatures, are directly related to the melting temperature. In the case of *Pt*, sintering is expected from $T_{Hüttig} = 0.3 T_{melting} \approx 608$ K, for small particles, already at lower temperatures. These observations also justify the use of metal oxides as support materials, as they are considered thermostable. In order to study sintering phenomena on a local level, particularly TEM [167, 168] and STM [169], have shown to be precise methods with insights into the fundamental mechanisms are, however disregard ensemble effects. Therefore, methods close to application [163, 164, 170] are the usual choice; new methods, correlating local phenomena with integral methods are highly desirable.

References

1. Ertl, G. (1994). *Surface Science*, *299–300*, 742.
2. Heiz, U., Sanchez, A., Abbet, S., & Schneider, W.-D. (1999). *The European Physical Journal D: Atomic Molecular, Optical and Plasma Physics*, *9*, 35.

3. Campbell, C. T., Ertl, G., Kuipers, H., & Segner, J. (1980). *Journal of Chemical Physics*, *73*, 5862.
4. Ertl, G., Neumann, M., & Streit, K. (1977). *Surface Science*, *64*, 393.
5. Engel, T., & Ertl, G. (1979). In D. D., Eley, H. P., & P. B., Weez (Eds.), *Advances in catalysis* (Vol. 28, p. 1). San Diego: Academic Press.
6. Ertl, G. (1980). *Pure and Applied Chemistry*, *52*, 2051.
7. Allian, A. D., Takanabe, K., Fujdala, K. L., Hao, X., Truex, T. J., & Cai, J., et al. (2011). *Journal of the American Chemical Society*, *133*, 4498.
8. Engel, T., & Ertl, G. (1978). *Journal of Chemical Physics*, *69*, 1267.
9. Matsushima, T. (1983). *Surface Science*, *127*, 403.
10. Zambelli, T., Barth, J. V., Wintterlin, J., & Ertl, G. (1997). *Nature*, *390*, 495.
11. Xu, J., & Yates, J. T. (1993). *Journal of Chemical Physics*, *99*, 725.
12. Ertl, G. (2001). *Chemical Record*, *1*, 33.
13. Kunz, S., Schweinberger, F. F., Habibpour, V., Röttgen, M., Harding, C., & Arenz, M., et al. (2010). *Journal of Physical Chemistry C*, *114*, 1651.
14. Heiz, U., Sherwood, R., Cox, D., Kaldor, A., & Yates, J. J. (1995). *Journal of Chemical Physics*, *99*, 8730.
15. Heiz, U., Sanchez, A., Abbet, S., & Schneider, W.-D. (1999). *Journal of the American Chemical Society*, *121*, 3214.
16. Sanchez, A. (2000). Ph.D. thesis, Unversité de Lausanne.
17. Heiz, U., Sanchez, A., Abbet, S., & Schneider, W. D. (2000). *Chemical Physics*, *262*, 189.
18. Hammer, B., & Norskov, J. K. (1995). *Nature*, *376*, 238.
19. Hammer, B., & Nørskov, J. K. (1995). *Surface Science*, *343*, 211.
20. Ruban, A., Hammer, B., Stoltze, P., Skriver, H., & Nørskov, J. (1997). *Journal of Molecular Catalysis A: Chemical*, *115*, 421.
21. Hammer, B., & Nørskov, J. (2000). *Advances in catalysis*, *45*, 71.
22. Meiwes-Broer, K.-H. (2000). *Metal clusters at surfaces: Structure, quantum properties, physical chemistry* (1st ed.). Berlin: Springer.
23. Kaden, W., Wu, T., Kunkel, W., & Anderson, S. (2009). *Science*, *326*, 826.
24. Watanabe, Y., & Isomura, N. (2009). *Journal of Vacuum Science & Technology A*, *27*, 1153.
25. Lundwall, M. J., McClure, S. M., & Goodman, D. W. (2010). *Journal of Physical Chemistry C*, *114*, 7904.
26. Boudart, M. (2000). *Topics in Catalysis*, *13*, 147.
27. McClure, S. M., Lundwall, M., Zhou, Z., Yang, F., & Goodman, D. W. (2009). *Catalysis Letters*, *133*, 298.
28. Larsson, E. M., Langhammer, C., Zorić, I., & Kasemo, B. (1091). *Science*, *2009*, 326.
29. McClure, S. M., & Goodman, D. W. (2011). *Topics in Catalysis*, *54*, 349.
30. Santos, V. P., Carabineiro, S. A., Tavares, P. B., Pereira, M. F., Órfão, J. J., & Figueiredo, J. L. (2010). *Applied Catalysis B: Environmental*, *99*, 198.
31. Watanabe, Y., Wu, X., Hirata, H., & Isomura, N. (2011). *Catalysis Science & Technology*, *1*, 1490.
32. Jensen, R. (2012). Ph.D. thesis, Danmarks Tekniske Universitet.
33. Ertl, G. (2007). In Noble lectures chemistry; Noble Foundation.
34. Godbey, D., Zaera, F., Yeates, R., & Somorjai, G. A. (1986). *Surface Science*, *167*, 150.
35. Somorjai, G. (1994). *Introduction to surface chemistry and catalysis* (Vol. 2). New York: Wiley-Interscience.
36. Zaera, F. (1996). *Langmuir*, *12*, 88.
37. Zaera, F., & Somorjai, G. A. (1984). *Journal of the American Chemical Society*, *106*, 2288.
38. King, D. A. (1984). The chemical physics of solid surfaces and heterogeneous catalysis: Chemisorption systems, Part B: 3. In D. A. King, & D. Woodruff (Eds.), *The chemical physics of solid surfaces and heterogeneous catalysis* (Vol. 3). Toronto: Elsevier Science Ltd.
39. Salmeron, M., & Somorjai, G. A. (1982). *Journal of Physical Chemistry*, *86*, 341.
40. Horiuti, I., & Polanyi, M. (1934). *Transactions of the Faraday Society*, *30*, 1164.

41. Chorkendorff, I., & Niemantsverdriet, J. W. (2007). *Concepts of modern catalysis and kinetics* (2nd ed.). Boca Raton: Wiley-VCH.
42. Dumesic, J. A., Rudd, D. F., Aparicio, L. M., Rekoske, J. E., & Treviño, A. A. (1993). *The microkinetics of heterogeneous catalysis* (1st ed.). ACS professional reference book. American Chemical Society.
43. Rioux, R. M., Komor, R., Song, H., Hoefelmeyer, J. D., Grass, M., & Niesz, K., et al. (2008). *Journal of Catalysis*, *254*, 1.
44. Zhao, Z., Moskaleva, L. V., Aleksandrov, H. A., Basaran, D., & Rösch, N. (2010). *Journal of Physical Chemistry C*, *114*, 12190.
45. Cassuto, A., Kiss, J., & White, J. (1991). *Surface Science*, *255*, 289.
46. Cassuto, A., Mane, M., Jupille, J., Tourillon, G., & Parent, P. (1992). *Journal of Physical Chemistry*, *96*, 5987.
47. Hatzikos, G., & Masel, R. (1987). *Surface Science*, *185*, 479.
48. Watson, G. W., Wells, R. P. K., Willock, D. J., & Hutchings, G. J. (2000). *Journal of Physical Chemistry B*, *104*, 6439.
49. Cremer, P. S., Su, X., Shen, Y. R., & Somorjai, G. A. (1996). *Journal of the American Chemical Society*, *118*, 2942.
50. Kubota, J., Ohtani, T., Kondo, J. N., Hirose, C., & Domen, K. (1997). *Applied Surface Science*, *121*, 548.
51. Aleksandrov, H. A., Moskaleva, L. V., Zhao, Z.-J., Basaran, D., Chen, Z.-X., Mei, D., et al. (2012). *Journal of Catalysis*, *285*, 187.
52. Beebe, T. P., & Yates, J. T. (1986). *Journal of the American Chemical Society*, *108*, 663.
53. Tang, D. C., Hwang, K. S., Salmeron, M., & Somorjai, G. A. (2004). *Journal of Physical Chemistry B*, *108*, 13300.
54. Öfner, H., & Zaera, F. (1997). *Journal of Physical Chemistry B*, *101*, 396.
55. Zaera, F., Janssens, T. V., & Öfner, H. (1996). *Surface Science*, *368*, 371.
56. Öfner, H., & Zaera, F. (2002). *Journal of the American Chemical Society*, *124*, 10982.
57. Grunes, J., Zhu, J., Yang, M., & Somorjai, G. A. (2003). *Catalysis Letters*, *86*, 157.
58. Fischer, T., & Kelemen, S. (1977). *Surface Science*, *69*, 485.
59. Watwe, R. M., Cortright, R. D., Nørskov, J. K., & Dumesic, J. A. (2000). *Journal of Physical Chemistry B*, *104*, 2299.
60. Chen, Y., & Vlachos, D. G. (2010). *Journal of Physical Chemistry C*, *114*, 4973.
61. Berlowitz, P., Megiris, C., Butt, J. B., & Kung, H. H. (1985). *Langmuir*, *1*, 206.
62. Cassuto, A., Touffaire, M., Hugenschmidt, M., Dolle, P., & Jupille, J. (1990). *Vacuum*, *41*, 161.
63. Rioux, R. M., Song, H., Hoefelmeyer, J. D., Yang, P., & Somorjai, G. A. (2004). *Journal of Physical Chemistry B*, *109*, 2192.
64. Henry, C. R. (1998). *Surface Science Reports*, *31*, 231.
65. Masson, A., Bellamy, B., Romdhane, Y., Che, M., Roulet, H., & Dufour, G. (1986). *Surface Science*, *173*, 479.
66. Ko, M. K., & Frei, H. (1805). *Journal of Physical Chemistry B*, *2004*, 108.
67. Rekoske, J. E., Cortright, R. D., Goddard, S. A., Sharma, S. B., & Dumesic, J. A. (1880). *Journal of Physical Chemistry*, *1992*, 96.
68. Mohsin, S. B., Trenary, M., & Robota, H. J. (1988). *Journal of Physical Chemistry*, *92*, 5229.
69. Zhu, J., & Zäch, M. (2009). *Current Opinion in Colloid & Interface Science*, *14*, 260.
70. Maeda, K., & Domen, K. (2007). *Journal of Physical Chemistry C*, *111*, 7851.
71. Kittel, C. (2006). *Einführung in die Festkörperphysik* Munich: Oldenbourg Verlag.
72. Wang, Y., & Herron, N. (1990). *Physical Review B*, *42*, 7253.
73. El-Sayed, M. (2004). *Accounts of Chemical Research*, *37*, 326.
74. Bao, N., Shen, L., Takata, T., & Domen, K. (2008). *Chemistry of Materials*, *20*, 110.
75. Vaneski, A. (2009). Master's thesis, Ludwigs-Maximilians Universität München.
76. Berr, M., Vaneski, A., Susha, A., Rodrigues-Fernandez, J., Döblinger, M., & Jäckel, F., et al. (2010). *Applied Physics Letters*, *97*, 093108.

77. Shemesh, Y., Macdonald, J. E., Menagen, G., & Banin, U. (2011). *Angewandte Chemie International Edition*, *50*, 1185.
78. Berr, M. J., Vaneski, A., Mauser, C., Fischbach, S., Susha, A. S., & Rogach, A. L. (2011). *Jäckel, F*. Feldmann: J. Small, *8*, 291–297.
79. Sathish, M., & Viswanath, R. (2007). *Catalysis Today*, *129*, 421.
80. Nørskov, J. K., Bligaard, T., Logadottir, A., Kitchin, J. R., Chen, J. G., & Pandelov, S., et al. (2005). *Journal of The Electrochemical Society*, *152*, J23.
81. Amirav, L., & Alivisatos, A. (1051). *Journal of Physical Chemistry Letters*, *2010*, 1.
82. Hoffmann, R. (1987). *Angewandte Chemie*, *99*, 871.
83. Cox, P. A. (1987). *The electronic structure and chemistry of solids*. New York: Oxford University Press.
84. Kittel, C. (1999). *Einführung in die Festkörperphysik* Munich: Oldenbourg Wissenschaftsverlag.
85. Ertl, G., Knözinger, H., Schüth, F., Weitkamp, J. (2008). *Handbook of heterogeneous catalysis* (2nd ed.). New York: Wiley-VCH.
86. Ertl, G., Küppers, J. (1985). *Low energy electrons and surface chemistry* (2nd ed.). New York: Wiley-VCH.
87. Norskov, J. K., Bligaard, T., Hvolbaek, B., Abild-Pedersen, F., Chorkendorff, I., & Christensen, C. H. (2008). *Chemical Society Reviews*, *37*, 2163.
88. Bligaard, T., Nørskov, J., Dahl, S., Matthiesen, J., Christensen, C., & Sehested, J. (2004). *Journal of Catalysis*, *224*, 206.
89. Falsig, H., Hvolbæk, B., Kristensen, I. S., Jiang, T., Bligaard, T., & Christensen, C. H., et al. (2008). *Angewandte Chemie International Edition*, *47*, 4835.
90. Mavrikakis, M., Hammer, B., & Nørskov, J. (1998). *Physical Review Letters*, *81*, 2819.
91. Greeley, J., Nørskov, J. K., & Mavrikakis, M. (2002). *Annual Review of Physical Chemistry*, *53*, 319.
92. Strasser, P., Koh, S., Anniyev, T., Greeley, J., More, K., & Yu, C., et al. (2010). *Nature Chemistry*, *2*, 454.
93. Kimura, K., Katsumata, S., Achiba, Y., Yamazaki, T., & Iwata, S. (1981). *Handbook of HeI photoelectron spectra of fundamental organic molecules: Ionization energies, ab initio assignments, and valence electronic structure for 200 molecules*. Tokyo: Japan Scientific Societies Press.
94. Blyholder, G. (1964). *Journal of Physical Chemistry*, *68*, 2772.
95. Kunz, S. (2010). Ph.D. thesis, Technische Universität München.
96. Crampton, A. (2011). Master's thesis, Technische Universität München.
97. Hüfner, S. (2003). *Photoelectron spectroscopy: Principles and applications* (3rd ed.). Berlin: Springer.
98. Brucker, C., & Rhodin, T. (1977). *Journal of Catalysis*, *47*, 214.
99. Demuth, J. E., & Eastman, D. E. (1974). *Physical Review Letters*, *32*, 1123.
100. Cassuto, A., Hugenschmidt, M., Parent, P., Laffon, C., & Tourillon, H. (1994). *Surface Science*, *310*, 390.
101. Kelemen, S., & Fischer, T. (1981). *Surface Science*, *102*, 45.
102. Wertheim, G. K., DiCenzo, S. B., & Buchanan, D. N. E. (1986). *Physical Review B*, *33*, 5384.
103. Cheshnovsky, O., Taylor, K., Conceicao, J., & Smalley, R. (1990). *Physical Review Letters*, *64*, 1785.
104. von Issendorff, B., & Cheshnovsky, O. (2005). *Annual Review of Physical Chemistry*, *56*, 549.
105. Wertheim, G. K., & DiCenzo, S. B. (1988). *Physical Review B*, *37*, 844.
106. Mason, M. G., & Baetzold, R. C. (1976). *Chemical Physics*, *64*, 271.
107. Mason, M. G., Gerenser, L. J., & Lee, S. T. (1977). *Physical Review Letters*, *39*, 288.
108. Takasu, Y., Unwin, R., Tesche, B., Bradshaw, A., & Grunze, M. (1978). *Surface Science*, *77*, 219.
109. Mason, M. G. (1983). *Physical Review B*, *27*, 748.

110. Eberhardt, W., Fayet, P., Cox, D. M., Fu, Z., Kaldor, A., & Sherwood, R., et al. (1990). *Physical Review Letters*, *64*, 780.
111. Fayet, P., Patthey, F., Roy, H. V., Detzel, T., & Schneider, W. D. (1992). *Surface Science*, *269–270*, 1101.
112. Roy, H.-V., Fayet, P., Patthey, F., Schneider, W.-D., Delley, B., & Massobrio, C. (1994). *Physical Review B*, *49*, 5611.
113. Wortmann, B., Mende, K., Duffe, S., Grönhagen, N., & von Issendorff, B., Hövel, H. (2010). *Physica Status Solidi (b)*, *247*, 1116.
114. Krischok, S., Höfft, O., & Kempter, V. (2002). *Nuclear Instruments and Methods in Physics Research B*, *193*, 466.
115. Stracke, P., Krischok, S., & Kempter, V. (2001). *Surface Science*, *473*, 86.
116. Krischok, S., Stracke, P., & Kempter, V. (2006). *Appllied Physics A*, *82*, 167.
117. Krischok, S., Stracke, P., Höfft, O., Kempter, V., Zhukovskii, Y., & Kotomin, E. (2006). *Surface Science*, *600*, 3815.
118. Brundle, C., & Baker, A. (1977). In C. Brundle & A. Baker (Eds.), *Electron spectroscopy: Theory, techniques and applications* (Vol. 1). New York: Academic Press Inc.
119. Niemantsverdriet, J. W. (2007). *Spectroscopy in catalysis: An introduction* (3rd ed.). New York: Wiley-VCH.
120. Brundle, C., & Baker, A. (1979). *Electron spectroscopy: Theory, techniques and applications* (Vol. 3). New York: Academic Press Inc
121. Henzler, M., Göpel, W. (2007). Oberflächenphysik des Festkörpers, unveränd. nachdr. ed. Teubner Verlag.
122. Broughton, J. Q., & Perry, D. L. (1978). *Surface Science*, *74*, 307.
123. Gadzuk, J. W. (1975). *Journal of Vacuum Science & Technology*, *12*, 289.
124. Anderson, S., & Nyberg, G. (1990). *Journal of Electron Spectroscopy and Related Phenomena*, *52*, 293.
125. Joyce, J., del Giudice, M., & Weaver, J. (1989). *Journal of Electron Spectroscopy and Related Phenomena*, *49*, 31.
126. Schweinberger, F. F., Crampton, A., Zimmermann, T., Kwon, G., Ridge, C., & Günther, S., et al. (2013). *Surface Science*, *609*, 18.
127. Harada, Y., Masuda, S., & Ozaki, H. (1897). *Chemical Reviews*, *1997*, 97.
128. Hagstrum, H. D. (1976). *Surface Science*, *54*, 197.
129. Somorjai, G., & Park, J. (2007). *Physics Today*, *48*, 293–302.
130. Stoltze, P., & Nørskov, J. K. (1985). *Physics Review Letters*, *55*, 2502.
131. Schloegl, R., Schoonmaker, R. C., Muhler, M., & Ertl, G. (1988). *Catalysis Letters*, *1*, 237.
132. Freund, H., Kuhlenbeck, H., Libuda, J., Rupprechter, G., Bäumer, M., & Hamann, H. (2001). *Topics in Catalysis*, *15*, 201.
133. Ciszewski, A., Kucharczyk, R., & Wandelt, K. (2013). *Surface Science*, *607*, 1.
134. Imbihl, R., Behm, R., & Schlögl, R. (2007). *PCCP*, *9*, 3459.
135. Somorjai, G. A., & Materer, N. (1994). *Topics in Catalysis*, *1*, 215.
136. Somorjai, G., & Park, J. (2007). *Catalysis Letters*, *115*, 87.
137. Pantförder, J. (2005). Ph.D. thesis, Friedrich-Alexander-Universität Erlangen-Nürnberg.
138. Libuda, J., Meusel, I., Hoffmann, J., Hartmann, J., Piccolo, L., Henry, C. R., et al. (2001). *Chemical Physics*, *114*, 4669.
139. Freund, H. (2002). *Surface Science*, *500*, 271.
140. Freund, H. J. (2007). *Surface Science*, *601*, 1438.
141. Goodman, D. W. (1995). *Chemical Reviews*, *95*, 523.
142. Heiz, U., Landman, U., & Henry, C. R. (2008). In U. Heiz, U. Landman (Eds.), Nanocatalysis. Berlin: Springer.
143. Heiz, U., & Bullock, E. (2004). *Journal of Materials Chemistry*, *14*, 564–577.
144. Johannson, S., Fridell, E., & Kasemo, B. (2000). *Journal of Vacuum Science & Technology A*, *18*, 1514.
145. Jacobs, P., Wind, S., Ribeiro, F., & Somorjai, G. (1997). *Surface Science*, *372*, 249.

146. Wegner, K., Piseri, P., Tafreshi, H. V., & Milani, P. (2006). *Journal of Physics D: Applied Physics*, *39*, R439.
147. Rößler, M. W. (2003). Ph.D. thesis, Freie Universität Berlin.
148. Reichelt, R. (2010). Ph.D. thesis, Ludwigs-Maximilians Universität München.
149. Hansen, T. (2006). Ph.D. thesis, Danmarks Tekniske Universitet.
150. Hansen, T. W., Wagner, J. B., Hansen, P. L., Dahl, S., Topsøe, H., & Jacobsen, C. J. H. (2001). *Science*, *294*, 1508.
151. Campbell, C. T. (2001). *Science*, *294*, 1471.
152. Rupprechter, G. (2004). *Annual Rreports Section "C"* (*Physical Chemistry*) *100*, 237.
153. Suchorski, Y., Beben, J., Imbihl, R., James, E. W., Liu, D.-J., & Evans, J. W. (2001). *Physical Review B*, *63*, 165417.
154. Henriksen, T. R., Olsen, J. L., Vesborg, P., Chorkendorff, I., & Hansen, O. (2009). *Review of Scientific Instruments*, *80*, 124101.
155. Ajmera, S., Delattre, C., Schmidt, M., & Jensen, K. (2002). *Sensors and Actuators B*, *82*, 297.
156. Fiordaliso, E., Murphy, S., Nielsen, R., Dahl, S., & Chorkendorff, I. (2012). *Surface Science*, *606*, 263.
157. Johansson, M., Lytken, O., & Chorkendorff, I. (1863). *Surface Science*, *2008*, 602.
158. Leppelt, R., Schumacher, B., Häring, T., Kinne, M., & Behm, R. J. (2005). *Review of Scientific Instruments*, *76*, 024102.
159. Langhammer, C., & Larsson, E. M. (2012). *ACS Catalysis*, *2*, 2036.
160. Tanabe, T., Nagai, Y., Dohmae, K., Sobukawa, H., & Shinjoh, H. (2008). *Journal of Catalysis*, *257*, 117.
161. Moulijn, J., van Diepen, A., & Kapteijn, F. (2001). *Applied Catalysis A: General*, *212*, 3.
162. Bartholomew, C. H. (2001). *Applied Catalysis A: General*, *212*, 17.
163. Bartholomew, C. H., & Farrauto, R. J. (2005). *Fundamentals of industrial catalytic processes* (2nd Ed.). New York: Wiley.
164. Bartholomew, C. H. (1993). *Applied Catalysis A: General*, *107*, 1.
165. Schlögl, K. (2011). Ph.D. thesis, Technische Universität München.
166. Datye, A. K., Xu, Q., Kharas, K. C., & McCarty, J. M. (2006). *Catalysis Today*, *111*, 59.
167. Hansen, T., Wagner, J., Hansen, P., Dahl, S., Topsoe, H., & Jacobsen, C. (2001). *Science*, *294*, 1508.
168. Harris, P., Boyes, E., & Cairns, J. (1983). *Journal of Catalysis*, *82*, 127.
169. Wang, B., Yoon, B., König, M., Fukamori, Y., Esch, F., & Heiz, U., et al. (2012). *Nano Letters*, *12*, 5907.
170. Campbell, C. T., Parker, S. C., & Starr, D. E. (2002). *Science*, *298*, 811.

Chapter 3
Experimental Methods

This chapter is dedicated to the utilized methods and their underlying theoretical background. The chapter is divided into three parts: in Sect. 3.1 the synthesis of size-selected metal clusters under vacuum conditions (for both UHV and ambient experiments) is described, Sect. 3.2 deals with the experimental techniques in the UHV regime, whereas Sect. 3.3 describes the methods used for the ambient experiments. Since some of the characterizations for the ambient experiments are performed in the UHV a strict separation of the methods is difficult; i.e. the electron emission spectroscopy (EES) techniques are treated in the UHV part including the XPS; despite being used for ambient experiments.

The cluster synthesis (for both UHV and ambient) as well as the UHV experiments have been performed at the **UHV setup** (nanocat) depicted in Fig. 3.1. The setup consists of three parts: the cluster source, the sample preparation and the UHV analysis chamber. Each of the sections can be separated by vacuum gates. The setup is equipped with two quadrupole mass spectrometers (QMS) which connect both the sample preparation and the UHV chamber to the cluster source and allow for deposition of mono disperse cluster catalysts either for UHV or for ambient experiments.

3.1 Cluster Synthesis

The formation of size-selected metal clusters requires sophisticated experimental conditions, which can be achieved by different approaches. The choice of the right cluster source is dependent on the subsequent experiments (i.e. gas phase or supported), the mass range and even the chosen material [6, 7]. As a prerequisite for study of clusters on surfaces, a optimal source needs high cluster flux with narrow size distribution and the possibility to deposit the cluster at low kinetic energy (soft-landing, Sect. 3.1.3). In this respect the laser ablation cluster source is one method of choice. Cluster catalysts reported in this work have all been generated using a high frequency laser evaporation source [1, 5, 8, 9]. Thus, only the performance and mode
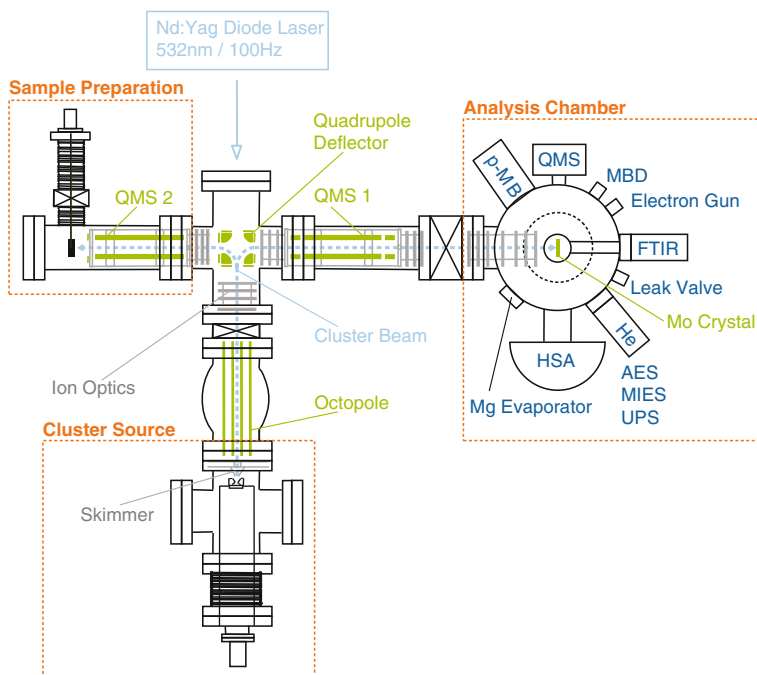
Fig. 3.1 Schematic sketch of the nanocat experimental setup (top-view). The setup is divided into three major parts (*boxes with dashed orange lines*): cluster source (*bottom*), sample preparation (*top left*) and analysis chamber (*top right*)[1–5]

of operation of this type of source (with *Pt* clusters as example) is described. Other concepts for cluster generation and an overview over existing sources are available in the literature [1, 6, 10–17].

3.1.1 Cluster Formation and Guidance

The setup for cluster formation by means of the high frequency **laser ablation cluster source** is depicted in Fig. 3.1. The beam (2nd harmonic, 532 nm) of a diode pumped solid state Nd:Yag Laser[1] (DPPS Spitlight, InnoLas, Germany; 70 mJ) with a frequency of 100 Hz is guided through the chamber and focussed (focal length 1.0 m) onto a rotating (1 Hz) metal target disc (*Pt*, 99.95 % purity, Goodfellow, U.S.A.). The produced metal plasma is subsequently cooled by two processes. In a thermalization chamber with a delayed (typical range 0.1–6 ms) helium (*He* 6.0, Westfalen, Germany) gas pulse, triggered by a piezo valve (piezo disc, PI, Germany; tunable

---

[1] The utilization of a diode pumped laser is preferential, because of high pointing stability and constant power output over time.

pulse width and intensity) and afterwards by an adiabatic (super sonic) expansion of the helium metal vapor through an expansion nozzle into the vacuum. This enables the cooling of the clusters' degrees of freedom and results in a beam of cold, charged and uncharged clusters with a tight kinetic energy distribution[2] [8, 18]. The cluster beam passes then through a skimmer (5 mm diameter) and afterwards proceed trough a linear octupole (150 mm length), details are described in Ref. [2]. The ions are guided further through the differentially pumped vacuum system through a pin hole and a first stack of Einzel lenses along the axis of the differentially pumped vacuum setup into the bender unit.

3.1.2 Mass and Charge Selection

The bender is a **quadrupole deflector** (including entrance and exit lens—D_{in} and D_{out}, respectively) and separates the charged clusters from the neutral ones. Uncharged clusters are unaffected by the potentials applied to the bender and deposited onto a quartz glass, perpendicular to the laser beam. The ion beam however is bent by 90° towards the direction of the analysis chamber or the sample preparation chamber ($\sim$ 90 % transmission). Generally, the potentials of the deflector rods are applied in such way, that cationic clusters are directed towards the direction of the used QMS. These clusters are focused into the QMS by an additional stack of einzel lenses (lenses 16, 17, 18). Depending on the bender settings, already a mass-preselection is achieved [20], as only clusters with a certain mass-to-charge ratio (m/z) can pass the bender on an appropriate trajectory through the exit hole into the following ion optics [4, 5, 21].

For **mass selection** down to a single mass, mass separation by the **QMS** (ABB Extrel Merlin, U.S.A.) is necessary and allows for choosing one single cluster size up to a mass range of $16000 \, m/z$.[3] Additionally, the QMS can be operated in an 'ion-guide' mode where a range of different sizes can pass. In the following a brief description of the general principles of a QMS are given, in order to explain the size distribution of the resulting cluster materials.

The separation of different ions in a QMS is based on the mass to charge ratio (m/z) and is achieved by applying electric fields that vary with respect to time (at

---

[2] The size distribution of the cluster beam can be tuned by the delay of the *He* pulse, its gas background pressure and is dependent on the geometry and distance between nozzle and thermalization chamber [2, 8, 18]. For smaller cluster sizes the *He* pressure (in the cluster source chamber) needs to be higher than for bigger ones [19]. The kinetic energy distribution upon impact is measured by a RFA (Sect. 3.1.3).

[3] The upgrade of the QMS mass range from previously 4000 [4] to 16000 m/z [22] increases the mass range in the case of *Pt* from Pt_{20} to Pt_{80} and thus opens up the room for the study of cluster sizes in the intermediate range between clusters and nanocrystallites without loosing the control of the size selection.

high frequencies).[4] The basic design is illustrated in Fig. 3.2a and consists of four
hyperbolic rod electrodes (the distance between the rod tips is $2r_0$) which create a
high-frequency quadrupole electric field. Usually the hyperbolic surfaces are well
approximated by rods with cylindrical cross sections, as it is in the QMS used in
this work. Onto these rods two voltage components are applied: a high-frequency
alternating (R.f.) potential $V \cos \omega t$ (phase shifted by $180°$ for rods next to each
other) and a superposed direct (DC) voltage U (the same sign for opposed rods) [23–
25]. An ion injected into the QMS in the direction of the axis of the field (z) starts
to oscillate at right angles to the axis of the field. For these ions equations of motion
can be formulated, the **Mathieu equations**, with u representing the displacement of
the particle along the x and y axis:

$$\frac{du^2}{d\xi^2} + \left[a - 2q\cos(2\xi)\right]u = 0 \quad \text{with } \xi = \frac{\omega t}{2} \tag{3.1}$$

Solutions of these differentials can be classified into stable and unstable
solutions—i.e. ones where an ion passes the mass filter (so called bounded solu-
tion where the displacement of the ion along x and y remains finite as $t \rightarrow \infty$)
and others that strike the rods and are filtered out (unbounded solutions, infinite for
$t \rightarrow \infty$), respectively. From these equations two parameters with dependence upon
the potentials applied can be defined: a (R.f. stability parameter) which depends
upon U and q (DC stability parameter) which depends upon V. These parameters
are defined as follows [25, 26]:

$$a = \frac{4eU}{m\omega^2 r_0^2} \quad and \quad q = \frac{2eV}{mr_0^2\omega^2} \tag{3.2}$$

For an ion to pass the mass filter the condition for stability in both x and y direction
must be fulfilled and can be plotted as a stability diagram (Fig. 3.2b). Here the
bounded, stable trajectories are colored in blue and the mode of operation of the
QMS is expressed in a function defined only by the two variables a and q.

In the case of **selected clusters** (Pt_x) the QMS is operated in such way that
$U/V = $ const.. In terms of the stability diagram, this is represented in the figure as
orange line, commonly known as the mass scan line. For fixed values of ω, r_0, V and
U and assuming singly charged particles/clusters[5] one can think of ion with different
masses being lined up along the mass scan line [27].

Adjusting the value for the U/V ratio appropriately, the slope of the mass scan
line can be set in such way that only ions of one mass fall in the stable region (dark
blue area in Fig. 3.2b). The QMS works as a band pass filter with defined boundaries
and ideally (here: $q = 0.706$, mass scan line passing through the peak) only one
mass is selected [23, 25–27].

---

[4] Other means, i.e. strong magnetic fields or flight time can also be used to separate ions based on
their m/z ratio.

[5] The assumption of singly charged clusters is justified, using a laser ablation cluster source
[1, 6, 9].

(a) **(b)**
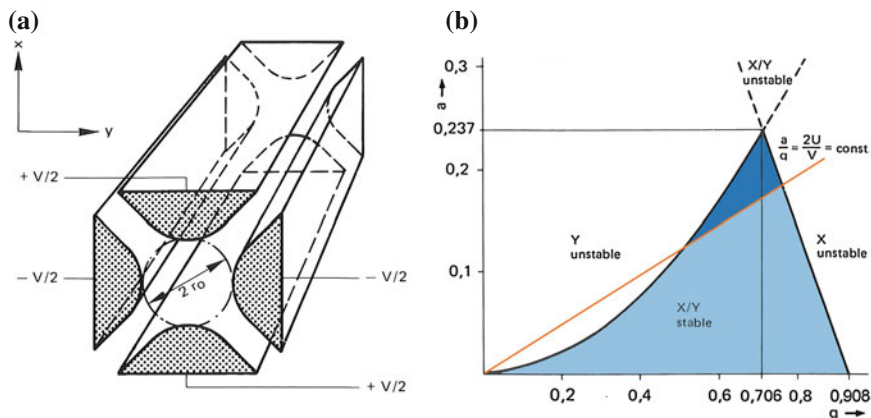
Fig. 3.2 Field generating potentials **a** and stability diagram (Mathieu diagram) **b** of a QMS. The *blue shaded areas* represent values of a and q which give rise to bounded trajectories. The *complete blue area* defines the stability region for ions when passings through the QMS for RF-only conditions ($a = 0$), however when applying an additional DC potential (in the plotted case the ratio $a/q = 2U/V$ = const.) only the *dark blue area* is stable, defined by the *orange line*—also known as the mass scan line [25]

For **unselected clusters** (Pt_n) the R.f. component is zero, thus $a = 0$ and consequently the mass scan line equals the q axis. As a result all ions in the (dark and light) blue area in Fig. 3.2b would pass the QMS ($0 < q < 0.908$) for small q. However, still a particular value for the R.f. voltage, i.e. q can be set (e.g. $q = 0.706$, as for the selected case). Now the QMS works as a high-pass mass filter [24, 25, 27] and the stable conditions are $0.706 < q < 0.905$, thus the smallest mass to pass the QMS is $q < \frac{0.706}{0.905} \approx 7/9$. This ratio can be readily applied to determine the lower mass limit to pass the QMS when depositing unselected clusters; i.e. for the case of selected Pt_{46} clusters with the mass 8970 u the smallest mass to pass when switching the DC current off is $7/9 \times 8970$ u $= 6970$ u corresponding to 35.7 atoms per cluster. The resulting smallest mass to pass is then Pt_{36}, which is stated in the following as $Pt_{n \geq 36}$, to describe the size range when depositing unselected clusters.

By changing the voltage for V a linear mass scan (as $m \sim V \sim 1/\omega^2$) [25] can be effected in order to characterize the abundance of different cluster sizes by the cluster source. **Mass scans** have been recorded by measuring the current on the sample in the UHV and the sample preparation chamber as a function of size, by means of the QMS. Different ranges and excerpts of mass scans are displayed in Fig. 3.3, showing well resolved peaks for different masses.

The optimization of the range of these mass scans is dependent on the optimization of the ion optics and in particular the bender; i.e. for the scan on the UHV side, the mass has been optimized for the deposition of Pt_{11}. Typical currents of the setup (on both sides) are in the range of up to 150–280 pA for selected Pt sizes with absolute mass selection. As a consequence of the natural isotope distribution of Pt (about 1/3
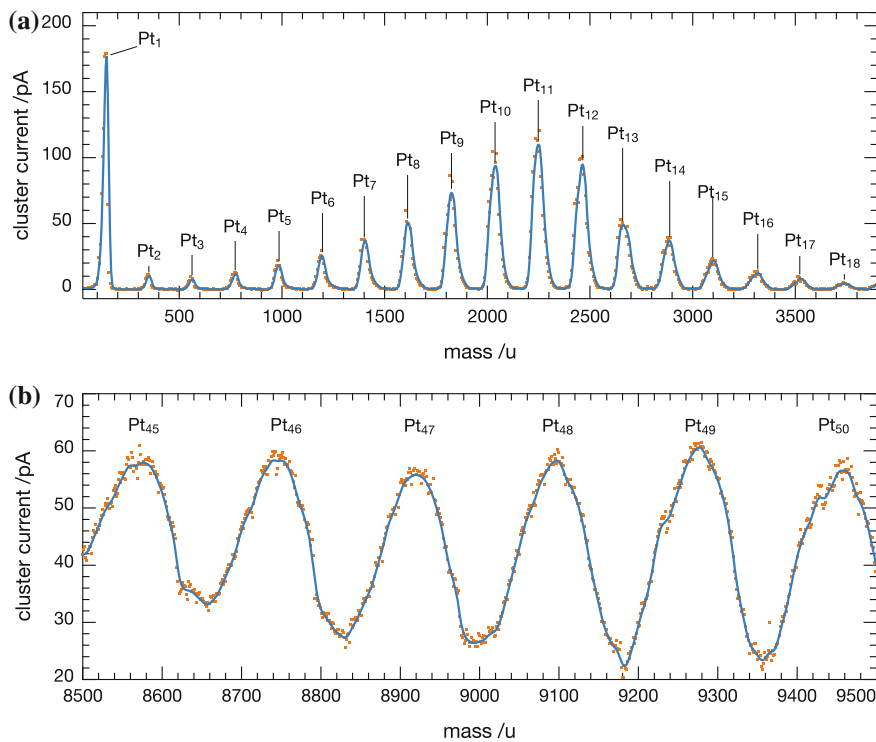
Fig. 3.3 Different ranges of mass scans, showing the size distributions of Pt^+ clusters selected by the QMS for the UHV part **a** optimized for Pt_{11} and for the sample preparation **b** for Pt_{46}. The *orange dots* represent the raw data, which has been smoothed for better visibility of the trend (*blue lines*)

for each of the major isotopes Pt^{194}, Pt^{195} and Pt^{196}) the peaks broaden towards higher masses. However, from an experimental point of view, this does not interfere with the mass selection down to one single cluster size [19], as during deposition the maximum of one mass is selected and thus only one clusters size is deposited. During optimization the resolution of the QMS can be adjusted by changing the U/V ratio on the QMS, as apparent from Fig. 3.2b—after the upgrade to $16000\,m/z$ both QMS utilized for mass selection have been working at a resolution of 6.4 (a particular value, used to achieve mass separation up to the high mass range).

3.1.3 Deposition

After size selection, the beam is guided through four more stacks of Einzel lenses and an single lens ('plate 2') towards the sample for UHV experiments.[6] The expansion

---

[6] For ambient experiment deposition, no additional lenses are used (see Sect. 3.3.1).
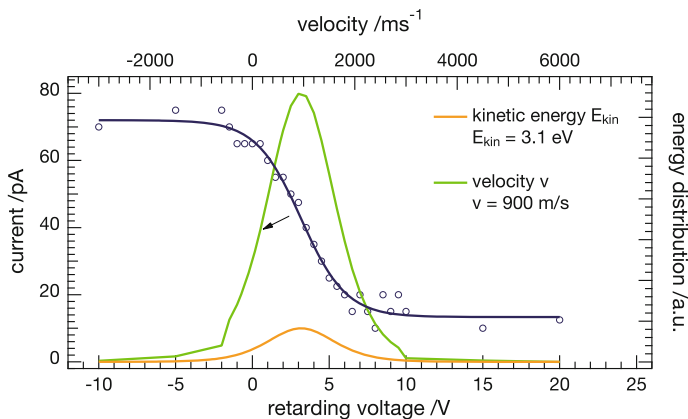
Fig. 3.4 Retarding field analysis for size-selected Pt_{11}^+ clusters deposited in the UHV chamber; measured current (*blue*) as a function of the retarding potential, the kinetic energy (derivative, *orange*) and the velocity distribution (*green*)

as well as the travel through octupole and QMS accelerate the clusters. At too high kinetic energies, one risks the destruction of the clusters upon impact by e.g. pinning, atom loss and consequently has no longer mono disperse cluster materials.

Therefore, the cluster catalysts need to be deposited onto the support under so called '**soft landing**' conditions at deposition energies **lower than 1 eV/atom** [6, 11, 28].[7] These conditions can be ensured by a **retarding field analysis** (RFA), where the cluster current is measured as function of an applied retarding potential on the samples. Figure 3.4 shows a representative RFA for size-selected Pt_{11}^+ clusters.

The blue curve is a fit of the measured cluster current as a function of the retarding voltage. The orange curve plots the first derivative of the blue curve and its maximum is the kinetic energy that the majority of the clusters have. The maximum kinetic energy is at about 9 eV,[8] which means for Pt_{11} a value of 0.81 eV/atom, thus assures soft landing. From the analysis it can further be seen, that the average velocity of the clusters equates to about 900 m/s [19, 31].

The deposition of size-selected *Si* clusters on *Ag*(111) [32] and *Pd* clusters on graphene [33] using a similar cluster source has been investigated using local probe experiments and supports the previous assumption of soft landing conditions. In order to focus the cluster beam onto the support an additional (attractive) potential of -2 V is applied for the UHV experiments, however no potential is applied for the cluster deposition of ambient samples.

The number of deposited clusters is obtained by integrating the measured ion current (617 Programmable Electrometer, Keithley Instruments, U.S.A.) on the substrate over the deposition time by means of a LabView program of in-house design [8, 31, 34]. The **cluster concentration** on the surface is determined under the assump-

---

[7] This value is further supported by theory, e.g. for Au [29] and Cu [30] clusters.

[8] The average of the clusters has actually only an energy of 3.1 eV, thus 0.28 eV/atom.

tion that all the clusters carry a single charge and are neutralized upon deposition. The concentration of clusters has usually been expressed in percentage of a *MgO* **monolayer** (**% ML**), with an atom density of 2.25×10^{15} atoms/cm^2 [2, 35, 36]. For the UHV studies the value needs then to be corrected for the actual single crystal area of 0.785 cm^2 at a diameter of $\emptyset = 10$ mm. With the recorded integral I and the elementary charge e the number of deposited clusters N on a single crystal in % ML is given by Eq. 3.3.

$$N \, [\%\text{ML}] = \frac{100 \times I}{0.785 \, \text{cm}^2 \cdot e \cdot 2.25 \times 10^{15}} \tag{3.3}$$

Despite the advantages for comparison of coverages on the MgO support (within the nanocat lab), this unit is not easily comparable to the commonly used total amount of particles deposited. For this purpose a unit based on the measured quantity (**discharge current of e per cluster per surface area**) **e/nm^2**, i.e. cluster per surface area is introduced. The conversion between the units is given by:

$$1 \, \%\text{ML} = 1.27 \, \%\text{ML}/crystal \, area = 0.029 \, \text{e/nm}^2 = 2.9 \times 10^{14} \, \text{e/cm}^2 \tag{3.4}$$

A conversion table (Table A.1) for some values can be found in the appendix on page 195. These new units are support independent and allow for quantification on both the local level (e/nm^2), as well as for integral measurements by simply changing the surface area and using e/cm^2. These introduced units are used throughout this thesis for comparability of the deposited amounts of clusters.

Knowing the exact amount of clusters deposited combined with the precise mass selection of one cluster size, one can calculate the amount of *Pt* atoms and the total amount of *Pt* used. This allows further for precise activity measurements, in case of calibrated methods for dosage and detection of the reactants and products. Beside the number of atoms, the important quantity from a catalysis perspective is the so called dispersion,[9] when measuring the reactivity of a heterogeneous catalyst material [38, 39]. Unfortunately, up to now no methods for the necessary calculation of surface atoms for (size-selected) clusters is known. Though there are plenty of theoretical calculations available for size-selected clusters in the gas phase [29, 40–42] and even results on surfaces [6, 43], experimental investigation (by means of local methods, e.g. STM or TEM) on the local structure have been (recently) reported [32, 33, 44–47] and are heavily dependent on cluster and support material as well the experimental conditions.[10] Further, with larger clusters support effects become more important along with an increasing number of structural isomers. Consequently, within this work only rough approximations of cluster shape (i.e. spherical) and surface atoms (Table A.2) are used and the more meaningful data is given by the number of clusters.

---

[9] The ratio of the number of surface atoms (available as reaction sites) to the total amount of atoms [37].

[10] Current experimental results suggest a transition from 2D to 3D structures for noble metal clusters in the size range of 8–10 atoms [18, 46–49] with strong support influence [43].

3.2 Ultra High Vacuum

All experiments under vacuum conditions have been performed in a bakeable, stainless steel UHV chamber (analysis chamber in Fig. 3.1) at a base pressure below 2×10^{-10} mbar.[11] For sample preparation, the setup is equipped with an e-gun and a *MgO* evaporator of in house design as well as an commercial sputter gun (EX03, Thermo Scientific, U.S.A.) and an evaporator (e-flux electron beam evaporator, Tectra physical instruments, Germany) for *Si* (or *Ti*) evaporation. The introduction of gases is possible by means of a leak valve (VG-MD7) and an molecular beam doser (MBD), both attached to a gas manifold. For cluster deposition the gate valve towards the cluster source is opened and closed afterwards to keep the base pressure in the chamber low.

Characterization and analysis are performed using the following surface science techniques: temperature programmed desorption/reaction (TPD/TPR), pulsed molecular beam reactive scattering (pMBRS) (IRRAS), metastable impact electron spectroscopy (MIES), ultraviolet photoelectron spectroscopy (UPS) and auger electron spectroscopy (AES). First the experimental setup is briefly described, followed by the support preparation and characterization as well procedures utilized in this work. These descriptions include a concise introduction to the underlying physical principles of the applied techniques (including experimental details).

3.2.1 Sample Holder

The single crystal samples are mounted onto a threefold *Cu* sample holder which can be moved by a manipulator stage in x, y (horizontal) and z (vertical) direction as well as rotated (by 360°) and thus allows to adjust the position of the crystals for each technique. Each of the single crystals (*Mo*(100), *Pt*(111) and *Mo*(112)—all MaTeck, Germany) is fixed by two W wires (Ø $= 0.3$ mm) spot-welded onto two Ta rods. Over these wires and the rods the crystals can be separately heated resistibly by applying a current on a feedthrough (outside of the vacuum) connected to the rods, as the different crystals are electrically isolated by *sapphire* plates. For temperature measurement of each crystal, a type C (*W*—5 % *Re*/*Re*/*W* 26 %) thermocouple (Omega Inc., U.K.) is spot welded onto the side of each single crystal. For details of the setup for temperature read-out and the control of the heating see appendix sub Sect. A.1.2. The crystal holder is brazed onto a hollow stainless steel tube, which is filled with *LN*$_2$ allowing for cooling the crystals as low as 95 K. A precise description of the sample holder can be found in the literature [2].

---

[11] A detailed overview over the used pumping systems is given in Ref. [3].

3.2.2 Support Preparation and Characterization

The following procedures have been applied for the cleaning and/or preparation of the supports. Representative EES spectra are shown in the appendix in Sect. A.1.6 and are in agreement with the literature.

The *Pt(111)* crystal has been cleaned by repeated cycles of oxidation ($T = 800\,K$, $p(O_2) = 5 \times 10^{-6}$ mbar, $\triangle t = 45\,min$), heating ($T = 1300\,K$, $\triangle t = 1\,min$) and Ar^+ sputtering ($T = 700\,K$, $p(Ar^+) = 5 \times 10^{-6}$ mbar, $\triangle t = 60\,min$, $U = 1\,keV$, $I \sim 11\mu A$). The procedure is followed by annealing ($T = 1300\,K$, $\triangle t = 1\,min$) and oxidation ($T = 650\,K$, $p(O_2) = 1 \times 10^{-7}$ mbar, $\triangle t = 2\,min$) [50]; subsequently the single crystal purity was checked by means of AES and MIES/UPS (detailed analysis in the following sections) and is in good agreement with the literature [51–53].

Impurities from both *Mo(100)* and *Mo(112)* crystals were removed by heating the crystals ($T = 2200\,K$, $\triangle t = 2\,min$), oxidation ($T = 800\,K$, $p(O_2) = 7 \times 10^{-7}$ mbar, $\triangle t = 15\,min$) [54] and heating ($T = 1150\,K$, $\triangle t = 2\,min$); the surfaces were then also analyzed by AES and MIES/UPS and are in agreement with the literature [36, 55].

The *MgO(100)* thin film was prepared accordingly to the literature [36], by evaporation of Mg (99.5 % purity, Merck Germany) in an oxygen back pressure ($T = 600\,K$, $p(O_2) = 5 \times 10^{-7}$ mbar, $\triangle t = 12\,min$) at an approximate growth rate of $1\,ML/min$ and was reordered by subsequent annealing ($T = 800\,K$). Recorded AES and MIES/UPS spectra show the features known from published data [35, 55–57].

3.2.3 Dosage of Gases

For dosage of molecules onto the surfaces the leak valve for conventional Langmuir dosage or a calibrated **molecular beam doser** (MBD) based on the design of Yates et al. [58, 59] is available in the setup. For all dosages in this work, the MBD was used,[12] allowing dosage of a well defined amount of molecules. This is achieved by calibrating the effusion of gas molecules from a known back pressure[13] through a micrometer sized pin hole into a second chamber with a micro-capillary plate providing separation from the analysis chamber. The better precision of this technique compared to Langmuir dosage is supported by an experimental comparison (appendix, Fig. A.1.2).

The number of molecules dN released by the doser in the time interval $\triangle t$ is given by Eq. 3.5 [2] as a function of the pressure p_g in the gas line and the molar mass m of the dosedmolecule.

---

[12] The crystals were brought into close proximity of the doser ($\sim$1 cm) and the molecules were adsorbed at $90\,K < T < 100\,K$.

[13] Measured using a baratron (MKS Instr., U.S.A.) with a precision of $\pm 1.0\,$mTorr.

$$dN = 2.5 \times 10^{13} \cdot p_G \cdot \Delta t \cdot 1/\sqrt{m} \qquad (3.5)$$

In order to express the dosed number of molecules in the unit ML, the number of surface atoms per area of the different surfaces need to be considered (a table stating the number of surface atoms for the different surfaces can be found in the appendix in Table A.1.4). As for the cluster coverage the surface area needs to be corrected by the area of the used single crystals (0.785 cm^2), e.g. the amount of surface atoms for the *MgO* surface accounts to 1.77×10^{15} atoms/crystal. The required back pressure p_G (in Torr) for a dosage time of 100 s is for that example given by:

$$p_G = \frac{1.17 \times 10^{15} \cdot \sqrt{m}}{100 \cdot 2.5 \cdot 10^{13}} \ (\textit{for } 1 \text{ molecule/SA}) \qquad (3.6)$$

All **dosage**s in this work are reported in the **unit molecules/SA**, the required back pressures for the dosed molecules onto the surfaces *MgO*(100) and *Pt*(111) are stated in the appendix in Table A.1.3.[14] For better comparability, the *TCE* dosage amounts in *TCE*/*SA* on all four surfaces and clusters (Sects. 4.4.1 and 4.4.2) are related to *MgO*(100), allowing one to compare the absolute amount of adsorbed *TCE* on the surfaces and clusters. In contrast all other dosages of *ethene*, *CO*, *oxygen* and *hydrogen* are related to the used surface *MgO*(100) and *Pt*(111), respectively.

3.2.4 Adsorbate and Product Detection (TPD/TPR)

Using Temperature Programmed (TP) experimental techniques, the desorption of a given molecule depending on the temperature is detected. The TP methods give access to the type of formed products on the surface, how strong molecules are bound, information on different reaction pathways and processes, such as adsorption or decomposition [39]. Temperature ranges in which a molecule desorbs, help to understand the interaction with the surface. Desorption in a low temperature range ($\sim$100–300 K), with weak adsorption correspond to physisorption. Stronger interactions, based on dative or weak chemical bonds, in the range between $\sim$300–600 K and are subsumed as chemisorbed species [60].

For a TP experiment, a mounted crystal is heated linearly with time,[15] using resistive heating and thermocouple controlled temperature measurement. The concentration of the desorbing species is monitored by a differentially pumped QMS and recorded.

---

[14] Under the assumption of a sticking probability of unity for the molecules at low temperatures [2].

[15] Changing the heating ramp, the resolution of the TP spectra can be influenced. A lower rate leads to separated peaks for molecules adsorbed in different states which do not differ significantly in adsorption energy.

The pumping speed of the UHV system is an important aspect, since it needs to be high enough in order to prevent re-adsorption. In the case of an infinitive pumping speed, re-adsorption can be neglected and the relative rate of desorption r (**TPD rate equation**) can be expressed as the change in adsorbate coverage θ (in ML) by time unit (with: reaction rate constant for desorption k_{des}, order of desorption n, pre-exponential factor v, desorption energy E_{des}, gas constant R, temperature T, start temperature T_o and heating rate β).

$$r = -\frac{d\theta}{dt} = k_{des} \cdot \theta^n = v(\theta) \cdot \theta^n \cdot exp(-\frac{E_{des}(\theta)}{R(T_o + \beta t)}) \qquad (3.7)$$

The activation energy and the pre-exponential factor both depend on the coverage as a result of the attractive or repulsive interactions between the adsorbate molecules [39, 61]. Different kinetic orders of reaction or desorption can be distinguished from variation of curve shape or variation of initial coverage [61]. The adsorbate coverage (quantitatively) and the surface coverage, can be obtained (if calibrated), because the integral under the curve is proportional to the initial coverage. Furthermore, the orientation of physisorbed adsorbates may be distinguishable [60]. Also, a value for the adsorption energy E_{ads}, which equals in general the energy of desorption E_{des} ($\Delta E_{des} = q_0 + \Delta E_{ads}$, with q_0 as the heat of adsorption) [62] can be obtained. This provides information on the adsorbate strength and also information on the temperature dependence of the adsorption strength. Lateral interactions between adsorbates can be derived through the coverage dependence of the adsorption energy and the pre-exponential factor which reflects the desorption mechanism.

A number of techniques, which can be applied to TP spectra in order to obtain kinetic data are known [37, 61, 63–66]. However, this further interpretation is time-consuming, if performed correctly; considering that the measured TPD data was not used for any kinetic analysis this is not further covered here.

With **TPR**,[16] a surface chemical reaction is investigated. The experimental procedure is the same as for TPD except that the increase in temperature provides the energy to overcome an activation barrier of a chemical reaction. The experimental conditions however may not correspond to 'real' reaction conditions, [61] as TPR are not measuring in steady state or even quasi-steady state conditions and thus no kinetic data can be obtained from the experiment.

The **TPD/TPR experiments** were performed using a differentially pumped quadrupole mass spectrometer (Balzer QMG 421, Switzerland) at a linear heating rate ($\beta = 2$ K/s) with the sample in line-of-sight to the QMS ($\sim$1 cm in front of the skimmer). The skimmer is mounted at the entrance near the ionizer of the quadrupole mass spectrometer, with an aperture of 3 mm, therefore only desorbing molecules from the sample are probed. Amplifying the ion current with a channeltron detector the setup has a detection limit of 10^{-15} Torr. The mass signals and corresponding temperature are recorded simultaneously, further details in the appendix (Sect. A.1.3).

---

[16] Both TPR and TDS are used for the description of the technique [61, 65].

3.2.5 Electron (Emission) Spectroscopies (EES)

Photoemission or (photo) electron emission spectroscopy (EES) is, in a strict sense, based on the photoelectric effect, where a sample irradiated by electromagnetic waves emits electrons. The number of emitted photo electrons is proportional to the intensity of the incident light, and the kinetic energy on the wavelength of the light (assuming that the minimum photon intensity is used).

Based on the discoveries of Hertz (photoelectric effect) and later Einstein [67] (describing light as quantized in photons of the energy *hv*), different developments led to the techniques XPS and UPS, which are essential tools in surface science [37, 68]. **XPS** (also called ESCA) using x-rays for excitation, was developed in the 1950s by Siegbahn et al. [69–71]. Using UV light instead, the development of **UPS**, is mainly based on the contributions of Turner et al. [72] in the gas phase as well as Spicer et al. [73] and Eastman [74, 75] on solids. Nowadays, synchrotron radiation makes the whole energy range between XPS and UPS available, overcoming the limitation of monochromatic light sources.

MIES traces its beginning to the discovery of Penning in 1927 [76] while studying discharge phenomena, suggesting an ionization process due to the collision between metastable atoms and target atoms. Therefore, MIES is often called Penning ionization electron spectroscopy (PIES) [77]. The underlying PIE processes involved in MIES are based on Auger de-excitation phenomena.

Last, **AES** is based on the emission of element characteristic Auger electrons, first observed by Auger in 1925 [78], interpreted as the result of a relaxation process of core-ionized atoms after irradiation with X-rays ("Auger decay").

For the presented methods, probe particle and the corresponding excitation energy are summarized in Fig. 3.5 and the appendix (Table A.1.6). As consequence of the different excitation wave length, core electrons (XPS/AES) or valence electrons (MIES/UPS) are probed (Fig. 3.6a). The mean free path of the ejected electrons for the methods XPS, UPS and AES defines their surface sensitivity. The relation between the mean free path λ of the electrons in metallic solids as a function of their kinetic energy (**universal curve**) is plotted in Fig. 3.6b. As visible from the graph, electrons in the range of 10–1000 eV have a mean free path in the order of only a few atomic layers (with a minimum for energies between 40 and 100 eV) and thus are ideal to probe the top most surface layers [80, 81]. The argumentation of the mean free path is also valid for MIES, however here the surface sensitivity is further increased by the probe particle, which is simply too big to penetrate into the surface and thus is absolutely surface sensitive.

The different methods are explained in the following subsections—some experimental details are stated in the appendix.
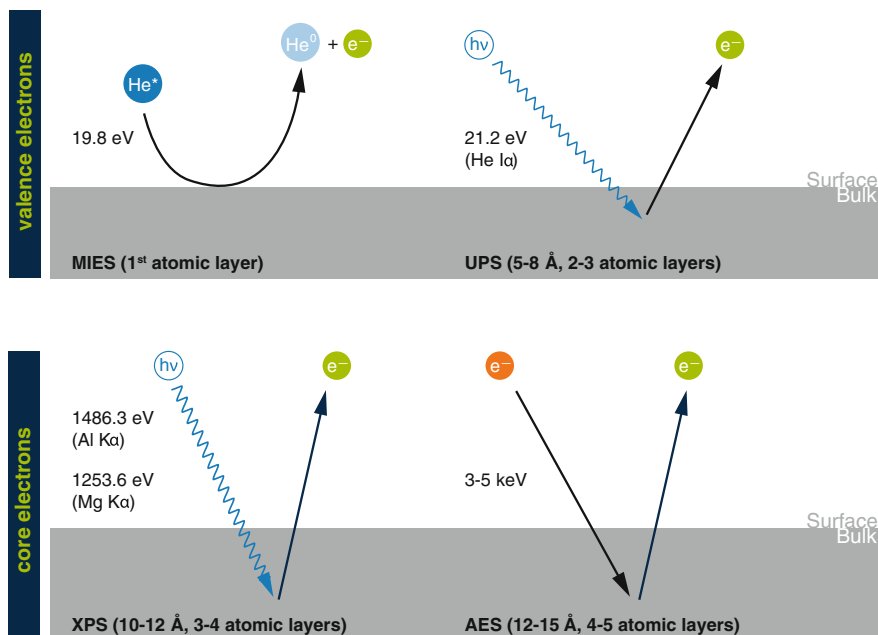
Fig. 3.5 Summary of the EES used in this work: probe particle, corresponding excitation energies and surface sensitivity

3.2.5.1 Auger Electron Spectroscopy

For AES the sample is excited by a beam of primary electrons (alternatively, with x-rays) with a kinetic energy between 1–10 keV. These electrons remove an electron from the (inner) core shells of a sample atom and the leaving electron creates a core hole. The ionized atom may return to its electron ground state via one of the two following de-excitation processes (Fig. 3.7) [68].

1. An electron from a higher shell fills the hole and the energy thereby released is emitted as a quantum of characteristic radiation (X-ray fluorescence),[17] Fig. 3.7a.
2. The hole gets filled by an outer shell electron; the available energy is then transferred in a radiation less process to a second electron (Auger electron) which leaves the atom with a specific kinetic energy (Auger process/decay), Fig. 3.7b.

In the case of the Auger-process the kinetic energy of the emitted Auger electron is not determined by the energy of the primary electrons, but its energy is a function entirely defined by the different energy levels of the orbitals involved in the process.[18]

---

[17] This gives rise to another non-destructive element specific spectroscopy, commonly used in analytical chemistry: X-ray fluorescence spectroscopy (XRF).

[18] Thus, varying the excitation energy of the electron beam one can distinguish between electrons which are emitted via an Auger process or not; the energy of an Auger electron does not change.
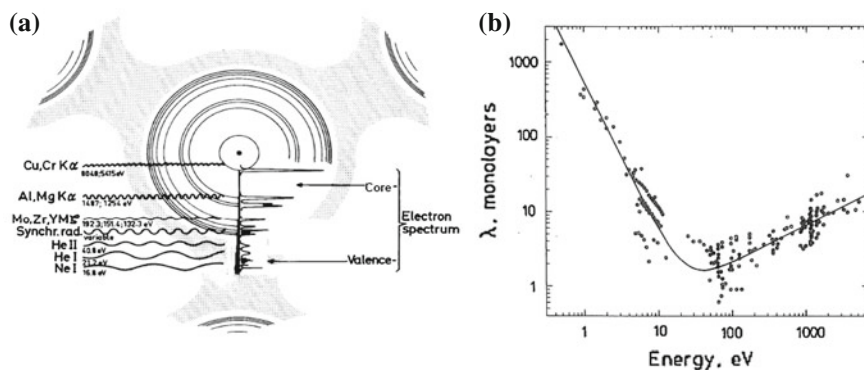
Fig. 3.6 Regions of BE accessible with different photon sources (**a**) *Solid circles*: localized, atom-like orbitals (core electrons). *Shaded area*: delocalized, molecular orbitals (valence electrons) [71]. Mean free path of electrons in metallic solids as a function of their energy (universal curve) [37, 68, 79] (**b**). *(a) Reprinted with permission from* [71], *Copyright © The Nobel Foundation 1981. (b) Reprinted from* [79], *Copyright (1979) Heyden & Son Ltd, with permission from John Wiley and Sons*
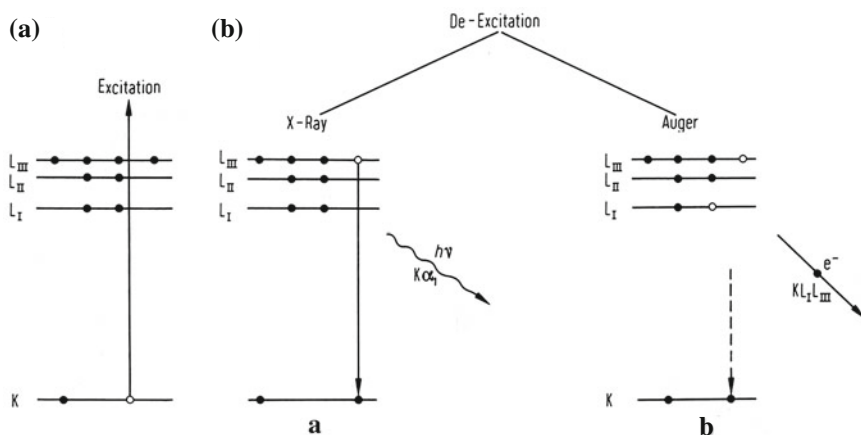
Fig. 3.7 Deexcitation processes for atomic core holes. **a** emission of X-ray radiation, **b** emission of an Auger electron [80]. *G. Ertl and J. Küppers: Low Energy Electrons and Surface Chemistry, page 29. 1985. Copyright Wiley-VCH Verlag GmbH & Co. KGaA. Reproduced with permission*

Furthermore, the Auger peaks are element specific, because they only depend on the orbital structure. The energy levels can be influenced by chemical bonds, causing a chemical shift. This allows one to gain information on the chemical bonding, if the transition involves valence levels [82].

The X-ray level **nomenclature** is used to describe Auger transitions; i.e. $KL_I L_{III}$ stands for a transition, where the initial core hole in the K-shell is filled by an electron from the L_I-shell, while the Auger electron is emitted from the L_{III}-shell (see Fig.

3.7b) [37, 60, 68]. As an approximation, the kinetic energy E_{kin} of the Auger electron emitted from a free atom can be described using the various binding energies $(E(X))$ of the involved shells with respect to the vacuum level. Including the work function ϕ and δE to compensate for relaxation processes the energy balance in Fig. 3.7b accounts to:

$$E_{kin}(KL_I L_{III}) = E(K) - E(L_I) - E(L_{III}) - \phi - \delta E \qquad (3.8)$$

The depth in the solid from which the information is recorded is mainly a function of the electron energy and only to a small extent dependent on the type of material (the probability for emitting an Auger electron decreases with increasing atomic number). Since the used primary electrons have about three times the energy than the emitted Auger electrons, the mean free path of the Auger electrons is determining the probe depth of the sample. The escape depth is in the range of a few ML, therefore an AES may not show the real surface composition but rather an average across the first atomic layers [68].[19]

In electron-excited spectra, the Auger electrons appear as small peaks in an intense background of inelastic scattered electrons (secondary electrons). In order to make the Auger peaks more visible, Auger spectra are plotted in a derivative spectrum as $dN(E)/dE$. As a convention the energy of an Auger peak is defined as the minimum in the high energy slope of the differentiated peak [39].

Experimental details—For this work the AES have been recorded using the electron gun of the hemispherical electron energy analyzer (VSW HAC 150) at an voltage of 3 kV for excitation. Modulation is achieved by applying an AC voltage on the sample using a function generator (HP 3310A). The lock-in technique (EG&G model 5204) is applied to extract the modulated signal, further details are stated in Sect. A.1.5.

3.2.5.2 X-Ray Photoelectron Spectroscopy

When a surface is bombarded with x-rays an electron may absorb all the energy of a photon and be able to escape the solid. The kinetic energy of that electron reflects the energy of the photon and, more importantly the BE of the electron [68]. The kinetic energy E_{kin} of such an electron with respect to the vacuum level is derived from Einstein's equation for the photoelectric effect [67].

The **conservation of energy** for all PES is expressed (in approximation) with ϕ as the work function of the bulk, the product $h\nu$ (with Planck's constant h and frequency ν) of the exciting electromagnetic wave equals the photon energy E and the binding energy E_B of the electron [60]:

---

[19] The variation of the angle of the primary beam with respect to the surface can alter the penetration depth, thus gives the possibility to determine absolute surface concentrations by comparing to well-known standard spectra [68].

$$E_{kin} = h\nu - E_B - \phi \qquad (3.9)$$

Using a monochromatic light source, it is thus possible to map out the electron density as a function of the BE, by measuring the kinetic energy of the emitted electrons. Since the electron density as a function of E_B is element specific the chemical composition of a sample can be determined, both qualitative and quantitative.[20] Further, the measured E_B is not only element-specific but also contains chemical information, because the energy levels of core electrons depend on the chemical state, i.e. the chemical environment of the atom. Such changes in binding energy in the range of 0–3 eV are known as **chemical shift** [81].

In order to correctly interpret the measured BEs, one has to further take into account **final state** effects. This is in contrast to the implicit assumption for the balance of energy (Eq. (3.9)), where based on Koopman's theorem, the measured IP equals the energy of the probed MO, thus does not change during the photoemission process. Therefore, one needs to consider the effect that photoemission data represent a state from which an electron has just left and not the case before the photoemission (**initial state**). As a result the measured BE is usually a convolution of both initial/final state and additional relaxation effects, complicating the interpretation of the measured spectra. Well known effects such as '**shake-off**' or '**shake-up**' are a consequence of relaxation process (loss of energy due to transfer to another electron of the atom, thus shift to higher E_B) and therefore amount to final state effects [83]. A deeper interpretation and explanation of more effects (e.g. multiplet splitting) goes beyond the scope of a short introduction, further information can be found elsewhere [37, 68, 81, 83, 84].

For excitation routinely monochromatic x-ray sources are used, also in this work a twin-anode setup with a *Mg Kα* (**1253.6 eV**) and *Al_Kα* (**1486.3 eV**) source is applied. Generally, the intensity of the electrons $N(E)$ as a function of kinetic energy is measured; however more often XPS spectra are plotted versus the BE. Other than the desired photoelectron peaks in a XPS spectrum, peaks originating form Auger decays are observed as a result of the mechanism introduced in the previous subsection. As a convention, photoelectron peaks are labeled according to the quantum number of the level (see previous AES subsection) from which the electron originates [39, 81].

An electron with orbital momentum l (0, 1, 2, . . . indicated as *s, p, d,...*) and spin momentum s has a total momentum $j = l + s$. As the spin may be either up or down ($s = \pm 1/2$), each level with $l \geq 1$ has two sub levels, with an energy difference called the **spin-orbit splitting**. As an example, the *Pt* 4_f level gives rise to two photoemission peaks, $4f_{7/2}$ (with and $l = 3$, $j = 3 + 1/2$) and $4f_{5/2}$ (with and $l = 3$, $j = 3 - 1/2$) [37, 68] and a fixed intensity ratio of $7/2 : 5/2 = 4 : 3$.

---

[20] Concentrations cannot be calculated without a structure model [37].

The resolution of XPS is determined by the uncertainties introduced by line width of the source ΔE_x, the broadening due to the analyzer ΔE_A, and the natural line width ΔE_{nat}[21] of the studied level:

$$(\Delta E)^2 = (\Delta E_x)^2 + (\Delta E_A)^2 + (\Delta E_{nat})^2 \tag{3.10}$$

Experimental details are stated along with the sample preparation for XPS measurements in the ambient Sect. 3.3.3.

3.2.5.3 Ultraviolet Photoelectron Spectroscopy

For UPS, for excitation UV photons with a considerably lower energy in the range of 10–100 eV [60] are used. In this work a *He* discharge lamp is employed, which emits photons with an energy of **He I**α (**21.2 eV**) [85]. The achieved energy resolution lies at best in the order of meV (for gas phase) due to the long life time of the ionized atoms. At these low excitation energies photo electron emission is limited to valence electrons.[22] Thus, it allows one to probe the electronic structure and bonding of the surface as well as changes in electronic levels due to the presence of adsorbates [37, 65].

With UPS the density of states (DOS) is measured, more precisely a convolution of the densities of unoccupied and occupied states (as a consequence of the final state sitting in unoccupied parts of the DOS of the studied material, obeying momentum conservation rules) which is therefore referred to as Joint Density of States (JDOS) [37]. In order to better understand these effects (and the difference between monochromatic and tuneable light sources), one can describe the flux of photo electrons in a specific direction R by using Fermi's golden rule. From this results, that the number N of the emitted photo electrons is due to the selection rule for the momentum $\Delta k = 0$, proportional to the combined DOS of the concerned bands. It is given in good approximation as [60, 86]:

$$N\left(R,\ E_f,\ hv\right) \sim \int D_i\left(E_i\right) \cdot D_f\left(E_i + hv\right) \cdot \left|\mu_{if}\right|^2 \cdot dE_i \tag{3.11}$$

D_i and D_f are the initial and the final DOS; E_i and E_f the energy of the initial and the final state, respectively and μ_{if} the matrix element for the dipole transition. However, the number of effectively emitted photo electrons is also dependent on other factors, such as the mean free path [3]. The simplest experiment is to measure at a fixed wavelength $hv = $ const. The distribution $N(E)$ is then both dependent

---

[21] ΔE_{nat} is given by the Heisenberg's uncertainty relationship $\Delta E_{nat}\Delta t \geq h/2\pi$, with Δt as the life time of the core ionized atom and h as Planck's constant.

[22] The emission of photo electrons is described in a three step model [60], addressing the processes before the electron leaves the solid—adsorption of the photon energy with excitation of a photo electron (1), that diffuses to the surfaces (2) and gets emitted from the surface (3) into the vacuum. Further details in [4, 80, 84].

on the initial density D_i and the final density D_f. This method results in an energy distribution curve (**EDC**), which includes the DOS of initial and final states, the aforementioned JDOS. The UPS spectra in the present work were recorded in the EDC method. Usually, the densities of the final state show less structures than the initial densities and is approximated by a free electron in the solid and so UPS spectra show mainly information about the initial DOS. This can be circumvented using synchrotron radiation, thus varying the wavelength. Keeping the KE of the emitted electrons fixed at a value, one probes at a fixed final state E_f the energy distribution of the initial states E_i; this method is known as constant final state (**CFS**). In constant initial state (**CIS**) one measures with a fixed initial state the energy distribution of the final states, thus keeping the energy difference constant [60, 87]. As the performed experiments within this work includes neither angle resolved measurements (ARUPS) nor variation of the excitation energy, the construction of the band structure of the investigated materials is impossible and the discussion of the underlying principles can be found elsewhere [31, 84].

Figure 3.8 shows a schematic sketch of the energy levels during the PES process. Based on the **conservation of energy**[23] E_{kin} is described by Eq. 3.9 as for XPS.

In order to measure the distribution of E_{kin}, the emitted electrons need to be sent through the energy analyzer into the detector. The analyzer A has a WF ϕ_A, different from ϕ_S. Through electrical contact between sample and analyzer the Fermi edges are equilibrated and a contact potential of $\Delta\phi = \phi_A - \phi_S$ exists. Assuming $\phi_S < \phi_A$, excited electrons with a low kinetic energy cannot reach the analyzer. In order to overcome this problem, an **accelerating potential** (in the presented work -30 V) is applied to the sample, with respect to the analyzer and shifts the spectrum for the value of the applied voltage. From the maximum kinetic energy
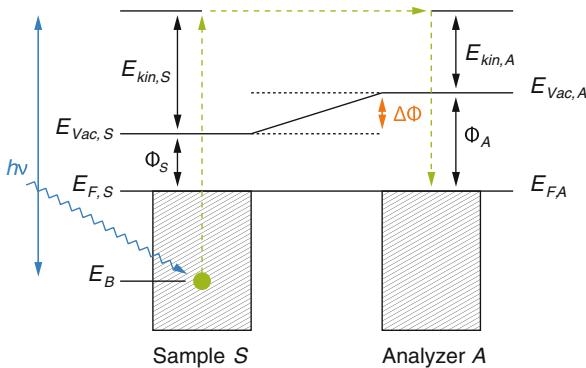

Fig. 3.8 Energy diagram of the PES process, sample (*left*) and analyzer (*right*) are in electrical contact [3]

---

[23] Concerning the conservation of momentum, compared to the momentum of an electron in the bulk, the momentum of the UV photon can be neglected. For this reason only perpendicular electron transitions in the band structure are allowed [4, 31, 88].

$E_{kin, A}^{max} (E_B = E_F) = hv - \phi_A$ for an electron (the higher edge of a resulting UPS spectrum) and the minimal kinetic energy $E_{kin, A}^{min} (E_{kin, S} = 0) = \phi_S - \phi_A = \Delta\phi$ (lower spectrum edge) follows the **width of the spectrum** ΔE (Eq. 3.12).

$$\Delta E = E_{kin, A}^{max} - E_{kin, A}^{min} = hv - \phi_S \tag{3.12}$$

Using Eq. (3.12) and the photon energy of 21.2 eV (for $He\,I\alpha$) one can calculate the macroscopic **WF** ϕ_S of the sample [37, 74, 84, 89]:

$$\phi_S = 21.2\,\text{eV} - \Delta E \tag{3.13}$$

Experimental details of the precise measurement conditions, the calibration and the used electronic setup are in the appendix in Sect. A.1.5. Details of the underlying ideas of the data treatment procedures for adsorbate EES are also found in the literature survey in Sect. 2.2.6.

3.2.5.4 Metastable Impact Electron Spectroscopy

Because UPS delivers information from several top atomic layers, it is difficult to characterize trace amounts of adsorbates. This limitation can be overcome e.g. by photoemission of adsorbed xenon (**PAX**) [90]. This technique is a site-selective titration technique, in which *Xe* adsorption sites are revealed by means of UPS; it has been used effectively to characterize catalytic systems [91, 92]. An alternative surface sensitive technique capable of determining trace amounts of adsorbates is metastable impact electron spectroscopy (MIES).

Metastable noble gas atoms with low kinetic energy[24] interact with the tails of the wave function of the surface atoms (and adsorbed species [93]) and eject electrons from the uppermost surface layer exclusively [77] as they cannot penetrate into the surface [94]. As a consequence, the kinetic energy distribution of ejected electrons (MIES spectrum) contains information on the electronic states of the solid surface [77] also known as SDOS (Surface DOS) [93].

Different processes (Fig. 3.9) can occur if a metastable atom is close to a solid surface; the interaction depends on the value of the WF of the solid and the solid material (i.e. insulator, semiconductor or metal). At the surface two possible deexcitation processes for the triplet state $He^*(2^3S)$ can occur, depending on the electronic properties of the material: Auger Deexcitation (AD) or Resonant Transfer (RT). AD leads directly to the ground state and occurs for all surfaces, but is about a factor of two magnitudes slower than RT. Thus, if possible, RT deexcitation occurs leading to either a negatively charged metastable or a positive ion. In the case of the cation the deexcitation into the ground state proceeds via Auger Neutralization (AN).

---

[24] MIES is obviously non-destructive, since the metastable atoms are introduced with low kinetic energies (< 0.1 eV [77]), preventing the metastable atoms from penetration into the surface and avoids sputtering effects.
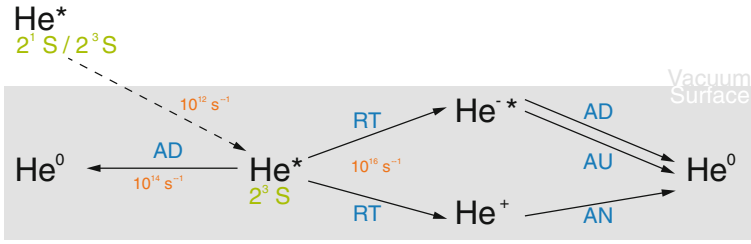
Fig. 3.9 Reaction scheme describing the possible interactions of a metastable He* atom with the surface [3]

For the negatively charged ion, again, one of two Auger decay processes (AD or Autodetachment, AU) lead to the ground state.

Within the scope of this work two processes are of importance: **AD** for the case of *MgO* as **insulator material** and the adsorbed organic molecules (no RT possible [3]) and RT followed by AN for the case of the metal single crystal surfaces (all $\phi \geq 3.8\,\text{eV}$ [3]). Further details on the other processes are well explained in the literature [3, 68, 76, 77, 88, 95–99].

Figure 3.10a shows the energy scheme of the **AD process**, where the metastable approaches the surface. In the mechanism an electron from the surface tunnels into the 1*s* orbital of the *He* and the electron in the 2*s* gets ejected, with a kinetic energy, that carries the the information of the BE of the electron originating from the solid.[25] The conservation of energy can be seen in Fig. 3.10a and as with UPS an expression for $E_{kin,}$ can be obtained [3, 31]:

$$E_{kin} = E^* - \phi_S - (E_F - E_B) \tag{3.14}$$

As this relation resembles the one derived for UPS (Eq. 3.12) again by simply balancing out the difference between the excitation energies for UPS (21.2 eV, *He Iα*) and **MIES *He* 2^3S** (**19.8 eV**) both spectra can be superimposed, so that the Fermi edges E_F match each other. This fact makes MIES and UPS spectra comparable. However, this is only possible for MIES driven solely by AD processes (thus, insulating materials).[26] Furthermore it needs to be kept in mind that MIES spectra include only information of the uppermost (surface) layer, whereas UPS is a convolution of the top two to three layers.

The faster **RT** process occurs on the majority of **metal surface**. RT followed by **AN** requires (Fig. 3.10b), that the 2*s*-electron of the *He** atom can tunnel into

---

[25] The presence of an adsorbate simply adds the adsorbates electronic energy levels to the band structure, along with any shifts due to bonding, and therefore the electron which tunnels into the 1s state can also come from an adsorbed molecule.

[26] Problems due to charging up the surface are observed for insulators [100]; the surface gets positively charged originating from the processes on the surface. Resulting spectra show a shift towards higher binding energies since the charging effects are rarely neutralized due to the limited conductivity.
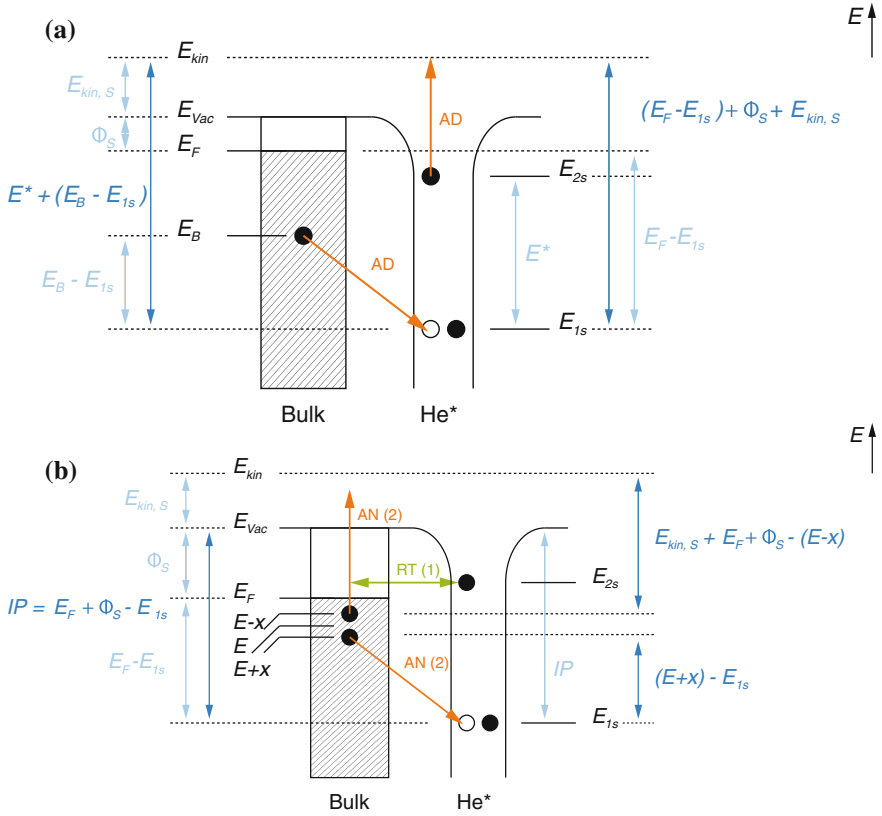
Fig. 3.10 Underlying MIES processes; AD for metals (**a**) and RT followed by AN for insulators (**b**) [3]

an unoccupied state of the solid. The He^+-ion, generated by RT is neutralized by an AN, where a surface electron tunnels into the $1s$ hole, while a second electron is emitted from the surface. Due to the fact that two electrons are involved in the deexcitation process, the detected electron holds information on the BE of both involved electrons and consequently the resulting spectrum cannot be interpreted easily and is not directly comparable to UPS (this is not the case for adsorbates on which the metastable still deexcites via AD). Nevertheless, conservation of energy allows the calculation of the width of the spectrum which gives access to the WF.[27]

$$\Delta E_{AN} = E_{kin, A}^{max} - E_{kin, A}^{min} = IP - 2\phi_S \tag{3.15}$$

---

[27] The values of the WF extracted from the MIES hold, as a result of the different processes involved, a higher error and thus need to be interpreted with care.

Data treatment in form of deconvolution of MIE spectra is reported in the literature [97], however involves quantum mechanical calculations. Since the MIE spectra of the bare metal surfaces are of minor interest, this is not done within this work. **Experimental details**—MIES spectra were recorded simultaneously with the UPS spectra, therefore the same experimental conditions apply and are discussed in Sects. 2.2.3 and A.1.5.

3.2.6 Vibrational Spectroscopy (IRRAS)

Within catalysis and surface science, vibrational spectroscopy techniques are important tools to identify adsorbates, study their binding behavior, can provide information on adsorption sites. In the case of infrared spectroscopy, the most common form of vibrational spectroscopy, the vibrations in molecules are excited by the absorption of photons in the infrared range. Since the IR has only been used for few measurements within this work the experimental setup is described below but no theory is presented here, but can be found elsewhere [37, 101–104]. In order to measure infrared adsorption spectra on single crystal surfaces, a variation of IR spectroscopy is used, called infrared reflection adsorption spectroscopy (IRRAS). A schematic sketch of the IRRAS setup of the nanocat is depicted in Fig. 3.11.

The IR beam leaves the N_2 purged infrared spectrometer (Thermo Scientific Nicolet 6700, U.S.A.—at single reflection mode) and passes through a CaF_2 window (1) into the mirror chamber (1×10^{-3} mbar). The mirror chamber focuses the beam onto the single crystal by means of a fixed flat mirror (2) and a focusing parabolic mirror (3) with a focal length of 25 cm (both mirrors are polished Al mirrors and can be adjusted in x, y direction). The beam enters then the UHV chamber through another CaF_2 window (1) and is reflected on the single crystal (4). The sample is part of the optical system and acts as a mirror. The silicate viewport (5) helps to position the crystal.
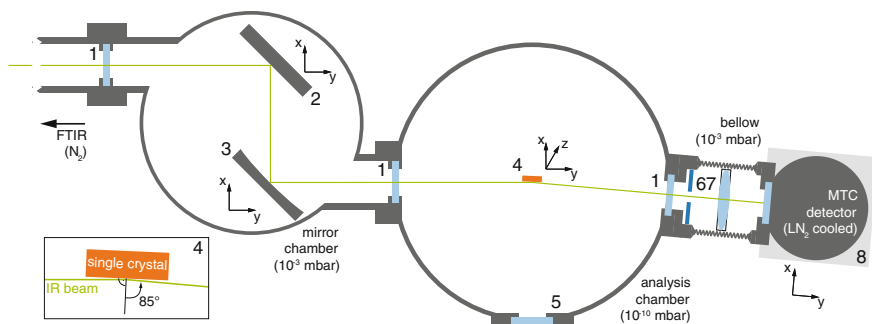

Fig. 3.11 Top view of the IRRAS setup in the nanocat lab, the insert (*left bottom corner*) shows the passing IR beam at a glazing angle of 85°, with respect to the surface normal of the single crystal (*4*). For details see text

The IR beam is focused onto the single crystal at a grazing angle and, during the reflection, of the **p-component**[28] of the IR light on the single crystal excites those vibrations of the adsorbed molecule for which the component of the dipole moment perpendicular to the surface changes (this is an additional **surface selection rule for IRRAS**).[29]

The IR beam leaves the UHV chamber, passes through another CaF_2 window and an aperture (6) (to exclude stray light) and gets focused through a KBr lens (7) onto the photo-element of the liquid nitrogen cooled mercury-cadmium-tellurium (MCT/A) detector (Thermo Scientific).[30] The detector and the lens system are connected under vacuum (1×10^{-3} mbar) consisting mainly of one bellow. The detector itself is mounted onto an x–y table (8); with this setup the detector can be moved along the three axis in order to obtain a perfect optical alignment [101, 105, 106].

Experimental details—At best a peak-to-peak noise level of 0.05 % (transmission at $4\,cm^{-1}$ resolution, a mirror velocity of 1.89 and averaging over 512 scans) is achieved. Data acquisition is performed by the software (IR software, Thermo Scientific Nicolet, U.S.A.), all spectra have been background corrected.

3.3 Ambient Techniques

All depositions of samples for later ambient experiments have been performed at the setup described in detail in Sect. 3.3.1. As mentioned in the introduction (Sect. 1.3) most of the experiments were conducted in a joined approach with a number of different collaboration partners. In the following the different applied techniques are presented, including a brief introduction of the underlying physical principles, the utilized samples (incl. preparation if applicable) and the measurement with experimental details.

3.3.1 Catalyst Preparation and Transfer

A schematic sketch of the sample deposition setup is shown in Fig. 3.12. After mass selection by means of the QMS (see Sect. 3.1.2) the clusters leave the QMS trough an exit lens attached to the QMS body. In an UHV chamber cross (2×10^{-9} mbar without deposition, 5×10^{-7} mbar during deposition) the cluster beam is then guided through a Mo shield (5) with an aperture of 9 mm (fixed on a grounded Cu feedthrough

---

[28] The steep angle results in a maximal electric field perpendicular to the surface (p-component) and therefore the largest absorption of the adsorbed molecules.

[29] For IR spectroscopy in general selection rules apply, i.e. which require for a molecule to be detected a dynamic dipole momentum which changes during the vibration.

[30] The cooled detector minimizes absorption by background *carbon dioxide*, *water* vapor and H-bonded *water*.
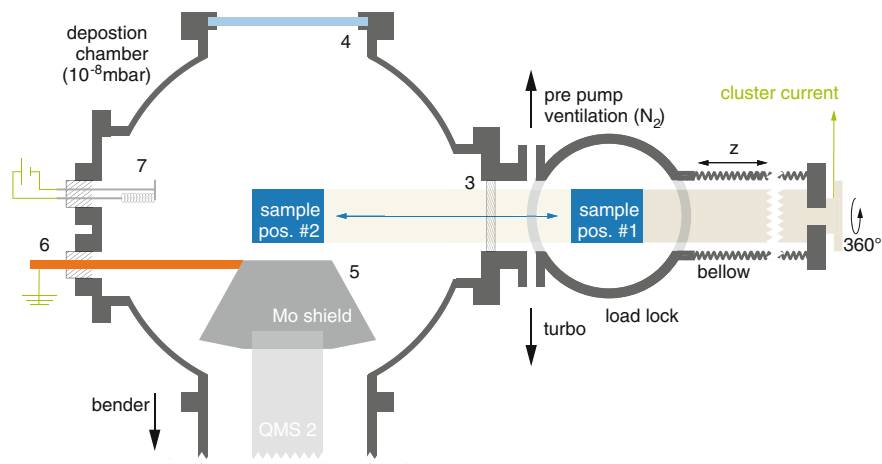
Fig. 3.12 Sample preparation setup consisting of a rotary, linear stainless z-slide transfer manipulator attached to a UHV chamber cross. On the manipulator tip customized sample holders are fixed and can be moved between the positions (#*1* and #*2*). The samples are prepared in a load lock, equipped with a differentially pumping system and separated by means of a pneumatic vacuum gate; for details see text

(6)) to protect the sensitive QMS electronics and to further achieve a homogeneous cluster beam. After leaving the aperture the clusters are deposited onto the samples (at sample position #2) under soft landing conditions (Sect. 3.1.3)—the distance between the sample and the aperture is 5–10 mm, depending on the used sample holder.

A precise position of the sample with respect to the aperture is achieved by visual control through a viewport opposite of the QMS (4) and on top (not shown). The sample holders are fixed at the tip of a rotary, linear stainless steel tube with motor driven z-slide transfer (150 mm—PI Instruments, Germany), which is electrically insulated from the vacuum setup. The neutralization current of the clusters can be read out by a pico ammeter (Keithley Instruments, U.S.A.) at the end of the manipulator arm and allows for coverage calculation similar to the UHV analysis chamber (see Sect. 3.1.3). Subsequent to deposition the sample is moved into (sample) position #1 in the load lock and automatically the pneumatic gate (3) closes, separating the deposition chamber from the load lock. The area behind the gate (incl. the load lock) is pumped by a turbo molecular pump and through a bypass also by a rotary pump. For venting the system the turbo pump (Leybold, Germany) is separated manually by a vacuum gate, the rotary pump by a valve (VAT, Switzerland) and the cavity is flooded with nitrogen. The sample can then be removed from the load lock and can transferred for further experiments. Loaded with a new sample the cavity gets pre-pumped and then evacuated by the turbo pump. Within minutes a pressure of 1×10^{-6} mbar is reached and allows one to introduce the sample into the preparation chamber.
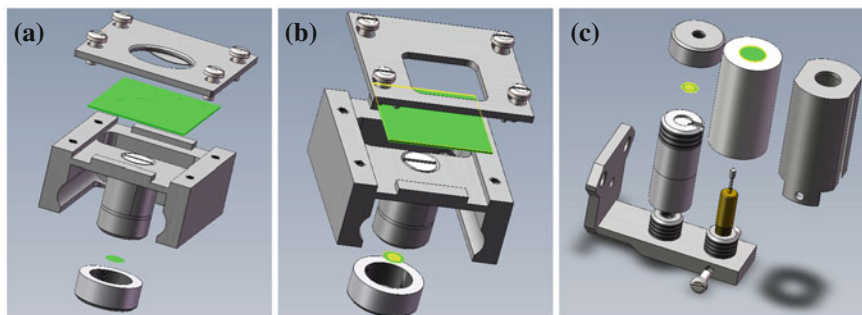
Fig. 3.13 Holders for sample preparation for ambient experiments, one holder at a time is attached to the manipulator arm by means of two screws. Holders (**a**) and (**b**) can accommodate one sample (*green*) of the indicated type and additional a TEM sample at a centro-symmetric position; on holder (**c**) also two TEM samples can be fixed

For deposition of clusters onto **insulating materials** (e.g. INPS chips, Sect. 3.3.4) it is necessary to provide negative charges for neutralization during deposition. Using an ion gauge (Bayard–Alpert type [107], tectra, Germany) *Ta* filament (7) an electron-shower for neutralization is available. Typically a current of 4 A and a potential of 10 V is applied, resulting in a emission of electrons with a stable current of 250–300 pA on the sample. The emission is tunable and set to a value to overcompensate for the arriving charges and avoid charging (the Mo shield protects the sensitive QMS from charges).

Different **sample holders** for the sample types have been constructed (Fig. 3.13); all holders can hold two samples at a time, increasing the efficiency of the setup. The holders can accommodate the following sample types: TEM grids, ETEM grids, μ-reactors, SiO_2 wavers (XPS), INPS chips, and GC samples.[31] A detailed list of sample types, support material and conductivity are stated in the appendix in Table A.2.1. All holders are constructed to fix the sample in line with the central axis of the manipulator arm and further fix the sample with either a screwable cap (TEM grids) or mask, with an opening corresponding to the desired deposition area.

The holders in Fig. 3.13a, b can hold a sample (XPS, INPS or μ-reactor) and a TEM grid at the same time with both samples being centro-symmetric. This allows one to deposit a sample of the mentioned type and a TEM sample without breaking the vacuum, changing the deposition conditions and at the same position by simply rotating the manipulator by 180°. This results in comparable deposition condition for the two samples.

With the holder in Fig. 3.13c also two TEM samples can be fixed and deposited subsequently without breaking vacuum. The area on which the current is read out, is at least the cap size for the TEM holders (diameter of Ø = 10 mm). Thus, it is slightly bigger than the aperture opening of the Mo shield and one can assume that

---

[31] Glassy carbon (GC) and TEM for electrochemical measurements were deposited, but the results not presented in this thesis.

all clusters exiting the aperture hit the sample and their discharge current is recorded. A characterization of the cluster beam and coverage is performed by means of XPS and TEM (see Sect. 5.1).

3.3.2 Transmission Electron Microscopy (TEM)

TEM allows to probe details on an atomic scale, as in microscopy the resolution is limited by the wavelength of the used probe entities. Thus, with a wavelength of 400–700 nm for photons in the visible light range features smaller than about 1 μm cannot be resolved with a standard optical microscope [37]. However, by lowering the used wavelength the resolution of a microscope can be improved and in the case of TEM this is achieved by means of electrons as probe entities, with wavelengths in the range a few picometer (e.g. 0.00197 nm for a 300 kV microscope). Further with the use of electrons, charged particles are used which can be accelerated to high energies with short wavelength and be focused by electromagnets [108, 109].

Figure 3.14a depicts a sketch of a **TEM**, which is analogous to an optical microscope, despite using electrons instead of photons and thus replacing optical lenses with electromagnetic ones.

From a source[32] (historically a *W* filament, nowadays a field emission gun) a primary electron beam is guided through condenser lenses to create a broad electron beam. The beam passes through the sample, where beside the transmission, diffraction or further interactions, like backscattering or photoelectron emission can occur [111]. TEM uses the transmitted electrons which are projected as a two dimensional image, that gets magnified by further electron optics to produce an image. The contrast of the micrographs depends on sample properties (i.e. thickness, density, diffraction condition) and adjustment of the microscope (i.e. focus). Three different kinds of **contrast** are observed in TEM: mass-thickness (results of incoherent scattering as a function of the atomic number *Z* and sample thickness),[33] diffraction (based on coherent Bragg scattering by the lattice planes) and phase contrast (caused by phase differences of the electrons) [37, 110].

The principle setup for **STEM** is shown in Fig. 3.14b and in more detail in Fig. 3.14c. The major difference compared to TEM is, that the electron beam gets focused by condensor lenses, is scanned over a sample area by scan coils and for each beam position an intensity is recorded. Further the objective lens is located before the sample and combined with an additional aperture. Two types of images can be

---

[32] The information limit of a TEM depends on temporal and spatial coherence of the e-beam, where the former is related to the energy spread of the electrons, the latter on the source size. In order to achieve the highest possible resolution, monochromatic and coherent electron sources are applied [110]. The error of non perfect sources results in chromatic aberration and is expressed by the coefficient C_C.

[33] The mass-thickness contrast is the reason why denser regions with higher scattering probability of the beam appear dark and light regions appear bright in TEM [112].
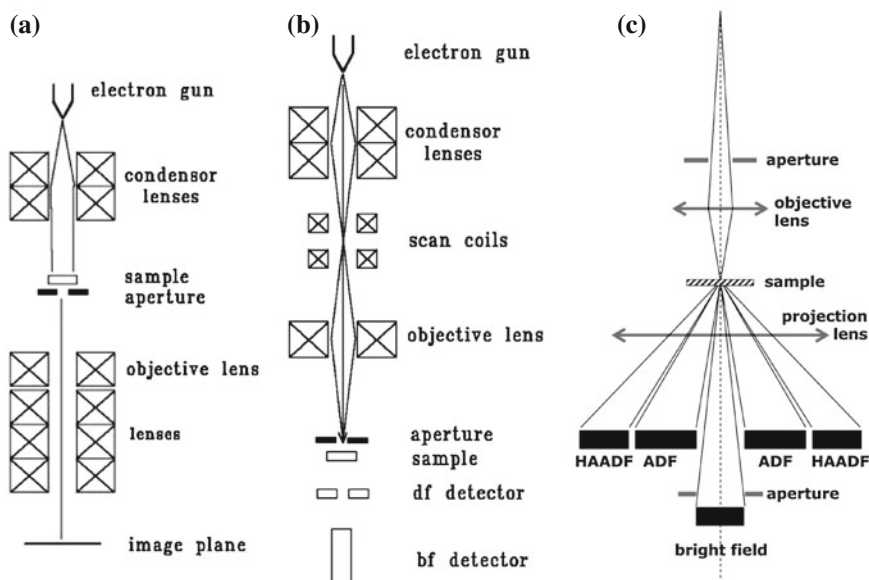
Fig. 3.14 Schematic set-up of an electron microscope in the transmission (TEM) (**a**) and combined (TEM and STEM) (**b**) modes. Note how the dark field detector is off the central axis, as the dark field image is based on scattered electrons. The HAADF-STEM operation mode with bright— (on the central axis) and dark-field detectors (of the central axis) is shown in (**c**). Two different modes are available for dark field imaging, i.e. annular dark field (ADF); high-angle annular dark field (HAADF). Figures modified after [37]. *J. W. Niemantsverdriet: Spectroscopy in Catalysis: An Introduction, pages 182 and 187. 2007. Copyright Wiley-VCH Verlag GmbH & Co. KGaA. Reproduced with permission*

obtained, a bright (BF) or dark field[34] (DF) [37]. For the BF the detector is positioned on the optical axis, however for DF the image is composed of electrons scattered out of the optic axis by the sample and thus recorded off axis by ring shaped detectors. Depending on the angle θ of detection one differentiates annular DF (ADF) and (at even higher scattering angles, $\theta > 50$ mrad off axis) high-angle ADF (HAADF). The last mode is also known as **Z-contrast** mode, where the scatter of electrons of heavy elements creates the image and the scattering probability to high angles is proportional ($\sim Z^{1.7}$) and very sensitive to the atomic number Z, i.e. the mass density and the number of atoms of the probed element [112].

   In approximation one can argue that for 'thin' objects a plain and ideal Z-contrast can be interpreted with a simple relation between Z number of the probed element (incl. the sample thickness, i.e. particle size) and image intensity.[35] This simple (ideal)

---

[34] In DF the obtained images are inverted, i.e. metal particles appear light (high scatter) on an dark background (low scattering).

[35] At the detection of the high scattering angle for HAADF of 50–200 mrad the intensity of the incoherent scattering is $\sim Z^2$ [113].

Table 3.1 List of the used TEM grids within this work sorted by the sample type used for the different application, support material and thickness

'Sample'	Section	Support		Deposited sizes	Venue
TEM	5.1.1	*Au/C*	2 nm	8, 22, 34, $n \leqslant 36$, 46, 68	TUM
STEM	5.1.1	*Cu/C*	2 nm	8, 22, 34, $n \leqslant 36$, 46, 68	LMU
ETEM	5.2.1	*Si/SiO$_2$*	8 nm	8, 22, 34, 46, 68	CEN
'INPS'	5.2.2	*SiO$_2$/SiO$_2$*	40 nm	$n \leqslant 53$, 68, 68, 22+68	CEN
Photocat	5.4	*Cu/C/CdS*	2 nm	8, 22, 34, $n \leqslant 36$, 46, 68	LMU

Additionally the deposited clusters sizes and the location of the measurements is indicated

interpretation is however not taking into account, that the image can be distorted by instrumental instabilities and is dependent on the focus of the objective lens (in particular the so called beam **convergence angle**) as well as the chosen aperture [112]. A major draw back of the technique is the potential **beam damage** of the sample, caused by the high energy electrons during image acquisition [112, 114].

An additional modification, overcoming the major (S)TEM drawbacks, being limited to vacuum conditions, is achieved using in-situ TEM also known as environmental TEM (**ETEM**). First TEM micrographs under elevated pressures were taken in the 1970s and today TEM imaging is possible at up to the mbar pressure range with resolutions comparable to that of an conventional (analytical) TEM. Using ETEM comparable reaction conditions for 'real' catalysts can be achieved, e.g. reactive gases under elevated temperatures and allow realistic insights into materials on a local level. Usually differential pumping and small reaction cell (with the sample) are used to obtain the desired experimental conditions [110, 115–117].

Experimental details—Micrographs for this thesis have been recorded at three different locations: TUM using TEM, LMU and CEN using both (BF) S/TEM and (HAADF)-STEM mode, with the latter method being preferential for *Pt* catalysts, due to *Z*-contrast. Assignments of the TEMs to the location and specimens as well as their instrumental specifications are stated in the appendix in Table A.2.2. Further a variety of different TEM samples were used, in order to mimic the support of the corresponding sample for actual reactivity measurements (e.g. INPS, nanorods, etc.) in the best possible manner; the different types, supports and the used TEM location are indicated in Table 3.1 and further details in the appendix in Table A.2.3.

Post detection **data treatment** has been performed using a computer based algorithm of in-house design, based on the image and particle analysis tool of IGOR PRO 6.22A (Wavemetrics, U.S.A.) on the raw STEM micrographs (after acquisition, HAADF-STEM micrographs are smoothed using a median filter). The following results can be obtained by the analysis: height, area and volume distribution function (HDF, ADF and VDF)[36]; the results in terms of precision are validated by analyzing similar images with three different tools (SPIP 5, Image Metrology A/S,

---

[36] The commonly obtained particle size distribution (PSD) is based on the diameter of the particles; however in light of the small subnanometer particles the use of the ADF is preferential.

Denmark; Image J, NIH, U.S.A. and a tool developed at the Physics Department, TUM, Dr. Bele).

3.3.3 X-Ray Photoelectron Spectroscopy (XPS)

A brief introduction of the underlying principles for XPS are stated in Sect. 3.2.5 along with the other used EES techniques, thus only the experimental details are stated.

Experimental details—The measurements of XPS spectra of supported cluster materials (Sect. 5.1.2) were performed on different samples. For comparing different sizes particular samples were prepared, by deposition of size-selected clusters on silicon wafers pieces (8×15 mm).

Prior to deposition the wafer pieces were cleaned in the following order in *acetone*, *methanol* and *iso-propanol* in an ultrasonic bath for 5 min [118]. After deposition, the samples were brought to ambient conditions and subsequently transferred to the separate XPS UHV setup in air.

Two samples at a time were mounted onto an electrically grounded z-transfer manipulator. The samples were introduced into a separate UHV analysis chamber with a typical pressure in the region of 1×10^{-9} mbar, equipped with a Leybold Heraeus LHS-IO X-ray photoelectron spectrometer. Non-monochromatized $Mg\,K\alpha$ (1253.6 eV) radiation was used for excitation of the electrons [119]; the spectra were recorded digitally using a multichannel scalar and a PC (Collect Spectra 8.0 software).

Post detection data treatment was performed with IGOR Pro 6.22, using Doniach-Sunjic [120] fit functions. Further details on the setup as well as measurement conditions and parameters are stated in the appendix in Sect. A.1.5.

3.3.4 Indirect Nanoplasmonic Sensing (INPS)

A rather new platform for characterization of heterogeneous catalyst materials is INPS, based on evaluation of localized surface plasmonic resonance (**LSPR**). The effects are generally well understood and thus only a short qualitative introduction is given [121–123].

'Plasmons' exist in bulk metal, metal surfaces as well as in metal nanoparticles and are based on the coherent oscillations of (s)-electrons under the influence of an external photon field. In the case of a bulk metal a collective charge density wave in the electron gas is built up and its plasmon frequency lies in the range of UV light. Above this plasma frequency the radiation is partly absorbed or transmitted, since the electrons in the field cannot follow the incident field. Its frequency is simply to fast for the electrons to respond. Below the plasma frequency, the incoming field is screened by the electrons and oscillates. As a consequence, the incoming radiation is

reflected—with the plasmon frequency in the UV range, visible light is thus reflected and makes a metal appear 'metallic'.

Whereas bulk plasmons as longitudinal modes cannot be excited by a transversal wave such as light, this works for small particles, where the k vector is not a good quantum number. Consequently for particles a LSPR (a result of collective coherent oscillations of the conducting electrons with respect to the charged atomic cores) can be detected. The observed plasmon frequency is strongly dependent on the temperature [124], particle geometry, size, (dielectric) environment and the material. These dependencies are used, for INPS in order to characterize and study materials [125–128], by observing the change in plasmon frequency.

The key element of the setups is an **INPS sensor chip** as shown in Fig. 3.15a. It consists of a conventional glass slide (10×10 mm) onto which an amorphous array of uniform and noninteracting *gold* discs (30/40 nm height and 76 nm diameter) are deposited by means of hole-mask colloidal lithography and covered with a 10 nm thin dielectric spacer layer (e.g. SiO_2, Si_3N_4) [122]. As the *gold* discs are covered with the spacer layer, they cannot physically interact with the studied material that is deposited ontop of the layer, except via the dipole field created from the LSPR in the gold discs and thus the method is 'indirect'. In this work different *Pt* cluster sizes and coverages have been deposited onto the spacer layer using the electron shower for charge neutralization of cluster anions (Sect. 3.1.3).

Figure 3.15b shows the possible induced spectra shifts in plasmon frequency (wavelength λ), maximum extinction and peak width (FWHM) of two different samples (red and green) induced by the previously mentioned dependencies [122].

The **experimental setup** 'Insplorer instrument' (Insplorion AB, Göteborg, Sweden) at CHALMERS (Fig. 3.15c) consists of two optical fibers for optical transmission measurement through a quartz tube in which the INPS chip with the clusters is mounted.

The temperature (Eurotherm, Germany) and the gas flow (Bronkhorst, the Netherlands) can be controlled and are monitored (C-type thermocouple) along with the changes of the plasmon features.

During INPS spectroscopy the wavelength of maximum light extinction (peak maxima) of the LSPR in the *Au* sensor particles is the main observable, and thus its shifts are recorded. Utilizing a curve-fitting procedure, introduced for LSPR by Dahlin et al. [129], the shifts are efficiently measured with a resolution of 0.01 nm under optimal conditions and by means of a simple pixel array spectrometer. In order to compensate for systematic experimental errors (i.e. different layer thickness or samples temperature) the relative variations of the peak positions are measured, and not absolute ones. Further, the applied curve-fitting procedure efficiently reduces noise—the obtained measurement value will in the following be denoted as centroid [127]. Additionally, changes in the FWHM of the peaks an the extinction maxima of the signals is recorded.
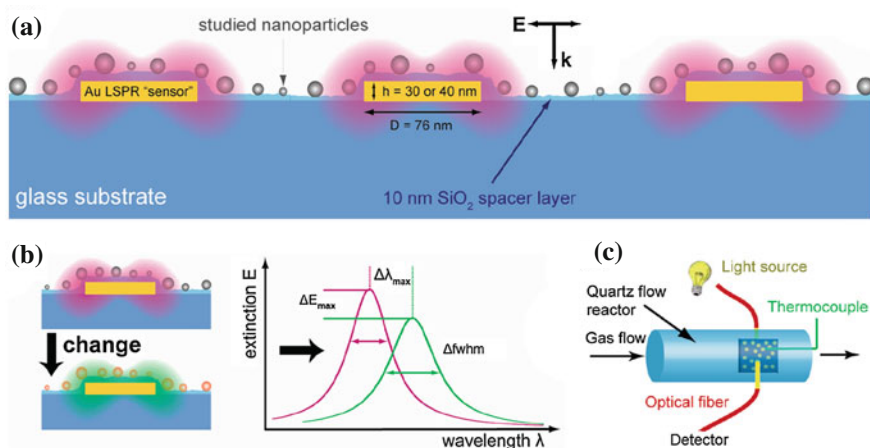
Fig. 3.15 INPS measurement platform. **a** Shows a sketch of the INPS chip design; based on a glass substrate gold discs in the nanometer size range are placed, which are covered by a dielectric spacer layer onto which the studied material is deposited. **b** Possible chemical and/or physical changes in the nanomaterial on the spacer layer induces a spectral shift (color change) of the Au nanodisk sensor LSPR. **c** The experimental setup is depicted in two optical fibers for optical transmission measurement through a quartz tube in which the INPS chip with the clusters is mounted. The gas flow and the temperature in the tube can be controlled and are monitored along the measurement [122]. *Reprinted (adapted) with permission from* [122]—*Copyright (2010) American Chemical Society*

3.3.5 μ-Reactors

The development of μ-reactors for study of heterogeneous catalysts has been pursued and envisioned by different research groups [130–136] and are based on the idea of scaling down a conventional reactor to dimensions in the micrometer range. This allows for better control of the reaction conditions (negligible temperature and partial gas pressure differences), possible (high through put) screening as well as testing low amounts of catalysts. The μ-reactor used in this work, was particularly designed to study gas-phase reactions of model catalysts.

The device and its fabrication, as well as the measurements setup has been described in large detail [137–143], thus only a very brief summary is given here. The advantages of the system are the small reactor volume, the efficient heating or cooling (due to the small dimensions) and by using a glass lid the possibility for photocatalytic experiments [144, 145]. Most important is, that due to the long diffusion length of the gases in the reactor volume (almost an order of magnitude longer than the radius of the reactor volume) full contact of the gas with the catalyst can be ensured and subsequently all reactants leaving the cavity are analyzed by the QMS.

The *Si*-based μ-reactors are **fabricated** under cleanroom conditions at Danchip/ DTU based on standard micro fabrication processes, i.e. Reactive Ion Etching (RIE) and photolithography. The reactor (16×20 mm) consist of two gas inlets (I1 and
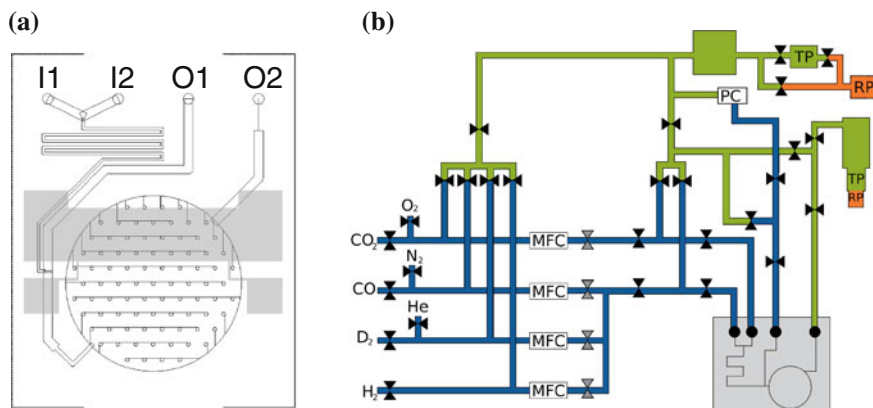
(a)

(b)

Fig. 3.16 CAD drawing of a (2nd gen.) μ-reactor including the *Pt* heating structure (*gray areas*) [142, 143] (**a**). Gas is introduced from the two inlets (*I1*, *I2*), which are connected to the mixing zone. The main flow exits through the main outlet (*O1*), whereas the products leave the reactor through the capillary outlet (*O2*) and are fed into a QMS for analysis. μ-reactor measurement setup at CINF (**b**). The reactor (*grey*) is connected via its outlets to a gas manifold system including, manual (*black*) and pneumatic (*grey*) valves, mass flow controller (MFC), turbo pumps (TP) as well as rotary pumps (RP) [142, 143]. The different pressure ranges are indicated by the colors: ambient pressure (*blue*), pre vacuum (*orange*) and high vacuum (*green*)

I2) connected to the mixing zone, allowing for diffusional mixing[37] of the two reactants (Fig. 3.16a). The outlet of the mixing zone is then connected to small outlet (capillary) leading to the reaction chamber and the outlet for the main flow (O1). The capillary limits the flow into the reaction cavity (236 nL volume) and after the reactants passed through the reactor (typical residence time 10 s; at 1 bar in reactor $\sim 10^{15}$ molecules/s), they exit through another capillary (1500 μm length) over a second outlet (O2) connected to the QMS. The channels I1, I2 and O1 have a depth of 250 μm, where as the capillaries and the reaction cavity have a depth of only 3 μm. As catalyst support a 50 nm thin SiO_2 film is grown thermally in the reaction cavity.

After deposition of catalyst material (Sect. 3.3.1) the reactors are subsequently **hermetically sealed** by means of **cooled anionic bonding** of a pyrex lid (0.5 mm thickness) [140]. This is achieved by a applying high potential between lid and reactor (1 kV) at a low current (mA) and at the same time heating the structures (using two halogen lamps) to temperatures above 400 °C (controlled by a C-type thermocouple) for 30–45 min. At these temperatures the pyrex lid becomes ionically conducting and forms strong chemical bonds between the lid and the sample. In order to not heat the reaction cavity and jeopardize that the deposited clusters materials sinter, on the reaction cavity a water cooled *Cu* finger is placed on the reactor back side (ensuring that the temperature of the cavity does not exceed 40 °C). Using a bonding setup within proximity of the deposition setup at TUM (rebuilt and adapted on the

---

[37] This is necessary, since the flow in the flow channels is laminar and thus mixing can only be achieved by diffusion [142].

design from CINF/DTU [140, 142]), the samples are sealed right after deposition
and contaminants can be kept low, as well as the reactors can be shipped to the
measurements location.

Originally **temperature measurements** of the reactors (1st gen.) was achieved
with four point measurement of resistance of a *Pt* thin film resistant temperature
detector (RTD) deposited onto the pyrex lids by photolithography. Since this was
troublesome not only for read-out but further also required a heating device, in the
2nd gen. reactors a combined *Pt* heating and RTD structure was implemented on
the backside of the reactor itself (Fig. 3.16a). For measurements within this work the
2nd gen. (Sect. 5.3) were used. Recently, however, it turned out that the temperature
being measured at the same position as heating causes a temperature gradient of
up to 25 °C (absolute maximum temperature) and thus underestimating the catalyst
performance. To that end, another new reactor design (3rd gen.) with three additional
heating structures is currently under testing.

In Fig. 3.16b the **setup** for μ-reactors measurements, located at CINF/DTU is
depicted. Briefly, the reactor is attached via its outlets (sealed by O-rings) to a stain-
less steel metal block. Inlets are connected to a gas manifold system (controlled by
manual valves), supplying the reactor with two different gases at a time and given
flux (mass flow controllers), the gas lines can be evacuated by means of a differential
pumping system. Outlet O1 is attached to a pressure controller (for measurement of
the reactor gas pressure) and is backed by a turbo; O2 is fed into the QMS, which is
as well backed by the turbo.[38] Several updates and changes have been performed due
to leaks at the O-rings, i.e. the setup is flushed with *Ar* to keep undesired gases out of
the reactor or in a new approach is overcome by evacuating the surroundings of the
reactor itself—in either case the performed measurements within this thesis are not
affected by contaminations. Once the reactor is attached to the system and evacu-
ated, measurements can be performed and are controlled automatically by software,
which is feed with flow files stating the chosen **experimental procedure** (time, gas
flows, temperature, etc.). The automatization is necessary in terms of reproducibility
and feasibility, since measurements often last for days. The procedure used for the
measurements in this work is stated in Sect. A.2.3. Details on how to measure the
active area of a catalyst by titration and further procedures are well described in Ref.
[143]; briefly also in the results, Sect. 5.3.

3.3.6 Photo Catalysis (PhotoCat)

Photocatalysis experiments were conducted using an established semiconductor sys-
tem and for decoration with noble metals, combining it with size-selected clusters.
The general synthesis and **measurement approach** is depicted in Fig. 3.17. Colloidal
semiconductor *CdS* nano rods are spin coated onto conducting *ITO* glass substrates

---

[38] Both the mass flow controllers (for different gases) and the QMS (for conversion of the measured
mA signals into number of molecules per *t*) need calibration [142].

(Fig. 3.17a), the substrates get decorated with *Pt* clusters (Fig. 3.17b) under UHV conditions (Sect. 3.3.1). After deposition the samples are transferred into aqueous solution and their photocatalytic activity in terms of hydrogen evolution efficiency under illumination is measured (Fig. 3.17c). The following contains a brief description of the steps, based on the literature [22, 113, 146–148].

The *CdS* **NRs synthesis** was performed at LMU on the basis of reported procedures [113, 149–152]. Briefly, *CdS* NRs with a narrow diameter and length distribution can be prepared via ligand assisted kinetically controlled growth, taking advantage of the anisotropic properties of the hexagonal (wurtzite type) crystal structure of *CdS* and using long-chained phosphoric acids as capping ligands. By means of the chosen synthesis approach an aqueous stock solution of *CdS* NRs stabilized with cysteine ligands is fabricated. *CdS* NR covered films of 8×14 mm size are prepared on ITO glass support. The glass rectangles are cleaned and after drying under a flow of nitrogen, the samples are transferred to a plasma cleaner for about 30 s in order to improve the hydrophilic properties of the ITO surface. The films are subsequently dipped into a 0.5 M *NaCl* solution containing 0.1 % polydiallyldimethylammonium chloride (*PDDA*) which acts as a wetting reagent. The samples are then spin-coated[39] with a uniform thin layer of *CdS* NRs using the *CdS* stock solution diluted 1:1 with Millipore water. Absorption spectra are taken on a Cary 5000 UV-VIS-NIR spectrometer (Varian Inc., USA) after the coating procedure to quantify the amount of NRs covering the ITO glass and to assure a highly reproducible prepara-
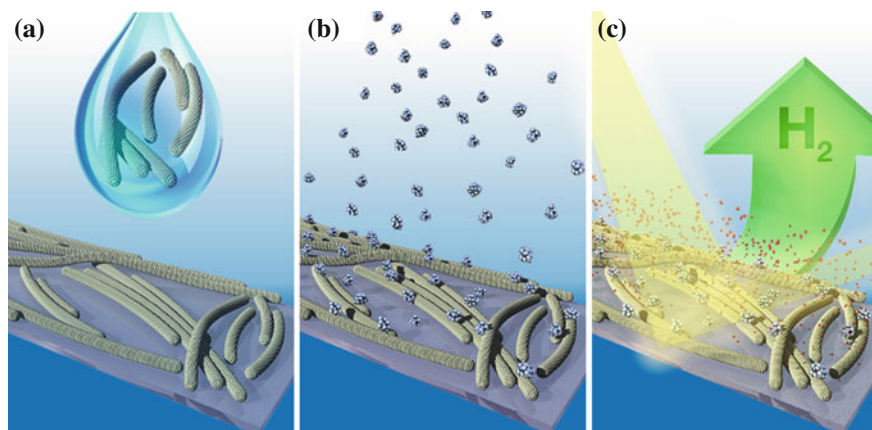
Fig. 3.17 Schematic representation of the experimental platform for atomic scale insight into photocatalytic nanosystems. Colloidal semiconductor nano crystals (CdS nanorods) are spin-coated onto ITO substrates (a) followed by deposition of cluster under UHV conditions (b). The resulting samples are investigated for their photocatalytic activity in terms of hydrogen generation efficiency in aqueous solution (c). *Reprinted (adapted) with permission from* [22] *- Copyright (2012) American Chemical Society.*

---

[39] Corresponding TEM samples were prepared by means of drop casting NR solution onto TEM grids, since spin coating is not feasible.

tion procedure. On each sample spin coating is repeated until the height of the exciton peak appearing at 470 nm, which can be taken as a measurement of the amount of *CdS* deposited, is in the range of $OD = (15 \pm 3) \times 10^{-3}$ corresponding to a coverage of 1–2 ML of *CdS* NRs [146]. Finally, organic residues are removed in the plasma cleaner and the clusters were deposited as described in Sect. 3.3.1.

Experimental details—*Hydrogen* generation and photocatalytic efficiency measurements are carried out at RT using the as prepared films in a 5 cm long gas tight quartz cuvette filled with 500 μL of a 10 vol% aqueous solution of triethanolamine (*TEA*) as a hole scavenger at LMU. The films are illuminated in the spectral range of 360–440 nm by the filtered light of a 450 *W Xe* lamp. The average sample excitation area is 1.12 cm^2 and an excitation power of averaged 27.0 mW/cm^2 is measured with a thermopile photo-sensor (Coherent PM3). Prior to all measurements the solution is deaerated by bubbling *argon* for several minutes through the liquid. During the measurements 10 μL aliquots are taken in situ from the remaining gas volume (about 1 mL) in the cuvette at regular times. For this purpose a syringe is lanced through a septum which forms the closure head of the reaction cuvette. Collected reaction gases are injected into and analyzed by a gas chromatograph (GC-2014, Shimadzu GmbH, Germany) using *Ar* as a carrier gas. The **quantum efficiency** (*QE*) for *hydrogen* generation (the ratio of photoelectrons consumed for *hydrogen* production to the number of photons absorbed by the solution) is evaluated accounting for small measured variations of absorption areas, optical densities between the sample films and minimal fluctuations of the exciting *Xe*-lamp intensity between the experiments. Further for contamination of *nitrogen* and *oxygen* in the syringe during to transfer and injection in the the GC is accounted [146]. For the calculation of the **monolayer quantum efficiency** (*MLQE*) the measured optical density of the samples, exceeding that of a monolayer, were exchanged by the calculated optical density of a perfectly aligned nano rod monolayer. This modeled *QE* takes into account that only the uppermost layer of *CdS* nano rods is decorated with *Pt* clusters and is thus photo catalytically active [147, 22].

References

1. Heiz, U., Vanolli, F., Trento, L., & Schneider, W.-D. (1986). Chemical reactivity of size-selected supported clusters: an experimental setup. *Review of Scientific Instruments*, *68*, 1986–1994.
2. Röttgen, M. A. (2007). Ph.D. thesis, Technische Universität München.
3. Schweinberger, F. F. (2009). Master's thesis, Technische Universität München.
4. Kunz, S. (2010). Ph.D. thesis, Technische Universität München.
5. Kunz, S., Hartl, K., Nesselberger, M., Schweinberger, F. F., Kwon, G., & Hanzlik, M., et al. (2010). Size-selected clusters as heterogeneous model catalysts under applied reaction conditions. *Physical Chemistry Chemical Physics*, *12*, 10288–10291.
6. Heiz, U., Landman, U., & Henry, C. R. (2008). In U. Heiz & U. Landman (Eds.), *Nanocatalysis*. Berlin: Springer.
7. Haberland, H., Insepov, Z., & Moseler, M. (1995). Molecular dynamis simulation of thin film growth by energetic cluster impact. *Physical Review B*, *51*, 11061–11067.

8. Vanolli, F. (1997). Ph.D. thesis, Unversité de Lausanne.

9. Heiz, U., Vayloyan, A., & Schumacher, E. (1997). *Review of Scientific Instruments*, *68*, 3718.

10. Eberhardt, W., Fayet, P., Cox, D. M., Fu, Z., Kaldor, A., Sherwood, R., et al. (1990). *Physical Review Letters*, *64*, 780.

11. Meiwes-Broer, K.-H. (Ed.). (2000). *Metal clusters at surfaces: structure, quantum properties, physical chemistry* (1st ed.). Berlin: Springer.

12. von Issendorff, B., & Cheshnovsky, O. (2005). Metal to insulator transitions in clusters. *The Annual Review of Physical Chemistry*, *56*, 549–580.

13. Tong, X., Benz, L., Kempter, P., Metiu, H., Bowers, M., & Buratto, S. (2005). *Journal of the American Chemical Society*, *127*, 13516–13518.

14. Wegner, K., Piseri, P., Tafreshi, H. V., & Milani, P. (2006). *Journal of Physics D: Applied Physics*, *39*, R439.

15. Hartl, K. (2008). Master's thesis, Technische Universität München.

16. Lang, S. M., Bernhardt, T. M., Barnett, R. N., & Landman, U. (2010). *ChemPhysChem*, *11*, 1570.

17. Dietz, T. G., Duncan, M. A., Powers, D. E., & Smalley, R. E. (1981). *The Journal of Chemical Physics*, *74*, 6511.

18. Sanchez, A. (2000). Ph.D. thesis, Unversité de Lausanne.

19. Friedrich, W. (2011). Master's thesis, Technische Universität München.

20. Alayan, R., Arnaud, L., Bourgey, A., Broyer, M., Cottancin, E., Huntzinger, J. R., et al. (2004). *Review of Scientific Instruments*, *75*, 2461.

21. Hartl, K., Nesselberger, M., Mayrhofer, K. J., Kunz, S., Schweinberger, F. F., Kwon, G., et al. (2010). *Electrochimica Acta*, *56*, 810–816.

22. Berr, M. J., Schweinberger, F. F., Döblinger, M., Sanwald, K. E., Wolff, C., Breimeier, J., et al. (2012). *Nano Letters*, *12*(11), 5903.

23. Paul, W., & Steinwedel, H. (1953). *Zeitschrift Naturforschung Teil A*, *8*, 448.

24. Paul, W., Reinhard, H., & von Zahn, U. (1958). *Zeitschrift für Physik*, *152*, 143.

25. BALZERS, A. G. (1983). *Partial pressure measurement in vacuum technology*. Technical Report BG 800 169 PE (8907). BALZERS AG, Liechtenstein.

26. Dawson, P. H. (1976). *Quadrupole mass spectrometry and its applications*. Amsterdam: Elsevier.

27. Miller, P., & Denton, M. (1986). *International Journal of Mass Spectrometry*, *72*, 223.

28. Popok, V. N., Barke, I., Campbell, E. E., & Meiwes-Broer, K.-H. (2011). *Surface Science Reports*, *66*, 347.

29. Häkkinen, H., & Landman, U. (2000). *Physical Review B*, *62*, R2287.

30. Delley, B., Ellis, D. E., Freeman, A. J., Baerends, E. J., & Post, D. (1983). *Physical Review B*, *27*, 2132.

31. Crampton, A. (2011). Master's thesis, Technische Universität München.

32. Messerli, S., Schintke, S., Morgenstern, K., Sanchez, A., Heiz, U., & Schneider, W.-D. (2000). *Surface Science*, *465*, 331.

33. Wang, B., Yoon, B., König, M., Fukamori, Y., Esch, F., Heiz, U., et al. (2012). *Nano Letters*, *12*, 5907.

34. Heiz, U., Vanolli, F., Sanchez, A., & Schneider, W.-D. J. (1998). *Journal of the American Chemical Society*, *120*, 9668–9671.

35. Wu, M.-C., Comeille, J. S., Estrada, C. A., He, J.-W., & Goodman, D. (1991). *Chemical Physics Letters*, *182*, 472.

36. He, J.-W., Estrada, C. A., Corneille, J., Wu, M.-C., & Goodman, D. (1992). *Surface Science*, *261*, 164.

37. Niemantsverdriet, J. W. (2007). *Spectroscopy in catalysis: An introduction* (3rd ed.). Weinheim: Wiley.

38. Somorjai, G. (1994). *Introduction to surface chemistry and catalysis* (Vol. 2). New York: Wiley.

39. Chorkendorff, I., & Niemantsverdriet, J. W. (2007). *Concepts of modern catalysis and kinetics* (2nd ed.). Weinheim: Wiley.

40. Häkkinen, H., Yoon, B., Landman, U., Li, X., Zhai, H., & Wang, L. (2003). *Journal of Physical Chemistry A*, *107*, 6168.
41. Lang, S. M., Bernhardt, T. M., Barnett, R. N., & Landman, U. (2011). *Journal of Physical Chemistry C*, *115*, 6788.
42. Lang, S., Bernhardt, T., Barnett, R., & Landman, U. (2010). *Angewandte Chemie International Edition*, *49*, 980.
43. Harding, C., Habibpour, V., Kunz, S., Farnbacher, A. N., Heiz, U., Yoon, B., et al. (2009). *Journal of the American Chemical Society*, *131*, 538.
44. Wang, Z. W., Toikkanen, O., Yin, F., Li, Z. Y., Quinn, B. M., & Palmer, R. E. (2010). *Journal of the American Chemical Society*, *132*, 2854.
45. Wang, Z. W., Li, Z. Y., Park, S. J., Abdela, A., Tang, D., & Palmer, R. E. (2011). *Physical Review B*, *84*, 073408.
46. Watanabe, Y., Wu, X., Hirata, H., & Isomura, N. (2011). *Catalysis Science and Technology*, *1*, 1490.
47. Bals, S., Aert, S. V., Romero, C. P., Lauwaet, K., Bael, M. J. V., Schoeters, B., et al. (2012). *Nature Communications*, *3*, 897.
48. Heiz, U., Sanchez, A., Abbet, S., & Schneider, W.-D. (1999). *Journal of the American Chemical Society*, *121*, 3214.
49. Sanchez, A., Abbet, S., Heiz, U., Schneider, W.-D., Häkkinen, H., Barnett, R. N., et al. (1999). *Journal of Physical Chemistry A*, *103*, 9573.
50. Powell, C., Czanderna, A., & Madey, T. (1998). In C. Powell, A. Czanderna, T. Madey, & U. Landman (Eds.), *Specimen handling, preparation, and treatments in surface characterization*. New York: Kluwer Academic Publisher.
51. Physical Electronics Industries Inc. (1972). *Handbook of auger electron spectroscopy*.
52. Bürgi, T., Atamny, F., Schlögl, R., & Baiker, A. (2000). *Journal of Physical Chemistry B*, *104*, 5953.
53. Somers, J., Bridge, M., & Lloyd, D. (1987). *Spectrochimica Acta Part A: Molecular Spectroscopy*, *43*, 1549.
54. Grunze, M., Ruppender, H., & Elshazly, O. (1988). *Journal of Vacuum Science and Technology A*, *6*, 1266.
55. Günster, J., Liu, G., Kempter, V., & Goodman, D. (1998). *Surface Science*, *415*, 303.
56. Abbet, S., Sanchez, A., Heiz, U., Schneider, W., Ferrari, A. M., Pacchioni, G., et al. (2000). *Journal of the American Chemical Society*, *122*, 3453.
57. Kunz, S., Schweinberger, F. F., Kwon, G., Kiermaier, J., Moal, S. L., Henry, C., et al. (2010). *Surface Science*, *406*, 2184.
58. Winkler, A., & Yates, J. J. (1988). *Journal of Vacuum Science and Technology A*, *6*, 2929.
59. Bozack, M., Muehlhoff, L., Russell, J. J., Choyke, W., & Yates, J. J. (1987). *Journal of Vacuum Science and Technology A*, *5*, 1.
60. Henzler, M., Göpel, W. (2007). Oberflächenphysik des Festkörpers, Teubner Verlag.
61. Falconer, J., & Schwarz, J. (1983). *Catalysis Reviews-Science and Engineering*, *25*, 141.
62. Wedler, G. (1970). *Adsorption—eine einführung in die physisorption und chemiesorption*. Weinheim: Verlag-Chemie.
63. King, D. (1975). *Surface Science*, *47*, 384.
64. Readhead, P. (1962). *Vacuum*, *12*, 203.
65. Masel, R. (1996). *Principles of adsorption and reaction on solid surfaces* (1st ed.). New York: Wiley.
66. Somorjai, G. (1996). *Chemical Reviews*, *96*, 1223.
67. Einstein, A. (1905). *Annalen der Physik*, *322*, 132.
68. Ertl, G., & Küppers, J. (1974). *Low energy electrons and surface chemistry; monographs in modern chemistry*. Weinheim: Verlag-Chemie.
69. Siegbahn, K., Nordling, C., Fahlmann, A., Nordberg, H., Hamrin, K., Hedman, J., et al. (1967). *Electron spectroscopy for chemical analysis: Atomic, molecular and solid state structure studies by means of electron spectroscopy*. Stockholm: Almquist and Wiksells.
70. Siegbahn, K. (1976). *Pure and Applied Chemistry*, *48*, 77.

71. Siegbahn, K. K. (2011). In *Noble lectures chemistry*. Noble Foundation.
72. Turner, D., Baker, C., Baker, A., & Brundle, C. (1970). *Molecular photoelectron spectroscopy*. London: Wiley.
73. Spicer, W. E. (1958). *Physical Review*, *112*, 114.
74. Eastman, D. E. (1970). *Physical Review B*, *2*, 1.
75. Eastman, D. E. (1971). *Physical Review B*, *3*, 1769.
76. Penning, F. (1927). *Naturwissenschaften*, *15*, 818.
77. Harada, Y., Masuda, S., & Ozaki, H. (1897). *Chemical Reviews*, *1997*, 97.
78. Auger, P. (1925). *Journal de Physique et le Radium*, *6*, 205.
79. Seah, M., & Dench, W. (1979). *Surface and Interface Analysis*, *1*, 2.
80. Ertl, G., & Küppers, J. (1985). *Low energy electrons and surface chemistry* (2nd ed.). Weinheim: Wiley.
81. Brundle, C., & Baker, A. (1977). In C. Brundle, A. Baker, & U. Landman (Eds.), *Electron spectroscopy: theory, techniques and applications* (Vol. 1). London: Academic Press Inc.
82. Höfft, O. (2002). Master's thesis, TU Clausthal.
83. Brundle, C., & Baker, A. (1979). In C. Brundle, A. Baker, & U. Landman (Eds.), *Electron spectroscopy: theory, techniques and applications* (Vol. 3)
84. Hüfner, S. (2003). *Photoelectron spectroscopy: Principles and applications* (3rd ed.). Berlin: Springer.
85. Atkins, P. W. (2006). *Physical chemistry* (8th ed.). Oxford: Oxford University Press.
86. Frerichs, M. (2002). Master's thesis, TU Clausthal.
87. Heinrich, V., & Cox, P. (1994). *The surface science of metal oxides*. Cambridge: Cambridge University Press.
88. Stracke, P. R. (2000) Ph.D. thesis, TU Clausthal.
89. Helander, M., Greiner, M., Wang, Z., & Lu, Z. (2010). *Applied Surface Science*, *256*, 2602.
90. Raaen, S., Ruckman, M., & Strongin, M. (1985). *Physical Review B*, *31*, 623.
91. Wandelt, K., Markert, K., Dolle, P., Jablonski, A., & Niemantsverdriet, J. (1987). *Surface Science*, *189*, 114.
92. Jablonski, A., & Wandelt, K. (1991). *Surface and Interface Analysis*, *17*, 611.
93. Kempter, V. (2004). *Instruction manual on assembling and putting into operation of the MIES/UPS-source*. Clausthal-Zellerfeld: TU Clausthal.
94. Maus-Friedrichs, W., Wehrhahn, M., Dieckhoff, S., & Kempter, V. (1990). *Surface Science*, *237*, 257.
95. Krischok, S. (2001). Ph.D. thesis, TU Clausthal.
96. Borodin, A. (2004). Ph.D. thesis, TU Clausthal.
97. Heinz, B., & Morgner, H. (1998). *Journal of Electron Spectroscopy and Related Phenomena*, *96*, 83.
98. Kantorovich, L., Shluger, A., Sushko, P., Günster, J., Stracke, P., Goodman, D., et al. (1999). *Faraday Discussions*, *114*, 173.
99. Sesselmann, W., Woratschek, B., Küppers, J., Ertl, G., & Haberland, H. (1987). *Physical Review B*, *35*, 1547.
100. Kempter, V. (1997). *Materials Science Forum*, *239–41*, 621.
101. Hoffmann, F. (1983). *Surface Science Reports*, *3*, 107.
102. Libuda, J., Meusel, I., Hoffmann, J., Hartmann, J., Piccolo, L., Henry, C. R., et al. (2001). *Journal of Chemical Physics*, *114*, 4669.
103. Rupprechter, G. (2004). Annual reports section "C". *Physical Chemistry*, *100*, 237.
104. Hollins, P. (1992). *Surface Science Reports*, *16*, 51.
105. Wörz, A. (2005). Ph.D. thesis, Universität Ulm.
106. Kunz, S., Schweinberger, F. F., Habibpour, V., Röttgen, M., Harding, C., Arenz, M., et al. (2010). *Journal of Physical Chemistry C*, *114*, 1651.
107. Bayard, R. T., & Alpert, D. (1950). *Review of Scientific Instruments*, *21*, 571.
108. Ruska, E. Z. (1931). *Technical Physics*, *12*(389), 448.
109. Ruska, E. K. (1972). In *Noble lectures chemistry*. Noble Foundation.
110. Hansen, T. (2006). Ph.D. thesis, Danmarks Tekniske Universitet.

111. Schlögl, K. (2011). Ph.D. thesis, Technische Universität München.
112. Williams, D. B., & Carter, C. B. (2009). *Transmission electron microscopy: A textbook for materials science* (2nd ed.). New York: Springer.
113. Berr, M. J. (2012). Ph.D. thesis, Ludwigs-Maximilians Universität München.
114. Ernst, F., & Rühle, M. (1997). *Current Opinion in Colloid and Interface Science*, *2*, 469.
115. Hansen, T., Wagner, J., Hansen, P., Dahl, S., Topsoe, H., & Jacobsen, C. (2001). *Science*, *294*, 1508.
116. Hansen, T. W., Wagner, J. B., Hansen, P. L., Dahl, S., Topsøe, H., & Jacobsen, C. J. H. (2001). *Science*, *294*, 1508.
117. Hansen, P., Wagner, J., Helveg, S., Rostrup-Nielsen, J., Clausen, B., & Topsøe, H. (2002). *Science*, *295*, 2053.
118. Rötzer, M. (2012). Internship report.
119. Gimzewski, J., & Vepřek, S. (1983). *Solid State Communications*, *47*, 747.
120. Doniach, S., & Sunjic, M. (1970). *Journal of Physics C: Solid State Physics*, *3*, 285.
121. Langhammer, C., Yuan, Z., Zorić, I., & Kasemo, B. (2006). *Nano Letters*, *6*, 833.
122. Langhammer, C., Larsson, E. M., Kasemo, B., & Zorić, I. (2010). *Nano Letters*, *10*, 3529.
123. Zorić, I., Larsson, E. M., Kasemo, B., & Langhammer, C. (2010). *Advanced Materials*, *22*, 4628.
124. Yeshchenko, O., Bondarchuk, I., Gurin, V., Dmitruk, I., & Kotko, A. (2013). *Surface Science*, *608*, 275.
125. Langhammer, C. (2009). Ph.D. thesis, Chalmers University of Technology.
126. Larsson, E. M., Langhammer, C., Zorić, I., & Kasemo, B. (1091). *Science*, *2009*, 326.
127. Langhammer, C., & Larsson, E. M. (2012). *ACS Catalysis*, *2*, 2036.
128. Larsson, E. M., Millet, J., Gustafsson, S., Skoglundh, M., Zhdanov, V. P., & Langhammer, C. (2012). *ACS Catalysis*, *2*, 238.
129. Dahlin, A. B., Tegenfeldt, J. O., & Höök, F. (2006). *Analytical Chemistry*, *78*, 4416.
130. Johannson, S., Fridell, E., & Kasemo, B. (2000). *Journal of Vacuum Science and Technology A*, *18*, 1514.
131. Jensen, K. (2001). *Chemical Engineering Science*, *56*, 293.
132. Ajmera, S., Delattre, C., Schmidt, M., & Jensen, K. (2002). *Sensors and Actuators B*, *82*, 297.
133. Kolb, G., & Hessel, V. (2004). *Chemical Engineering Journal*, *98*, 1.
134. Jähnisch, K., Hessel, V., Löwe, H., & Baerns, M. (2004). *Angewandte Chemie International Edition*, *43*, 406.
135. Kiwi-Minisker, L., & Renken, A. (2005). *Catalysis Today*, *110*, 2.
136. Leppelt, R., Schumacher, B., Häring, T., Kinne, M., & Behm, R. J. (2005). *Review of Scientific Instruments*, *76*, 024102.
137. Henriksen, T. R., Olsen, J. L., Vesborg, P., Chorkendorff, I., & Hansen, O. (2009). *Review of Scientific Instruments*, *80*, 124101.
138. Vesborg, P., Olsen, J., Henriksen, T. Chorkendorff, I., & Hansen, O. (2009). *Chemical Engineering Journal*, *160*, 738–741.
139. Vesborg, P. C. K. (2010). Ph.D. thesis, Danmarks Tekniske Universitet.
140. Vesborg, P. C. K., Olsen, J. L., Henriksen, T. R., Chorkendorff, I., & Hansen, O. (2010). *Review of Scientific Instruments*, *81*, 016111.
141. Henriksen, T. R. (2010). Ph.D. thesis, Danmarks Tekniske Universitet.
142. Olsen, J. (2010). Ph.D. thesis, Danmarks Tekniske Universitet.
143. Jensen, R. (2012). Ph.D. thesis, Danmarks Tekniske Universitet.
144. Vesborg, P., In, S., Ol, Hen, Abrams, B., Hou, Y., et al. (2010). *Journal of Physical Chemistry C*, *114*, 11162.
145. Dionigi, F., Vesborg, P. C. K., Pedersen, T., Hansen, O., Dahl, S., Xiong, A., et al. (2011). *Energy & Environmental Science*, *4*, 2937.
146. Sanwald, K. E. (2012). Internship report.
147. Wolff, C. (2012). Bachelor thesis.
148. Schweinberger, F.F., Berr, M.J., Döblinger, M., Wolff, C., Sanwald, K.E., Crampton, A.S., et al. (2013). Cluster size effects in the photocatalytic hydrogen evolution reaction. *Journal of the American Chemical Society*.

149. Vaneski, A. (2009). Master's thesis, Ludwigs-Maximilians Universität München.
150. Berr, M., Vaneski, A., Susha, A., Rodrigues-Fernandez, J., Döblinger, M., Jäckel, F., et al. (2010). *Applied Physics Letters*, *97*, 093108.
151. Berr, M. J., Vaneski, A., Mauser, C., Fischbach, S., Susha, A. S., Rogach, A. L., et al. (2011). *Small*, *8*, 291.
152. Vaneski, A., Susha, A. S., Rodríguez-Fernández, J., Berr, M., Jäckel, F., Feldmann, J., et al. (2011). *Advanced Functional Materials*, *21*, 1547.

Part II
Ultra High Vacuum

Chapter 4
Model Catalysts Under Vacuum Conditions

The chapter is divided into four major parts, illustrating the capabilities of the MIES/ UPS setup towards application for adsorption studies and cluster science as well as investigation of the reactivity of olefins on *Pt* clusters. For comparison, the experiments on the clusters are repeated on 'inert' *MgO* support and a *Pt*(111) single crystal.

First, the **sensitivity** of the recently introduced and **improved EES setup** [1–3] is characterized. This is achieved by evaluating the measurements of the electronic structure of *TCE* adsorbed on surfaces (in Sect. 4.4.1) and correlating them to TPD measurements.

Second, the results of **MIES/UPS measurements** of the electronic structure of **size-selected, supported Pt$_x$** clusters of two different sizes are presented and evaluated with help of the literature.

In a third part, the known **adsorption properties of CO**, and adsorbates after a *CO* oxidation TPR, both on *Pt*(111) are investigated as a test reaction. The EES results show the capability of MIES to probe the electronic structure of a surface reaction, i.e. their adsorbates respectively.

Last, the **interaction and reactivity of the olefins** *TCE* and *ethene* on metal surfaces and size-selected *Pt* clusters is investigated using a combination of TP and EES techniques. The interaction is probed on different surfaces utilizing the introduced data treatment (see Sects. 2.2.3 and A.1.5).

In particular, the adsorption behavior of *TCE* is studied on the surfaces *MgO*(100), *Mo*(100), *Pt*(111) and *Mo*(112) [4] and on *MgO* supported *Pt$_x$* clusters of different sizes. *Ethene* adsorption is probed on *MgO*(100), *Pt*(111) as well as supported *Pt$_x$* clusters. As a function of cluster size, the reactivity of *Pt$_x$* clusters towards *ethene* hydrogenation is probed by means of TPR. To further elucidate the reactivity of *ethene* on *Pt* clusters in contrast to the *Pt* single crystal surface, also initial experiments using AES and IRRAS are presented.

For assignment of the observed MOs of the adsorbed molecules, corresponding **gas phase PES spectra** for all reactants and products are shown in the **Appendix** in Sect. A.3. The assignment of the spectral features to the corresponding MOs is based on theoretical calculations found in the literature [5] and supported by additional calculations [6].
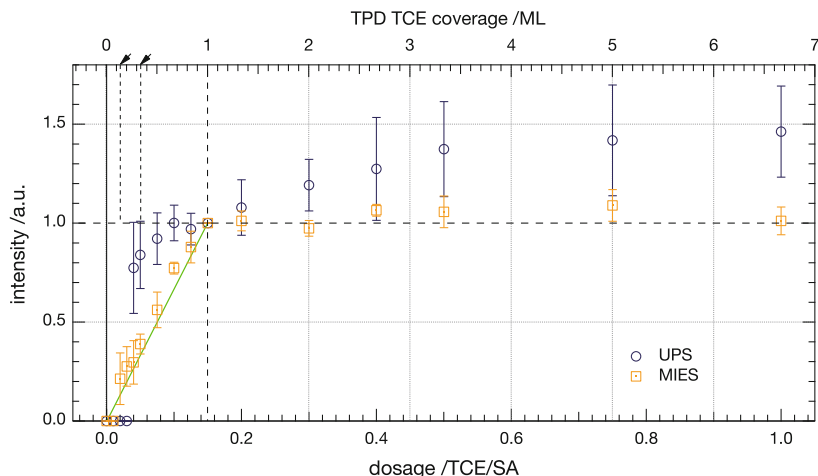
Fig. 4.1 Representative MIES/UPS peak intensities for *TCE* on *Mo*(112) plotted against the dosed amounts of *TCE* (*bottom*) and the corresponding coverage in *ML* (*top*) as determined from TPD. For each data point the peak intensities of the peaks I–IV have been averaged and normalized to the filled first *ML* (completion of the physisorbed layer in TPD, *dashed line*). The errors of the data points are the standard deviation of the four averaged peak intensities. For MIES data a saturation of the peak intensity is visible for a filled first *ML*, whereas for UPS the intensities increase up to a coverage of four *ML* corresponding well to the expected probe depth of the method. The *arrows* indicate 1/6 *ML* and 1/3 *ML*. Reprinted (adapted) with permission from [4]—Copyright (2012) *Elsevier*

4.1 MIES/UPS Sensitivity for Adsorption Studies

The sensitivity of the redesigned MIES/UPS experimental setup [2, 3, 7] was evaluated by studying the adsorption of *TCE*. Previous measurements with *TCE* on *MgO*(100) [1, 2] had only given a qualitative picture of the sensitivity. Thus, in order to quantify the results a systematic study on the adsorption of *TCE* on single crystal surfaces was measured as a function of coverage, determined additionally by means of TPD. *TCE* as adsorbate molecule is an ideal choice, since the molecule shows distinct peaks in EES (see Sect. A.3 for gas phase PE spectra) and has a high ionization cross section. The results of this part are based on the results of Sect. 4.4.1, but only focus on the surface sensitivity.

The results of the peak integration as a part of the post-detection data treatment (see Sects. 2.2.3 and A.1.5) of the *TCE* MOs (see Fig. 4.22) on the **Mo(112)** surface are discussed as a representative example. Applying the background correction procedure for EES data, introduced in this work, all five *TCE* related peaks of the adsorbed molecule on the surfaces can be resolved and fitted.

Figure 4.1 displays the sum intensity of peak I to IV acquired from EES measurements on *Mo*(112) after dosing the indicated amount of *TCE*. Peak V is excluded
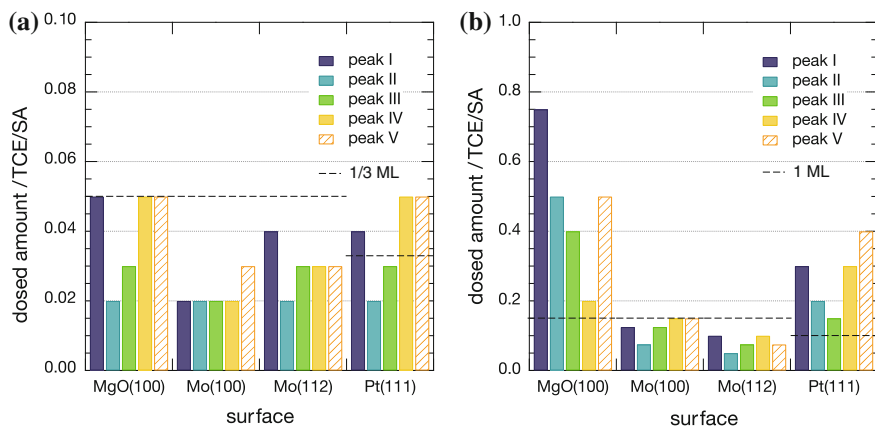
Fig. 4.2 Minimum amount of *TCE* necessary to detect the different MOs of the molecule by means of MIES (a) and UPS (b) on the surfaces *MgO*(100), *Mo*(100), *Mo*(112) and *Pt*(111). The bar graphs are based on the evaluation of the corresponding MIES/UPS spectra recorded as a function of coverage (see Sect. 4.4.1) and are based on Table 4.1. The *left* scale for MIES is increased by a factor of 10 compared to UPS for better visibility, the *dashed lines* indicate the coverage determined from TPD

due to possible influence of the applied background correction,[1] for details see Sect. A.1.5. The intensities are normalized to the completion of the first *ML* (obtained from TPD measurements). The indicated error bars are calculated from the standard deviation of the four averaged peak intensities with respect to the normalized intensity. The systematic error introduced by defining a unity intensity for the first complete filled adsorbate layer (*ML*) determines if the spectroscopy is suitable for submonolayer quantification. This is clearly the case for the MIES data, as the peak intensities saturate after the completion of the first layer, which is evidence of exclusive surface sensitivity. In contrast, for UPS a saturation of the normalized intensities occurs between three to four *ML*, corresponding to the expected probe depth of the method. Further, the strict linear increase of the MIES data clearly indicates that assumption of a constant sticking coefficient for *TCE* is justified (up to one *ML*). UPS data suffers much more from scatter in the submonolayer regime. As visible from the graph, the measured **MIES** data can be used to **reliably quantify at least the amount of** $1/3\,ML$.

Figure 4.2 shows the minimum amount of adsorbed *TCE* necessary to resolve each MO peak feature in the MIES/UPS spectra, based on the results stated in Table 4.1. The graphs allow for comparing the data sets obtained on the different surfaces *MgO*(100), *Mo*(100), *Mo*(112) and *Pt*(111). Generally it can be stated, that depend-

---

[1] As shown later (Sect. 4.4.1), systematic errors seem to be introduced by the background fitting procedure for peak V. Thus, possible errors introduced by the normalization procedure including all five peak components, might be reduced excluding peak V. However, doing so, the rest of the MIES data remains almost unaffected and UPS data does not gain in quality.

ing on the substrate, the **MIES data are about five times more sensitive to** *TCE*
with respect to the UPS data set.

Quantitively, with MIES the first indications of *TCE* MOs after dosage of
an equivalent amount of **0.02** TCE/SA (**detection limit, for all surfaces**) can be
resolved, corresponding to 13 % of a filled physisorbed first *ML* (4.5×10^{13} TCE/cm²).
In order to detect all five *TCE* MOs with MIES for the less sensitive cases of
MgO(100) and *Pt*(111) a dosage of an equivalent coverage of about 0.05 TCE/SA
($\sim 1/3\,ML = 1.1 \times 10^{14}$ TCE/cm²) is necessary. For UPS the first indication of *TCE*
MOs on *Mo*(112) are seen at 0.05 TCE/SA and all five peaks can be detected above
2/3 of a complete physisorbed *TCE* layer (2.2×10^{14} TCE/cm²). The results show a
superior submonolayer surface sensitivity for MIES compared to UPS, also in com-
parison to NEXAFS and UPS results from Cassuto et al. where the detection limit
for *TCE* on *Pt*(111) was estimated to be $\theta \sim 1\,ML$ [8].

Summary—MIES has at least a three times higher surface sensitivity compared
to UPS with respect to TCE. The achieved detection limit of as low as 0.02 TCE/SA
is particularly important if molecular adsorption at specific surface sites are to be
monitored. For example the prospect for application of MIES on supported model cat-
alysts, i.e. cluster or cluster-adsorbate complexes. A typical, average coverage for, i.e.
Pt clusters in reactivity measurements is 0.058 e/nm² (equal to 5.8×10^{13} clusters/cm²)
On such a cluster catalyst surface MIES would be able to resolve one *TCE* mole-
cule per cluster. Consequently, the redesign and the modifications applied to the
MIES/UPS setup allow for probing with submonolayer surface sensitivity in a range
applicable for cluster adsorbate complexes.

4.2 EES of Supported Pristine Clusters

This section is dedicated to the potential of the MIES/UPS setup towards probing
the electronic structure of pristine supported clusters. Preliminary experiments with
Pt [9] and *Pd* [2] clusters supported on *MgO*(100) (using a less sensitive MIES/UPS
setup and unselected clusters in the later case), were used as a basis for studying *Pt*$_{11}$
and *Pt*$_{30}$ clusters on *MgO*(100) support, as a function of coverage by EES.

The coverage of clusters was varied in such a way that comparable amounts of
Pt surface area were probed under the assumption of a spherical cluster shape[2]
(Appendix Table A.2); in the present case, double the amount of *Pt*$_{11}$ was deposited
compared to *Pt*$_{30}$. For the measurements a spectrum of the blank support was taken,
clusters deposited, heated to 180 K in order to desorb potential adsorbates introduced
during deposition, the sample cooled to $T < 100$ K and measured again. The resulting
UP/MIE spectra are depicted in Fig. 4.3 for *Pt*$_{11}$ and in Fig. 4.4 for *Pt*$_{30}$. The raw
spectra along with spectra normalized with respect to the secondary electron peak

---

[2] TEM results in Sect. 5.1.1 support the assumption of a spherical cluster shape.

in the range of 15–17 eV, are shown. This normalization compensates for apparent fluctuations in number of photons and metastables over the long duration of the measurements. The effects as a function of coverage become more obvious after normalization. In general charging of the surface for all acquired spectra can be excluded, as a potential charging effect would shift the spectra towards higher BE (see *TCE* on *MgO*(100) in Sect. 4.4.1), which is not observed.

For both cluster sizes the effects observed in the **MIES** spectra are similar and proportional to the amount of deposited metal. Increasing cluster coverage reduces the *MgO*(100) O2p feature at 6 eV (most probably because increasing coverage on the surface), increases the electron density in the range 8–13 eV and further shifts the peak maximum of the secondary peak towards lower energies. Additionally, a closer look at the high BE cut-off reveals indications for two slopes, which can probably be related to a second WF introduced, when depositing the clusters. The applied coverages (max. of $0.116\,e/nm^2$ corresponding to $0.5\,\%\,ML$, a usual range for cluster experiments) are too low to have a more significant impact on the MIE spectra. This observation is in agreement with MIES data of vapor deposited *Ag* on *MgO* on which particular metal features (in particular *s* orbitals, the outmost lying valence orbitals)[3] could only be seen at coverages above $1/3\,ML$ [11] corresponding to a coverage of $8.7\,e/nm^2$ (assuming atoms). Further, these features can only be seen as they are located in the energy range from 0–5 eV, where the *MgO*(100) support shows no spectral features.

Due to the RT/AN de-excitation process on metal surfaces (see Sect. 3.2.5) no particular metal features (i.e. 5*d* features as for UPS) can be seen of *Pt*(111) using MIES (see Appendix Fig. A.7) and thus also not for the clusters. Expectations of Krischok et al. [12], that a controlled size reduction of metal clusters below 1 nm will give rise to the change of the interaction process between *He** and the adsorbate from AN to AD as soon as the transition from metallic-like to molecular behavior of the cluster takes place, cannot be supported with the presented data. It might however simply be due to a yet too low sensitivity of the applied (EES) methods and used cluster coverage. Nevertheless, the observed spectral changes upon cluster deposition illustrate the possibility to probe in the submonolayer range with MIES, even if distinct spectral features are missing.

For **UPS**, similar observations with respect to MIES for the decrease in density at the *MgO*(100) feature at 6 eV for both sizes can be made. Additionally, the second O2p feature, visible only in UPS at 9.1 eV, gets reduced (to a larger extent for the Pt_{30} sample), in agreement with [13]. Further a shift in the secondaries is visible, for both samples, towards lower BE with increasing coverage. Again, careful inspections of the high BE cut-offs reveals two slopes that might be attributed to a second WF arising from the deposited metal. Features originating from the characteristic 5*d* band double peak structure of *Pt* are not visible and might be explained by the low cluster coverage. The most important difference between the two sizes is, however, the increasing electron density at the Fermi edge (E_F) for Pt_{30}.

---

[3] Also experiments probing the electronic structure of supported alkali metals *Li* and *Na* on metal oxide support, show *s* orbital features at high enough coverages [10].
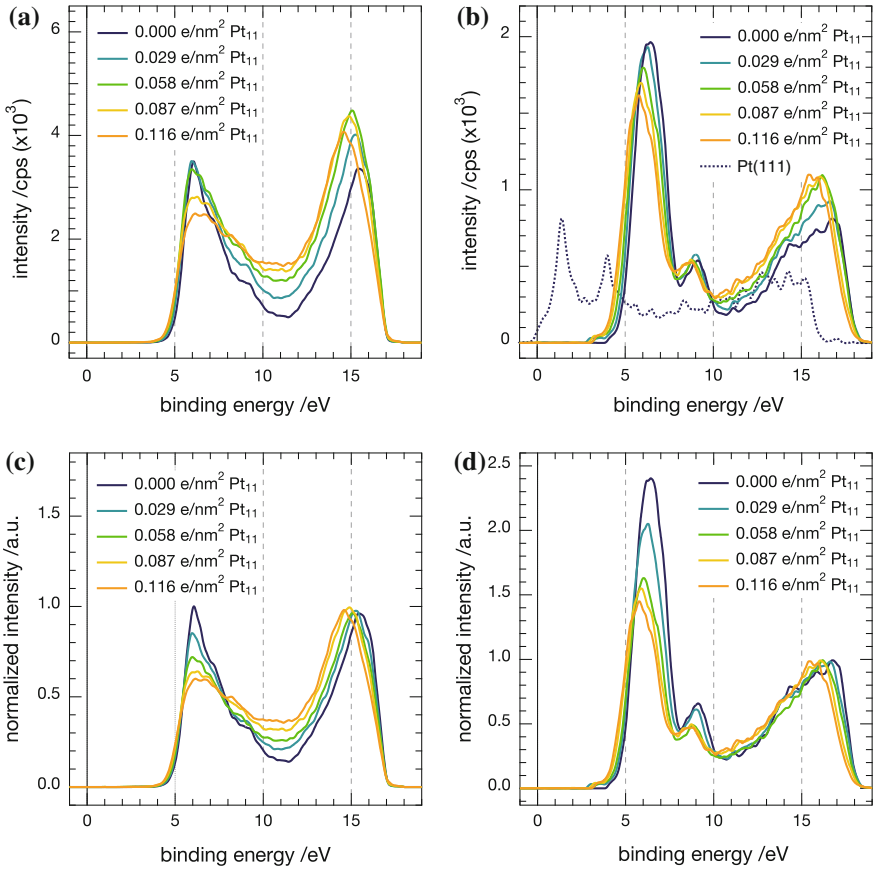
Fig. 4.3 EES of four different Pt_{11} coverages on MgO support. Raw spectra (*top - a,b*) as well as normalized spectra with respect to the peak of the secondary electron emission (*bottom - c,d*) are shown. MIES (*left - a,c*) and UPS (*right - b,d*) are plotted on an BE scale. The maximum coverage of $0.116 \, e/nm^2$ corresponds to a coverage of $0.5 \%ML$. For (**b**) the Pt(111) spectra is shown for comparison

Figure 4.5 shows excerpts of the normalized UPS spectra in the region of E_F. Whereas for Pt_{11} no electron density can be seen in the range of 0–3 eV at all coverages, for Pt_{30} (already at coverages as low as $0.015 \, e/nm^2$) a small, but clear, signal (higher than noise, compare Pt_{11} spectra) up to the Fermi edge is observed. However, this behaviour is surprising if comparing with reports in the literature, as discussed below.

Form a sensitivity point of view, the low coverage at which the density is detected ($1.5 \times 10^{12} \, e/cm^2 = 0.005 \% \, ML$) is one of the lowest reported in the literature so far in this cluster size range.
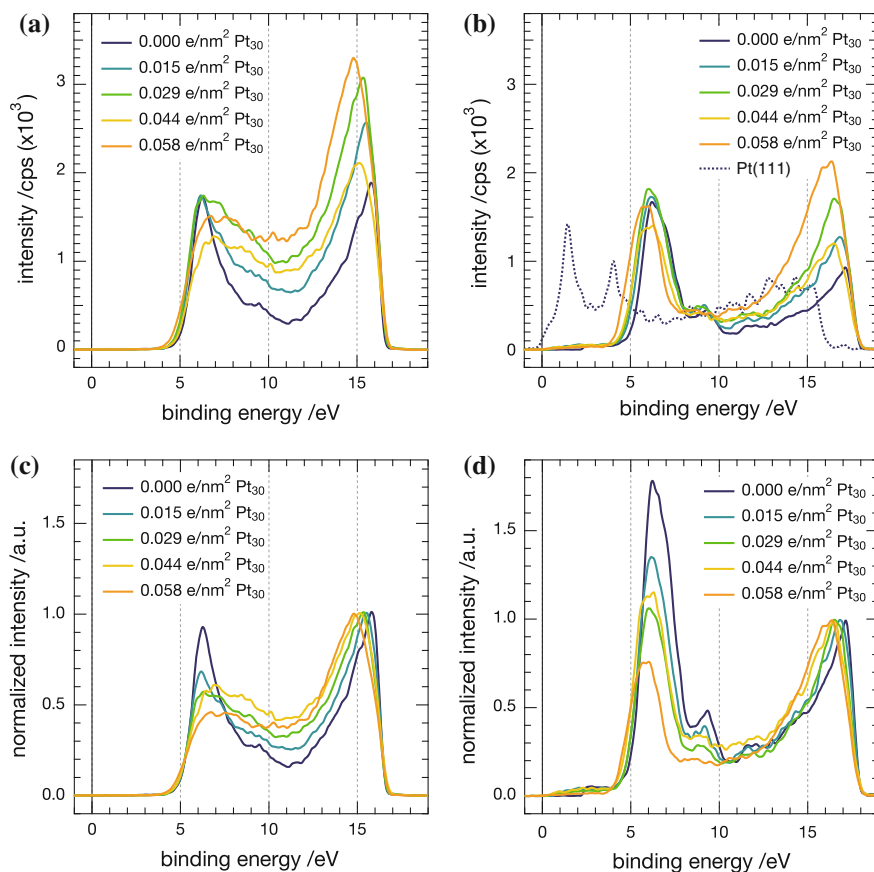
Fig. 4.4 EES of different Pt_{30} coverages on MgO support. Raw spectra (*top - a,b*) as well as normalized spectra with respect to the peak corresponding to the emission of secondary electrons at the high binding energy cut off (*bottom - c,d*) are shown. MIES (*left - a,c*) and UPS (*right - b,d*) are plotted on an BE scale. The maximum coverage of 0.058 enm^2 corresponds to a coverage of 0.2 %ML. For (**b**) the Pt(111) spectra is shown for comparison

Comparable minimum amounts for the density at the Fermi edge reported are 1.5×10^{15} atoms/cm^2 (5 % ML of Pd on C) [14, 15], 7×10^{14} e/cm^2 (Pd on SiO_2) [16], 3×10^{14} e/cm^2 (Pd on SiO_2) [17] for vapor deposition[4] and $\sim 1 \times 10^{14}$ e/cm^2 ($Pt_{1-6,10}$ on SiO_2) [18, 19] as well as $\sim 3 \times 10^{12}$ e/cm^2 ($Ag_{55,923}$ on $HOPG$) [20] for size-selected clusters. Pt bulk features (in UPS) and also the observed electron density at E_F are not seen, but this is not surprising, as the amount

---

[4] As stated previously (Sect. 2.2.2), using this preparation method, particularly at the reported coverages, agglomeration of the particles cannot be excluded and consequently it is doubtful that the results reflect the behavior of small particles. Further the method limits the minimum amount of 'clusters' deposited to the number of nucleation sites, with a typically density in the order of 3×10^{12} e/cm^2 [15].

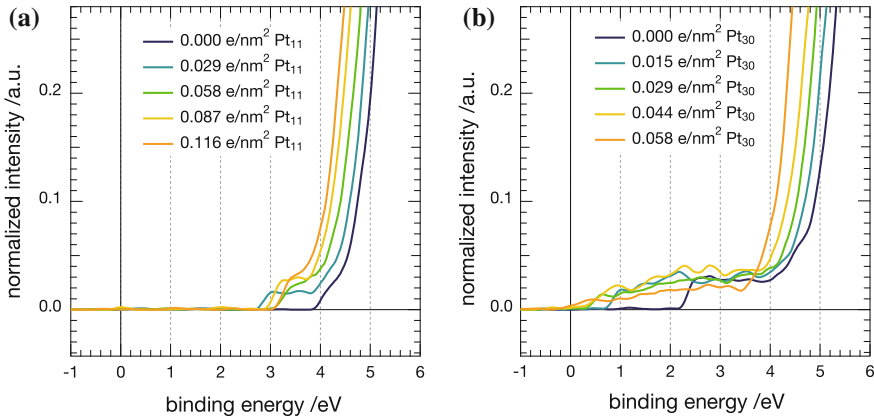**Fig. 4.5** Excerpt of the normalized UPS spectra for better visibility in the region of the E_F as a function of Pt_{11} (**a**) and Pt_{30} (**b**) coverage

of Pt required to see such spectral features in UPS is $\sim 14 \times 10^{15}$ atoms/cm^2 ($\sim 1/2\,ML$) [16, 17]. Turning towards the widely discussed metal to insulator transition for clusters [21] the observed electron density for the bigger cluster size might be an indication for somewhat metallic behavior compared to the smaller Pt_{11} clusters and consequently be a possible explanation of the different behavior in reactivity for supported metal clusters. However, to the best of (our) knowledge, no comparable observations have been made for supported clusters in that particular size range, therefore the significance of this result is hard to judge.

Additionally, from Fig. 4.5, it can be seen that for both sizes the shift towards the low energy cut off is proportional to the amount of cluster coverage. The total shift of 0.9–1 eV is far above the resolution limit, and may allow for quantification with respect to coverage.

Last, the evaluation of the WF for both MIES and UPS (not shown in a graph) and both sizes show a small increase (slightly larger than the experimental error of ± 0.05 eV), probably originating from the deposited metal with a WF value above the support. The effect of an increasing WF, considering the low coverage studied, is in agreement with the literature [13] for other systems (Ag, Cu and Pd on MgO).

Summary—it can be stated, that with the used setup, the EES of supported size-selected clusters at submonolayer coverages can be achieved. For MIES no additional features originating from cluster materials can be observed, due to the very low coverages and probably the deexcitation mechanisms occurring on metal surfaces. Yet changes in the spectra are observe. UPS changes for different cluster coverages are more pronounced and particularly the appearance of electron density at the Fermi edge for Pt_{30} might be an indication for metallic behavior. To verify these interesting observations the use of local methods (i.e. scanning tunneling spectroscopy, STS) for probing the electronic structure of a single cluster supported on a metal oxide material might further the understanding of these phenomena.

4.3 Interaction of Carbon Monoxide

On $Pt(111)$ the well studied adsorption of CO and, CO oxidation by means of TPR, was used as test system for investigating the capabilities of the MIES/UPS setup for probing the surface electronic structure of adsorbates, before and after a surface reaction. In a first part using TPD and EES, as well as MIES as a function of temperature, the adsorption properties of CO on $Pt(111)$ and $MgO(100)$ (with TPD only) are investigated and compared to the literature. Second, with EES, the surface is studied after a TPR experiment and again compared to findings on the electronic structure in the literature. Both of the reactants have been subject to MIES studies on single crystals already (*oxygen* [22–24] and CO [25]). In this work, the use of the CO molecule as a test system with the available MIES/UPS setup helps to judge further the reliability and precision of the methods.

The evaluation of the observed features in the electronic structure within this chapter is performed manually, without the help of the automated treatment tool (Sect. 2.2.3) as the spectral features were simply too weak to do so. This is due to the fact that the channeltron of the HAC was replaced before the measurements reported in this section and consequently EE spectra were not obtained with an optimized setup at full sensitivity.

4.3.1 CO Adsorption Properties

In a first step comparable **TPD** experiments of CO interaction on $MgO(100)$ and $Pt(111)$ as a function of coverage were recorded and are depicted in Fig. 4.6.

Spectra on **MgO(100)** show the expected behavior of a weakly physisorbed molecule with one desorption peak α (maximum at 112 K), independent of the coverage.[5] The observed peak is in good agreement with the literature [27], the low amount of detected CO is related to a very small sticking coefficient.

In contrast, the TPD spectra on the **Pt(111)** surface are a typical example for a chemisorbed molecule. The lowest coverage of 0.01 CO/SA exhibits a desorption peak α at 400 K. With increasing coverage, α shifts towards lower temperatures (340 K for 0.3 CO/SA). This shift should not be interpreted as 2nd order desorption behavior, but rather as a result of repulsive interactions of adsorbed CO molecules at higher coverages. An additional small peak present in all spectra at 110 K is originating from CO desorbing from the tungsten heating wires. Both the spectral shape and the peak positions as a function of coverage, correspond to data from the literature [25, 28–30] (considering different heating rates and adsorption temperatures).

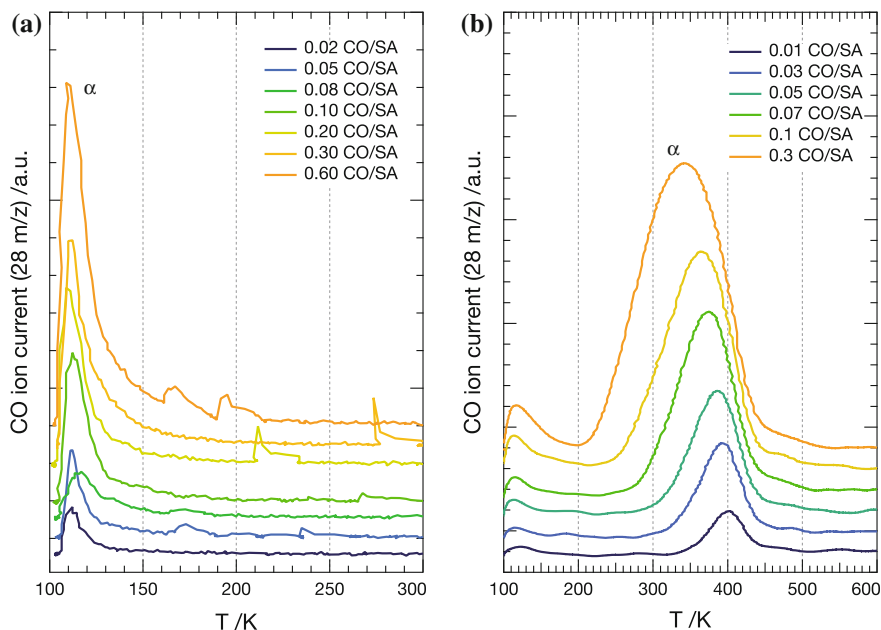[5] This is not a first order characteristic, but an effect of the weak adsorption [26].

Fig. 4.6 TPD ($\beta = 2\,K/s$) spectra of CO desorption on $MgO(100)/Mo(100)$ (**a**) and $Pt(111)$ (**b**). For MgO peak α is assigned to desorption of physisorbed CO. In the case of $Pt(111)$ peak α is attributed to chemisorbed CO

The integration of the peak areas from the TPD spectra (not shown), reveal an linear increase in area with respect to the presented coverage range,[6] a saturation coverage is not reached. As the observed behavior correlate well with literature further discussion is omitted.

Figure 4.7 shows **MIE/UP spectra** of different amounts of CO on $Pt(111)$, to further study the chemisorption behavior. The MIE spectra of CO show the superior surface sensitivity of MIES compared to UPS. With MIES for $0.1\,CO/SA$ ($\sim 1/4\,ML$) first CO features can be seen, whereas with UPS only with increasing coverages small features are visible, that are dominated by those from the support. Consequently, in the following argumentation only the MIES data set is further described and discussed (IP energies are used for description unless noted differently). The **MIE spectrum** at $0.03\,CO/SA$ coverage shows no clear peaks from CO, further the spectrum shape differs in comparison to those seen for other adsorbates on $Pt(111)$ in later sections.[7] For $0.05\,CO/SA$ and $0.07\,CO/SA$ a peak at $18.3\,eV$ and a small peak at $15.8\,eV$ is

---

[6] A saturation of the area, thus completion of the first ML has been determined for $Pt(111)$ at a dosage amount of $0.4\,CO/SA$ [6].

[7] An explanation might be that the spectra have been acquired shortly after new channeltron was installed in the HAC and the positions and settings were not optimized. Also, the spectra were taken at a scan velocity of $0.1\,eV/s$, resulting in a reduced data rate with lower resolution.
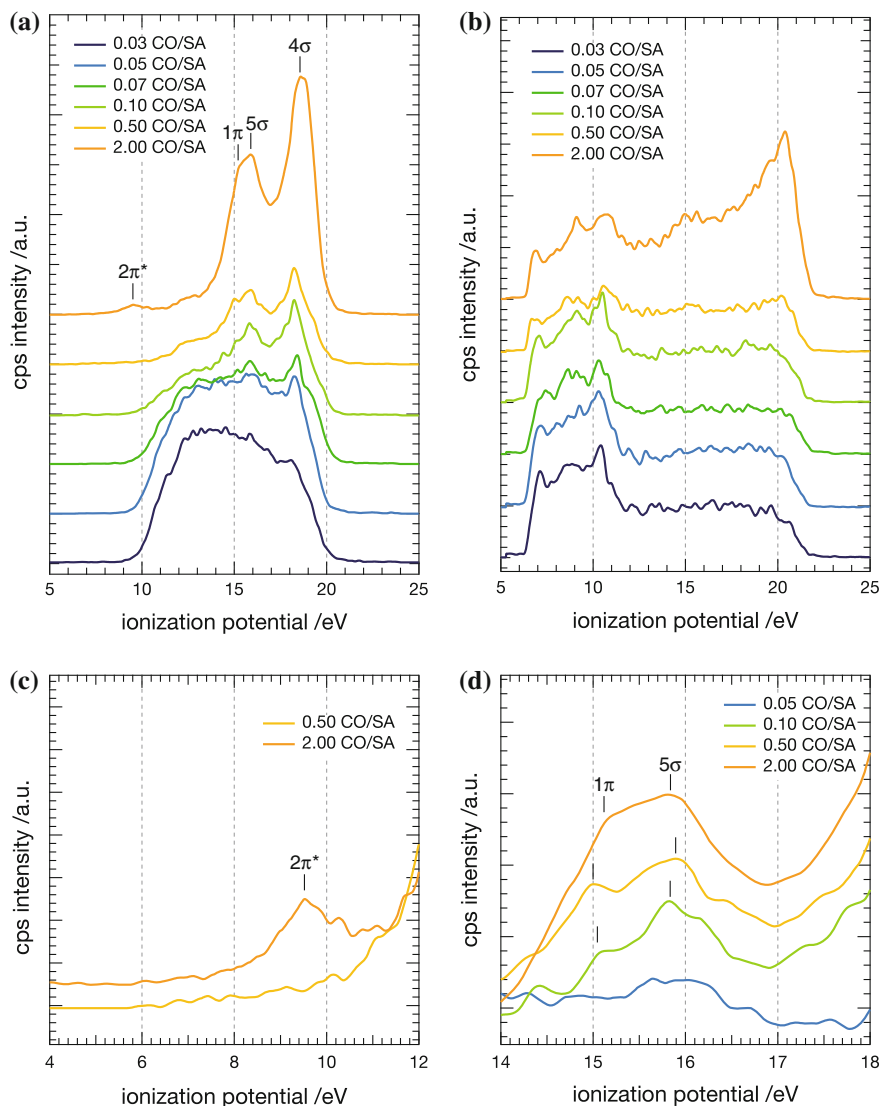
Fig. 4.7 EES spectra of different amounts of *CO* adsorbed on *Pt*(111)—MIES (**a**) and UPS (**b**). Subfigures (**c**) and (**d**) show excerpts of the MIE spectra of selected coverages for better visibility of the *CO* peak features. For assignment of the *CO* MOs see text

apparent, both peaks correspond well to literature values measured with *He II* UPS of *CO* on *Pt*(111) [31].

From $0.1\, CO/SA$ for the peak at 15.8 eV a shoulder at 15.0 eV begins to appear and becomes more pronounced at $0.5\, CO/SA$. For coverages well over a *ML* ($2\, CO/SA$) these features are clearly visible along with two smaller, broader peaks at 9.5 eV
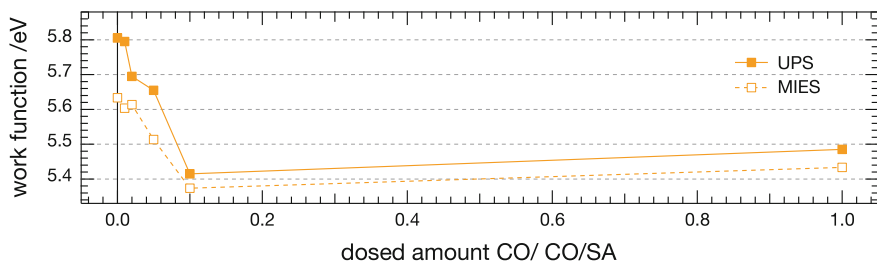
Fig. 4.8 Absolute WF changes with increasing coverage of *CO* on *Pt*(111). The values are determined from the corresponding EES measurements and have a statistical error of ± 0.05 eV

and 12.8 eV. As marked in Fig. 4.7a the peaks observed can be assigned to $1\pi/5\sigma$ MOs[8] at 15.8 eV and the 4σ MO at 18.3 eV by comparing the energies to the measured gas phase IPs/MOs (5σ –14.0 eV, 1π –16.9 eV and 4σ –19.7 eV; see Appendix Sect. A.3.3). With respect to the measured IP energies, the 1π and 4σ MOs, not involved in the surface bond exhibit a **relaxation shift of -1.1 eV and -1.2 eV**, respectively. In contrast, the 5σ orbital involved in the **chemical bond**, shifts positive by **+1.8 eV**. Thus, for coverages as low as 0.05 *CO/SA* MIES accurately detects the interaction of *CO* on a *Pt*(111) surface, correlating well with reported values at surface saturation coverages [31, 32].

At higher coverages a better resolution of the *CO* MOs can be observed, excerpts of the MIES spectra of different energy ranges are shown is Fig. 4.7c, d. Better visible now is the additional shoulder at 15.0 eV for spectra with 0.1 *CO/SA* or more coverage. As mentioned in Sect. 2.2.3 upon adsorption the 5σ and 1π MOs are energetically almost degenerate, thus their emission peaks are often joined together. However, using sensitive methods it was shown experimentally [31] and described in the literature [32], that this single peak is in fact made up of two MOs[9] with a separation of 0.8 eV. The separation value fits well the energy difference between main peak and shoulder observed in the MIES data at higher coverages. In contrast to the reported results however, resolving these two MOs with MIES was achieved in a fraction of the time (2 h [31] vs. few minutes [26]). In Fig. 4.7c a broad peak, visible only for coverages above the *ML* (2 *CO/SA*) can be seen, most certainly induced from condensed *CO* molecules on top of the chemisorbed ones. Originating from condensed *CO*, these molecules should exhibit relaxation shifts for all MOs, since no chemical bond to the surface can be formed. A peak at 9.5 eV (BE 3.35 eV) might be assigned to the partially occupied $2\pi^*$ orbital, as reported in [33]; however this assignment is not entirely convincing considering the high coverage [26].

---

[8] As mentioned in Sect. 2.2.3, the observed peak at 15.8 eV corresponds to a convolution of the 5σ MO and 1π MO.

[9] Also the use of polarized light in a UPS experiment can resolve the two peak features, by exploiting symmetry considerations (mentioned in Sect. 2.2.3).
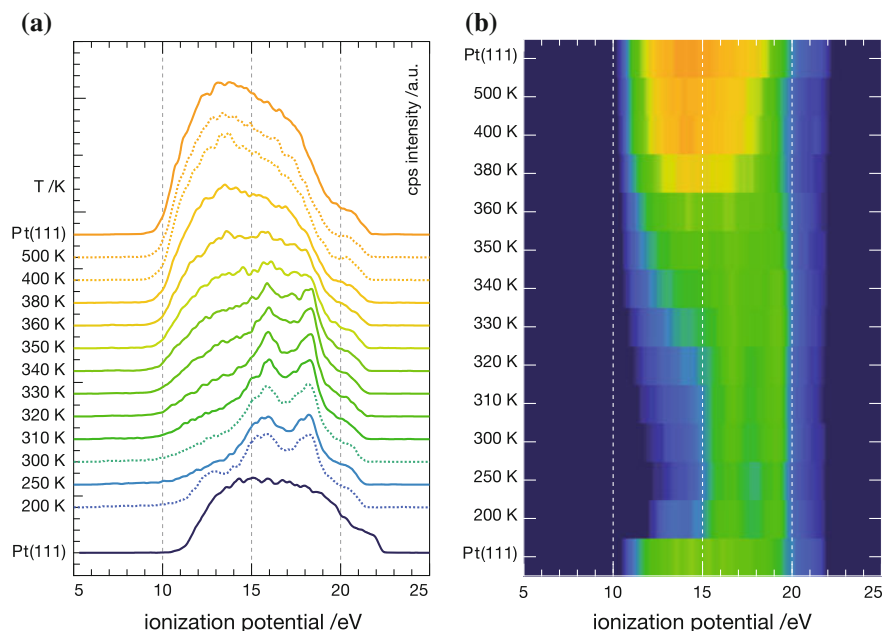
(a)

(b)

Fig. 4.9 MIE spectra of CO desorption after stepwise heating on $Pt(111)$. On the surface $0.4\,CO/SA$ are adsorbed at $100\,K$, the crystal is then heated in several steps and cooled down before each MIE spectra. The desorption reveals the support features after $360\,K$—MIES raw spectra (**a**) and image plot (**b**)

Additionally, the **WF changes** upon adsorption were evaluated and are shown for both UPS and MIES in Fig. 4.8. CO adsorption in the submonolayer range decreases the WF by $-0.4\,eV$ and stays for multi layers; the observations are in good agreement with the literature, despite revealing a slightly stronger decrease than reported [34].

In order to further elucidate the CO adsorption properties on **Pt(111)** a series of **temperature dependent MIE spectra** was recorded and is depicted in Fig. 4.9. For these spectra $0.4\,CO/SA$, equivalent to approximately one ML, was dosed. The temperature was increased stepwise, and MIE spectra were always taken at $T < 100\,K$, to exclude possible temperature effects. After dosage the features of the $1\pi/5\sigma$ MOs at $16.0\,eV$ an the 4σ MO at $17.8\,eV$ are visible—showing a comparable relaxation shift and a slightly higher chemisorption shift than presented above. With increasing temperature the features start to vanish at $330\,K$ and disappear completely above $360\,K$. At even higher temperatures the spectra resemble the $Pt(111)$ bulk spectrum.

The temperature below which the CO molecule is bonded stably to the surface can be assigned to 340–$350\,K$. Above that temperature a the MO of CO disappears, well in agreement with the TPD data above (peak maxima at $\sim350\,K$ for $0.3\,CO/SA$) and also different data in the literature [30, 34, 35].

As in CO oxidation reaction, the binding behavior of the CO molecule, is of particular importance, i.e. with respect to poisoning, the presented data may serve
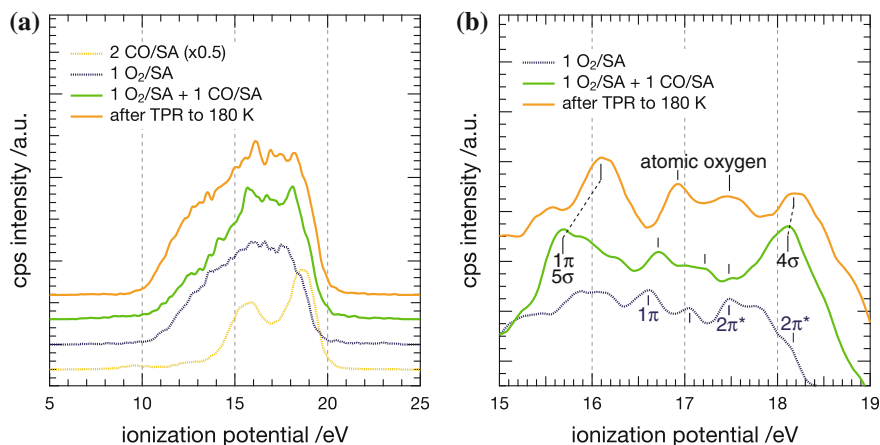
Fig. 4.10 MIE spectra with $1\,O_2/SA$, $2\,CO/SA$ as well as $1\,O_2/SA$ with $1\,CO/SA$ before and after TPR reaction to $180\,K$ on $Pt(111)$. Overview spectra (**a**) including the CO spectra from the previous section for comparison; in excerpt (**b**) the spectral features are assigned to MOs, for details see text

as a tool to probe for this phenomena. Hereby, the applied MIES setup is a sensitive enough tool to probe (adsorbates) in the submonolayer range and gives reliable results in peak energy positions with respect to the literature.

4.3.2 EES of CO Oxidation on Pt(111)

In order to probe for changes during the CO oxidation reaction, MIE spectra of the adsorbed reactants at the coverages $1\,O_2/SA$ as well as $1\,O_2/SA$ with $1\,CO/SA$ before and after TPR (the corresponding TPR spectra is in accordance with the literature and not shown explicitly) reaction to $180\,K$ were recorded. The resulting spectra are shown in Fig. 4.10, unfortunately revealing only weak spectral features. Because of the poor background, MOs in the oxygen spectrum can be hardly assigned, possibly visible MOs based on the gas phase spectra (Appendix Sect. A.3.2) are the 1π and $2\pi^*$ orbital.

Nevertheless, the spectrum with both CO and O_2 adsorbed before heating, reveals the two CO peaks of the $1\pi/5\sigma$ MOs at $15.6\,eV$ and the 4σ MO at $18.2\,eV$ as assigned in Fig. 4.7a. After the TPR to $180\,K$, the CO peak position remains unchanged at $18.2\,eV$, however the $1\pi/5\sigma$ peak has shifted up to $15.6\,eV$ and an additional shoulder at $15.5\,eV$ is visible. Further, between the CO peaks in both spectra there are two peaks at $16.9\,eV$ and $17.5\,eV$ apparent, which are also visible in the O_2 spectrum. Several observations in the electronic structure upon heating can be made. The peak corresponding to the CO 4σ MO at $18.2\,eV$ remains in the same position after the TPR (to $180\,K$), but the $1\pi/5\sigma$ MOs peak shifts by $+0.5\,eV$.

This shift was not visible for *CO* on the clean surface, thus it must be due to adsorbed atomic oxygen, as molecular oxygen desorbs from the surface or is completely dissociated to react with *CO* to form CO_2 at temperatures below 180 K.

Another possible explanation for this observation might be, that the mixture of *oxygen* and *CO* adsorbed on the surface causes a change in the excitation energy of the metastable atom, a previously reported phenomena [22].

The appearance of a double peak at 16.9 eV and 17.5 eV with both reactants present and its better resolution after the TPR could belong to atomic *oxygen* as it was not visible in the *CO* MIE spectra and increased after desorbing or reacting molecularly adsorbed *oxygen*. The presence of atomic *oxygen* peaks would be most beneficial for studies on clusters as one main problem encountered is not knowing whether the clusters are oxidized by contaminants from the cluster source during deposition. Further the possibility to probe for molecular *oxygen* could help to understand the mechanism of *CO* oxidation for very small clusters, as it is believed to be a possible reaction pathway [36–38].

Summary—the EES results of *CO* adsorption and *CO* oxidation 'reactivity' on *Pt*(111) proves the general possibility to use the setup to probe for small changes in electronic structure of surface reactions in the submonolayer range. A thorough and systematic study is necessary to provide a clear picture and clarify the obtained promising results.

4.4 Adsorption and Reactivity of Olefins

The discussion of the interaction of C_2 molecules is separated in two parts, probing *TCE* and *ethene*—each molecule on surfaces and supported size-selected *Pt* clusters.

The adsorption properties of **TCE on surfaces** are studied with a combination of EES and TPD measurements and act as a model system of a weakly interacting molecule on surfaces. With the confirmation of physisorption behavior on the studied surfaces, the adsorption on different sizes of **supported Pt clusters** were probed and evaluated in comparison to the surfaces.

Second, the well known chemisorption behavior of **ethene** is characterized with the same combination of EES and TPD **on surfaces** and serves as a future comparison for the study of the chemisorption behavior of **ethene on size-selected Pt clusters** by means of EES. The reactivity of *ethene* towards the hydrogenation reaction is probed by TPR and also further preliminary experiments (AES and IRRAS) are shown in order to investigate the mechanism of the *ethene* hydrogenation reaction on size-selected clusters.

4.4.1 TCE Adsorption Properties on Surfaces

Based on previous results [7] obtained on $MgO(100)$ and interesting findings herein, the adsorption properties with varying coverages of *TCE* were studied with EES and TPD on the single crystal surfaces $MgO(100)$, $Mo(100)$, $Pt(111)$ and $Mo(112)$.

The $Pt(111)$ surface is used for comparison to previous EES studies, where *TCE* only weakly adsorbs [8] in contrast to strong interaction for *ethene* [39–41] and further acts as a reference system for the later measurements on clusters (Sect. 4.4.2). The measurements on the two *Mo* surfaces are preformed to investigate the influence of the crystal plane on the adsorption properties (e.g. geometry).

The data recorded ranges from the submonolayer to the multilayer coverage regime and is compared the gasphase PE spectra of *TCE* [5] (see Appendix Sect. A.3.5). For interpretation of the data the previously mentioned data treatment procedures (Sects. 2.2.3 and A.1.5) are applied with successful extraction of previously superimposed features in the spectra.

The **TPD** spectra of *TCE* on all the studied surfaces (incl. *MgO*) are shown in Fig. 4.11 starting with a spectrum with zero coverage at the bottom. From bottom to top the dosage of the molecules is increased in 0.025 TCE/SA steps up to 0.15 TCE/SA coverage and from there on in 0.1 TCE/SA steps up to 0.5 TCE/SA coverage. Additionally, the peaks have been integrated and in Fig. 4.12 the corresponding peak integrals for the surfaces are shown.

For **MgO(100)** two peaks, β at higher temperatures and α at lower temperatures, are observed. Peak β is assigned to physisorbed *TCE* and starts from 0.025 TCE/SA with its peak maximum at 178 K, shifting towards lower temperatures with increasing coverage, reaching $T = 143$ K above 0.15 TCE/SA on. Above this coverage a second sharp peak α with a peak maximum between 126 K and 130 K is found. According to the peak shape and coverage dependency peak β is attributed to a physisorbed layer while peak α corresponds to desorption from a condensed *TCE* multilayer ontop of the physisorbed layer (a previously observed single peak for 0.1 TCE/SA at $T = 126$ K [7] could not be reproduced).

A similar behaviour can be seen for **Mo(100)**, where the β peak (physisorption) appears above 0.05 TCE/SA and the peak maximum shifts with increasing dosage from 200 to 143 K. Feature α attributed to condensed molecules, starts from 0.15 TCE/SA on and the peak maximum shifts from 125 to 129 K. The corresponding integral areas of both peaks β and α for $MgO(100)/Mo(100)$ and $Mo(100)$, are shown in Fig. 4.12 and show a similar trend. The physisorbed layer is filled at a coverage of 0.15 TCE/SA, as the integrated area of the peak β stays stable and only the condensed molecules add to the total integral area.

The fact, that the peak maxima of the β feature shifts to lower temperatures might be attributed to an order of desorption greater than one [42]; on the other hand the observed temperature shifts can be related as well to lateral interactions applying the previously suggested depolarization model for $MgO(100)/Mo(100)$. At low coverages van-der-Waals interactions between the *TCE* molecules and the
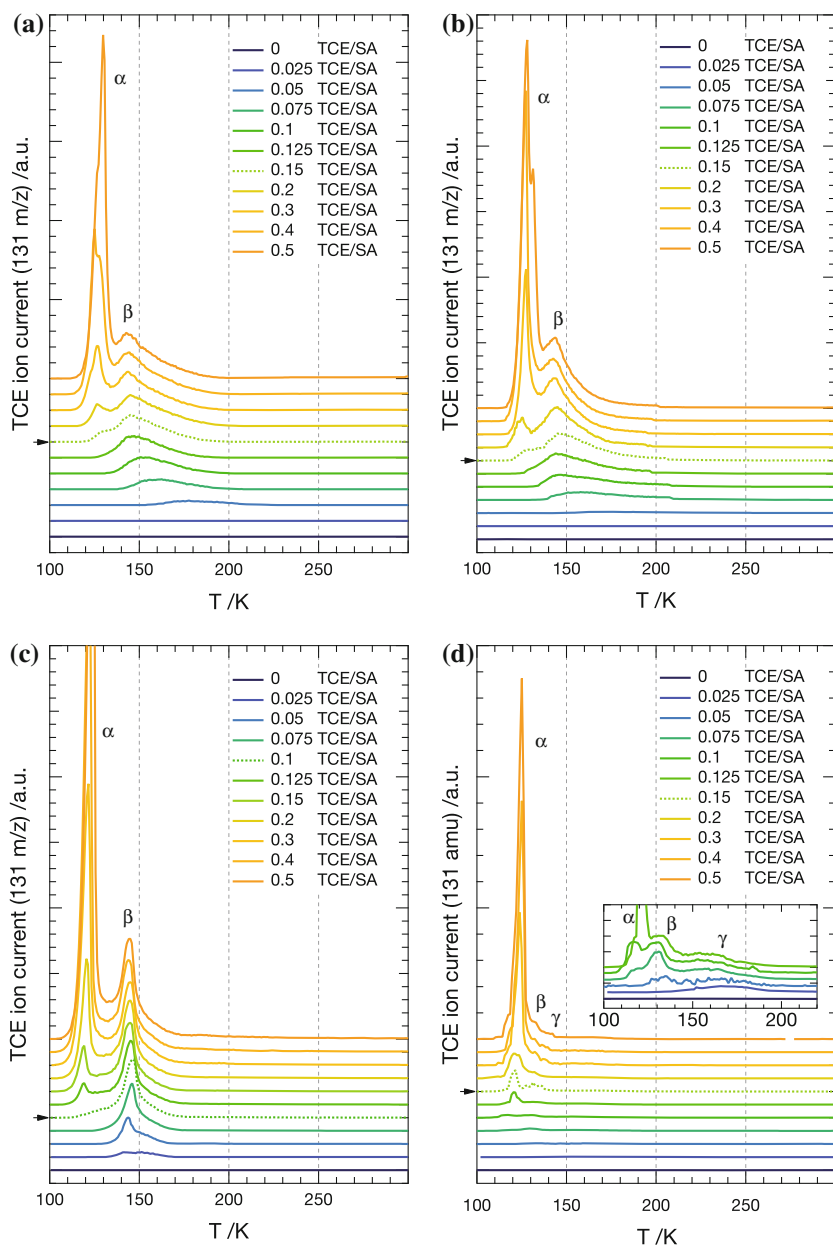
Fig. 4.11 TPD ($\beta = 2\,K/s$) spectra of *TCE* desorption on $MgO(100)/Mo(100)$ (**a**), $Mo(100)$ (**b**), $Mo(112)$ (**c**) and $Pt(111)$ (**d**); α peaks are assigned to desorption of a condensed TCE multilayer, while peak β and γ are attributed to a physisorbed layer. The corresponding inset in (d) shows a selection of spectra at low coverages. In addition, the spectra corresponding to the coverage of a completed physisorbed layer are indicated by a *dashed line* and a small *arrow*. *Reprinted (adapted) with permission from* [4]—*Copyright (2012) Elsevier*

surface dominate; whereas, with increasing coverage the lateral interaction between the molecules increases and thus weakens the interaction with the surface [7].

Two desorption peaks are also seen for **Pt(111)**. Peak β, corresponding to physisorbed *TCE* appears from 0.05 TCE/SA on with a peak maximum at 145 K. Peak α starts from 0.125 TCE/SA on and shifts slightly from 119 to 124 K. In contrast to the above described cases the position of the β peak is unaffected by the *TCE* coverage, indicating a simple first order desorption kinetics. Again, the integrated peak areas (Fig. 4.12c) clearly show that the β peak levels off with initial coverage which indicates the completion of the first physisorbed layer.

The completion of the first layer takes place at a nominal coverage of 0.1 TCE/SA which is attributed to a less dense packing of the *TCE* molecules on *Pt*(111) in comparison with the other two surfaces. The ($\sim$2/3) lower adsorbate density of physisorbed *TCE* on *Pt*(111) may result from a different adsorption geometry of the adsorbed molecule.

In the TPDs of *TCE* adsorbed on **Mo(112)** three different peaks appear. Two are attributed to physisorbed layers (β and γ for low coverages) while peak α corresponds to condensed *TCE* at higher coverages. Peak γ starts to be visible from 0.025 TCE/SA and has a peak maximum at 168 K (shifting to 160 K); peak β is found at coverages above 0.05 TCE/SA with a peak maximum at 135 K (shifting to 132 K). The peak α, corresponding to the condensed phase starts to grow from 0.075 TCE/SA and the maxima shift from 119 to 124 K. The two peaks β and γ are attributed to a physisorbed layer since the sum of the integrated peak areas show the typical levelling off, similar to the other graph in Fig. 4.12.

The fact, that *Mo*(112) consists of a more open surface, is a natural explanation of the existence of more than one adsorption site, leading to two peaks. On the other hand, the fact that multilayer formation sets in slightly before the completion of the first layer may be explained as well by the high indexed *Mo*(112) surface. Apart from these deviations the TPD study proves, that *TCE* weakly interacts with all investigated substrates and results in the formation of a physisorbed first layer followed by multilayer condensation.

EES MIES/UPS measurements were performed in parallel to the above described TPD experiments. For all surfaces the same *TCE* dosing sequence was applied with the following equivalent dosages: in the range from 0–0.05 TCE/SA the coverage was increased in 0.01 TCE/SA steps, from 0.05–0.15 TCE/SA in 0.025 TCE/SA steps and from 0.2-0.5 TCE/SA in 0.1 TCE/SA, respectively; additionally 0.75 TCE/SA and 1.0 TCE/SA were dosed and measured. Figures 4.13, 4.15, 4.16 and 4.17 show the obtained EE spectra for *MgO*(100), *Mo*(100), *Mo*(112) and *Pt*(111), respectively, after background treatment (i.e. step 4 in Fig. A.5, Appendix). The spectra displayed at the bottom of each graph belong to the clean surfaces, from bottom to top the *TCE* dosage increases.

In order to facilitate the following descriptions of the spectra, the peaks are numbered from I to V with increasing IP energy according to the gas phase peaks (Appendix, Sect. A.3.5). Briefly, the following MOs (I) $\pi_{C=C}$, n_{Cl}; (II) n_{Cl}; (III) $\pi_{C=C}$, n_{Cl}, σ_{CCl}; (IV) $\sigma_{C=C}$, σ_{CCl} and (V) s are assigned. The changes in the MIES/UPS spectra for each surface are summarized in Table 4.1, where the dosages
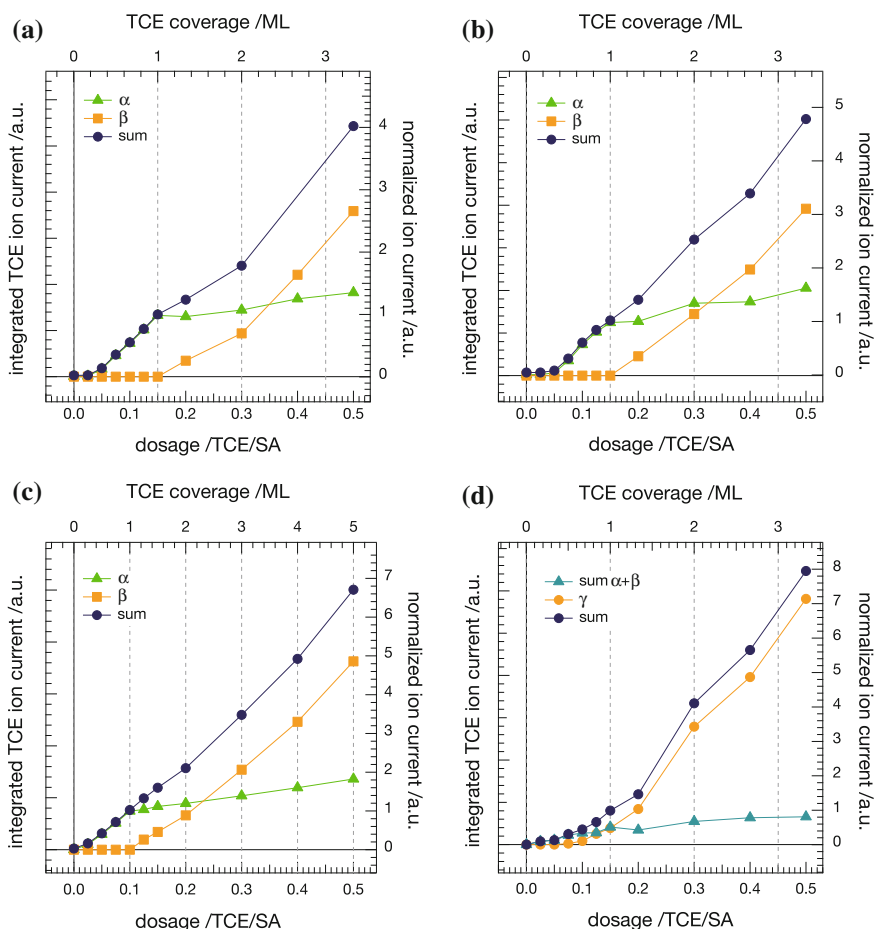
Fig. 4.12 Integrated areas of the individual peaks and total area for the measured TPD series of *TCE* on *MgO*(100) (**a**), *Mo*(100) (**b**), *Pt*(111) (**c**) and *Mo*(112) (**d**); the scales on the *right* and on *top* normalize the determined integrals for comparability of the different surfaces; the *dashed lines* mark the transition from physisorption to condensation. *Reprinted (adapted) with permission from* [4]—*Copyright (2012) Elsevier*

after which a peak can be resolved are stated. Also, the energy peak positions of the five peaks obtained after saturation dosage (measured with TPD at 0.5 TCE/SA) are listed.

For **MgO(100)** both the UP/MIE spectra (Fig. 4.13) the MOs from *TCE* overlap with the O2p peak of the *MgO* substrate. As the data set suffers from charging due to the insulating nature of the *MgO* layer, energy calibration was achieved by referencing to the pronounced O2p peak with a nominal BE of 6 eV corresponding to oxygen orbitals oriented normal to the *MgO*(100) surface. As seen in Fig. 4.14, the second O2p feature at a BE of 9.1 eV corresponding to O2p (MOs parallel to the
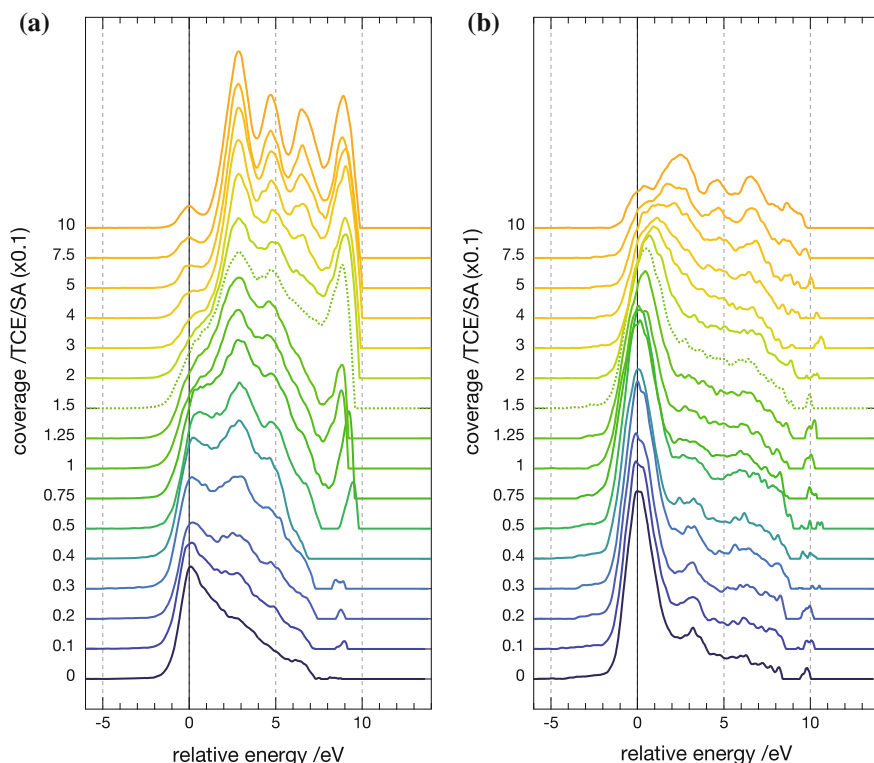
(a)

(b)

Fig. 4.13 EE spectra (MIES **a** and UPS **b**) of adsorbed *TCE* on *MgO*(100), referenced on the first peak (relative energy E_R = zero) and background corrected. The plot shows increasing dosage of *TCE* from *bottom* to *top*. The *bottom* spectra show the clean *MgO*(100) surface; the *dashed line* indicates the saturation of the first *ML*, determined from TPD measurements. *Reprinted (adapted) with permission from* [4]—*Copyright (2012) Elsevier*

surface plane) is less suitable as it is visible exclusively in UPS [43, 44] at coverages below 0.15 TCE/SA.

For MIES the *TCE* features are detected after dosage of an equivalent amount of 0.02 TCE/SA, while the sensitivity in UPS is greatly reduced (to 0.4 TCE/SA) due to the overlap with the O2p features of the oxide support. Summarizing the findings for *MgO*(100), the observations are in good agreement with the data of Kunz et al. [7], however show yet a better resolution of the adsorbate MOs. For 0.5 TCE/SA the peak fitting, after background correction on all five *TCE* MOs is exemplarily shown in Fig. 4.13.

In the following MIE spectra obtained from the clean metal surfaces the peaks of *TCE* evolve more clearly than on the insulating material (*MgO*), because the data suffer less from secondary electron signals and profit further from the missing O2p peaks which dominate the *MgO* spectra. It has to be mentioned that a direct comparison of MIES and UPS only holds for the case of *TCE* molecules adsorbed
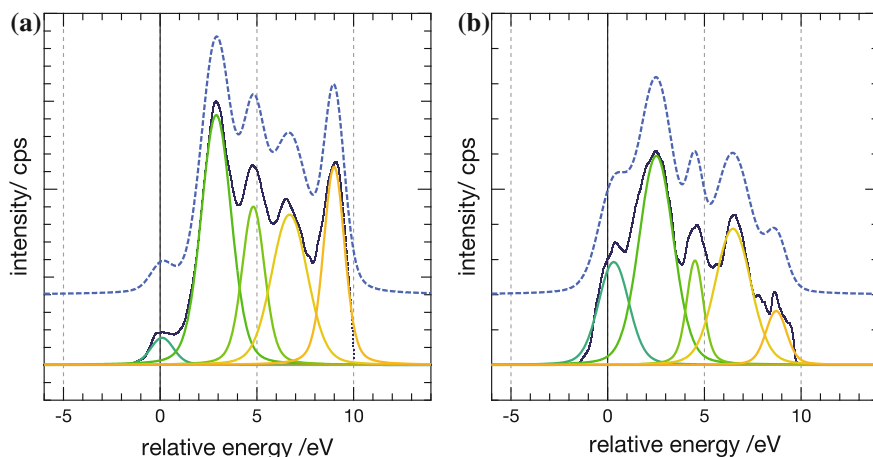
Fig. 4.14 EES spectra (MIES (**a**), UPS (**b**)—*dark blue*) for 0.5 TCE/SA on *MgO*(100) and the corresponding fit functions (*green to yellow*) for the five TCE features, as well as the corresponding sum of the fit functions (*dashed light blue*)

on the *MgO* surface. This is because only the (slower) Auger Deexcitation (AD) mechanism is occurring on the insulating *MgO* whereas the metal surfaces allow for Resonant Transfer (RT) with the conducting surface (see Sect. 2.2.3) states strongly influencing the peak shape and intensity of the MIE spectra [7, 33, 44].[10]

As visible from Table 4.1 and Fig. 4.15 the MIE data set obtained from the *TCE* adsorption study on **Mo**(**100**) is the most sensitive. *TCE* features appear at dosing greater than an equivalent of 0.02 TCE/SA (all five MOs visible from 0.03 TCE/SA on). In UPS the detection limit is about three times less (0.075 TCE/SA for first indication, 0.125 TCE/SA if all peaks are fully resolved).

A similar behaviour is observed for **Mo**(**112**), where in the MIE spectra all features of *TCE* can be seen from 0.04 TCE/SA on and the UP spectra reveal all *TCE* MOs from 0.1 TCE/SA on (see Fig. 4.16).

The MIE spectra (Fig. 4.17 a and c) recorded for **Pt**(**111**) show *TCE* features at a coverage of 0.02 TCE/SA and are all visible from 0.05 TCE/SA on. In the UP spectra (Fig. 4.17 b and d) of the clean surface the characteristic *5d* band double peak structure (due to spin orbit splitting) dominates the spectrum until a dosage corresponding to 0.1 TCE/SA (equivalent to the first *ML* in TPD). As a consequence peak III can be resolved only at coverages above 0.15 TCE/SA and more than 0.4 TCE/SA are required to identify all MOs.

For comparison Fig. 4.18 shows the MIE and UP spectra of the studied surfaces with 0.5 TCE/SA, the highest coverage of the TPD data displayed in Fig. 4.11 and 4.12, corresponding to a physisorbed *TCE* layer covered by multiple condensed layers ontop. All five peaks known from the gas phase can be assigned. The spectra show

---

[10] In a strict sense this is again only true for the submonolayer range, as for adsorbate multilayers the deexcitation mechanisms resemble probably more the insulator surface.
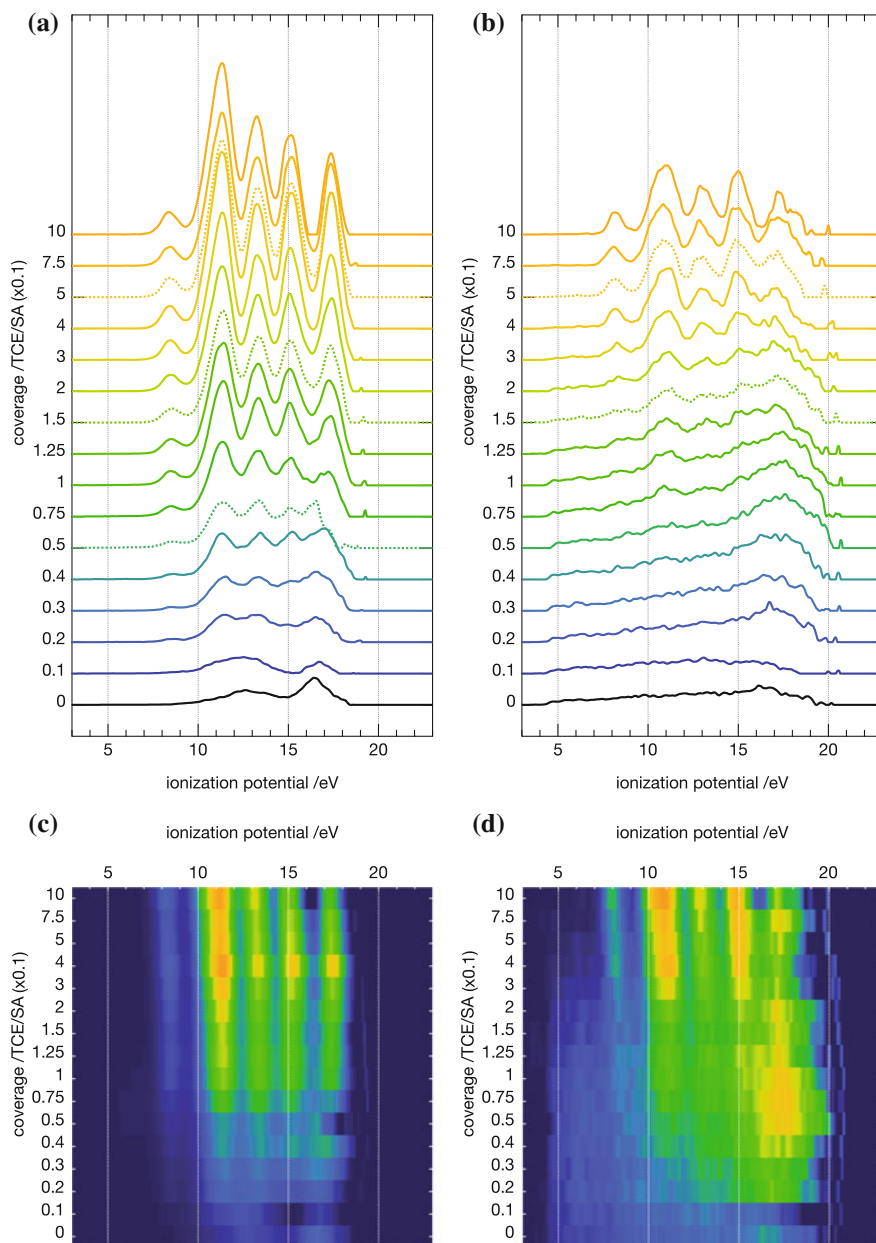
Fig. 4.15 EE spectra of adsorbed *TCE* on *Mo*(100); referenced against the vacuum level and background corrected. Increasing dosage of *TCE* from *bottom* to *top*; MIES (**a**) and UPS (**b**). The *bottom* spectra show the clean *Mo*(100) surface. The *dashed lines* indicate the coverages (0.05, 0.15 and 0.5 TCE/SA) for which the IP peak energy shifts are shown in Fig. 4.20; with 0.15 TCE/SA corresponding to data from a completed first monolayer (*dashed line*). Subfigures (**c**) and (**d**) show the corresponding image plots for better visibility of the appearance of the *TCE* peak features for MIES and UPS, respectively. *Reprinted (adapted) with permission from* [4]— *Copyright (2012) Elsevier*
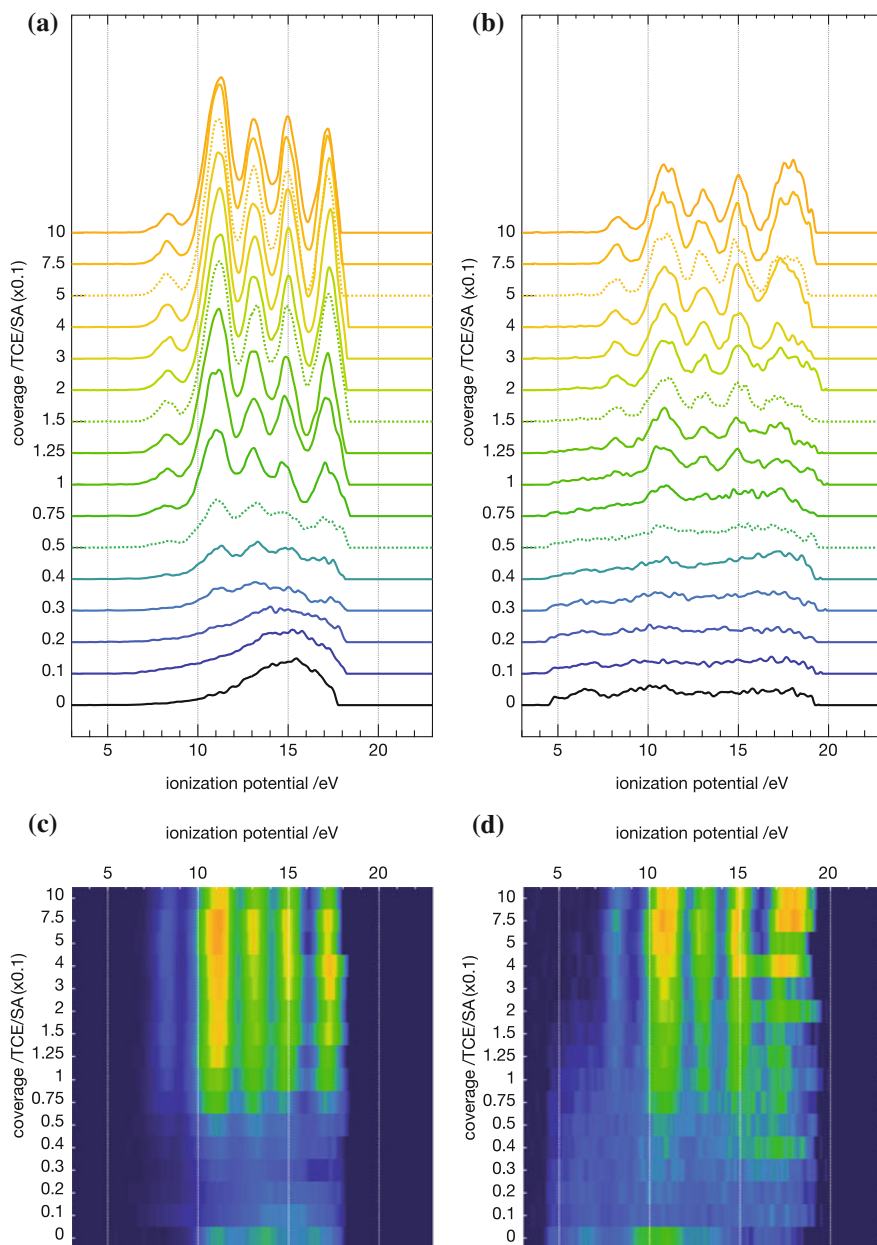
Fig. 4.16 EE spectra of adsorbed *TCE* on *Mo*(112), referenced with respect to the vacuum level of the clean substrate and background corrected. Increasing dosage of TCE from *bottom* to *top*; MIES (**a**) and UPS (**b**). The *bottom* spectra show the clean *Mo*(112) surface. The *dashed lines* indicate the coverages (0.05, 0.15 and 0.5 $^{TCE}/_{SA}$) for which the IP energy shift is shown in Fig. 4.20. Subfigures (**c**) and (**d**), show the corresponding image plots for better visibility of the appearance of the *TCE* peak features for MIES and UPS, respectively. *Reprinted (adapted) with permission from* [4]— *Copyright (2012) Elsevier*
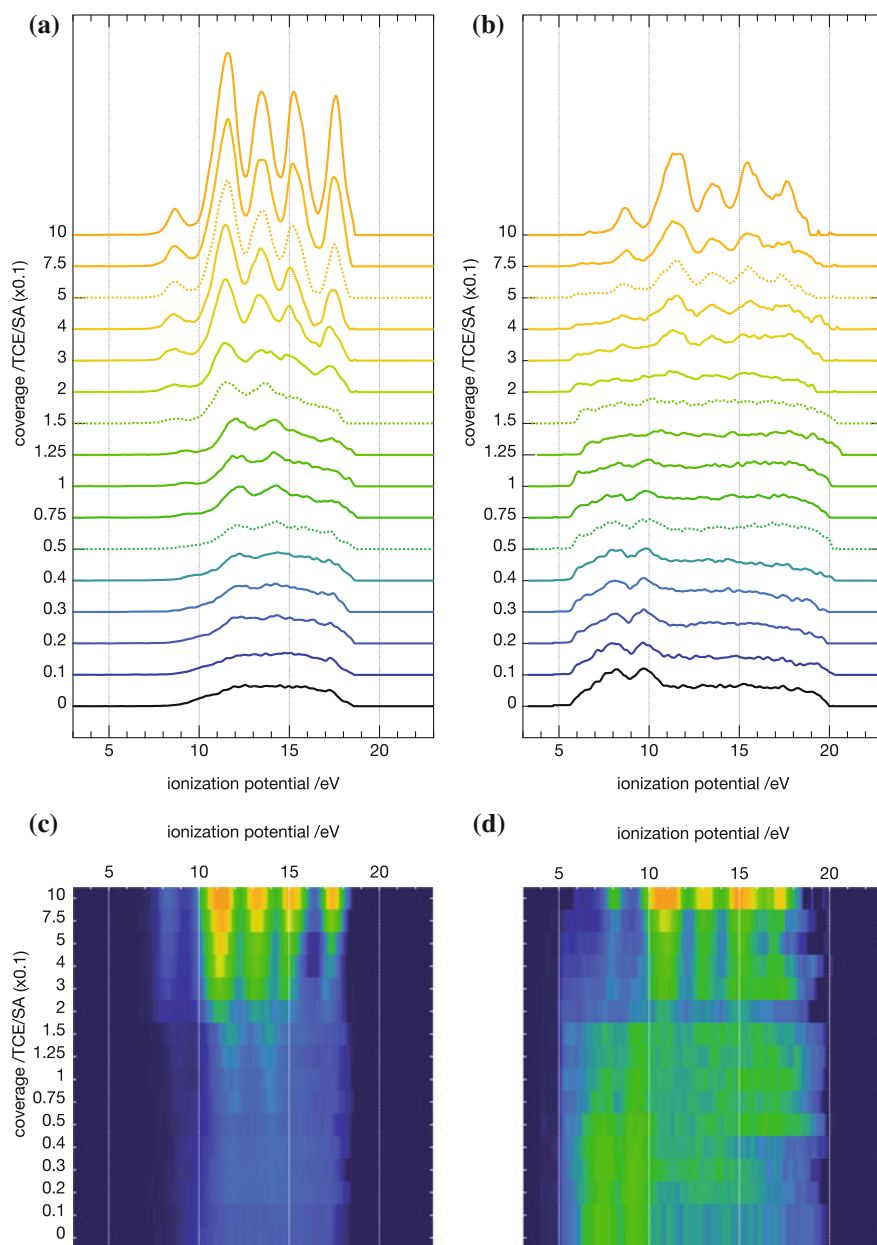
Fig. 4.17 EE spectra of adsorbed *TCE* on P*t*(111), referenced with respect to the vacuum level of the clean substrate and background corrected. Increasing dosage of TCE from *bottom* to *top*; MIES (**a**) and UPS (**b**). The *bottom* spectra show the clean *Pt*(111) surface. The *dashed lines* indicate the coverages (0.05, 0.15 and 0.5 TCE/SA) for which the IP energy shift is shown in Fig. 4.20. Subfigures (**c**) and (**d**), show the corresponding image plots for better visibility of the appearance of the *TCE* peak features for MIES and UPS, respectively. *Reprinted (adapted) with permission from* [4]— *Copyright (2012) Elsevier*

Table 4.1 Dosage after which each peak (I-V) can be resolved with EES (MIES a, UPS b) in TCE/SA and observed values of ionization potential (IP /eV) for the corresponding peak positions for studied metal surfaces at saturation coverage of 0.5 TCE/SA

Peak	First appearance /TCE/SA					Energy position @0.5 TCE/SA /eV				
	I	II	III	IV	V	I	II	III	IV	V
Gas phase	–	–	–	–	–	9.70	12.30	14.50	16.40	18.60
MgO(100)	0.050	0.020	0.030	0.050	0.050	–	–	–	–	–
Mo(100)	0.020	0.020	0.020	0.020	0.030	8.43	11.28	13.33	15.18	17.38
Mo(112)	0.040	0.020	0.030	0.030	0.030	8.26	11.06	13.13	14.99	17.18
Pt(111)	0.040	0.020	0.030	0.050	0.050	8.66	11.48	13.49	15.25	17.52
					(a)MIES					
Gas phase	–	–	–	–	–	9.70	12.30	14.50	16.40	18.60
MgO(100)	0.750	0.500	0.400	0.200	0.500	–	–	–	–	–
Mo(100)	0.125	0.075	0.125	0.150	0.150	8.10	10.90	12.90	14.99	17.15
Mo(112)	0.100	0.050	0.075	0.100	0.075	8.17	10.87	13.01	14.93	17.37
Pt(111)	0.300	0.200	0.150	0.300	0.400	8.59	11.44	13.61	15.44	17.34
					(b)UPS					

Gas phase data are presented for comparison. Detection of peak I of *TCE* is less sensitive due to the smallness of the peak. On the *MgO* film this peak cannot be detected at all in the submonolayer regime with both MIES and UPS due to overlap with the O2p peak of the oxide surface. *Reprinted (adapted) with permission from* [4]—*Copyright (2012) Elsevier*

the successful application of the background correction and evidence the superior quality of the MIE spectra when compared to the UPS data.

The **WF** changes with respect to the *TCE* coverage have been determined for UPS data and the results for all surfaces are shown in Fig. 4.19. We refrain from extracting WF values from MIES data, since with missing electron density at the Fermi edge for the metals (on an BE scale) in the spectra, the determination of the WF through the chosen approach (by using the width of the spectra as described in Sect. A.1.5) is not applicable/defined. As mentioned, the data obtained from **MgO**(**100**) suffered from charging, so no WF values could be extracted. The WF of the clean surfaces are in agreement with the literature, further details are stated in the Appendix in Sect. A.1.6.

The values have a statistical error of ± 0.05 eV, estimated from the deviations of fifteen measurements on the clean surfaces. The general trend of a decreasing WF with increasing *TCE* coverage in the submonolayer regime may be explained by a charge transfer from the *TCE* molecule to the surface, or by electron correlation effects in weakly interacting systems, thus decreasing the surface dipole moment and has been found for a variety of different systems [7, 45–47].

For **Mo**(**100**) up to a coverage of 0.05 TCE/SA a minimum ($\triangle \phi \sim -0.35$ eV) is found. With additional dosage the WF reaches the starting value at 0.4 TCE/SA from where on it stays stable ($\triangle \phi \sim +0.0$ eV).

The values for **Mo**(**112**) show a slight decrease in the beginning ($\triangle \phi \sim -0.12$ eV) with a minimum at 0.05 TCE/SA, as *Mo*(100); further dosage increases the WF and reaches a saturation value at 0.4 TCE/SA, and saturates from there on ($\triangle \phi \sim +0.1$ eV).
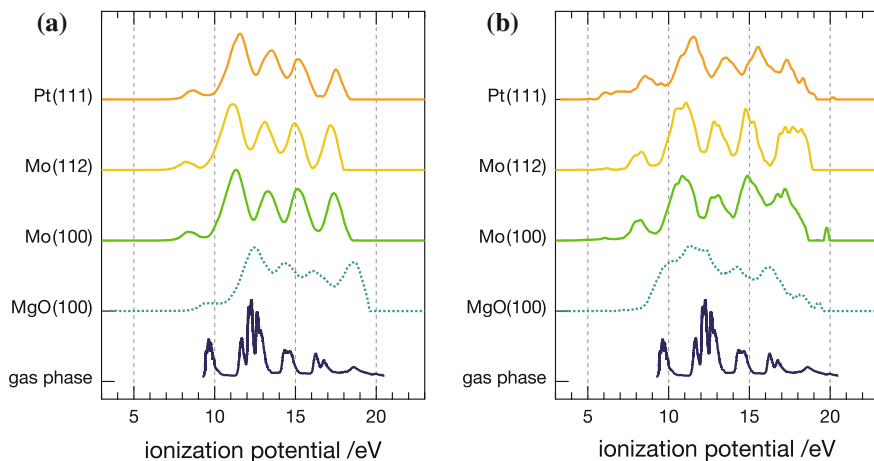
Fig. 4.18 EE spectra of 0.5 TCE/SA (equal to physisorbed and multilayer *TCE*) for the investigated surfaces. From *bottom* to *top*: gas phase PE spectrum from Kimura et al. [5] and *MgO*(100)/*Mo*(100) displayed for comparison (aligned to the gas phase spectra, by adding the gas phase value of the *TCE* peak I with 9.7 eV to the arbitrary origin on the relative energy scale at the first O2p feature of the *MgO* support, see text); *Mo*(100), *Mo*(112) and *Pt*(111) on IP energy scale; MIES (**a**) and UPS (**b**). *Reprinted (adapted) with permission from* [4]—*Copyright (2012) Elsevier*

For **Pt(111)** a decrease ($\triangle\phi \sim -0.4$ eV) until 0.15 TCE/SA is visible, for additional coverage saturation at this value is observed ($\triangle\phi \sim -0.3$ eV). These observations show the same trend as previously reported WF measurements for *ethene* adsorption on *Pt*(111), where a decrease in the submonolayer range ($\triangle\phi \sim -1.2$ eV) and later saturation after the first monolayer were reported [40]. The larger WF change for *ethene* on *Pt*(111) can be related to the formation of a di-σ bond, which seems to be absent in the case of the weak interacting *TCE*, as indicated by the TPD data and the discussion in Sect. 2.1.2.

Close inspection of the MIE spectra of *TCE* on the different surfaces plotted in Fig. 4.18 show a **shift of the energy position (IP)** of the five resolved peaks with increasing coverage. These peak energy shifts are depicted in Fig. 4.20, as well in more detail in Fig. 4.21 and are discussed in the following.

All peak energies obtained from adsorbed *TCE* at saturation coverage are shifted towards lower energy with respect to the gas phase spectra, thus show a relaxation shift (Sect. 2.2.3). Figure 4.20 summarizes the peak energy shifts determined by MIES and UPS for all surfaces after *TCE* adsorption (submonolayer: 0.05 TCE/SA, completed physisorbed layer: 0.15 TCE/SA and physisorbed plus multilayer saturation: 0.5 TCE/SA).

In general, the observed **uniform shifts between 0.8–1.5 eV** for both, the MIES and UPS spectra (for *Mo*(100) 1–1.2 eV, for *Mo*(112) 1.3–1.5 eV and *Pt*(111) 0.8–1.2 eV) are in good agreement with published data of hydrocarbons on metal surfaces (1–3 eV) [48, 49].
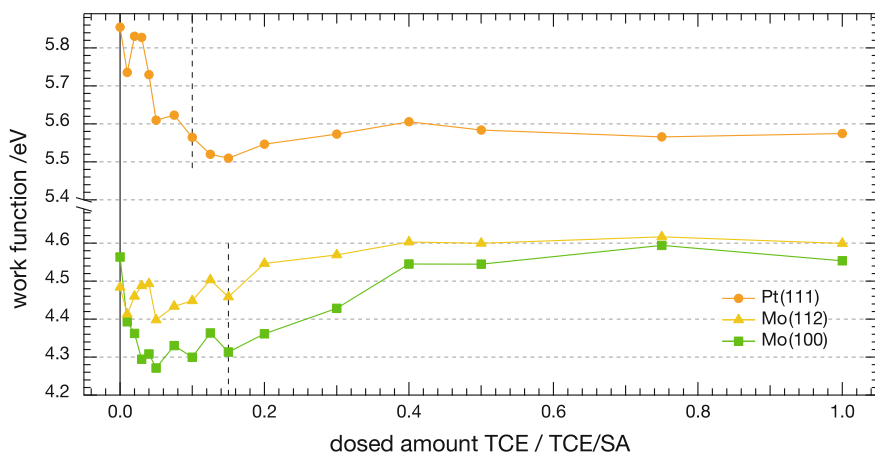
Fig. 4.19 WF with increasing coverage of *TCE* on the studied surfaces. The values are determined from the corresponding UPS measurements; the *dashed lines* represent the corresponding *ML* determined by TPD measurements. The values have a statistical error of ± 0.05 eV, for details see text. *Reprinted (adapted) with permission from* [4]—*Copyright (2012) Elsevier*

For each data set the energy positions of all five peaks do not shift with respect to each other. The fact that all peaks shift by an equal amount exclude the formation of a specific chemical bond of *TCE* with the substrate, which would affect one or more specific MOs. The absence of such an effect clearly supports the picture of a weakly adsorbed *TCE* molecule. The relative peak shifts are more clearly visible in Fig. 4.21. In this graph the deviation of each peak energy position with respect to the one obtained at saturation coverage is plotted. The peak positions have been fixed relative to each other within ± 0.2 eV in the applied fit procedure.

In fact the relative energy positions vary even less (as visible from the data scatter in Fig. 4.21) in the multilayer regime the error is about (± 0.05 eV). Save for peak V, where systematic errors seem to be introduced by the applied background subtraction.

Comparing the (global) energy shift of all MO peaks Fig. 4.21 acquired from the different metal substrates, evidences different trends. For the MIES data sets obtained from **Mo** single crystal surfaces the energy position of the peaks I–V are almost coverage independent (variation < 0.2 eV). In contrast, on the **Pt**(**111**) a larger energy variation with coverage (within 0.6 eV) in the submonolayer regime is observed. Here, the peaks show a distinct shift compared to the multilayer regime with condensed *TCE*. Whether or not *TCE* coverage dependent electron BE shifts are expected is related to role of the corresponding WF and the BE reference level. As visible from Fig. 4.19 the WF changes with increasing amount of adsorbed *TCE* molecules. At a first glance one would expect a weakly adsorbed molecule to reference against the vacuum level above the substrate surface. A variation in the WF would result in a variation of the peak energy positions with respect to a fixed reference level, such as the Fermi energy or the vacuum level of the clean substrate. The fact that this is not the case for the *Mo* surfaces, whereas to a minor degree for *Pt* indicates compensating effects of potential energy and electron relaxation, which are intimately
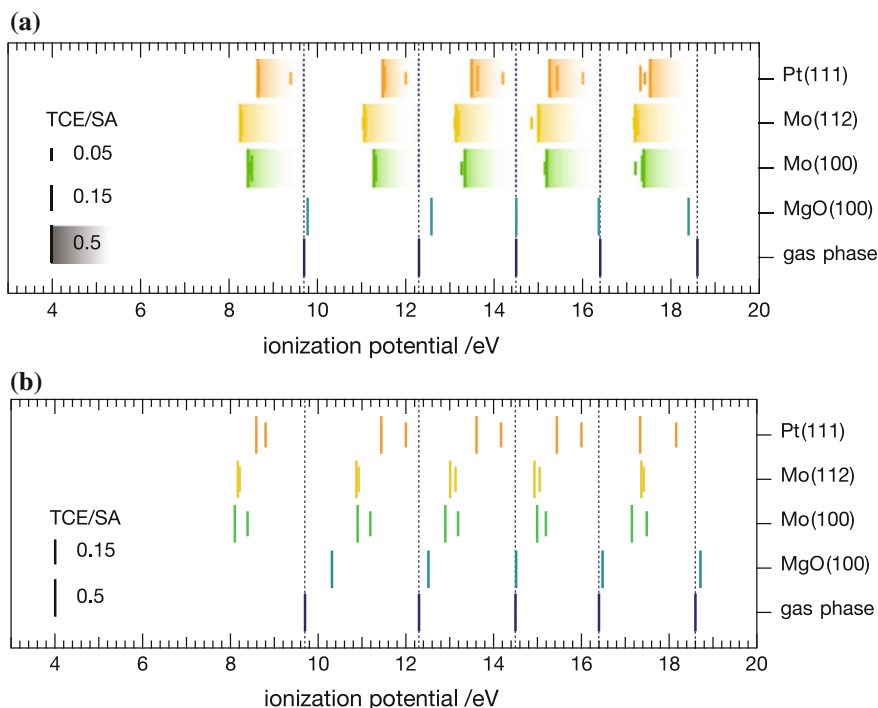
Fig. 4.20 Shifts of peak energy positions on the various surfaces with respect to the peak positions of the gas phase spectra of Kimura et al. [5]; MIES (**a**) and UPS (**b**). For MIES three selected coverages, for UPS two coverages (above the *ML*) are shown. The height of the *lines* reflect the dosed *TCE* concentrations on the surface: 0.05 (MIES only), 0.15 and 0.5 TCE/SA, corresponding to physisorbed species only, filled first *ML* and physisorption with condensation ontop, respectively. Due to charging of the *MgO* substrate (see text) only the peaks for the highest *TCE* coverage are shown with the energy position of peak II aligned to the one of the gas phase spectrum. *Reprinted (adapted) with permission from* [4]— *Copyright (2012) Elsevier*

related to the image charge potential of the molecule in front of the surface, as has been discussed in [48]. Seemingly, the observed differences in energy shifts for *Pt* and *Mo*, lead to to the conclusion, that the contribution of core-hole screening and image potential, differs for *TCE* in front of the *Pt* and *Mo* metal surfaces.

For the UPS data set the trends for shifts on the different surfaces are comparable, however less evident due to the higher scatter of the data. Furthermore, due to the higher probe depth of the method determined peak energies may be influenced by eventual different bulk and surface effects.

Besides the energy positions of the five *TCE* peaks, their **intensities** were studied by extracting the peak areas. In Fig. 4.22 their relative intensities (peak I–IV)[11] with

---

[11] Eventual errors introduced by the normalization procedure including all five peak components, might be reduced excluding peak V. However, MIES data remain almost unaffected and UPS data do not gain in quality.

respect to the sum intensity are plotted (on a percent scale). It is clearly seen that the intensities remain almost fixed throughout the entire coverage range of the performed experiment. Due to the lower sensitivity of the UPS data the scatter is significantly enhanced when compared to the MIES data set. This data is used for evaluating the sensitivity of the methods UPS and MIES in Sect. 4.1.

An eventual geometrical reorientation of the molecule would become obvious in such plot, since the cross section for electron emission from a MO is generally sensitive to its symmetry with respect to the geometry and the probe method of the experiment. With MIES as very sensitive method exclusively probing the uppermost layer of a surface and the symmetry of the MO with respect to the He^*2s state, leads to sensitive selection rules. With this technique the reorientation of benzene in the physisorbed layer on $MgO(100)$ upon variation of the adsorbate coverage could be verified [43] as well as on $Ru(0001)$ and $Mo(100)$ [50]. As visible from Fig. 4.22 a similar reorientation of *TCE* does not take place on the studied surfaces, since all relative peak intensities are unaffected by the amount of adsorbed molecular *TCE* within the experimental error. Thus, we conclude that the geometry of the adsorbate does not change with coverage [33, 51].

One can consider the *TCE* molecule as lying flat on the **Pt** and **Mo** metal substrates, in accordance with the NEXAFS study performed on $Pt(111)$ [8]. For *Pt* in the submonolayer range no changes of the orientations are observed based on the presented MIES data, for the multilayer however changes are visible. These changes could originate from changing orientation of the *TCE* molecules or simply bigger deviations in the data scatter compared to the *Mo* surfaces. That a certain disorder of *TCE* in the multilayer range seems a possible explanation for our observed MIES data scatter is in agreement with the NEXAFS study of Cassuto et al. [8]. Note that for both *Mo* surfaces the peak intensities in the MIES and UPS data are almost identical, indicative for an equal molecule orientation on $Mo(100)$ and $Mo(112)$. The different TPD peaks found for $Mo(112)$ may be attributed different adsorption strength due to the more open geometry of the surface plane, while not affecting the molecular orientation.

Summary—results from measurements by means of TPD in combination with MIES/UPS assign *TCE* adsorption on surfaces to physisorption followed by multilayer formation. The picture of a weakly interacting *TCE* molecule is supported by findings from analysis of the electron BE peak positions and intensities as well as WF measurements. No orientational changes of the *TCE* molecule with coverage can be evidenced, thus it is concluded, that the molecules lie most probably flat on all metal surfaces, in both the physisorbed and multilayer phase (in accordance with NEXAFS data reported in the literature). The observed changes in WF and BE shifts of the five *TCE* MOs are in agreement with such an adsorption geometry. Minor differences in peak energy shifts observed on *Pt* and *Mo* are attributed to different compensation of relaxation and potential energy effects on these surfaces.
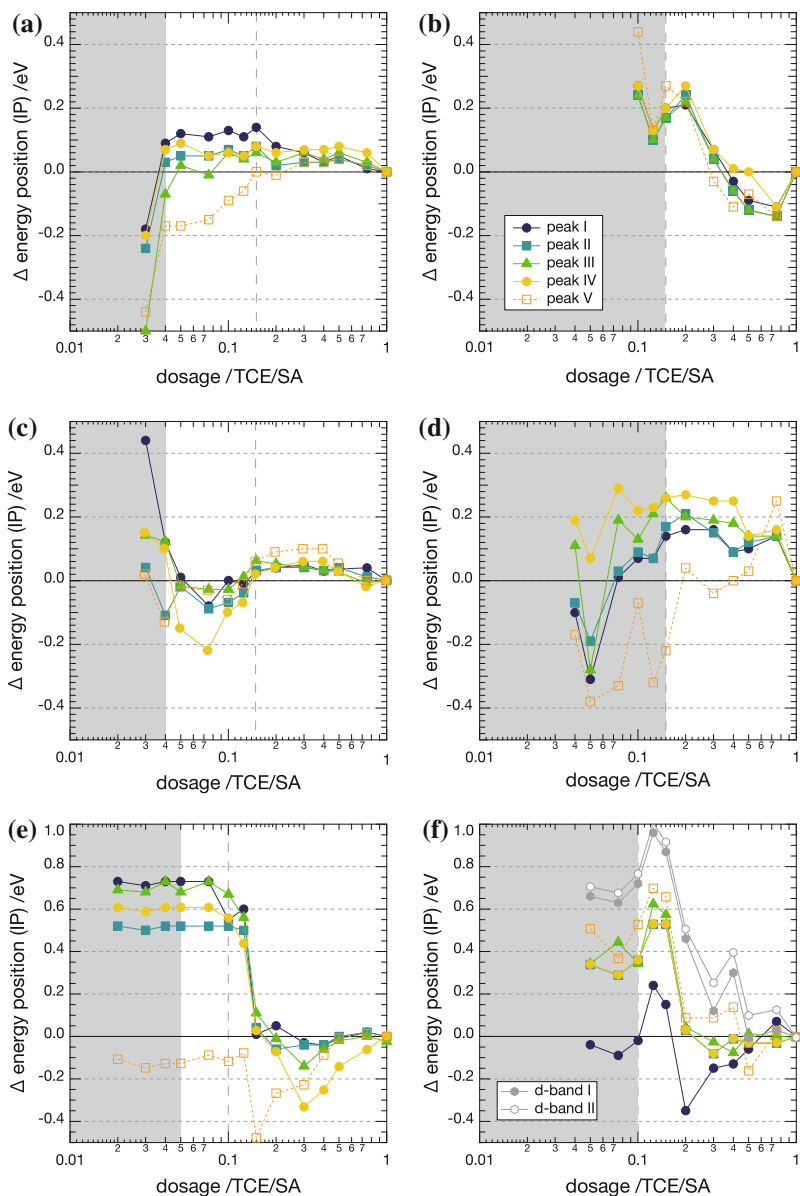
Fig. 4.21 Shifts of the peak energy positions in EES of the *TCE* MOs on the studied surfaces. The dosed amounts are plotted in log scale for better visibility of the submonolayer range. Corresponding *ML* (*dashed line*) and range in which not all peaks are visible in accordance with the values from Table 4.1 (*gray areas*). The relative energies are plotted with respect to the position at the final coverage of 1 TCE/SA. Peak V is plotted in *dashed lines*, as systematic errors seem introduced by the background fitting procedure. The error of these data is apparent from the data scatter. *Reprinted (adapted) with permission from* [4]—*Copyright (2012) Elsevier*
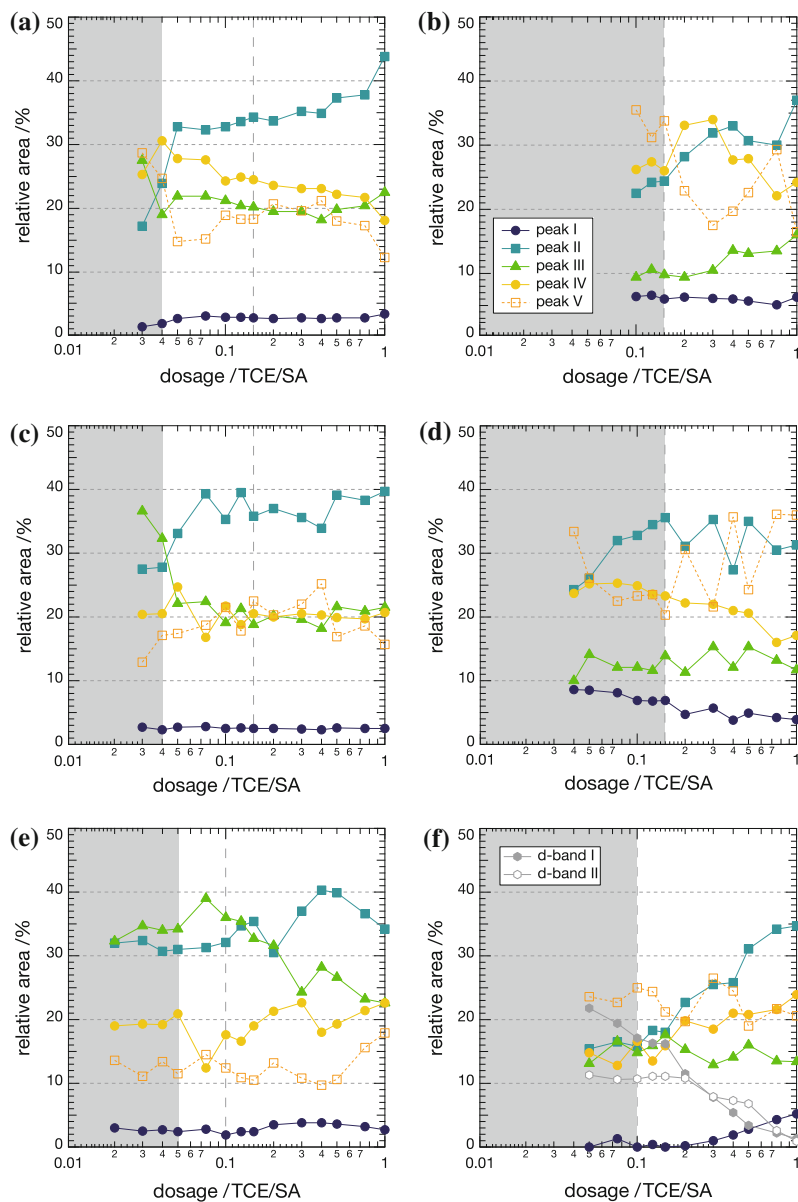
Fig. 4.22 Changes in relative area for obtained from the fit values (peak I–IV) from 0.03 TCE/SA for MIES (a,c,e) and from 0.1 TCE/SA on for UPS (b,d,f). The dosed amounts are plotted in log scale for better visibility of the submonolayer range; corresponding *ML* marked with *dashed line* and *gray area* represents the range in which not all peaks are visible (Table 4.1). For *Pt* the *d*-band peak positions are shown, peak V is plotted in *dashed lines* (systematic errors). The error of these data is apparent from the data scatter, for details see text. *Reprinted (adapted) with permission from* [4]—*Copyright (2012) Elsevier*

4.4.2 TCE Interaction on Pt_x Clusters

The previous section has shown, that *TCE* interacts only weakly with different surfaces. In contrast, small noble metal particles have shown to catalyze the conversion [52, 53] successfully. Thus, in this section the reactivity of supported size-selected *Pt_x* clusters towards *TCE* conversion is investigated. Again a combination of TPD and EES experiments are performed and compared to the findings on the surfaces, to check if the binding of the molecule is different on clusters. For all following experiments (TPD and EES) a coverage of $0.1\,^{TCE}/_{SA}$ (thus, below $1\,ML$) was chosen, in order to circumvent possible effects from condensed molecules. The low cluster coverages make it challenging to see changes, yet considering alternative reaction pathways (i.e. spill-over from the support) could allow for reactivity.

Before and after cluster deposition **TPD** spectra of *TCE* were recorded and are depicted in Fig. 4.23. Two sets of spectra are shown, covering two temperature ranges from 100–180 K and 100–600 K (note different scales for temperature and ion current). This step wise approach ensures, that possible contaminants deposited along with the clusters during the synthesis process, get desorbed in the first TPD run. The amount of deposited clusters was kept constant at $0.03\,e/nm^2\,Pt_x$, leading to an increase in *Pt* amount with cluster size.

In agreement with the spectra of the surfaces (Sect. 4.4.1), the TPD spectra in the low temperature range show a peak, with a maximum of 138 K before cluster deposition, corresponding to physisorbed *TCE* on the $MgO(100)$ support. This peak feature remains with additional deposited clusters and a tendency of increased signals for bigger cluster sizes is visible. Most probably this signal has its origin in a convolution of *TCE* physisorbed on clusters and support material, since on the surfaces the peak maximum temperatures lie close together (Sect. 4.11). The intensity of the peak, (their areas) fit also well with the ones from the surfaces (peak areas not explicitly shown here).

For the second TPD data set, an additional broad peak feature with a maximum at 350 K is observed, however for both support with and without clusters. This peak, with a very small intensity (10^{-12} A range) can be attributed to defect sites of the support film, which chemisorb a small fraction of *TCE*. The small increase of this peak for bigger sizes, maybe be explained as an additional small fraction of *TCE* molecules that can be adsorbed on these clusters. However, comparing the low intensities for the chemisorption peaks at higher temperatures, with the intensities observed for the physisorption peaks, the later ones have about a two orders of magnitude higher intensity. Thus, the amount of chemisorbed *TCE* on size-selected *Pt* clusters in the presented data can be neglected. The observed chemisorption peaks can not clearly be assigned to be cluster induced, since the support shows a similar behavior. The fact that for the large sized clusters, with a considerably higher coverage of *Pt*, in a range that should allow to see changes also no activation is visible also excludes a possible reaction pathway involving spill-over. All together, the TPD results give the picture of a weakly interacting *TCE* molecule on clusters as a pure adsorbate system in the studied coverage regime, without signs for activation. This is further supported,
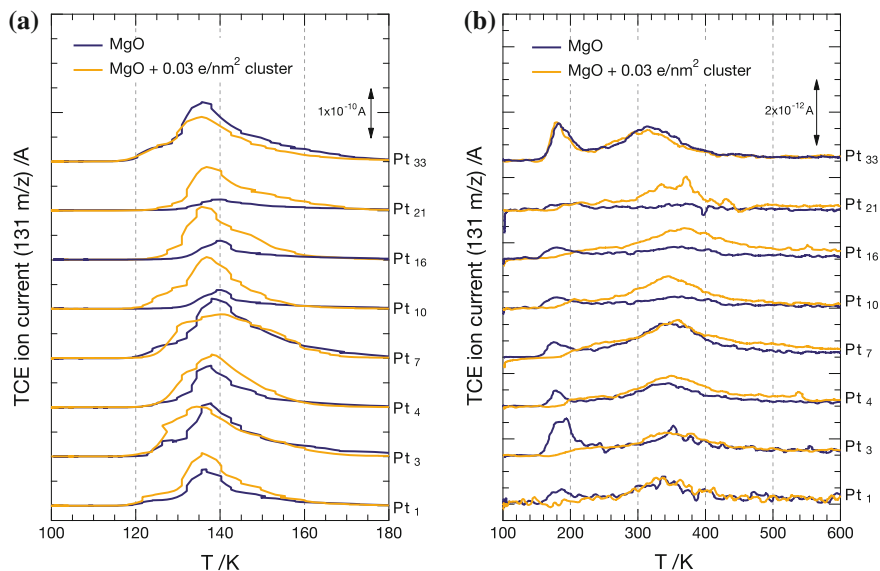
Fig. 4.23 TPD spectra of $0.1\,TCE/SA$ adsorbed TCE on supported Pt_x clusters on $MgO(100)/Mo(100)$. Two different temperature ranges, TPD from 100–180 K (**a**) and subsequent TPD from 100–600 K (**b**) as well as TPDs from the pristine support (*blue*) and TPDs after deposition of $0.03\,e/nm^2\,Pt_x$ (*yellow*) are shown. Note different scales for temperature and ion current

as additional TPD measurements with probing for possible decomposition products (e.g. *phosgene*) did not show (additional) peaks in TPD spectra.

Despite the failure of the activation of *TCE* on clusters observed in TPD, **EES** experiments of deposited selected clusters of similar sizes were performed. The exclusion of additional molecules and the chemisorption behavior for selected clusters, reduces the origin of possible shifts in peak energy positions in EE spectra to the effect of physisorption induced relaxation shifts. Thus, it allows for uncomplicated comparison of the differences in physisorption on the surfaces and supported clusters (if omitting compensating effects of potential energy and electron relaxation, as discussed in Sect. 2.2.4).

The MIES and UPS data set for different cluster sizes, after dosage of $0.1\,^{TCE}/_{SA}$ and subsequent heating to 180 K is presented in Fig. 4.24. For the EES, the number of deposited clusters was chosen in such way, that the total amount of *platinum* is constant and consequently possible cluster induced effects are normalized to the *Pt* on the surface.

Further, for two sizes a double amount of clusters has been deposited (two top spectra). Due to the insulating nature of MgO (thus not having density at the E_F in contrast to metals) referencing of the spectra could not be done by individually measuring the WF and adding it to the BE scale. To account for slight different films for each measurements, the WF literature value of 3.5 eV [54] for MgO was added as a fixed value for all surfaces; consequently also no WF evaluation is presented in
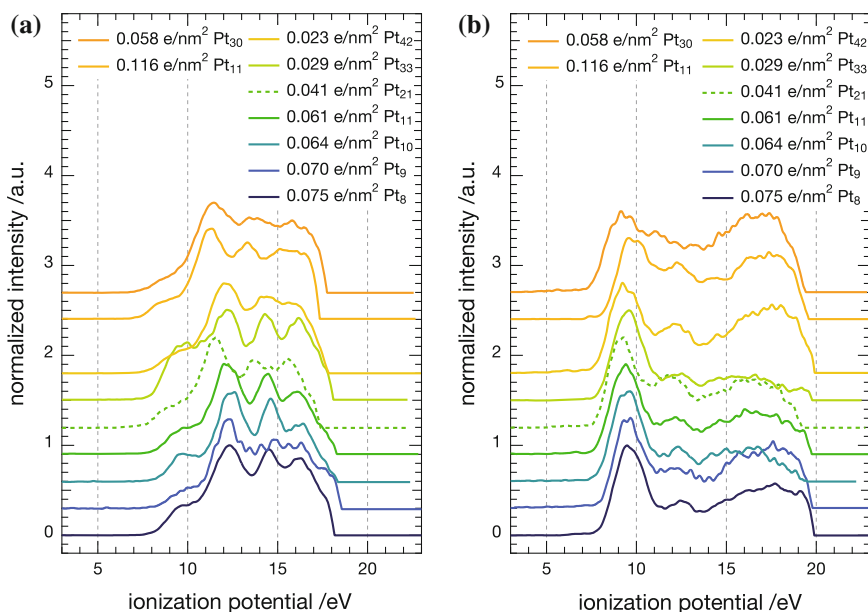
Fig. 4.24 EE spectra of 0.1 TCE/SA adsorbed *TCE* on supported *Pt_x* clusters on $MgO(100)/Mo(100)$, referenced with respect to the vacuum level by addition of a fixed WF value of 3.5 eV of the clean support (*MgO*) and background corrected. Increasing *Pt_x* cluster size from *bottom* to *top*; MIES (**a**) and UPS (**b**). The *dashed line* indicates a not trustworthy spectra of *Pt_21*

the following. The spectral *TCE* features observed in the EES spectra on supported clusters resemble the ones observed on the bare support. However, no charging could be observed for the spectra, probably due to thinner *MgO* films. The data for *Pt_21* (dashed lines) is excluded from the following discussion, as the data shows a significantly higher shift towards lower IP compared to the other sizes, most probably a systematic error in the measurement.

For **UPS** with its lower surface sensitivity, the spectra are dominated by the features of the underlying support material (see Appendix Sect. A.1.6) as submonolayer amounts of *TCE* are dosed. Spectral features of the clusters, e.g. electron density at E_F, or even the characteristic *Pt 5d* band double peak structure are not visible (in agreement with results in Sect. 4.2).

Very small indications of *TCE* MOs can be seen in few spectra, an assignment of peak or even fitting is however not feasible—a further interpretation of the UPS data is therefore not performed.

In contrast with the superior sensitivity of **MIES** and the applied correction for secondary electrons, the *TCE* MOs can be resolved on most samples, save for peak V. In fact the data allows even for peak fitting. The obtained peak energy positions are plotted along with the positions of an equal amount of *TCE* adsorbed corresponding
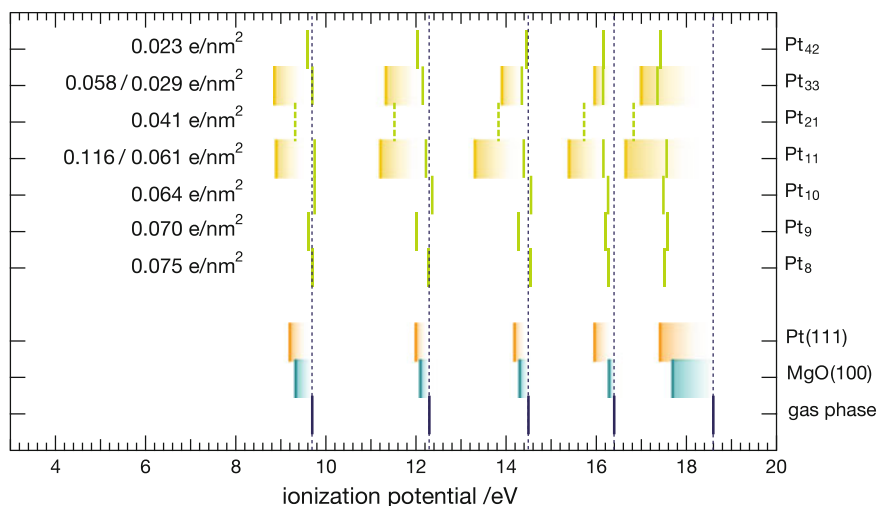
Fig. 4.25 Shifts of the peak energy positions in MIES of the adsorbed 0.1 TCE/SA *TCE* on the various cluster sizes with respect to the peak positions of the gas phase spectra of Kimura et al. [5]. As comparison the shifts for an equal amount of *TCE* adsorbed on the *MgO* (*blue*) and the *Pt* (*orange*) single crystal surfaces (Sect. 4.4.1) are shown. *Green* bars represent low cluster coverage; for Pt_{11} and Pt_{33} additionally a higher coverage was probed (*yellow*)

MgO surface before cluster deposition, the *Pt* surface (from Sect. 4.4.1) and the gas phase energies in Fig. 4.25.

A general trend towards slightly lower IP for all cluster sizes can be observed for the low coverage (green bars). The **relaxation shift** is in all cases less pronounced if compared to the behaviour on surfaces. Further the peak to peak distances remain constant (except peak V, heavily influenced by the correction) as they are fixed by the fitting procedure and thus a reorientation of the molecule can be excluded. The obtained results are thus in agreement with the TPD data of an only weak interaction of *TCE* on the clusters.

Interestingly, the two spectra with higher cluster coverages (yellow bars) show a significantly **higher shift** ($\sim +0.6$–0.9 eV) towards lower IP, even exceeding the shift on the bare surfaces in this submonolayer regime. In the light of the argumentation of a pure physisorption system and comparing to the bare surfaces, this might be due to contribution of the clusters. The higher IP shift is maybe related to a better screening on the clusters and could in consequence be evidence for a different contribution of core-hole screening and image potential for *TCE* in front of *Pt* clusters. However, this effect could also be related to undesired adsorbates, present on the surface. These would be pronounced for higher coverages, because of longer deposition times, despite heating after deposition and dosage. A further evaluation, particularly of the peak intensities is in light of the physisorption behaviour, omitted.

Summary—unfortunately, indications of cluster induced degradation of *TCE* could not be confirmed by TPD and EES experiments. In light of the low coverages

of both clusters and adsorbates, this is however not necessary a failure of the approach, but rather a still missing sensitivity and precision. Yet the results suggest, that EES, and MIES experiments in particular, allow for probing the electronic structure of adsorption properties of cluster-adsorbate complexes in the submonolayer range. Using size-selected clusters as a part of a photocatalytic system, they might be active towards *TCE* degradation nonetheless. This might be a more successful approach, since the photocatalytic conversion of *TCE* has been achieved in both gasphase [55] and on supported clusters [56].

4.4.3 Ethene Adsorption and Reactivity on Surfaces

This section describes the adsorption properties of *ethene* on the surfaces $MgO(100)$ and $Pt(111)$, probed by means of TPD and EES. Additionally, with TPR the *ethene* self-/hydrogenation on $Pt(111)$ is investigated. The surfaces properties and reactivity serve as control with respect to the literature and as a comparison for experiments on Pt_n and Pt_x clusters on $MgO(100)$ in the next section as well as for future studies. Hereby, the $MgO(100)$ surface is used as inert support material [27, 57], whereas $Pt(111)$ is applied as a well known hydrogenation catalyst [58, 59].

Comparable **TPD** experiments (measurement on $28\,m/z$) of *ethene* interaction on $MgO(100)$ and $Pt(111)$ as a function of coverage were measured and are depicted in Fig. 4.26.

As for *CO* and *TCE* the spectra on the inert **MgO(100)** support show the expected behavior of a weakly physisorbed molecule with a desorption peak α, with a corresponding maximum at 112–115 K, independent of the coverage. The corresponding TPD peak areas increases linearly with dosage, a possible difference between physisorbed and condensed *ethene* cannot be observed (as for i.e. *TCE*) in the studied coverage range. In contrast, the TPD spectra on the **Pt(111)** surface reveal two peaks in good agreement with the literature [39, 41]. Peak α (maximum at 135 K) corresponding to physisorbed π-bonded, and peak β (maxima at 220–235 K, shifting towards lower T for increasing coverages) originating from chemisorbed di-σ *ethene*. An additional small peak, present in the spectra with high coverages at 110 K, originates from desorbing *ethene* from the tungsten heating wires. The evaluation of the peak integrals of the TPD spectra of different coverages dosed in random order, reveal a linear increase for peak α, however a decrease in area for peak β in the course of the experiment. A saturation of the area (completion of the first *ML*) is not apparent in the studied coverage range [6].

The decrease in peak area for β (and the shift in peak maxima) can be explained by the known **formation of carbon**[12] (Sect. 2.1.2) at temperatures above 450–500 K, which blocks active sites on the $Pt(111)$ surfaces for chemisorption of *ethene*. With repeated TPD experiments, the surface gets more and more poisoned and thus shows

---

[12] A further proof of the presence of *carbon* on the surface is given by the AES results in Fig. 4.38 of a surface, after a *ethane* TPR on page 129.
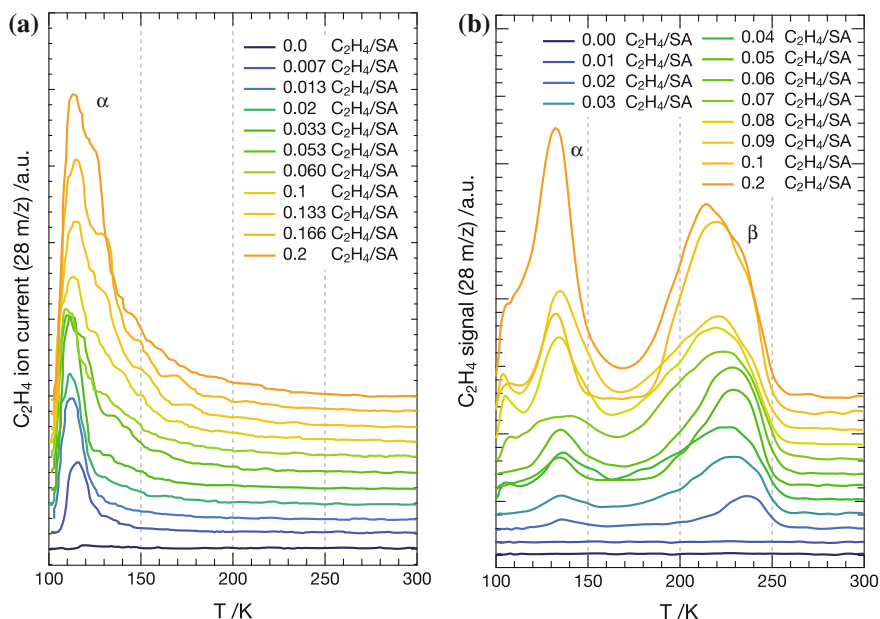
Fig. 4.26 TPD spectra ($\beta = 2K/s$) of *ethene* desorption on $MgO(100)/Mo(100)$ (**a**) and $Pt(111)$ (**b**). For MgO peak α is assigned to desorption of condensed and physisorbed ethene. In the case of $Pt(111)$ peak α is physisorbed ethene only, while peak β is attributed to chemisorbed *ethene*. Note, that the spectra for $Pt(111)$ were recorded in random order and without cleaning in between dosage and thus do not reflect for each coverage the behaviour on clean $Pt(111)$

a smaller area in the TPD. To further illustrate this behavior, TPDs on a cleaned $Pt(111)$ have been repeated twice at three different *ethene* coverages. The spectra along with in the corresponding peak area integrals are shown in Fig. 4.27. The TPD spectra show already a change in shape between first and second TPD run, particularly the formation of a shoulder (a possible adsorption site with different lateral interaction of *ethene*) in the range of 180–200 K can be observed.

The resulting areas show a slight increase for the lower coverages, for the highest probed coverage a slight decrease in peak β is apparent. The fact of such a small increase is caused by the opposing effect of the decreasing adsorption sites on the Pt and the increase in alternative sites, represented by the shoulder. Thus, repeated TPDs of *ethene* will poison the surface, reduce consequently the reactivity towards hydrogenation, as previously described [58, 60, 61]. This observation, makes a cleaning of the $Pt(111)$ surface a prerequisite before reactivity experiments. For the following EES experiments the $Pt(111)$ surface has therefore been cleaned after each desorption of *ethene*.

Figures 4.28 and 4.29 show **MIE/UP spectra** of different amounts of *ethene* adsorbed (at $T < 100$ K) on $MgO(100)$ and $Pt(111)$, respectively. The spectra have been corrected for the background (with $x_0 = 15$ eV, in contrast to *TCE*—
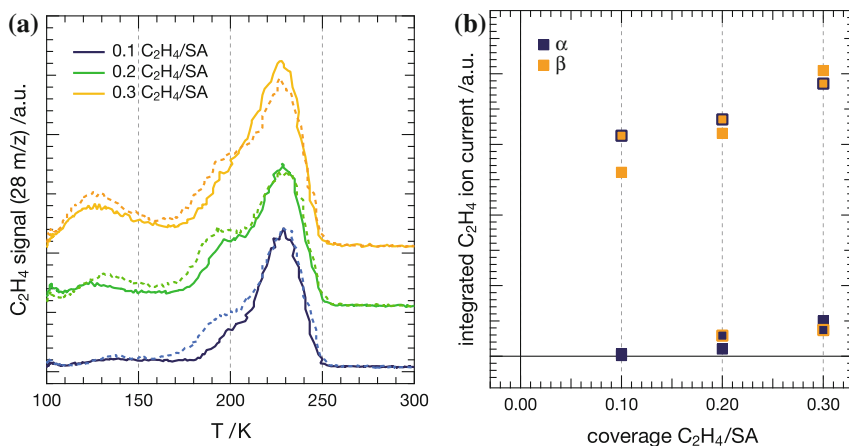
Fig. 4.27 TPD spectra of *ethene* desorption on *Pt*(111) (**a**) with and without cleaning by means of sputtering in between. The *dashed lines* show the repetition experiment to the first TPD run on the clean surface. Three different coverages were studied and the corresponding peak integral values are plotted in (**b**), the points with border represent the corresponding second runs

see Sect. A.1.5 for details) and are plotted on an IP scale (all stated energies are thus with respect to IP). The spectra are plotted without offset, in order to make the (minor) changes better visible. At a first impression, the EES of *ethene* in comparison to *TCE* show less pronounced peaks originating from the adsorbate MOs. For the UP spectra only very small changes are visible. The spectra are strongly dominated from features of the support support (O2p for *MgO* at 9.5 and 12.9 eV and the *Pt* double peak structure at 8.2 eV and 9.9 eV). This is surprising, since using unpolarized light all orbitals can be probed, in contrast to probing with polarized light, where certain orbitals are not accessible due to symmetry selection rules [41].[13] Further, one expects at least at the multilayer coverages to see clear adsorbate induced MO features. A possible explanations might be radiation induced adsorbate desorption. With MIES, using its higher sensitivity and consequently fewer support contributions, allows one to detect adsorbate MOs better. As previously, the argumentation in the following is mainly based on the MIES results; UPS related observations go along well with these results, however are in most cases not explicitly mentioned. Further, the weak *ethene* induced signals do not allow for peak fitting, thus the presented assignment is performed manually. It should also be noted that the adsorption and the subsequent EES measurements reported herein, are performed at $T < 100$ K; thus, in light of the temperature dependent adsorption behavior of *ethene* on *Pt* (Sect. 2.1.2) the spectra reflect only the adsorption properties at this particular temperature (range). For better visualization of the peak evolution as a function of coverage, excerpts of the spectra for the blank support and two coverages (submonolayer coverage at 0.1 C_2H_4/SA

---

[13] This fact is not only a draw back, but was useful in clarifying, that *ethene* is adsorbed parallel on the surface with respect of its molecular plane [41].
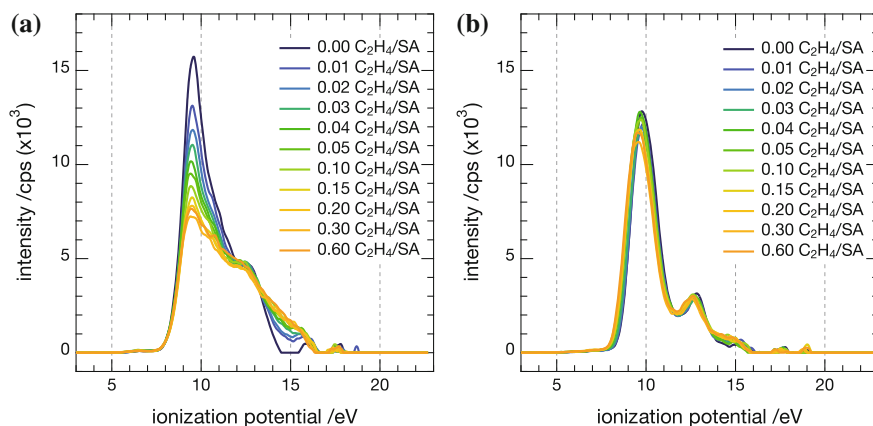
Fig. 4.28 EE spectra of adsorbed C_2H_4 on $MgO(100)$ as a function of coverage, referenced with respect to the vacuum level of the clean substrate and background corrected—MIES (**a**) and UPS (**b**)

and multilayer coverage at $0.6\,C_2H_4/SA$) are depicted in Fig. 4.30 for MgO and in Fig. 4.31 for Pt.

The detailed spectra are shown along with the possible assignments of gas phase MOs and the literature [8, 39–41, 49, 62–64] described below.

The **MIE spectrum** on **MgO(100)** (Fig. 4.30) show, for both the lowest coverage of $0.1\,C_2H_4/SA$ and the highest at $0.6\,C_2H_4/SA$, also only small features. A shift of the support peak from 9.6 eV to 9.4 eV might be related to a convoluted peak I ($\pi_{C=C}$). The peak would show a relaxation shift of -1.1 eV with respect to the gas phase due to the weak interaction on the inert support; the decreasing signal intensity however, makes this assignment questionable. Further, a shoulder at 12.6 eV is possibly originating from peak II (σ_{CH_2})—also seen in the UP spectra; however would then have a relaxation shift of only -0.2 eV; thus is also uncertain. Last a small peak at 15.0 eV is likely to be an indication of the MO corresponding to peak IV (σ_{CH_2}) of the gasphase, with a relaxation of -0.8 eV.

The MIES data on **Pt(111)** (Fig. 4.31) suggest an expected adsorption behavior (Sect. 2.2), a strong chemisorption, as observed with TPD. The spectra show at least two spectral features upon adsorption, already at the lowest studied coverage of $0.1\,C_2H_4/SA$. A major feature arises at 12.1 eV, which might account for two different MOs at once. Under the assumption of a chemisorption behavior (as seen in TPD) the peak might correspond to **peak I** ($\pi_{C=C}$) and thus have a **shift to higher energies** of $+1.6$ eV induced by the strong surface bond, a high value if considering an additionally present relaxation shift with opposite sign. Nevertheless, the assignment is conceivable when compared to a literature value of $+0.9$ eV for adsorption on $Ni(111)$ [63] or $+(0.6–1.0)$ eV for adsorption on $Fe(100)$ [65] and the knowledge of a stronger adsorption on Pt, with possible distortion of the molecule [64]. This shift might further be obscured by the MO of **peak II** (σ_{CH_2}) with a **relaxation shift** of -0.8 eV with respect to the gas phase IP. A second even broader peak, most probably
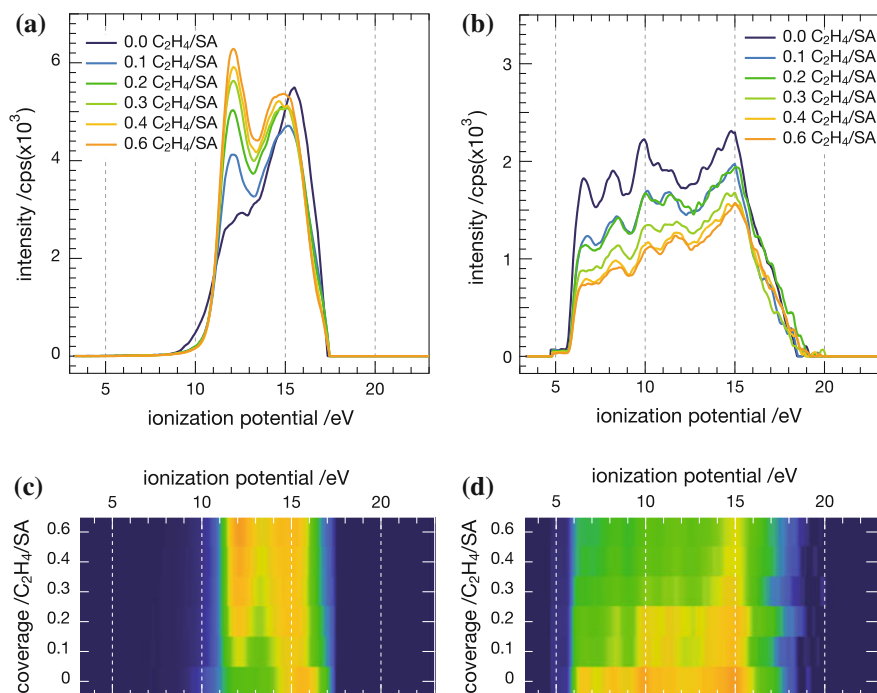
Fig. 4.29 EE spectra of adsorbed C_2H_4 on $Pt(111)$ as a function of coverage, referenced with respect to the vacuum level of the clean substrate and background corrected—MIES (**a**) and UPS (**b**). Subfigures (**c**) and (**d**), show the corresponding image plots for better visibility of the appearance of the C_2H_4 peak features for MIES and UPS, respectively

also consisting of two convoluted peaks and influenced by the background treatment procedure towards higher energies, can be seen. The lower energy peak at 14.2 eV fits with a **relaxation shift** of -0.6 eV well to the MO of **peak III** (σ_{C-C}) and with the shift of peak II to the picture of a uniform relaxation shift. The feature at 15.3 eV is questionable in terms of possibly being induced by the data treatment, however could be related to the **peak IV** (σ_{CH_2}), having a **relaxation shift** of -0.6 eV. The observed global relaxation shift of $\sim -(0.6\text{--}0.8)$ eV for the peaks II, III and IV is in agreement with observations made by Cassuto et al. [40] from UPS measurements with a value of ~ -0.8 eV at slightly lower temperatures. They are also in good agreement with published data of other hydrocarbons on metal surfaces (1–3 eV) [48, 49], and the observed data on *TCE* (Sect. 4.4.1). To further illustrate the changes in the EE spectra upon adsorption of *ethene* on the two surfaces $MgO(100)$ and $Pt(111)$ are shown in Fig. 4.32 for a coverage of $0.6\,C_2H_4/SA$. For comparison the spectra of the blank support and the gas phase spectra are also depicted. The spectra on $Pt(111)$ evidence once more the superior quality of the MIE spectra when compared to the UPS data.
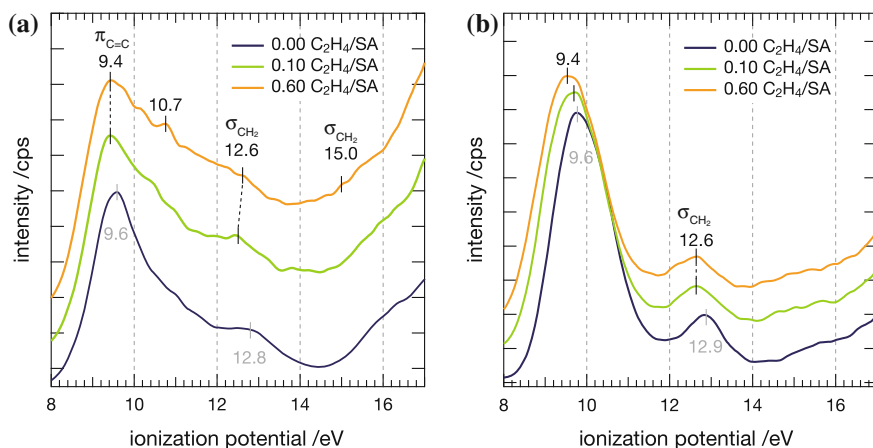
Fig. 4.30 Selected excerpts of EE spectra of adsorbed C_2H_4 on $MgO(100)$—blank support (*blue*), submonolayer coverage (0.1 C_2H_4/SA, green) and multilayer coverage (0.6 C_2H_4/SA, *blue*). MIES (**a**) and UPS (**b**); the assignment of the C_2H_4 MOs from features observed is gas phase spectra and literature is described in the text
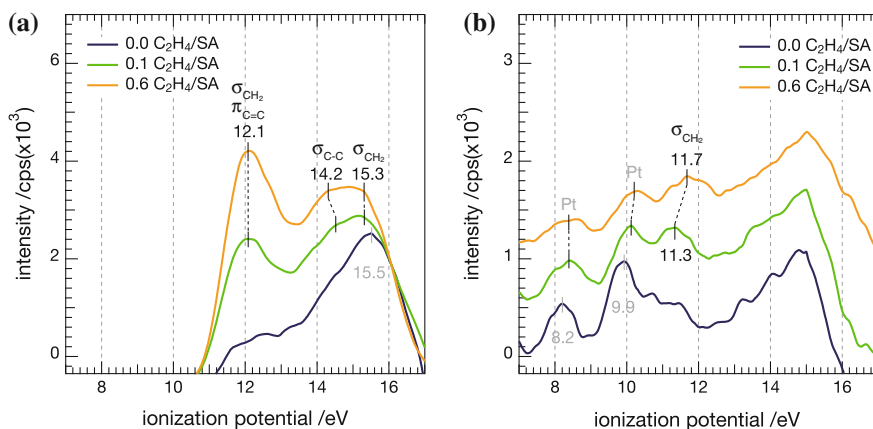

Fig. 4.31 Selected excerpts of EE spectra of adsorbed C_2H_4 on $Pt(111)$—blank support (blue), submonolayer coverage (0.1 C_2H_4/SA, *green*) and multilayer coverage (0.6 C_2H_4/SA, *blue*). MIES (**a**) and UPS (**b**); the assignment of the C_2H_4 MOs from features observed is gas phase spectra and literature is described in the text

With respect to the literature, as for *TCE* the adsorption properties of *ethene* were probed for the first time in a submonolayer coverage range. The relaxation shifts and shifts due to chemical bonds observed in the MIES data are summarized in Fig. 4.33.

The EE spectra have further been used to extract the surface **WF** and the corresponding values as a function of adsorbate coverage are shown in Fig. 4.34. The pristine support is in excellent agreement with the literature for the *Pt* crystal.
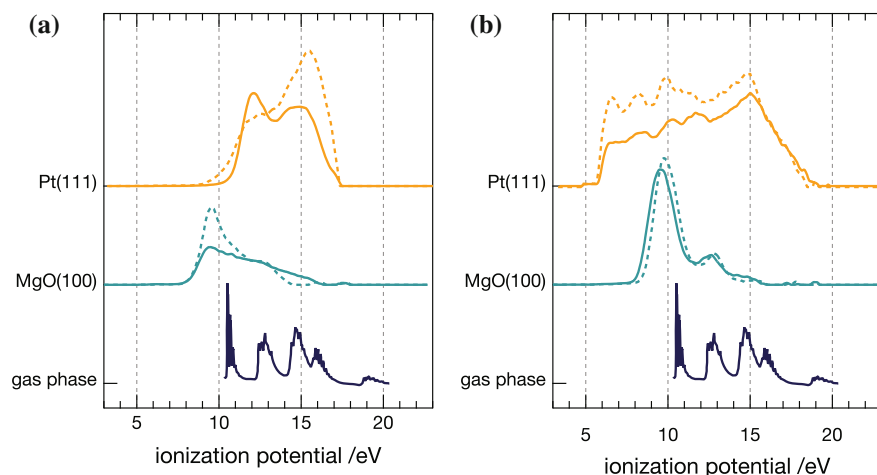
Fig. 4.32 EE spectra of $0.6\,C_2H_4/SA$ on $MgO(100)$ and $Pt(111)$, for comparison the pristine surface spectra are shown in *dashed lines* in the same colour. From *bottom* to *top*: gas phase spectrum from Kimura et al. [5] and $MgO(100)/Mo(100)$ and $Pt(111)$ on IP energy scale; MIES (**a**) and UPS (**b**)

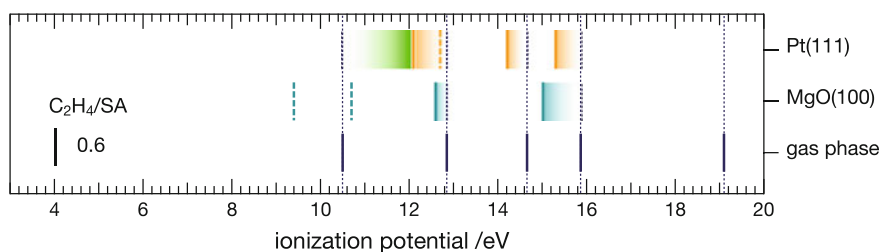**Fig. 4.33** Shifts of the peak energy positions in MIES of the adsorbed C_2H_4 on $MgO(100)$ and $Pt(111)$ with respect to the peak positions of the gas phase spectra of Kimura et al. [5]. The *orange* and turquoise gradients represent relaxation shifts, the *green* gradient the possible chemical bond induced shift of peak I ($\pi_{C=C}$) on $Pt(111)$

For the *MgO* thin film, the absolute value is slightly too high (see Sect. A.1.6). Concentrating on the relative WF changes, for **MgO** no changes upon adsorption of *ethene* is observed, which could be interpreted as further proof for a very weak interaction. For **Pt(111)** the WF decreases with higher coverages and reaches a saturation at the *ML* value of $0.4\,C_2H_4/SA$, as determined from TPD. The total change in WF $\Delta\phi = -0.35\,\text{eV}$ is a smaller decrease as reported in the literature on $Pt(111)$ [40] ($\Delta\phi = -1.25\,\text{eV}$ while measuring during dosage at 45 K), however with the same leveling-off for multilayer growth. For $Fe(100)$, a similar behavior with a smaller shift of only $-0.5\,\text{eV}$ is reported [65]. For comparison to the cluster experiments reported in the next section, **TPR** of *ethene* self-/hydrogenation on **Pt(111)** were recorded and are shown in Fig. 4.35. The spectra are taken after dosage of $0.4\,C_2H_4/SA$, corresponding to an equivalent of a full *ML* of *ethene* for the self-hydrogenation, and an
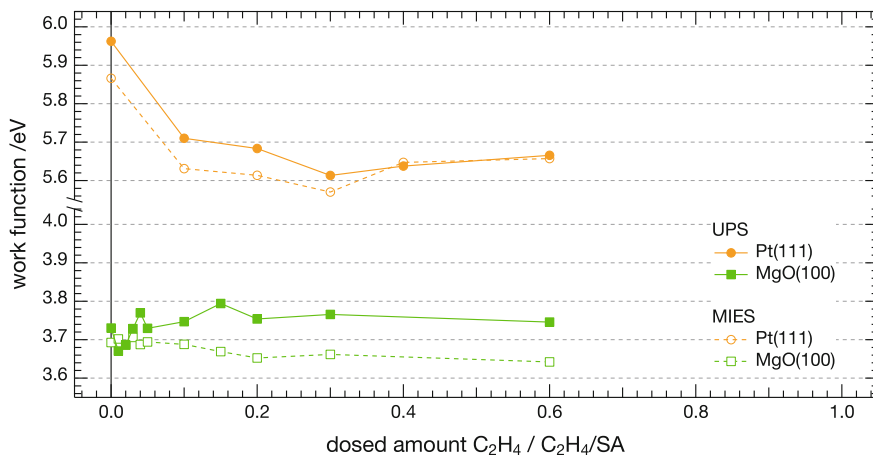
Fig. 4.34 Absolute WF changes with increasing coverage of C_2H_4 on the studied surfaces ($Pt(111)$ *blue* and $MgO(100)$ *green*). The values are determined from the corresponding UPS measurements; the *dashed lines* represent the corresponding values from the MIES measurements for comparison. The values have a statistical error of $\pm 0.05\,eV$, for details see text

additional dosage of $0.4\,H_2/SA$ of *hydrogen* before[14] *ethene* for the hydrogenation. With the molecular weight of the reaction product *ethane*, corresponding to $30\,u$ and ionization in the QMS under loss of one *hydrogen* it is common to measure the product *ethane* in the QMS as $29\,m/z$. However, with perspective to the sensitivity needed for cluster reactivity measurement later and the mentioned low conversion rate to *ethane* (Sect. 2.1.2), the signal at $29\,m/z$ is disturbed by the ^{13}C isotopes of the reactant *ethene*. As a consequence for later comparison, all following measurements of *ethane* are measured on $30\,m/z$ [67]. In addition to the TPR for ethane desorption on $30\,m/z$, the desorption of molecular *hydrogen* has been recorded in parallel and is shown in Fig. 4.35.

Comparing the results of self-hydrogenation with those of hydrogenation (by additional previous *hydrogen* dosage) for both *ethane* and *hydrogen* TPR, the spectra show similar peaks; however with smaller intensities for the self-hydrogenation experiments. This is an obvious observation, since with additional adsorbed *hydrogen* simply more *ethane* can be produce as without. The low *ethane* 'production' is here further illustrated, when comparing the signal strength of *hydrogen* (max. at $\sim 320\,pA$) and *ethane* (max. at $\sim 25\,pA$) in the TPD signals for hydrogenation; thus an order of magnitude difference.

A rough approximation of the **reaction probability** can be done based on the comparison of the integrated areas of the *ethane* TPD and the *ethene* TPR.

---

[14] The influence of dosage order and dosage amount have been studied as well [6, 66], however are not explicitly shown. Briefly, dosage of *hydrogen* prior to *ethene* reveals a slightly higher/bigger *ethane* TPR signal. The dosage amount seems optimum at equal dosage of both reactants. With respect to the *ML* (TPD integration) amount of *ethene*, $0.4\,C_2H_4/SA$ and $0.4\,H_2SA$ were chosen in order to yield highest possible amounts without contributions from condensed molecules.
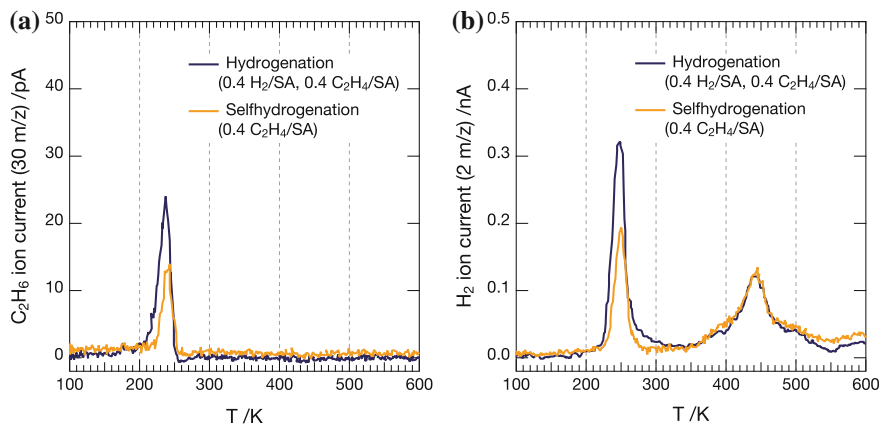
Fig. 4.35 TPR of C_2H_6 (a) and H_2 (b) desorption on $Pt(111)$ for hydrogenation (*blue spectra*) and self-hydrogenation (*orange spectra*). For self-hydrogenation 0.4 C_2H_4/SA of *ethene* was dosed prior to the TPR, for hydrogenation additionally 0.4 H_2/SA of *hydrogen* were dosed. Note the different scales for the current for both experiments

Ignoring the different ionization probabilities in the QMS and the using 30 m/z in the case of *ethene*, gives an probability of ∼4–6 % in agreement with values of ∼10 % in the literature (see Sect. 2.1.2).

The *ethane* TPRs reveal one peak with a maximum at 240 K corresponding to the desorption of the hydrogenation product as reported in the literature [67]. A described peak broadening for hydrogenation and a slightly lower peak maximum in comparison the self-hydrogenation could not be reproduced. The observed peak maxima is in the same temperature range as the observed desorption peak of *ethene* at ∼230 K described above.

For *hydrogen* two peaks are visible, one with a peak maximum at 250 K and a second broader peak at around 450 K. These results are also in accordance with previous results [67] (particularly if considering the different heating rate used). The peak at lower temperatures corresponds to *hydrogen*, released from formation of *ethylidyne* species on the surface. The broader peak at higher temperatures originates from the 'slower' decomposition of *ethene/ethylidyne* on the surface in the later process of *carbon* formation. Both temperature ranges are in very good accordance with the literature [58, 59, 67–69], describing the temperature dependent adsorption of *ethene* on $Pt(111)$ presented in Sect. 2.1.2. Consequently a further interpretation of the TPR results on $Pt(111)$ is not given.

Summary—in conclusion, the TPD and EES data on *ethene* adsorption evidence a weak physisorption on *MgO* and strong chemisorption on *Pt*. Signals in the EES are considerably weak and with a detailed look, MO of the adsorbate can be seen and interpreted. The additional use of MIES is hereby a particular asset as it allows the probing of a submonolayer range. In general, the results are in agreement with comparable experiments reported in literature. The performed *ethane* and *hydrogen*
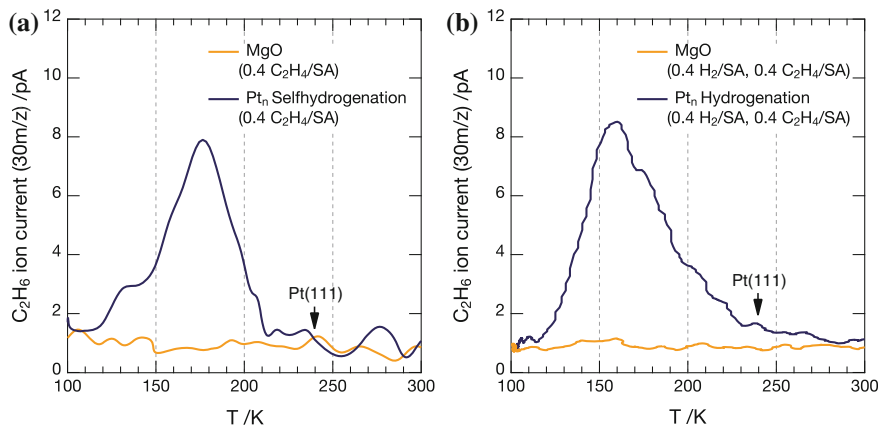
Fig. 4.36 TPR spectra ($\beta = 2K/s$) of self-hydrogenation (**a**) and hydrogenation (**b**) of *ethene* on $0.203\,e/nm^2$ unselected Pt_n clusters (*blue spectra*). The previous taken TPR on the corresponding pristine *MgO* supports is additionally shown (*orange spectra*), however reveal no reactivity. An *arrow* indicates the position of the peak maximum for the experiment on the $Pt(111)$ for comparison

TPR experiments of the self-/hydrogenation reaction are also in good agreement with the literature, with respect to both peak positions and reaction probability. They are a basis for comparison with measurements on supported clusters in the same UHV setup described in the next section.

4.4.4 Ethene Reactivity on $Pt_{x,n}$ Clusters

With the TPR experiments on $Pt(111)$ (discussed in the previous section) as a basis for comparison, the reactivity of the supported, unselected **Pt_n** (**$n \geq 9$**) clusters were probed for reactivity by **TPR**.

The results of the self-hydrogenation and hydrogenation TPR of *ethene* under similar experimental conditions (dosage of $0.4\,C_2H_4/SA$ and $0.4\,H_2/SA$, respectively and the same TPR settings) as for $Pt(111)$ are shown in Fig. 4.36. The TPR spectra on the support evidence the inertness of *MgO* in both experiments. Deposition of $0.203\,e/nm^2$ $Pt_{n\geq9}$ clusters and subsequent TPR corroborate the catalytic reactivity of Pt particles in this size range. For self-hydrogenation a peak at $170\,K$, for hydrogenation at $160\,K$ with slightly higher reactivity can be observed. In both cases the peak maximum is shifted for $\sim50\,K$ and $\sim60\,K$ with respect to the $Pt(111)$ surface, evidencing a higher catalytic activity of the particles compared to the single crystal surface in agreement with the literature (Sect. 2.1.2).

The further peak shift for hydrogenation might be related to the presence of the additional *hydrogen*. This enabling a reaction at even lower temperatures, as the presence of *hydrogen* is a prerequisite for self-/hydrogenation, however for the
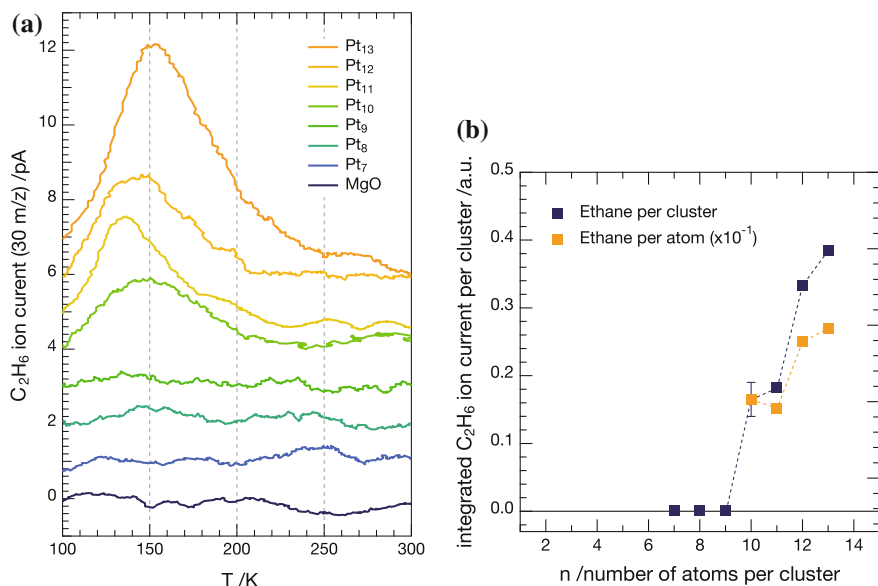
Fig. 4.37 TPR spectra ($\beta = 2K/s$) of hydrogenation on $0.116\,e/nm^2$ selected Pt_x ($x = 7 - 13$) clusters on $MgO(100)$. The recorded ion signals ($30\,m/z$) for the pristine MgO and the different sizes are shown in (**a**). The corresponding integrated peak area (averaged in case of Pt_{10} and Pt_{11}, because of multiple experiments) are plotted as a function of size (**b**). The indicated error for Pt_{10} is based on the standard deviation of five TPR measurements; the *dashed lines* serve as guide to the eye

self-hydrogenation to occur *ethene* decomposition needs to take place first. The temperature observed difference between the TPR signals compared to $Pt(111)$ could be due to a lowered activation barrier for the formation of adsorbed ethyl species.

In order to elucidate possible size effects on the hydrogenation reactivity (**TPR**) as a function of Pt_x ($7 \leq x \leq 13$) cluster size at a coverage of $0.116\,e/nm^2$ was measured. The results of the TPR are presented, along with the integrals of the peak areas, in Fig. 4.37. An indicated error bar for Pt_{10} based on the standard deviation of five independent measurements, illustrates the high reproducibility of the measurements.

Up to a size of Pt_9 no *ethane* signal can be detected and the spectra resemble the TPR on the blank support. From Pt_{10} on a peak can be detected, thus already these small clusters reveal a catalytic reactivity. The reactivity increases steadily with cluster size and up to the probed maximum size of Pt_{14} no saturation of the signal can be observed (see integrated peak areas). The peak maximum is in a comparable range to the one observed in the Pt_n measurements. However, the peak maxima shift slightly for different sizes, probably a sign for slight differences in reactivity for smaller sizes. A comparable trend is apparent, when expressing the integrated peak signals ('reactivity') as reactivity per atom and plotting as a function of size. A previously visible jump between Pt_9 and Pt_{10} as well as Pt_{12} and Pt_{13}, with an
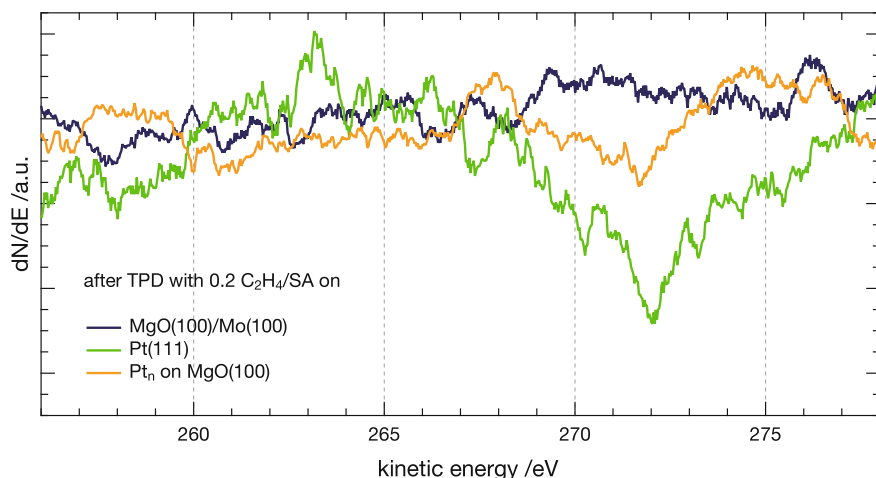
Fig. 4.38 Excerpt of Auger electron spectra of the energy range between 255–278 eV after ethene desorption on $MgO(100)/Mo(100)$, $Pt(111)$ and $0.203\,\text{e/nm}^2$ Pt_n on $MgO(100)$ excited with an electron energy of 3 kV. The characteristic carbon peak C(KLL) at 272 eV is present for both the Pt single crystal, as the unselected clusters, however is not present for the support film $MgO(100)$ [6, 72]

almost doubled TPR peak area remains and shows, that the amount of formed *ethane* is not proportional to the number of *Pt* atoms.

The observed trend, of starting reactivity at a cluster size of ten atoms, fits well the observation that sizes smaller than 6 Å are not reactive [17, 70]. The onset of reactivity is at a larger size for *ethene* hydrogenation, than for *CO* oxidation (Pt_{10} vs Pt_6), but the trend thereafter is the same (increasing activity with larger clusters) [36]. A possible explanation for this 'earlier' reactivity might be the larger size of the reactant molecule *ethene* in comparison to *oxygen* or *CO*. A similar stepwise increase in reactivity is observed for size-selected *Pd* cluster in the study of acetylene cyclotrimerization [71].

Additional experiments with larger clusters are necessary in order to elucidate their size dependent reactivity. However, the presented TPR data already shows a tuneability of the hydrogenation reactivity of small supported clusters, in which each single atom in a cluster counts. These results are a starting point for further investigations of cluster reactivity on more complex and industrial relevant reactions. Correlating the obtained data of the reactivity in the single-pass heating cycle TPR experiments with other surface science methods, it is likely to further the understanding of the *ethene* hydrogenation on a molecular level.

In the following paragraphs, preliminary results on unselected clusters, obtained by additional methods are described and discussed. These results of currently ongoing experiments are meant to show the potential of these methods to give supplementary and complementary information for the understanding of *ethene* hydrogenation on size-selected clusters.
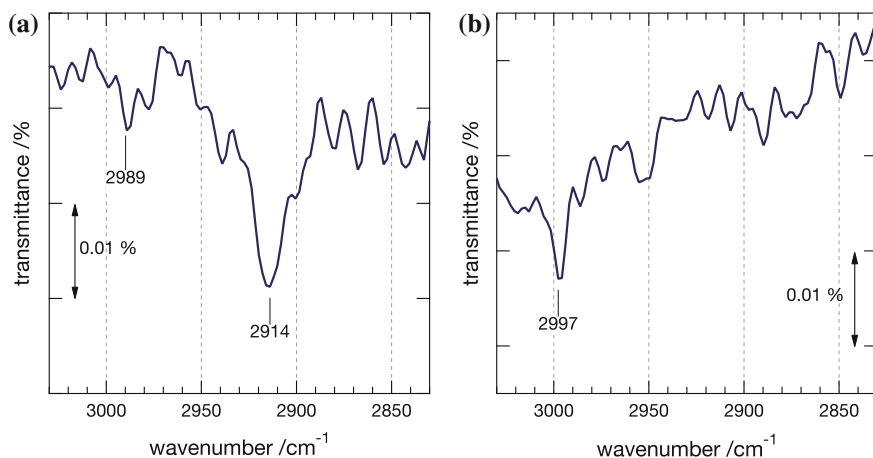
(a)

(b)

Fig. 4.39 IRRAS of $0.4\,C_2H_4/SA$ adsorbed C_2H_4 on $Pt(111)$ (**a**) and $0.203\,e/nm^2\,Pt_n$ (**b**). The molecule was adsorbed at $100\,K$

For probing possible formation of surface *carbon* on clusters, as seen in the case of $Pt(111)$, **AES** measurements after a self-hydrogenation TPR with $0.2\,C_2H_4/SA$ were performed on $0.203\,e/nm^2$ unselected Pt_n ($n > 9$) clusters supported on $MgO(100)$. The spectrum is compared to AE spectra after a similar TPR run on $MgO(100)$ and $Pt(111)$. An excerpt of the relevant area for the characteristic carbon peak C(KLL) at $272\,eV$ of the three measurements is shown in Fig. 4.38.

The spectrum on the 'clean' MgO support reveals no *carbon* related features in the relevant range and serves as a reference. For **Pt(111)** the known formation of carbonaceous species at higher temperatures is evidenced by a clear signal originating from the C(KLL) transition. A smaller, but clear peak signal is also present for **unselected Pt$_n$** clusters. An possible decomposition of *ethene* by means of the e-gun can be excluded as no *carbon* formation is seen on the bare $MgO(100)$ support. Despite the presence of the signal for unselected clusters, additional measurements on size-selected clusters are necessary to gain a more complete picture on the *carbon* formation. An additional approach for quantification of the *carbon* deposition has been mentioned in the literature [58]. The author reports, that the amount of poisoned active sites on the metal can be probed by titration of the available adsorption sites of the *Pt* surface with *CO*. Experiments for proof of principle have been performed and support the obtained AES data [6, 72]. Yet a more systematic study is necessary to quantify and reproduce these results; possible effects of cluster size on *carbon* formation might shed light into catalyst deactivation mechanisms for this reaction.

Results of first **IRRAS** measurements of adsorbed *ethene* on $Pt(111)$ and $0.203\,e/nm^2$ unselected Pt_n clusters at $100\,K$ are depicted in Fig. 4.39. On the **Pt(111)** reference spectra two peaks are visible. The intense peak at $2914\,cm^{-1}$ is the symmetric CH_2 stretch of di-σ bonded *ethene*, the weaker peak at $2989\,cm^{-1}$ might be corresponding to one of the symmetric or asymmetric stretches of π-bonded *ethene*;

both peak positions are in good agreement with literature data on *Pt*(111) [59, 68, 73]. The **Pt$_n$** clusters show only one clear peak at 2997 cm^{-1}, likely to correspond to π-bonded *ethene*—the observed blue shift for the peak with respect to the single crystal surface, might be an indication of a stronger π-bond of *ethene* to the clusters than to the surface. It has to be noted again, that these vibrational information are preliminary and need further measurements, particularly with size-selected clusters in the range where a change in reactivity is found in the TPR.

Summary—the presented data in this section reveals a size dependent reactivity of the hydrogenation of *ethene* on small size-selected *Pt* clusters. First, preliminary results from AES and IRRAS measurements are promising towards an understanding of the differences between single crystal and cluster reactivity, however are at an early stage and need a more detailed study.

Along with these studies the application of EES, in particular MIES with higher sensitivity, a better insight into the changes of the adsorption behaviour (extracted from changes in the electronic structure) and reactivity in general on a molecular level should be feasible. As a part of the **ongoing efforts**, the self-hydrogenation reaction as a function of cluster size is planned. Further studies using isotope labelling experiments (i.e. using *deuterium* instead of *hydrogen*) will also be performed to elucidate the role of the *hydrogen* activation in the hydrogenation reaction. In particular using *HD*-exchange to probe the *hydrogen* adsorption shows promising results towards gaining a better understanding of the cluster reactivity.

Additionally to the presented results, the adsorption behaviour of the reactants at different temperatures on the clusters need to be investigated, this is a particular necessity in the case of *ethene* reactivity because of the temperature dependent adsorption properties on surfaces. In a last step the reactivity of clusters will be probed by means of available isothermal pMBRS experiments. This is a logical step, in order to attaining kinetic data which will make the results more widely applicable.

References

1. Schweinberger, F. F. (2009). Master's thesis, Technische Universität München.
2. Kunz, S. (2010). Ph.D. thesis, Technische Universität München.
3. Spirkl, F. M., Kunz, S., Schweinberger, F. F., Farnbacher, A. N., Schröter, R., & Heiz, U. (2012). *Review of Scientific Instruments*, *83*, 013114.
4. Schweinberger, F. F., Crampton, A., Zimmermann, T., Kwon, G., Ridge, C., Günther, S., et al. (2013). *Surface Science*, *609*, 18.
5. Kimura, K., Katsumata, S., Achiba, Y., Yamazaki, T., & Iwata, S. (1981). *Handbook of HeI photoelectron spectra of fundamental organic molecules: ionization energies, ab initio assignments, and valence electronic structure for 200 molecules*. New York: Japan Scientific Societies Press Halsted Press.
6. Heenen, H. (2012). Internship report.
7. Kunz, S., Schweinberger, F. F., Kwon, G., Kiermaier, J., Moal, S. L., Henry, C., et al. (2010). *Surface Science*, *406*, 2184.
8. Cassuto, A., Hugenschmidt, M., Parent, P., Laffon, C., & Tourillon, H. (1994). *Surface Science*, *310*, 390.
9. Zimmermann, T. (2011). Master's thesis, Technische Universität München.

10. Krischok, S., Höfft, O., & Kempter, V. (2002). *Nuclear Instruments and Methods in Physics Research B*, *193*, 466.
11. Stracke, P., Krischok, S., & Kempter, V. (2001). *Surface Science*, *473*, 86.
12. Krischok, S., Stracke, P., Höfft, O., Kempter, V., Zhukovskii, Y., & Kotomin, E. (2006). *Surface Science*, *600*, 3815.
13. Krischok, S. (2001). Ph.D. thesis, TU Clausthal.
14. Wertheim, G. K., & DiCenzo, S. B. (1988). *Physical Review B*, *37*, 844.
15. Wertheim, G. K., DiCenzo, S. B., & Buchanan, D. N. E. (1986). *Physical Review B*, *33*, 5384.
16. Takasu, Y., Unwin, R., Tesche, B., Bradshaw, A., & Grunze, M. (1978). *Surface Science*, *77*, 219.
17. Henry, C. R. (1998). *Surface Science Reports*, *31*, 231.
18. Eberhardt, W., Fayet, P., Cox, D. M., Fu, Z., Kaldor, A., Sherwood, R., et al. (1990). *Physical Review Letters*, *64*, 780.
19. Fayet, P., Patthey, F., Roy, H. V., Detzel, T., & Schneider, W. D. (1992). *Surface Science*, *269–270*, 1101.
20. Wortmann, B., Mende, K., Duffe, S., Grönhagen, N., von Issendorff, B., & Hövel, H. (2010). *Physica Status Solidi (b)*, *247*, 1116.
21. von Issendorff, B., & Cheshnovsky, O. (2005). *Annual Review of Physical Chemistry*, *56*, 549.
22. Sesselmann, W., Conrad, H., Ertl, G., Küppers, J., Woratschek, B., & Haberland, H. (1983). *Physical Review Letters*, *50*, 446.
23. Sesselmann, W., Woratschek, B., Küppers, J., Ertl, G., & Haberland, H. (1987). *Physical Review B*, *35*, 1547.
24. Sesselmann, W., Woratschek, B., Küppers, J., Ertl, G., & Haberland, H. (1987). *Physical Review B*, *35*, 8348.
25. Conrad, H., Ertl, G., Küppers, J., Wang, S. W., Gérard, K., & Haberland, H. (1082). *Physical Review Letters*, *1979*, 42.
26. Crampton, A. (2011). Master's thesis, Technische Universität München.
27. Abbet, S. (2001). Ph.D. thesis, Unversité de Lausanne.
28. Matsushima, T. (1983). *Surface Science*, *127*, 403.
29. Winkler, A., & Yates, J. J. J. (1988). *Journal of Vacuum Science and Technology A*, *6*, 2929.
30. Hayden, B., & Bradshaw, A. (1983). *Surface Science*, *787*, 174.
31. Norton, P., Goodale, J., & Selkirk, E. (1979). *Surface Science*, *83*, 189.
32. Hüfner, S. (2003). *Photoelectron spectroscopy: Principles and applications* (3rd ed.). Berlin: Springer.
33. Harada, Y., Masuda, S., & Ozaki, H. (1997). *Chemical Reviews*, *1897*, 97.
34. Ertl, G., Neumann, M., & Streit, K. (1977). *Surface Science*, *64*, 393.
35. Golden, W.G., Dunn, D.S., & Overend, J. (1981). *Journal of Catalysis*, *71*, 395–404.
36. Heiz, U., Sanchez, A., Abbet, S., & Schneider, W.-D. J. (1999). *Journal of the American Chemical Society*, *121*, 3214.
37. Heiz, U., Sanchez, A., Abbet, S., & Schneider, W.-D. (1999). *The European Physical Journal D—Atomic, Molecular, Optical and Plasma Physics*, *9*, 35.
38. Heiz, U., Sanchez, A., Abbet, S., & Schneider, W. D. (2000). *Chemical Physics*, *262*, 189.
39. Cassuto, A., Touffaire, M., Hugenschmidt, M., Dolle, P., & Jupille, J. (1990). *Vacuum*, *41*, 161.
40. Cassuto, A., Kiss, J., & White, J. (1991). *Surface Science*, *255*, 289.
41. Cassuto, A., Mane, M., Jupille, J., Tourillon, G., & Parent, P. J. (1992). *Physical Chemistry*, *96*, 5987.
42. Niemantsverdriet, J. W. (2007). *Spectroscopy in catalysis: An introduction* (3rd ed.). Weinheim: Wiley-VCH.
43. Günster, J., Liu, G., Kempter, V., & Goodman, D. (1998). *Surface Science*, *415*, 1001–1078.
44. Günster, J., Liu, G., Stultz, J., Krischok, S., & Goodman, D. (2000). *The Journal of Physical Chemistry B*, *104*, 43–5738.
45. Heskett, D., Tang, D., Shi, X., & Tsuei, K.-D. (1993). *Journal of Physics, Condensed Matter*, *5*, 4601.

46. Michaelides, A., Hu, P., Lee, M., Alavi, A., & King, D. A. (2003). *Physical Review Letters*, *90*, 246103.
47. Prada, S., Martinez, U., & Pacchioni, G. (2008). *Physical Review B*, *78*, 235423.
48. Gadzuk, J. W. (1975). *Journal of Vacuum Science and Technology*, *12*, 289.
49. Kelemen, S., & Fischer, T. (1981). *Surface Science*, *102*, 45.
50. Günster, J., Stultz, J., Krischok, S., & Goodman, D. (1999). *Chemical Physics Letters*, *306*, 335.
51. Morgner, H. (2000). *In advances in atomic, molecular, and optical physics* In B. Bederson & H. Walther (Eds.), (Vol. 42, p. 387). Amsterdam: Academic Press.
52. Schüth, C., Disser, S., Schüth, F., & Reinhard, M. (2000). *Applied Catalysis B: Environmental*, *28*, 147.
53. Barrabes, N., Cornado, D., Foettinger, K., Dafinov, A., Llorca, J., Medina, F., et al. (2009). *Journal of Catalysis*, *263*, 239.
54. Günster, J., Stultz, J., Krischok, S., Goodman, D., Stracke, P., & Kempter, V. (1999). *Journal of Vacuum Science and Technology A*, *17*, 1657.
55. Nimlos, M. R., Jacoby, W. A., Blake, D. M., & Milne, T. A. (1993). *Environmental Science and Technology*, *27*, 732.
56. Fan, J., & Yates, J. J. (1996). *Journal of the American Chemical Society*, *118*, 4686.
57. Heiz, U., Vanolli, F., Trento, L., & Schneider, W.-D. (1986). *Review of Scientific Instruments*, *1997*, 68.
58. Somorjai, G. (1994). *Introduction to surface chemistry and catalysis* (Vol. 2). New York: Wiley-Interscience.
59. Cremer, P. S., Su, X., Shen, Y. R., & Somorjai, G. A. (1996). *Journal of the American Chemical Society*, *118*, 2942.
60. Zaera, F., & Somorjai, G. A. (1984). *Journal of the American Chemical Society*, *106*, 2288.
61. Somorjai, G. (1996). *Chemical Reviews*, *96*, 1223.
62. Fischer, T., & Kelemen, S. (1977). *Surface Science*, *69*, 485.
63. Demuth, J. E., & Eastman, D. E. (1974). *Physical Review Letters*, *32*, 1123.
64. Demuth, J. (1979). *Surface Science*, *80*, 367.
65. Brucker, C., & Rhodin, T. (1977). *Journal of Catalysis*, *47*, 214.
66. Riedel, J. N. (2012). Internship report.
67. Wieckowski, A., Rosasco, S. D., Salaita, G. N., Hubbard, A., Bent, B. E., Zaera, F., et al. (1985). *Journal of the American Chemical Society*, *107*, 5910.
68. Kubota, J., Ohtani, T., Kondo, J. N., Hirose, C., & Domen, K. (1997). *Applied Surface Science*, *121*, 548.
69. Grunes, J., Zhu, J., Yang, M., & Somorjai, G. A. (2003). *Catalysis Letters*, *86*, 157.
70. Masson, A., Bellamy, B., Romdhane, Y., Che, M., Roulet, H., & Dufour, G. (1986). *Surface Science*, *173*, 479.
71. Abbet, S., Sanchez, A., Heiz, U., Schneider, W., Ferrari, A. M., Pacchioni, G., et al. (2000). *Journal of the American Chemical Society*, *122*, 3453.
72. Stecher, J. (2012). Bachelor thesis.
73. Mohsin, S. B., Trenary, M., & Robota, H. J. (1988). *Journal of Physical Chemistry*, *92*, 5229.

Part III
Ambient

Chapter 5
Cluster Catalysts Under Applied Conditions

The results of investigations of supported size-selected *Pt* cluster catalysts under ambient and more applied conditions is described in this chapter. Based on the successful experiments with unselected clusters and application under electrochemical conditions [1–4], within this work both unselected and selected cluster materials (of different sizes) are investigated. Exemplarily for selected sizes, in a highly collaborative approach, results on characterization, stability and reactivity are presented.

As a first part of this chapter, a **characterization** of the cluster materials is performed on the basis of **(HAADF)-STEM** and **XPS** results. The complementary methods offer insight to the samples transferred to *ex situ* on the local and integral level and to some extent to the characterization of the deposition method. Further, the presented experiments and their outcome, in particular characterization by means of STEM, are a basis for supplementary measurements in the following chapters.

In the second part, first results on the **stability** of the cluster based materials is presented. A data set from **ETEM** measurements at different temperatures shows the influence of temperature on a selected cluster sample. Further, by monitoring changes in the plasmon signal by means of **INPS** the stability of size-selected and unselected cluster samples is investigated as a function of temperature and correlated with (conventional) STEM results.

The last two sections deal with reactivity of different Pt_x clusters sizes under ambient conditions. Using *CO* oxidation as test reaction the Pt_x reactivity is probed by means of μ-reactors. First results of this ongoing project are presented.

Investigating the *hydrogen* evolution of the water splitting reaction, Pt_x clusters supported on a semiconductor material serve as part of a new well defined **photocatalyst** material, which is tested as a function of coverage and size in the liquid phase in a systematic study.

An overview of the different sections and the corresponding prepared samples is presented in Table 5.1; a more detailed list is stated in the appendix in Sect. A.2.1.

Table 5.1   List of samples prepared for ambient experiments, sorted by section

Section	Sample type	Support	Deposited sizes
5.1.1	STEM	Cu/C	8, 22, 34, $n \geqslant 36$, 46, 68
5.1.2	XPS	SiO_2	8, 22, 34, $n \geqslant 36$, 46, 68
5.2.1	ETEM	SiO_2/SiO_2	46
5.2.2	INPS	Si_3N_4	$n \geqslant 53$, 68, 22+68
	STEM	Si_3N_4	$n \geqslant 53$, 68, 22+68
5.3	μ-reactor	SiO_2 (2nd gen.)	8, 10, 20, 22, 34, 46, 68
5.4	Photocat	SiO_2/CdS	8, 22, 34, $n \geqslant 36$, 46, 68
5.4.1	STEM	$CdS/Cu/C$	8, 22, 34, $n \geqslant 36$, 46, 68

Additionally, the support material and the studied sizes are stated. A more detailed list stated in the appendix in Table A.8

5.1   Characterization and Statistics

The prepared samples for ambient experiments cannot be immediately probed and investigated by techniques as under UHV conditions. In order to nonetheless ensure a successful preparation, samples of different sized clusters have been probed after transfer to ambient conditions by means of (HAADF)-STEM and XPS. TEM as a well established characterization method is then used in combination with other experiments (INPS and photocat) to characterize samples routinely and track changes after the 'main' experiment.

5.1.1   HR-STEM

In order to characterize clusters with different sizes, a resolution on an atomic scale is necessary. The available **TEM** instrument at TUM was able to confirm successful deposition of cluster materials, and allowed for simple statistical analysis of larger (unselected) clusters [1, 3]. However, a reliable analysis with focus on even smaller sizes towards discrimination of selected cluster with different sizes was not possible due to low resolution in the lower size range. Therefore, acquired TEM images are not explicitly shown.

HAADF-STEM as an alternative method, providing a high resolution (exploiting the high Z contrast for Pt) was therefore applied to all measurements. The experiments were performed at LMU, and DTU for comparison. Excerpts of representative STEM micrographs ($30 \times 30 \, \text{nm}^2$) for $Pt_{n,x}$ clusters of different sizes and coverages supported on 2 nm carbon support are shown in Fig. 5.1.

From the images an increasing particle size and for the unselected samples different sized particles are apparent.

Multiple images with different areas (thus higher number of clusters) were **systematically analyzed** by means of a IGOR based software of in house design (see Sect. 3.3.3a). The results of the computer based analysis (based on at least
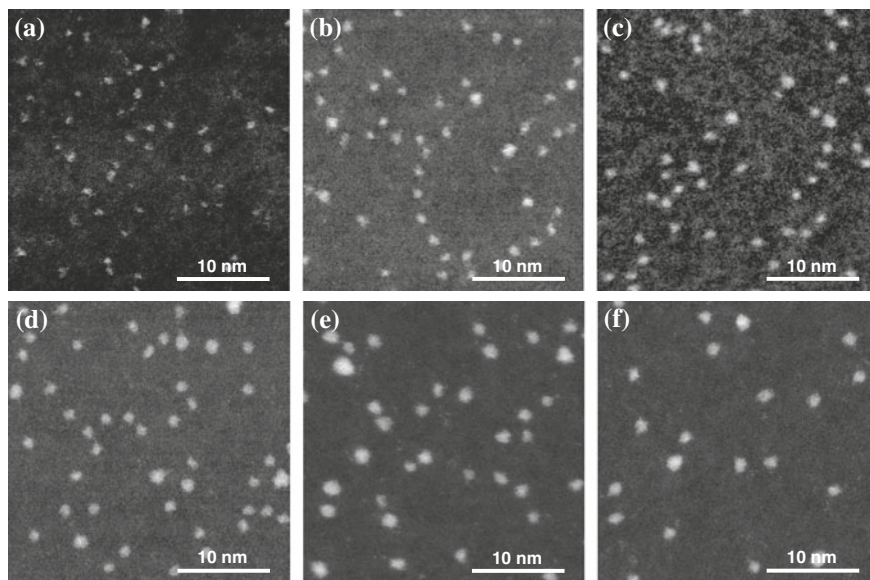
Fig. 5.1 STEM micrographs ($30 \times 30\,nm^2$) for $Pt_{n,x}$ ($n > 36$; $x = 8, 22, 34, 46, 68$) clusters supported on $2\,nm$ carbon. The corresponding coverages are shown in Fig. 5.2. **a** $0.04\,e/nm^2$ Pt_8, **b** $0.04\,e/nm^2$ Pt_{22}, **c** $0.04\,e/nm^2$ Pt_{34}, **d** $0.04\,e/nm^2$ Pt_{46}, **e** $0.03\,e/nm^2$ $Pt_{n>36}$, **f** $0.03\,e/nm^2$ Pt_{68}

five micrographs per size and an average of >2000 particles) are discussed in the following.

Besides the measurement of neutralization current upon deposition the overall **cluster coverage** is determined by counting clusters on STEM micrographs as a function of surface area. The results of the comparison for different sizes and three different coverages are displayed in Fig. 5.2. In general, the counted numbers of clusters are in good agreement to the integral measurement of cluster current within the indicated error (based on the standard deviation of counts on different micrographs of the same size, 14%). A reproducible deposition with respect to the coverage is thus evidenced, and is a superior method compared to vapor deposition [5].

In addition to the coverage, the **size of the particles** was obtained from automated measurements of the (projected) particle area, i.e. area distribution functions (**ADF**). Representative STEM micrographs ($100 \times 100\,nm^2$) for $Pt_{n \geq 36}$ ($0.03\,e/nm^2$) and two coverages of Pt_{46} (0.04 and $0.06\,e/nm^2$) clusters are shown in Fig. 5.3. In addition, the corresponding ADF of these excerpts, plotted as histograms are depicted. The use of the area in contrast to the commonly applied measure of the particle diameter is preferential in the case of these clusters, since in that size range the presence of different structural isomers influences the diameter of a particle more strongly than for larger particles. The micrographs for unselected $Pt_{n \geq 36}$ (a) and selected Pt_{46} clusters (c, e) show a homogeneous and well separated distribution of clusters over the surface. Different amounts, corresponding to the expected coverages are seen; for the unselected samples different sized clusters are present.
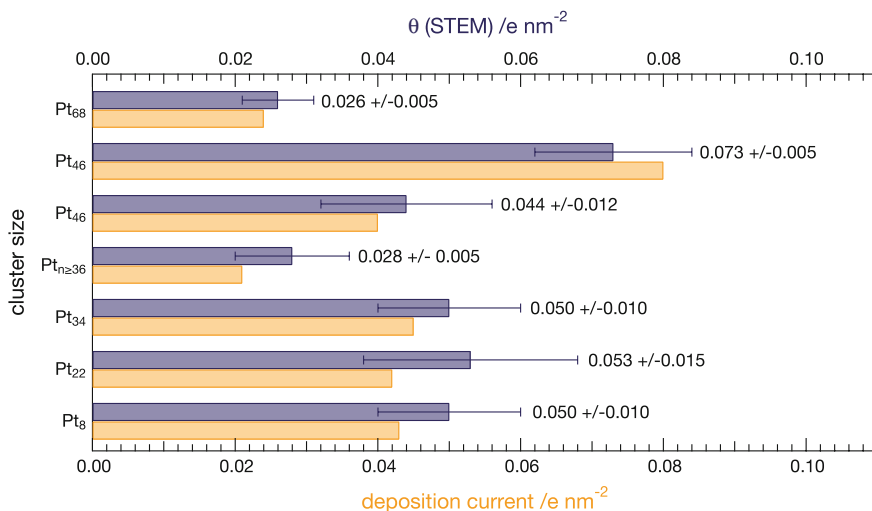
Fig. 5.2 Statistical analysis of the coverage control of $Pt_{n,x}$. Discharge current during deposition as comparison (*orange*), counts from TEM (*blue*). A minimum of five micrographs per size and for different coverages are taken for the counts. The indicated error for the counted particles is based on the standard deviation of the counts of the individual micrographs

The broad area distribution encountered for **unselected** samples (b) reflects the cluster production within the cluster source, the transmission of the ion optics and the transmission of the QMS used as a high pass filter. The ADF reveals cluster areas in the range from 0.5–$3\,\text{nm}^2$, with a peak maximum at $0.91\,\text{nm}^2$ (determined from the log normal fit) with a homogeneous size distribution (see orange line for integration). These findings agree with the expectation that masses corresponding to cluster sizes of $Pt_{n\geq 36}$ can pass the QMS setup when operated in the ion-guide mode (see Sect. 3.1.2).

In the histogram for the **selected** Pt_{46} samples (d,f), peaks corresponding to cluster ensembles of a distinct size can be seen.

The first peaks possess a narrow, well-defined and separated area regime and accounts to $82\,\%$ of the total amount of particles (see green line for integration). This peak can be fitted using a gaussian function (orange curve); resulting in a peak maximum, i.e. an average area of $0.98\,\text{nm}^2$. The additional, smaller peaks at ~ 2 and $\sim 3\,\text{nm}^2$ with lower abundance exhibit two and three times higher particle areas compared to the predominant fraction of clusters which is assigned to Pt_{46}. These fractions are attributed to agglomerates of two and three clusters which are most likely formed by TEM electron beam induced coalescence since migration of Pt clusters could be identified during acquisition of high-resolution images (see below for examples). To a small extent statistical particle collisions upon deposition have to be considered for high cluster coverages, as even for a perfectly size-selected cluster deposition process, the poisson statistic predicts the formation of a minor amount of dimer clusters [6]. The corresponding area values at the maxima remain unchanged
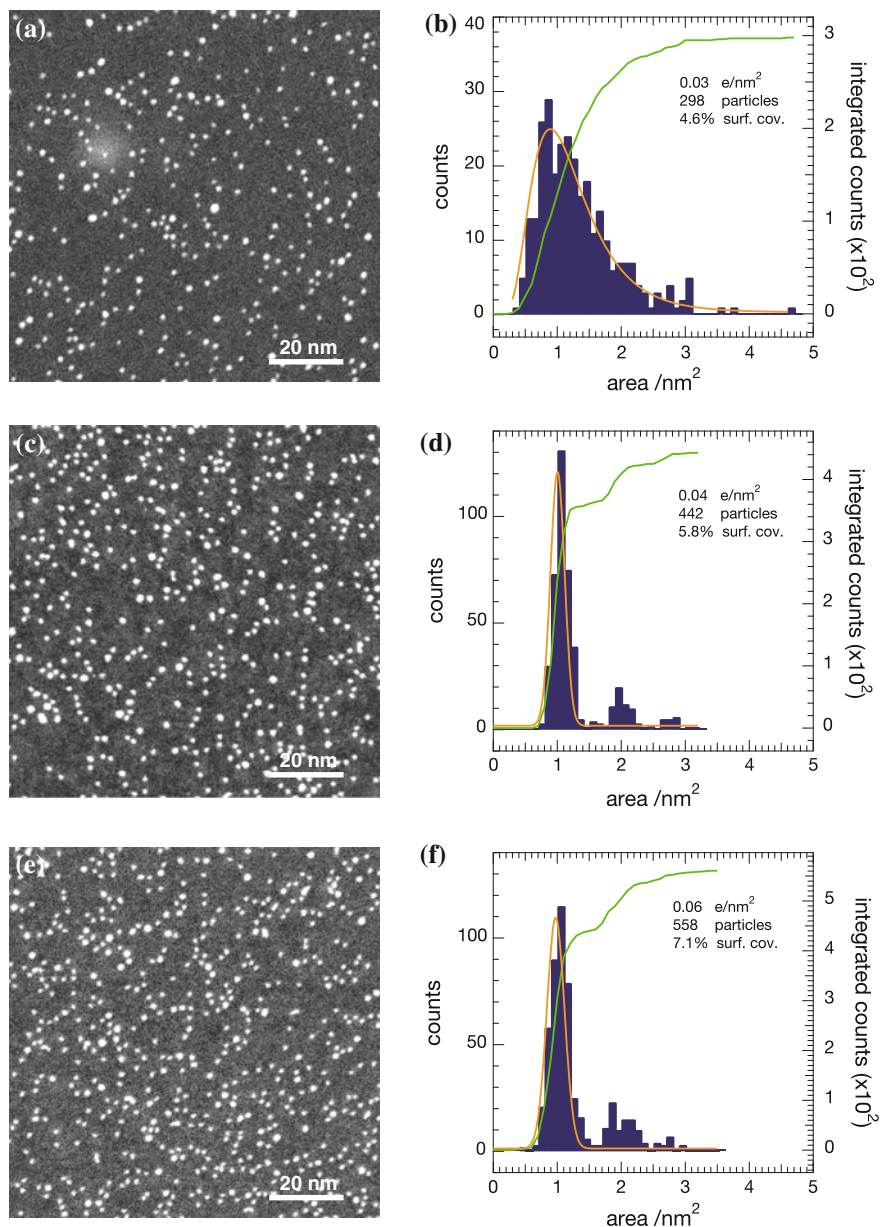
Fig. 5.3 Representative STEM micrographs for $Pt_{n\geq 36}$ (0.03 e/nm^2) and Pt_{46} (0.04 and 0.06 e/nm^2) clusters and their corresponding PSD, i.e. area statistics. The micrographs (100×100 nm^2) for uns-elected $Pt_{n\geq 36}$ (**a**) and two coverages of selected Pt_{46} clusters (**c**, **e**) on ultra thin carbon support are shown. Additionally the area statistics (**b**, **d**, **f**) are plotted as histograms. The obtained distrib-utions are fitted (*orange lines*)—for the unselected by a log normal distribution and for the selected samples the primary peak by a gaussian function. The *green curves* show the integrated counts
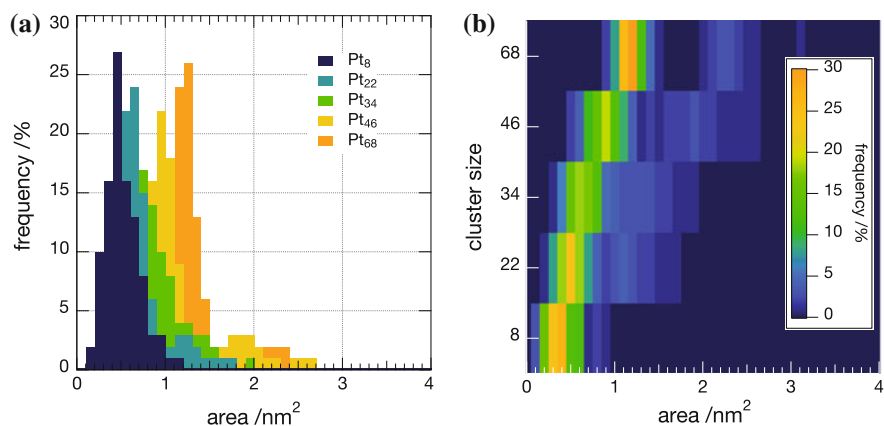
Fig. 5.4 Statistical analysis of different cluster sizes measured by STEM via histograms. The results of the analysis of multiple TEM micrographs, i.e. the ADF is plotted as for different selected cluster sizes as histograms (**a**) and as image plot (**b**)

upon increase of cluster coverage. Compared to the size-selected sample with lower coverage the fraction of particles revealing cross section areas in between the peaks is increased. Furthermore an additional fraction of particles exhibiting bigger cross section and volume values than three times the values of the predominant fraction is observed.

Figure 5.4 shows the ADF, thus results of the area measurements for **different selected** samples. The histograms are plotted as frequency of occurrence for comparison between the sizes, accounting for different amounts of clusters for different sizes. The choice of the bin width of $0.1\,nm^2$ in the histograms is slightly below the resolution limit of the microscope in STEM mode. The obtained distributions evidence different projected areas for different sized particles, as expected. In the image plot the trend towards increasing area for the main peak as well as the small fractions at double the area are visible. The results obtained have been validated by values obtained from three different programs used on the same images, as stated in Sect. 3.3.2. The main peaks of the histograms have been fitted assuming a gaussian distribution (a valid assumption considering the size selection down to a single atomic mass), and the obtained values are summarized in Table 5.2. From the measured projected areas the corresponding particle diameters are calculated under the assumption of a perfect, spherical particle [7, 8].[1] The listed values suggest, that size-selected clusters, can be discriminated by their projected area (within the given error) in STEM micrographs, at least with differences as low as 12 atoms. This approach is only problematic for very small clusters, since a 2D structure of the particles my be present, as in the case of Pt_8 [10].

---

[1] For Pt_8 this assumption not valid as there is experimental proof, that cluster in this size range are present as flat, 2D structure on the support [9].

Table 5.2 Particle sizes as projected area for different size-selected *Pt* clusters as obtained from the gaussian fit on the main peak of the histograms shown in Fig. 5.4

Cluster size/number of atoms	Area/Å^2	Diameter/nm
8	45 ± 15	(0.76 ± 0.08)
22	58 ± 8	0.86 ± 0.08
34	71 ± 15	0.95 ± 0.10
≥ 36 (peak maximum)	$91(\pm 6)$	$1.08(\pm 0.11)$
46	98 ± 6	1.12 ± 0.11
68	115 ± 14	1.21 ± 0.12

The error is based on the FWHM for the corresponding peaks. Additionally the particle diameter is calculated under the assumption of a spherical particle. For Pt_8 this is not valid as there is experimental proof for a 2D structure [9]; $Pt_{n \geq 36}$ is given for comparison

Discussion and comparison to literature—Only few works using STEM as local characterization method on small clusters have been published in literature, thus a real comparison is hardly feasible. Conventional TEM results reach a resolution limit for such small sizes and consequently reported studies [8, 11, 12] are not in the right size range to be compared, except for earlier work with clusters mass selected by means of the quadrupole deflector [1, 2]. The authors assign a cluster size to Pt_{46} clusters and measure an average diameter of 1.34 ± 0.16 nm, which is in the error range of the value obtained in this work with STEM, considering the applied less sophisticated mass selection and the use of TEM.

For STEM, no study on size-selected *Pt* clusters is reported. For other metals with high atomic number Z, i.e. *Au*, *Pd* [13–16], the dependency of the STEM image intensity on Z, so called Z-contrast imaging, in the ADF mode was used in order to discriminate between different sized clusters. The feasibility of this approach is shown, however the work suffers from poor size selection ($\pm 5\,\%$), the use of considerably large clusters and neglecting the influence of other parameters on the Z-contrast [17]. It is the opinion of the author that at the large sizes probed within these works possible influences on the Z-contrast might be neglectable, however for small sizes as presented here this assumption will fail. Consequently a measure of the volume of the particle, considering the obvious variation of microscope parameters during acquisition will not allow later comparison. Further, measurements on small clusters (without particular size selection) of *Au* [18] and *Ge* [19] have been performed, however the aim of the studies was the investigation of single clusters with respect to stability and resolution in the sub nanometer scale, thus do not provide a comparison in terms of size.

Using STM as alternative local method, is advantageous compared to TEM when aiming for determination of the particle height. The height can be measured, with only small errors [20, 21] and exploiting the fact of different atomic layers for different cluster sizes it has the capability to discriminate between cluster sizes with differences of only one atom [9] and even different isomers [6]. The method however, suffers from to the well know tip convolution effect in STM for measurements of area/diameter, thus resulting in values with high error. Here TEM is advantageous, as it measures in general the 2D projection of the sample specimen and allows therefore
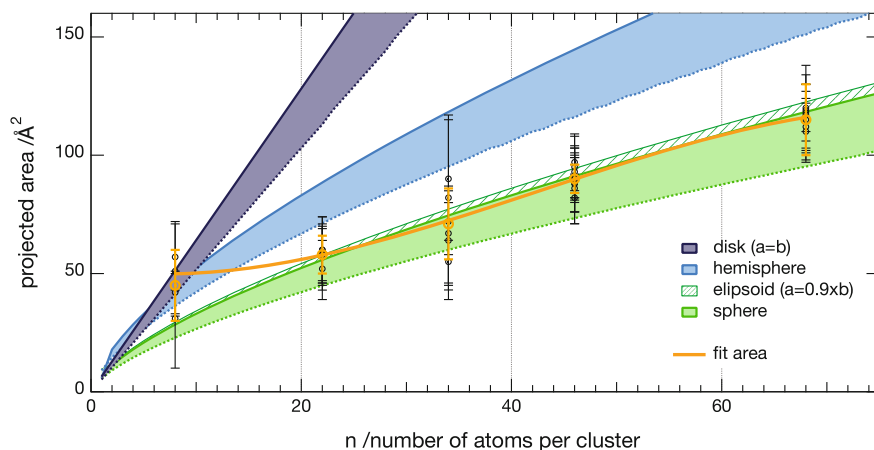
Fig. 5.5 Approximation of the cluster shape by comparing the measured projected areas by means of STEM to simple geometrical models. The peak maxima of the gaussian fit from the main peak of each individual analyzed STEM micrograph along with the corresponding error (FWHM of the gaussian) is plotted as a function of cluster size (*blue points*). From the individual values a mean value is calculated and shown with the standard deviation as error (*orange points*); the *orange line*, extrapolating the five measured sizes serves as a guide to the eye. The values of the mean areas are further compared to a disk (*dark blue*), hemisphere (*blue area*) and sphere model (*green area*). For details see text, for used values Table A.11

for a precise determination of the area. Nevertheless, STM investigations of supported *Pt* clusters in the very small size range of 1–15 atoms are reported [9, 10], where the authors measured the 'diameter' of the Pt_4 tetramer to 0.33 nm, however with a high error due to tip convolution. Comparing this value to the Pt_8 measured here and assuming as well a 2D structure the obtained area/diameter are reasonable. The precise size selection during preparation of the cluster materials in the presented case, in combination with the sensitive measure of the area in STEM should allow one for using the obtained values for the particle sizes as a comparison for particle, synthesized by different means. This method is superior compared to the discussed use of the Z-contrast in order to measure the particles size [13–16], as it is applicable towards smaller sizes and can be used without further assumptions.

In fact, the measure of the area can be even applied to get an idea on the three dimensional **cluster shape**. In Fig. 5.5 the determined peak maxima of the gaussian fit of the main peak of each individual analyzed STEM micrograph is plotted as a function of cluster size.

An average size is calculated, based on the single measurements and evidences an increase of projected area with size. Additionally, the projected area for three different, simple geometrical models of possible cluster shape are depicted (a comparable approach as in [13]). The disk considers a flat lying cluster, were all atoms are located in one layer. For a perfectly hemispherical and spherical cluster its potential volume is calculated using the volume of an individual *Pt* atom times the number of atoms per clusters (see Table A.11 in appendix for details). Two extreme packing cases are

considered. First, the smallest possible size (dashed lines), based on the *Pt* dimer distance of 2.44 Å (a theoretically [22, 23] and experimentally [24] determined value) is calculated. Second, a common *fcc* packing density, as known for a single crystal surface is assumed, leading to the biggest possible size (drawn trough lines). The two extrema give rise to two areas, which allow to distinguish between a spherical or half-spherical shape of the clusters. For the *fcc* packed sphere additionally the area corresponding to an ellipsoid with an aspect ratio of ($a = 0.9 \times b$) is calculated, leading to slightly higher area values. Comparing now the models with the measured areas (orange points and trend line), both the case of a disk and a hemisphere can be excluded in the case of *Pt* clusters supported on thin carbon films, except for Pt_8. For the smallest measured cluster size, an assignment of the shape is difficult due to the high error, however comparing to the overall trend and with the literature presented above a tendency towards a disk like, 2D shape can be observed. For larger clusters the real shape of the clusters is sphere like, probably slightly distorted (due to different isomers) and thus evidences a rather weak wetting behavior of the clusters on the surface [25]. The observed trend of increasing area with bigger clusters, described by both the model as well as the experimental data proves the prospect of the use of size-selected clusters as a standard for estimating the number of atoms in an unknown particle measured by STEM.

Despite the presented results, the use of TEM, and particularly STEM, has the major disadvantage of **beam damage** due to the use of a (focused) high energy electron beam during image acquisition [17, 26]. A series of STEM images ($40 \times 40\,nm^2$) covered with 0.03 e/nm^2 Pt_{68} of the same sample position measured four times (at 300 kV) in a row is shown in Fig. 5.6. The micrographs are not corrected for image drift, thus the probed excerpts vary for the different images. At first, the clusters are all separated and homogeneously distributed over the surface. As a consequence of the electron beam scanning over the specimen three clusters in the lower left of the micrographs approach between the first two images and coalescence during further imaging process, another pair starts to approach and merge in the last image of the series. It is likely, that the coalescence of these particles is observed, as they happened to be positioned particularly close to one another. Further external factors, possibly influencing the stability of the clusters during image acquisition can be excluded. In addition to the coalescent particles, a change in shape and contour of nearly all clusters from one image to the next illustrates the flexibility of these small particles as well as the presence of a multitude of different structural isomers. Inducing external energy by the electron beam, the clusters readily interconvert between different structural isomers. Beam damage on cluster samples is one major reason for the observation of di- and trimers in the ADF histograms (Fig. 5.3).

Summary—In conclusion, the observations using STEM as a local probe method for characterization of cluster materials, in combination with a computer assisted analysis of the recorded images gave the following results. The deposition methods yields a highly reproducible cluster coverage, which corresponds within 14 % (average error) to the independently measured integrated current over time during deposition. Selected clusters can be distinguished from unselected ones by their different PSD of the projected areas. In the case of unselected clusters this can be
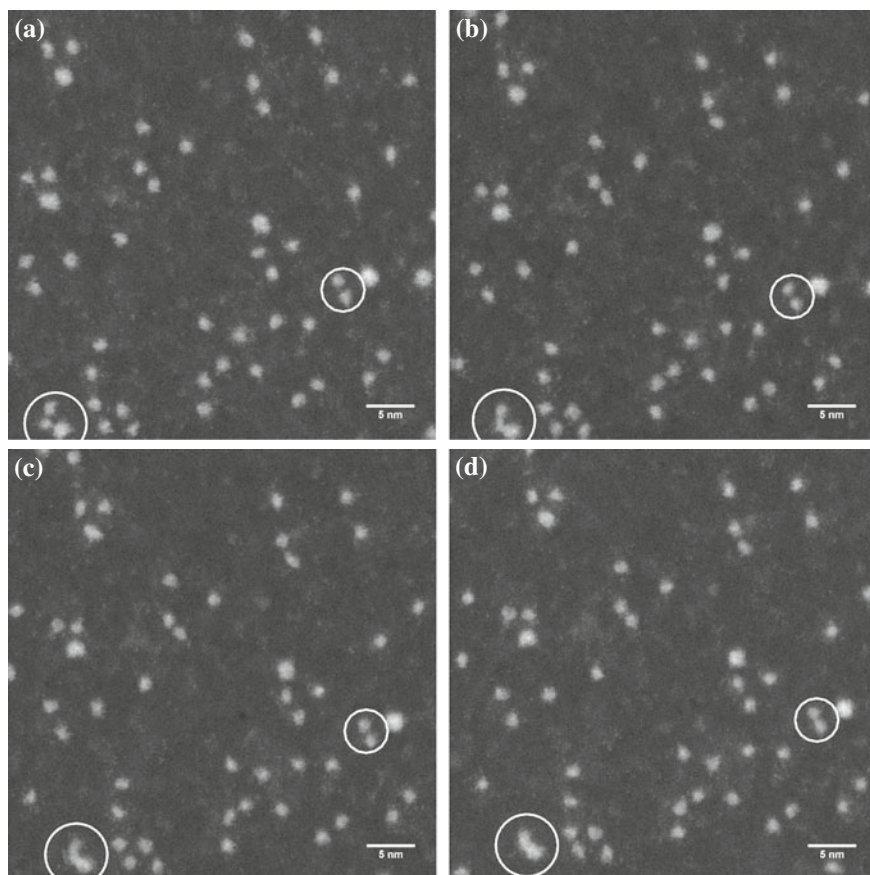
Fig. 5.6 Series of four subsequent STEM micrographs of $0.03 \, e/nm^2$ Pt_{68}. The images are recorded with an electron beam of $300 \, kV$; two cluster pairs that coalescence as a result of the high beam intensity are marked with *circles*. **a** $t = 0 \, s$, **b** $t = 82 \, s$, **c** $t = 138 \, s$, **d** $t = 219 \, s$

approximated by a log normal distribution; for the selected clusters by a gaussian fit. The areas reflect the production of the source, ion optics and QMS, for the selected clusters of all probed sizes, and the PSD shows cluster ensembles with distinct size (about 80 % of all clusters). The comparison of the areas of different sizes, allows one to distinguish between different clusters sizes with differences of at least 12 atoms. Further, comparing the obtained area values to calculations, based on simple geometric considerations, suggest a sphere like cluster shape, with the exception of very small clusters, that appear as flat 2D structures. The obtained area values for different cluster sizes may serve as a guide to estimate sizes of cluster synthesized by different means. Further, the findings in combination with the analysis are a basis for routine characterization of cluster materials in the future, with the only draw back of beam damage.

5.1.2 XPS

In addition to the local characterization by means of TEM in the previous section, the integral characterization of the prepared samples is described in the following. As a first step different sample types were probed to see if the sensitivity of the setup is sufficient to detect the low cluster catalyst amounts. Furthermore, a representative line scan for Pt_{68} clusters was performed in order to get an idea of the spatial distribution of clusters on the sample materials.

Different selected $Pt_x (x = 8, 22, 34, 46, 68)$ clusters were investigated in order to elucidate differences in core electronic structure. In addition Pt_{46} was compared to an unselected $Pt_{n\geq36}$ sample. For the selected cluster sizes a coverage of $0.029 \, e/nm^2$, for the unselected a coverage of $0.058 \, e/nm^2$ was deposited onto the wafer.

In Fig. 5.7 representative **survey scans** for a XPS wafer sample and an unsealed μ-reactor, before and after deposition of size-selected Pt clusters are shown. For better comparability, the spectra are normalized with respect to the $Si \, 2p$ signal of the underlying silicate support.

Beside several other elements,[2] that can be detected in the XPS spectra, the contributions of the *silicate* support and the Pt (after deposition) are of main interest and are briefly discussed in the following. Representative spectra of the Pt and Si peaks are shown in Fig. 5.8.
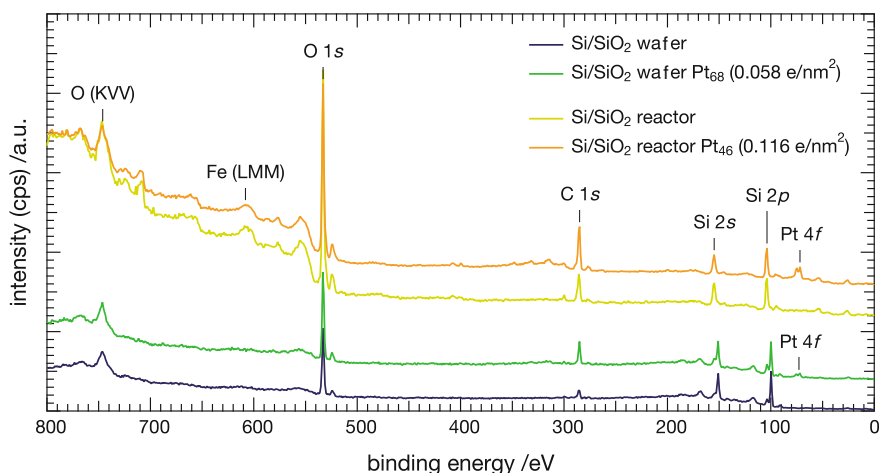

Fig. 5.7 Survey scans of a XPS waver sample and an unsealed μ-reactor before and after deposition of size-selected Pt clusters. Coverage of $0.029 \, e/nm^2 \, Pt_{68}$ for the waver, $0.058 \, e/nm^2 \, Pt_{46}$ for the μ-reactor, respectively. For better comparability, the spectra are normalized with respect to the $Si \, 2p$ signal of the underlying silicate support

[2] As a minor fraction the presence of Fe (particularly for the reactor samples) can be seen by different Auger transitions in the BE range of 700–550 eV, which is a contribution of the underlying sample holder and the fixation of the sample, however is not affecting the other measurements.
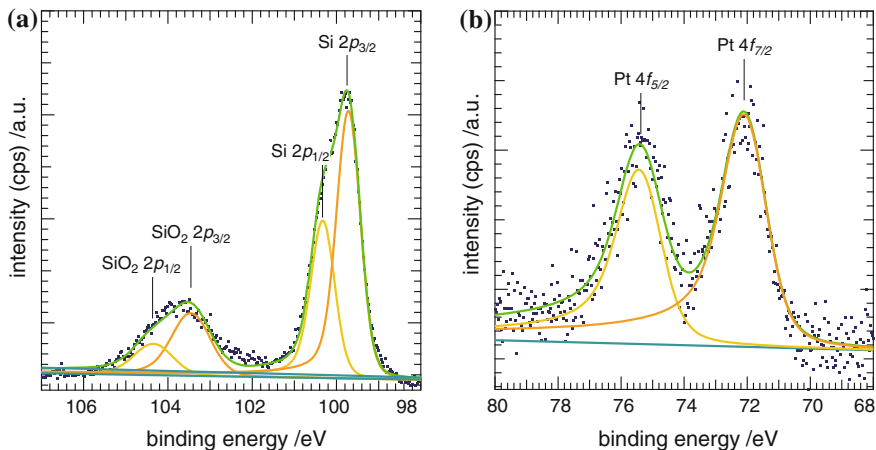
Fig. 5.8 Representative (**a**) *Si 2p* and (**b**) *Pt 4f* peak and corresponding fits for 0.029 e/nm^2 *Pt$_{68}$* supported on a *Si* waver. The results of the presented fits, for each position of the line scan are used to calculate the spatial distribution of clusters in Fig. 5.10b

From the underlying support (for all shown samples) for **silicon** two signals at 150 and 100 eV can be detected, which correspond to the photoemission of the *Si 2s* and *Si 2p*, respectively. These silicon signals are accompanied by two plasmons, which are shifted by 20 eV towards higher BE (particularly visible for the wafer). The *Si 2p* signal consists of two peaks, corresponding to two silicon species; one at 99.5 eV corresponding to elemental *silicon* of the wafer and a second one at 103 eV arises from photoemission of *silicon oxide* with a chemical shift compared to the *silicon* bulk. Further, the *2p* spin–orbit coupling has to be considered, with a separation value of 0.60 eV for *silicon*. Thus, the signals consist of two components arising from $2p_{3/2}$ and $2p_{1/2}$ (with a 2:1 intensity ratio), which are consequently used for fitting of the silicon peaks as shown in Fig. 5.8a. Although the existence of further interphases has been proposed in literature [27], within this work only two phases are included in the data treatment.

The signal of the elemental $2p_{3/2}$ peak is observed at 99.6 eV, however, the literature value of pure silicon is listed at 99.3 eV [28]. The observed shift is most likely caused by charging effects of the sample,[3] due to silicon and silicate being a semiconductor or insulator material, respectively. In the following sections it is assumed that this charging effect is homogeneous distributed over the sample. The spectra shown are therefore compensated for the observed charging, by referencing the $2p_{3/2}$ peak to the literature value of 99.3 eV and thus using it as an internal standard for **calibration** of the energy scale as performed in [29]. Other possible

---

[3] Using a simple consideration, the charging of the surfaces can be explained as follows. After ejection of an photoelectron a positive charge remains at the surface, which is neutralized after a certain time. Therefore, during measurements an equilibrium between creation and neutralization of the remaining charge is established and results in a constant charging shift.

forms of *Si* hardly influence the correct determination of the peak energies and it is therefore justified to neglected them (for the interpretation within this work). In the case of the μ-reactor, the surface has a thick, thermally grown SiO_2 film as support and thus only the *Si* 2*p* signal, arising from the oxide can be detected, compared to the thin silicon wafer oxide film.

After deposition of **Pt** clusters, in both cases (wafer and reactor) the *Pt* 4*f* signal at 72 eV is apparent and confirms successful deposition.[4] Although *Pt* (bulk) gives rise to further signals (from 4*d* and 4*p* orbitals), only the 4*f* signal is detectable due to the low amount of *platinum* on the surface. Comparison of the signal intensity for the *Pt* 4*f* peaks on the two different supports, reflects the total amount of *Pt* present on the surface. Also the *Pt* 4*f* signal has two contributions, because of the spin–orbit splitting (Sect. 3.2.5). The resulting 4$f_{7/2}$ and 4$f_{5/2}$ signals are separated by 3.33 eV (intensity ratio 4:3). These values are used for peak fitting (see Fig. 5.8b); the Lorentzian parameter is adopted from the *Pt* bulk measurement [30], whereas the asymmetry parameter is kept free.

The **spatial cluster distribution** on the support is studied by means of a **XPS line scan**, representatively for a Pt_{68} sample with 0.029 e/nm^2. On twelve positions with a separation of 1 mm measurements of the *Si* 2*p* and the *Pt* 4*f* are performed. The resulting spectra at the different positions are shown in Fig. 5.9.

With respect to the spatial distribution of *Pt* on the surface, the discussion of the peak intensities, i.e. the integrated peak areas are of interest. Differences in the absolute peak energy positions (in particular for the *Pt* 4*f* signal) are part of the discussion of the different cluster sizes below and are omitted here. The *Si* 2*p* and
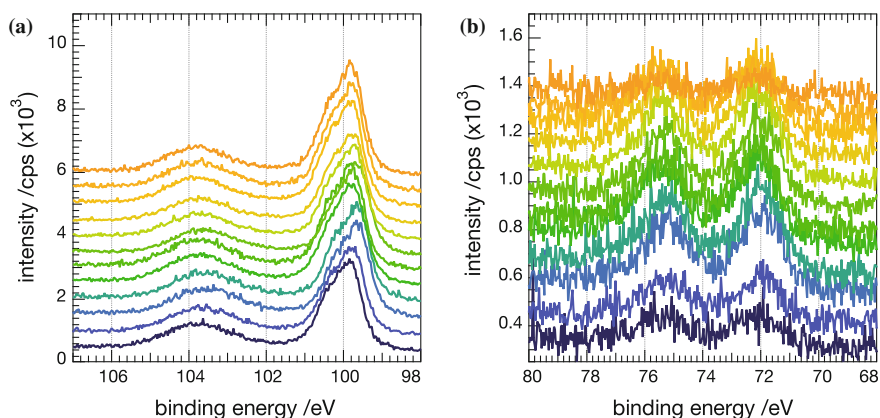

Fig. 5.9 XPS line scan excerpts of the *Si* 2*p* (**a**) and *Pt* 4*f* (**b**) peaks for the sample with 0.029 e/nm^2 Pt_{68} supported on a *Si* waver. The obtained fit results of these signals (i.e. *Pt* in figure) are used to calculate the spatial distribution of clusters in Fig. 5.10b

---

[4] An additional survey scan on a INPS sample (not shown here) also reveals *Pt* features [30], and confirms therefore not only a deposition, but further the successful application of the electron shower for deposition on insulating materials.
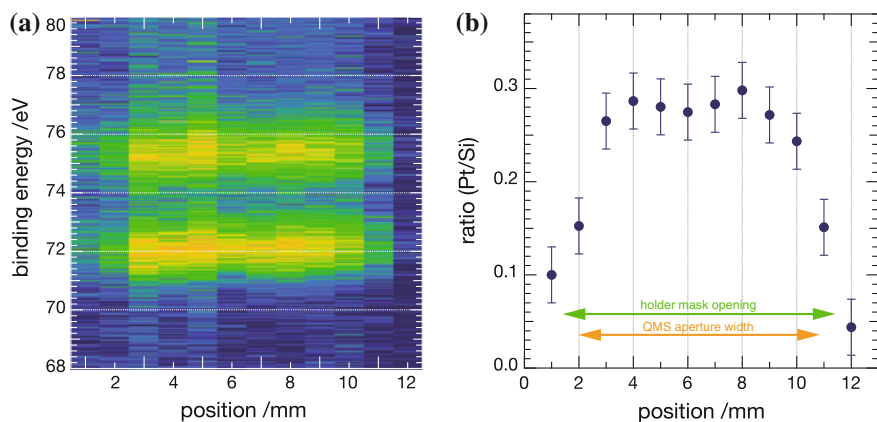
Fig. 5.10 Image plot of *Pt* 4*f* signals of 0.029 e/nm² *Pt₆₈* (corrected by the *Pt* to *Si* ratio) as a function of different spatial positions (**a**) and spatial distribution of clusters on the support, shown as ratio of the obtained areas from the fitted *Si* 2*p* and *Pt* 4*f* signals (**b**) for each measured position from Fig. 5.9

Pt 4*f* signals for each position are fitted (Fig. 5.8), according to the considerations and assumptions mentioned above (two phases, elemental and oxide for *Si* and spin–orbit splitting for both *Pt* and *Si*). For each spatial position the fit results of the peak areas for *Pt* and *Si* are used to calculate the ratio of the two elements. The resulting ratios of the peak fits as a function of the position are shown in Fig. 5.10.

In both figures, the major presence of *platinum* is detected between 2 and 11 mm and shows in this position range a homogeneous distribution of *Pt* on the sample. This distribution reflects well the used aperture in front of the QMS (9 mm diameter) as well as the cap opening of the used sample holder (10 mm for XPS samples), as additionally indicated in Fig. 5.9. Towards the edges a lower amount of *Pt* is observed, a result of both apertures as well as the XPS spot size (<1 mm).

To estimate the error, the arithmetic average for the positions 3 to 10 is shown, supporting well the observed homogenous distribution over the sample. The ratio of the integrated areas of the *Pt* and *Si* signals is further used to eliminate fluctuations in the detection of the photo emitted electrons for the measurement of different positions. Therefore, the *Pt* 4*f* signals in the image plot in Fig. 5.9 is corrected by a factor taking into account this ratio for each position.

Figure 5.11 presents the results of the **comparison** between **selected and unselected** clusters, along with the results of the size dependent measurements. The obtained spectra of the *Pt* 4*f* signal for 0.058 e/nm² *Pt$_{n \geq 36}$* and 0.029 e/nm² *Pt₄₆*, along with the fit results (fixed spin–orbit splitting, ratio and Lorentzian) are shown in Fig. 5.11a. The *Pt* 4*f* signal of the *Pt$_{n \geq 36}$* clusters is shifted by 0.09 eV towards higher BE compared to the *Pt₄₆* clusters. Further, from the fit results the broadness of the *Pt* 4*f* signal is described by the 'gaussian' parameter, for *Pt$_{n \geq 36}$* the parameter with a value 1.762 indicates a slightly broader peak compared to the selected sample
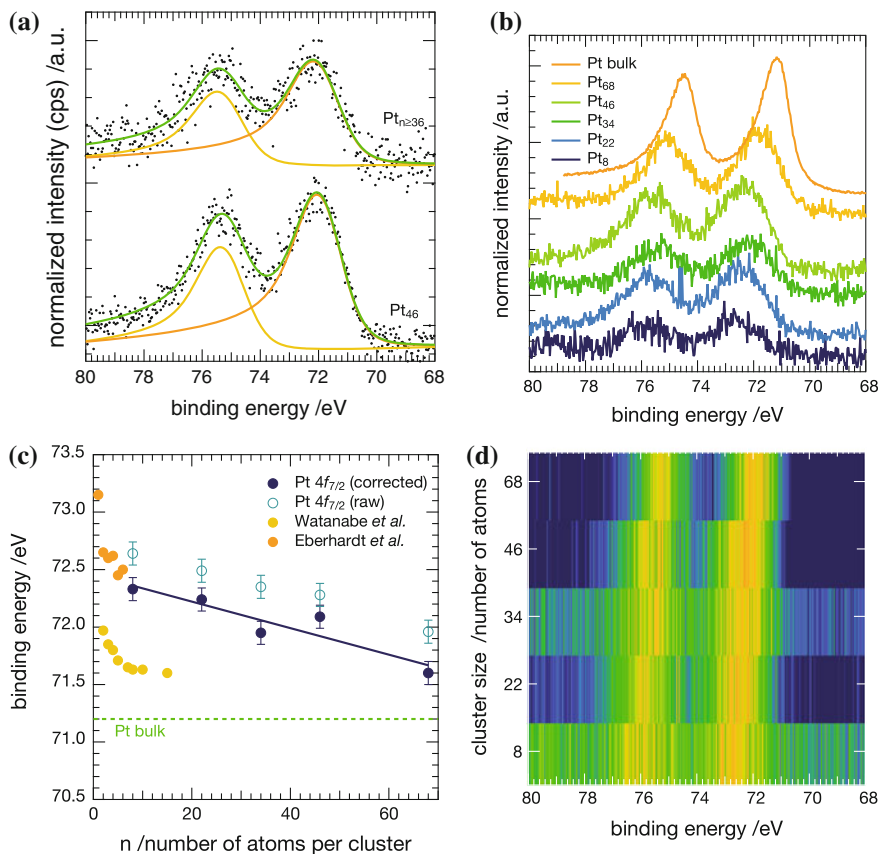
Fig. 5.11 XPS of *Pt* 4*f* peaks for different sizes and comparison to literature values. XPS *Pt* 4*f* signals for selected and unselected clusters (**a**) including the corresponding line fit. The normalized *Pt* 4*f* signals for different selected cluster sizes and *Pt* bulk as waterfall plot (**b**); different sizes as image plot (**d**). The BE values of the *Pt* 4$f_{7/2}$ signals as a function of cluster size (**c**), for comparison the bulk value and BE from measurements in the literature [9, 29] are included

with a value of 1.705. Additionally, the unselected clusters exhibit a bigger asymmetric parameter (0.131 compared to 0.115). All these observations (broader peaks, change in asymmetry and shift in BE) can be explained as a result of a mixture of different sized clusters with an average below size 46 ($n \geq 36$), as visible from the TEM treatment (Sect. 5.1.1). The mixture results in a convolution of all core level signals stemming from the single clusters with different sizes in the XPS spectra, leading to higher values for the fit parameter, compared to a single sized sample. The *Pt* 4*f* signals as a function of **cluster sizes** are depicted in Fig. 5.11b (including a *Pt* bulk sample) and Fig. 5.11d; the spectra are normalized to the corresponding *Si* 2*p* support signal for comparability. Further, the peak maxima of the 4$f_{7/2}$ signals are shown in Fig. 5.11c as 'measured' as well as corrected with respect to the silicate

literature value of the *Si* $2p_{3/2}$ peak. Compared to the bulk metal (dashed green line), the clusters are shifted by $\sim 1\,$eV towards higher BE. For smaller clusters the highest BEs are observed, with increasing cluster sizes the value converges to the bulk value. In general, this can be explained by a finale state effect, where the remaining charge after photoemission on the cluster shift the peak features on a BE scale.

Discussion and comparison to literature—Additionally to the measured sizes, *Pt* $4f_{7/2}$ values from two data sets reported in the literature are included as comparison in Fig. 5.11c. Results from Eberhardt et al. for Pt_x ($x = 1 - 6$) clusters supported on an oxidized *Si*(100) surface [29], as well as results from Y. Watanabe et al. for size-selected Pt_x ($x = 1 - 8$, 10, 15) clusters on a TiO_2(110) surface [9, 10]. The different values for the *Pt* $4f_{7/2}$ position show a linear trend (within the stated error range), save for Pt_{46} where a slight tendency towards higher BE can be observed. The values, corrected for charging effect, for the *Pt* $4f_{7/2}$ fit well to the results obtained by Eberhardt et al. [29], for a similar system. Considering that in this study, the samples were transferred in air to the synchrotron source for measurement, contaminations of the samples can not be excluded (as in the presented data here). In particular the oxidation state of the *Pt* clusters, visible as chemical shift could give an insight on this. The authors claim that the clusters are not contaminated mainly for the following two reasons.

First, the chemical shifts for *Pt* oxides and hydroxides are typically about $3\,$eV (for the stoichiometric compounds) and therefore significantly larger than the measured maximum shift ($1.3\,$eV for the *Pt* atom). Second, comparing the results to studies on commercial *Pt* catalysts, these systems exhibit an oxide core-level shift of about $2\,$eV, again larger than the observed values.

Since these very small $Pt_x(x = 1-6)$ clusters are considered as nonmetallic in the study no asymmetry in the *Pt* $4f$ was observed. Using clusters covering a larger size range, as in this work, indeed it can be observed, that with increasing cluster sizes the asymmetric parameter also increases (0.071 for Pt_8 to 0.121 for Pt_{68}) and can be interpreted as an consequence of the transformation to a metallic character with larger particle size. The broadness of the signals might have its origin in the inhomogeneity of the support, i.e. that different adsorption sites are available for clusters.

In order to estimate the oxidation state, a few considerations are given in the following. A possible oxidation state of $+IV$ can be excluded, based on the observed chemical shift of $3\,$eV compared to the pure metallic platinum as mentioned above. Unfortunately, the oxidation states $+II$ and *0* cannot be distinguished based on their chemical shift, as the difference between those states is too small. For the results of Watanabe et al. [9, 10] for *Pt* clusters containing up to 15 atoms measured under UHV conditions, an oxidation state of 0 can be assumed and shows considerably lower BE than the ones from Eberhardt et al. The question arises, whether this difference of $0.6\,$eV is solely caused by the different supports or also by the conditions to which the samples were exposed and later treated. An oxidation state of 0 could be present considering the contamination of the clusters (physisorbed species) and the observed asymmetric line shape. To achieve an ultimate insight, further experiments for the same type of samples under constant UHV conditions are necessary, however it seems likely that an oxidation state of $+II$ (e.g. $Pt(OH)_x$) is present.

Further it can be stated, that with the measured BE shifts a full oxidation of the clusters after transfer to ambient conditions can be excluded and thus might be an explanation for the observed persisting reactivity after transfer [2, 31].

Summary—The results of the XPS measurement of supported size-selected *Pt* clusters after transfer to ambient conditions can be summarized as follows. A successful deposition on both conducting and insulating support materials is confirmed by the *Pt* 4*f* signal, visible for all samples. The deposition method was characterized by determining the cluster distribution over the support representatively for Pt_{68} by means of a line scan and quantified by the ratio of the *Pt* 4*f* to the *Si* 2*p* signal. The results evidence a homogenous distribution over the support in the range of the used apertures during deposition.

Further selected and unselected samples can be discriminated by their peak signal shape and broadness. For different sized selected samples, an observed BE shift converges with increasing cluster sizes for the *Pt* 4*f* signal towards the bulk value. The observed shifts, along with observed changes in fit parameters are in good agreement with the literature and can be explained by a final state effect. Comparison to similar systems allows one to estimate the oxidation state of the cluster materials between *+II* and 0. This is an explanation for the reactivity of such small supported clusters, which are despite transfer to ambient conditions not fully oxidized, and thus reactive.

Based on these first experiments, future XPS experiments are planned in order to learn about the change in core electronic structure, in particular related to the reactivity of clusters. For example, probing clusters under oxidative and reducing atmosphere and subsequent shifts in BE could help to understand the underlying changes in electronic structure of such model systems during reactions. Further, because of the dependency of the BE shift on the size, XPS is able to probe e.g. temperature stability for size-selected clusters with prospect to investigate sintering mechanisms.

In combination with TEM, thus probing on both integral as local (individual) level a deeper understanding of the interplay between geometry, electronic structure and consequently chemical and physical properties of clusters supported on various substrates is possible.

5.2 Stability

First preliminary results of ongoing studies with respect to the stability of size-selected clusters are discussed in this section. By means of ETEM (in collaboration with CEN/DTU) as well as INPS (in collaboration with Chalmers) in combination with STEM (at CEN/DTU), two conceptional different approaches are chosen to probe the temperature stability. The data serve as a basis for future experiments when probing the stability at elevated pressures under a reactive atmosphere.

In ETEM the stability of size-selected Pt_{46} clusters on a SiO_2 support was measured a elevated temperatures under UHV conditions. With INPS, different selected and unselected clusters samples supported on Si_3N_4 were heated and the stability was monitored by measuring the changes in the plasmon peak position of the INPS

sensor and correlating them with structural changes of the clusters (i.e. sintering). Additional TEM windows measured before and after treatment under the same experimental conditions and analyzed with respect to changes in the PSD. Both projects are ongoing work, however the first results with respect to temperature stability are presented.

5.2.1 Environmental-TEM

As a first size-selected cluster sample, Pt_{46} (0.01 e/nm^2) deposited on a 8 nm thick SiO_2 thin film was measured in the ETEM (Titan E-Cell 80-300ST at CEN/DTU) at different temperatures under UHV conditions. The sample was first imaged at room temperature and afterwards the temperature was increased with a ramp of 0.1 K/s to reach the next temperature for measurement (375, 400, 425, 450 and 475 K, respectively). Before measurement, the sample was equilibrated at each temperature for 15 min, in order to allow for stabilization of the sample drift. Using this procedure micrographs at different sample positions and in total six different temperatures were taken; representative excerpts of $60 \times 60 \, nm^2$ are shown in Fig. 5.12. The micrographs show a homogeneous cluster distribution over the sample for all temperatures with similar sizes. Further, a consistent number of particles per excerpt (33 ± 4 clusters)
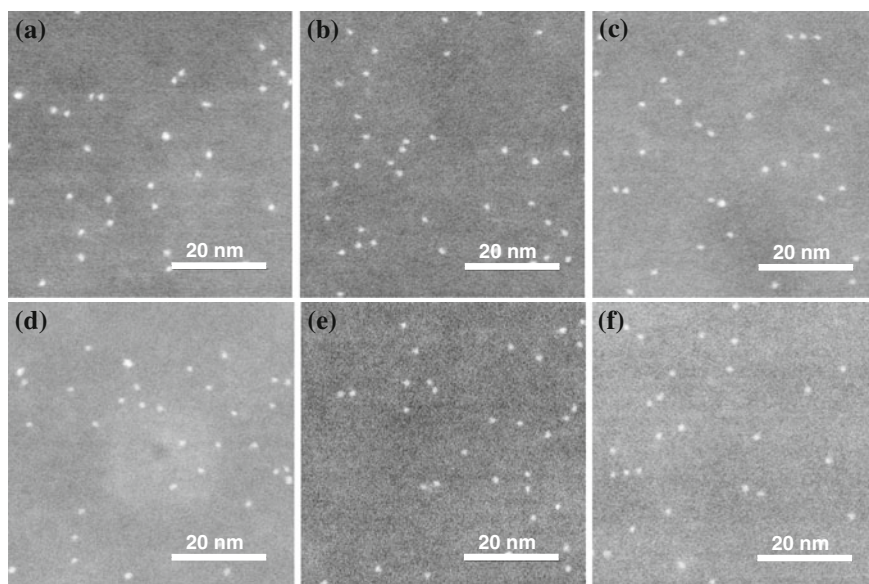

Fig. 5.12 Excerpts ($60 \times 60 \, nm^2$) of size-selected Pt_{46} clusters deposited onto 8 nm SiO_2 at a coverage of 0.01 e/nm^2. The samples are probed under UHV conditions at the following temperatures. **a** 300 K, **b** 375 K, **c** 400 K, **d** 425 K, **e** 450 K, **f** 475 K
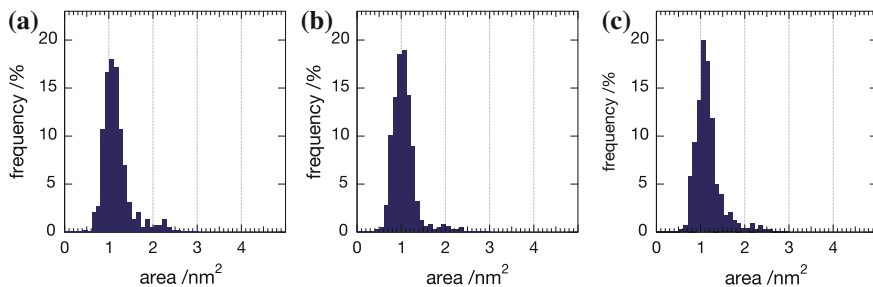
Fig. 5.13 Corresponding histograms of the ETEM images in Fig. 5.12 for the three different temperatures (**a**) 300, (**b**) 400 and (**c**) 475 K

evidences a similar coverage at all temperatures and is a first indication for stable clusters at all temperatures.

To check further on possible sintering, the corresponding **PSD** for the area were determined. Representative, the results for three different temperatures are shown as histograms in Fig. 5.13. For all temperatures the ADF show a sharp peak with a maximum at $1 \, nm^2$, in accordance with the results for Pt_{46} in Sect. 5.1.1 on carbon support. The similar shapes and stable peak maxima evidence that clusters are stable at temperatures up to 475 K on SiO_2 under UHV conditions.

Further experiments with different cluster sizes and temperatures as high as 600 K are currently in progress, in order to probe for possible changes in the stability for different sizes. Additionally, the samples will be imaged *in situ* during the exposure to gases, in particular under a reducing (H_2 or CO) and/or oxidative (O_2) atmosphere also at elevated temperatures [32]. Possible restructuring of the clusters, as observed for other supported particles [33–35] or induced sintering [36–38] could help to foster the understanding of these model systems on a local level under more realistic conditions.

5.2.2 Indirect Nanoplasmonic Sensing

In a different approach, the sintering of selected and unselected clusters in an inert gas atmosphere under elevated temperatures was tested using the INPS platform at Chalmers. Recent results showed the successful use of this technique for investigating sintering phenomena of supported metal particles with an average size of 3.3 nm *in situ* at atmospheric pressure [39, 40].

In a first step the **sensitivity** of the method towards small clusters was studied, by monitoring the change in LSPR centroid wavelength for both a blank INPS chip (reference) and a chip with $0.005 \, e/nm^2$ unselected $Pt_{n \geq 53}$ supported on Si_3N_4 as a **function of temperature**. The samples were heated in an *Ar* flow (200 mL/min) from 325 K in steps of 15 K and held at one temperature for 45 min (after 15 min,
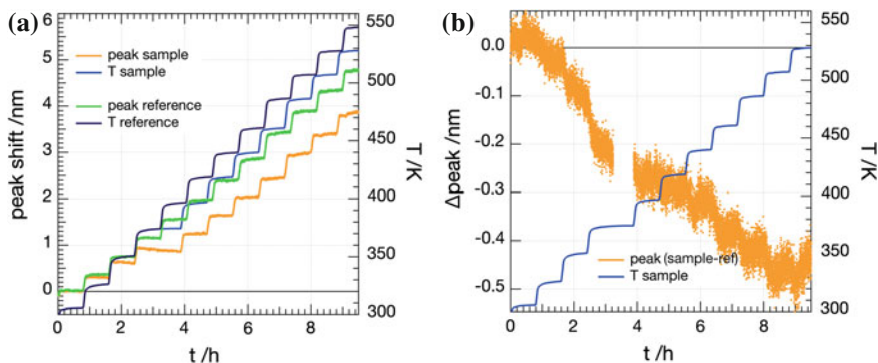
Fig. 5.14 Plasmon change for stepwise heating (in 15 K steps, with 45 min for each temperature) of a $Pt_{n\geq53}$ sample and a corresponding reference sample (**a**) in Ar. A longer step at ~400 K for the sample and the corresponding temperature is caused by a fail in the heating. Difference signal, obtained by correction the sample signal for the temperature influence obtained from the reference sample (**b**)

the gas mixture was changed including 4 % O_2). The measured peak positions for sample and reference are shown in Fig. 5.14 and evidence an expected temperature induced spectral red-shift of the sensor's LSPR peak with higher temperatures [41] for both, that can be accounted for by measuring and subtracting a reference (as done below).

A step in the sample signal and the corresponding temperature signal is an intentional check during measurement, however does disturb the observed trend only to a minor degree. Using the reference signal in order to correct the sample signal for the temperature induced peak shift to longer wavelength, a difference signal with the relative changes of the sample peak position is obtained. The plot evidences a relative decrease in peak position, thus a blue shift of ~0.5 nm for the sample with increasing temperature. The observed changes clearly show the feasibility to probe clusters with INPS and the blue shift, corresponding to increasing particle size can be interpreted as a sign for the sintering of the particles [39, 42].

In order to compare and unearth **different sintering** behaviors of **selected** and **unselected cluster** samples,[5] the changes in relative peak position of three different $Pt_{x,n}$ ($x = 68, 68 + 22, n \geq 53$) samples (0.004 and 0.003 e/nm^2) were probed.[6] For these experiments, the reactor was pre-heated to 453 K (to guarantee fast temperature equilibration upon sample insertion) and each of the samples inserted and the signals recorded for 21 h under an Ar flow (200 mL/min). The samples where then taken out of the reactor and the procedure was repeated using the same samples under the exact

---

[5] Assuming an Ostwald ripening mechanism and using clusters with the same number of atoms the question arises, if the particles, despite having the exact same size will sinter or not.

[6] The Pt_{22+68} sample consists hereby of a mixture of the two selected cluster sizes Pt_{22} and Pt_{68} at a ratio of 1 : 1 and is chosen for the reason to probe for Ostwald ripening like sintering, as introduced in Sect. 2.3.2.
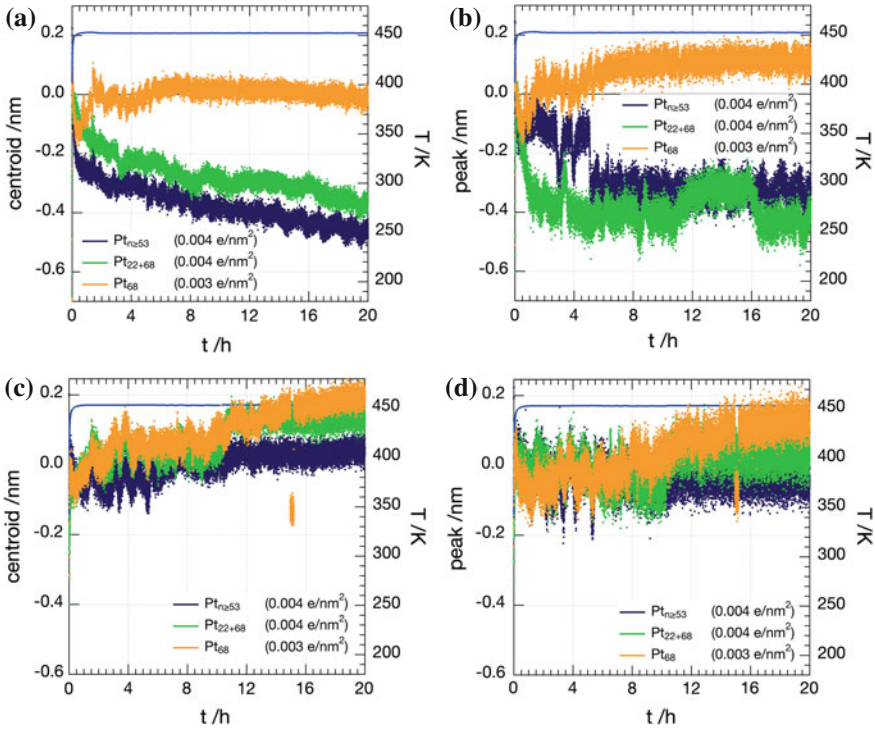
Fig. 5.15 INPS signals of $Pt_{x,n}$ ($x = 68, 68 + 22, n \geq 53$) at 453 K under *Ar* atmosphere, (**a, c**) centroid signal (*left*) and (**b, d**) peak shift (*right*) for two annealing cycles (first run *top*, second run *bottom*)

same conditions (heated to 453 K under *Ar* flow for 21 h). A similar experiment was performed on a blank reference sample for comparison.

Both annealing cycles are shown in Fig. 5.15 (first run top, second run bottom) as a centroid and as peak signal along with the temperature. For the first run no significant shift during the entire experiment for the selected Pt_{68} can be observed. However, for both the sample with two selected sizes Pt_{22+68} as well as the unselected clusters $Pt_{n \geq 53}$ a decrease in peak and centroid over the course of the measurement is visible. Analysis of the position during the course of the experiment, shows that the LSPR shift is fast in the beginning and then slower towards the end of the experiment, the extent of the shift is slightly smaller for the sample with the mixed sizes. The observation of a LSPR peak shifts towards shorter wavelengths is (as above in the step wise heating experiment) an indication, that these cluster samples undergo sintering. In the second run of all experiments only a small red shift of the signal, attributed to a slight drift in the experimental setup, is observed. This indicates that further sintering will not occur at a temperature of 453 K.

In order to understand the changes in LSPR on the INPS chip on a local level, TEM windows with a Si_3N_4 support were prepared with the same amount and size

of clusters. These TEM samples were run in parallel with the first run of the optical measurements and thus exposed to the same gas and temperature conditions as the INPS samples. The measurements of the samples were performed *post mortem* at the CEN/DTU using **STEM**. As in Sect. 5.1.1 described, the obtained micrographs of different positions are analyzed for particle size (ADF), number density and surface coverage. Preliminary results of this analysis with respect to the PSD are shown in Fig. 5.16, the underlying TEM micrographs are not explicitly shown. The histograms are compared to the initial state of the samples and interpreted in the sense of the argumentation given in Sect. 2.3.2.

Before the heat treatment, the shape of the obtained ADF for the **unselected** sample resembles the one from the $Pt_{n \geq 36}$ in Sect. 5.1.1 and could be fitted using a log normal function. Because of a minimum size of 53 atoms for $Pt_{n \geq 53}$ (with the QMS as a ion guide with a high pass filter) the area ranges from $\sim$1.0 to 4 nm^2 with a peak maximum at $\sim$1.5 nm^2. Upon heating the distribution shifts to larger areas, thus a decrease in counted particles with areas in the range of $\sim$1–2 nm^2 and an increase in the $\sim$3.5–5 nm^2 is apparent and the peak maximum shifts to $\sim$2.0 nm^2. This observation is illustrated further by the fact that the distribution resembles less a log normal distribution and comparing the integration curves before and after treatment [38]. The results of the PSD (peak shift) support the outcome of the INPS experiments and suggest a Ostwald ripening of the unselected clusters where the larger clusters grow at the expense of smaller ones. Looking at the ADF (missing sharp decrease of the distribution) it is obvious that this sintering is not completed at 453 K and thus higher temperatures will induce further sintering.

The ADF of the **mixed** sample with both Pt_{22} and Pt_{68} shows two peaks corresponding to cluster ensembles of those distinct sizes. The 1:1 ratio of the two sizes is reflected in two humps in the integration in between 40–50 and 90–100 %. The position of the peak maxima is slightly off, compared to the results from Sect. 5.1.1. This, however could be explained by different threshold values necessary for the simultaneous detection of two sizes and too low number of counts considering two sizes. After heating the sample, changes in the distribution are visible, the distinct peaks disappear and two interesting features are revealed. First, particles with very small area appear and could be a sign of an intermediate step in an Ostwald ripening process, where the smaller selected size is about to disappear due to the loss of atoms. Second, an Ostwald ripening would, as seen for the unselected sample, result in larger particles. However, a slight decrease in size compared to the initial sample is observed. Further measurements and/or a better statistics are necessary in order to explain this discrepancy. As for the unselected sample, it is likely that the temperature of 453 K only resulted in a partial sintering and thus the obtained results are characterizing one particular, intermediate step of the complete sintering process. Consequently, heating at higher temperatures is expected to give different and most probably results that differ more drastically from the initial state. In comparison to the unselected samples the changes in the PSD are less pronounced and thus also support the different shifts observed in the INPS experiments.

Last, for the **selected** Pt_{68} sample one peak corresponding to one selected size is seen in the histogram, the peak maximum at $\sim$1.1 nm^2 fits the previous statistics
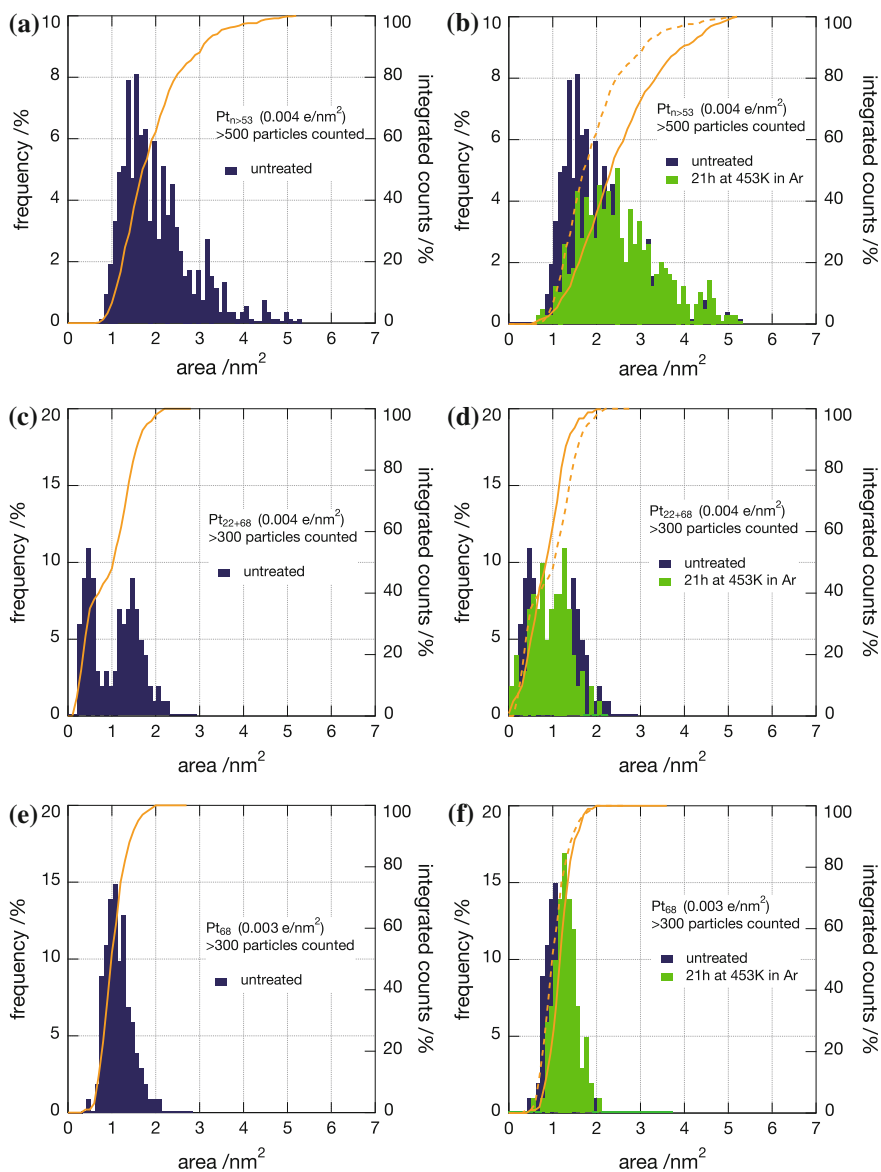
Fig. 5.16 Corresponding ADF histograms to the TEM samples treated in a similar way as the INPS samples in Fig. 5.15. The PSD on the *left* (**a, c, e**) represent the initial areas (*blue*) observed for the samples along with the integrated counts. The histograms on the right (**b, d, f**) show additionally the ADF for the samples heated to 453 K for 21 h under an *Ar* (*green*). For a better comparison, the PSD and integrations (*dashed lines*) of the initial state are shown as well. From *top* to *bottom*, $Pt_{n \geq 53}$, Pt_{22+68} and Pt_{68} are depicted

at that size (Sect. 5.1.1). Almost no changes in the particle distribution after the sintering are apparent in both the ADF and the integration, thus in agreement with the ETEM results for Pt_{46}, also Pt_{68} does not sinter at temperatures as high as 453 K. The results further fit the observations from the INPS, where no significant change in peak position was apparent. A possible explanation for this behavior might be the presence of identical particles with respect to the number of atoms. None of the present particles has an interest in loosing one atom as they are all just the same and thus are considerably more stable than the mixed or the unselected samples. Again, further heating might also sinter these particles; more experiments at elevated temperatures are part of ongoing work.

Discussion and comparison to literature—In the last years, fostered by the development and availability of *in situ* techniques to probe sintering [43], an increasing interest in the thermal stability of supported particles is reflected in the literature. For small *Pt* particles (2–8 nm in size) the Ostwald ripening mechanism was observed in ETEM under near atmospheric air pressures [36, 37, 44].

Further experiments under similar atmosphere, using TEM after treatment, support this observation [45]. However, these studies are hardly comparable with respect to the size of the clusters used in this work as *in situ* sintering experiments for smaller particles suggest a stability for $\sim$0.5 nm sized *Pt* particles [32]. Thus, considering the precise size selection down to a single atom, the conducted experiments are one of a kind to the best of the authors knowledge.

Summary—Using INPS in combination with STEM as a new approach in order to study size-selected clusters under *in situ* conditions has revealed interesting preliminary observations with respect to stability. The feasibility, i.e. an high enough sensitivity of the INPS technique towards the study of small clusters with sufficiently low surface coverage (as low as $0.003\,e/nm^2$) to avoid cluster aggregate formation, is confirmed. Further a change in plasmon peak position is observed for unselected samples as well as a sample of two mixed selected cluster sizes, whereas the signal of the selected sample stays stable over the heating at 453 K for 21 h under *Ar* atmosphere. The results of apparent changes in the unselected and mixed samples are corroborated by STEM micrographs and their respective PSD analysis before and after treatment. For $Pt_{n\geq53}$ and Pt_{22+68} the ADF changes and suggest an Ostwald ripening sintering mechanism, that is, however not complete at 453 K. In contrast to Pt_{68}, where the analysis of the STEM micrographs results in clusters with similar size also after the heat treatment—in agreement with ETEM measurements on SiO_2 for Pt_{46}.

In the future, experiments at higher temperatures, as well as under reactive gas atmosphere (H_2 or CO) and/or oxidative (O_2) are planned to further understand the stability of selected clusters. Also, support effects will be addressed as samples on Si_3N_4 and SiO_2 were prepared and are scheduled for measurements.

The particular use of the INPS platform is given by its applicability for *in situ* measurements, while still having a sensitivity suitable to probe changes in small catalyst amounts. Also, reactivity of the clusters will be probed by means of INPS, hereby being a complementary approach to other ambient condition measurements to probe cluster materials.

5.3 μ-Reactors

Within this section, first results on the reactivity of size-selected clusters, measured in gas phase μ-reactors are presented. For each size a coverage of 0.058 e/nm^2 Pt_x ($x = 8, 10, 20, 22, 34, 46$ and 68) was deposited into second generation μ-reactors and subsequently sealed at TUM using anionic bonding (Sect. 3.3.5). Note, that the use of second gen. reactors might lead to temperature gradients over the reactor area, thus overestimate the temperature by as much as 25 K. At DTU/CINF these reactors were attached to the measurement setup and the reactivity of the clusters for CO oxidation, under steady-state reaction conditions was measured as a function of temperature, along with titration for determining the active area [46]. Additionally, larger Pt particles with an average size of 9 nm (comparable coverage to the clusters) and a Pt thin film (1 % surface area of the reactor cavity) were also analyzed and serve as comparison for the clusters.

An overview of a **measurement protocol** is depicted in Fig. 5.17a, showing the temperature, as well as the gas flows (He, O_2 and CO) as a function of time; the corresponding text file can be found in the appendix. Over the course of the measurement area measurements (Fig. 5.17b, flat temperature signals) take turns with reactivity measurements (Fig. 5.17c, temperature ramps). This allows for monitoring possible changes in surface area along with reactivity measurements at different temperatures. The maximum temperature of 513 K has been measured only for some samples and is also not shown in the overview; the different area measurements are numbered consecutively.

For the **area measurements**, in order to determine the amount of active sites via titration, the sample is heated to 343 K and purged with O_2 at 0.25 bar for 10 min in order to saturate all free adsorption sites. After a waiting time of 25 min during which the reactor is pumped, it is flushed with 1 bar He for 10 min, both serve to eliminate all O_2 not adsorbed on active sites. Last, 1 bar of CO is dosed for 20 min and the CO_2 signal in the QMS (44 m/z) is recorded and is a good measure for the active/adsorption sites available. The protocol of two subsequent area measurements (7,8) is shown in Fig. 5.17b. The temperature of 343 K is a compromise for faster conversion of the adsorbed *oxygen* at elevated temperatures and a still relatively low temperature to avoid sintering processes [47]. In the beginning of the overall procedure a step wise increase in temperature for the first three measurements (1–3) is shown, a simple precaution in order heat the sample slowly.

An excerpt of the protocol for a **reactivity measurement** up to 413 K is depicted in Fig. 5.17c. A gas flow of a 4:1 mixture of O_2 and CO is dosed into the reactor (total pressure of $\sim$1 bar) and a 45 min waiting time allows the gas flow to stabilize. Subsequently the temperature is increased with a ramp of $\sim$2 K/s, in the shown case up to 413 K and afterwards cooled down at the same speed. When reaching almost room temperature, the gas flow gets turned off and the reactor is pumped empty. Over the course of the complete measurement procedure, the temperature maximum of the ramp is constantly increased—the lowest temperature being 353 K and the highest
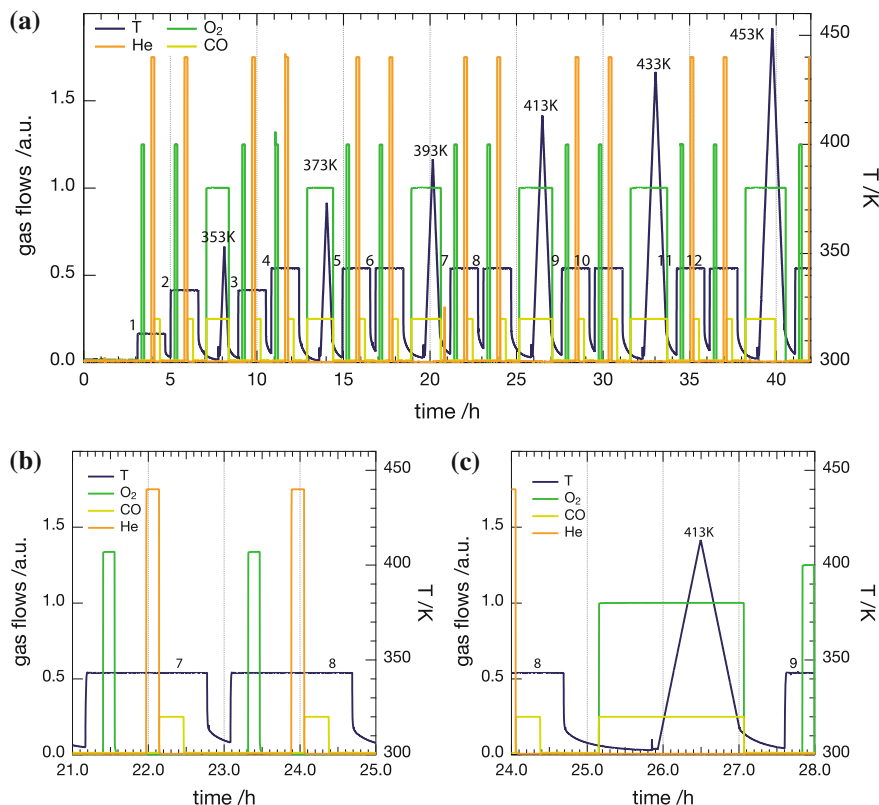
Fig. 5.17 μ-reactor measurement protocol for *CO* oxidation measurements. An overview (**a**) shows temperature, the different gas flows (*He*, O_2 and *CO*) as a function of the time. The smaller excerpts depict two cycles of an area measurement (**b**) and a cycle for an reactivity ramp (**c**)

513 K (not shown in Fig. 5.17a). After each reactivity measurement, the surface area is determined twice, to track possible changes.

The **results** of a representative set of area measurements of Pt_{68} is shown in Fig. 5.18a. For the first eight runs, no area can be measured and is probably related to contamination of the particles. With increasing temperatures for the reactivity measurements (i.e. 413, 433 and 453 K) the clusters get subsequently 'cleaner' and thus for runs 10, 12 and 14 an increasing area/number of active sites is reflected in the increasing peak signals. Surprisingly, only the second of the two measurements at higher temperatures shows a signal, a possible explanation for this behavior might be oxidation of the clusters during the activity ramp. The maximum area for different sizes obtained so far, along with the 9 nm particles and the *Pt* thin film are shown in Fig. 5.18b. Unfortunately, the spectra shown in this graph are not comparable, since for different sizes the maximal temperature of the corresponding reactivity ramp differs. Further, the signals shown are not calibrated with respect to the QMS,
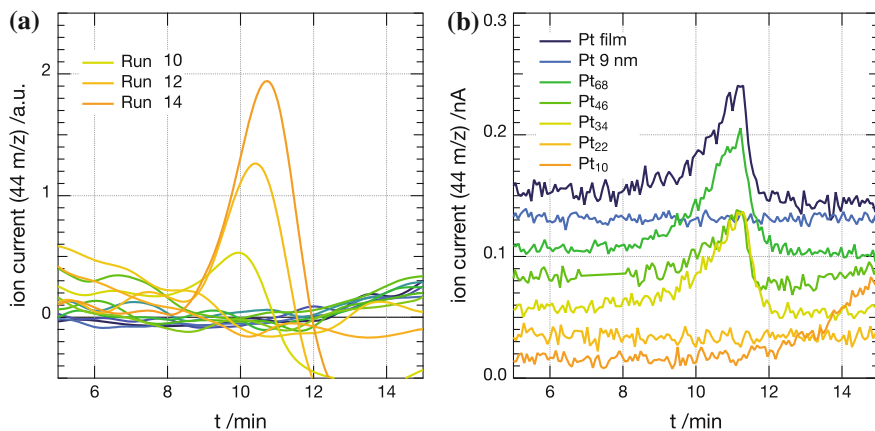
Fig. 5.18 Area measurements of Pt_{68} during a measurement up to 453 K, only the runs 10, 12, 14 show a signal (smoothed) and are labeled in the legend (**a**). Representative maximum areas, after measurement (up to 453 K), for different sizes along with larger particles and the thin film (**b**)

thus lack comparability in terms of signal intensities. Nevertheless, for sizes with a 'light off' at lower temperatures (see below) an area signal is detectable and proves the feasibility of this methods. Also, a deactivation or sintering of the particles in the studied size range can be ruled out, as this would require a decrease in peak area with increasing temperature. This is in good agreement with the results on the particle stability on comparable support in the previous section. Additional titration experiments in connection with reactivity measurements at higher temperatures are ongoing.

For Pt_{46} a data set of CO_2 production as a function of temperature with increasing temperature ramp is presented in Fig. 5.19a. With increasing number of runs, i.e. stepwise increase in temperature ramp the ion signal increases and for run 4 (heating to 493 K) a complete light off curve (Sect. 2.1.1) is visible with a full conversion from 480 K on. Further, going down in temperature an increase in reactivity of the system can be observed and the typical hysteresis curve. For all runs beyond 480 K the observed curves deviate only little from each other and show the reproducibility of the measurement. This reproducibility is also illustrated by an additional curve (2b) of a repeat experiment that fits well to the trend. The same observation also holds true for two different reactors, with the same coverage and cluster size, however is not explicitly shown here. For run 7 up from 540 K on an abrupt decrease in reactivity is visible and could be a indication for catalyst deactivation by sintering—lowering the temperatures the reactivity observed is slightly higher. This behavior could not be reproduced using a second reactor at the same size and is thus questionable and might be explained by a different temperature, due to the high error in the temperature read out.

In Fig. 5.19b the last runs (highest temperatures) are shown for Pt_x (x = 10, 22, 34, 46, 68) and 9 nm particles as well as a Pt thin film. Different light off temperatures and consequently different hysteresis curves are observed for the dif-
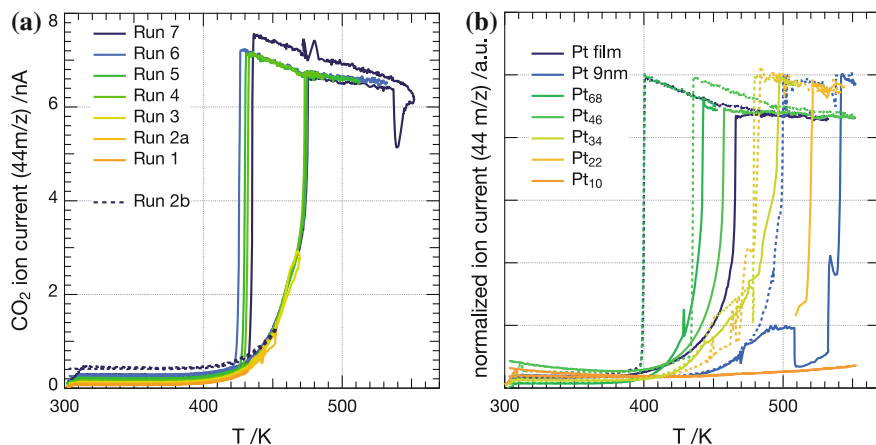
Fig. 5.19 μ-Reactor reactivity measurement on Pt_{46}, Pt_x, Pt_{9nm} and Pt_{film}. Increasing temperature ramps/runs with a maximum of 535 K (**a**); run 2a and a corresponding run 2b of a repeat experiment show the reproducibility of the measurement for Pt_{46}. Normalized runs (for comparability) at maximum temperature for Pt_x, Pt_{9nm} and Pt_{film} (**b**). The part with increasing temperature is depicted with a drawn trough *line*, the cooling ramp with a *dashed line*

ferent samples. The smallest size Pt_{10} does not yet show a light off or full conversion, however the increasing slope is a sign for reactivity of this sample at higher temperatures. Except for the 9 nm particles a lower light off temperature with increasing cluster size can be observed, for Pt_{68} the reactivity resembles the one of the thin film. Further, for Pt_{68} and Pt_{46} a lower light off temperature compared to larger particles and the thin film evidences a higher reactivity of those sizes.

The trends of the **light off** temperatures and **hysteresis** are summarized in Fig. 5.20a as a function of size. For all samples a similar trend between light off and hysteresis temperature is observed, where the later is usually by about ~50–70 K lower, due to the mentioned reasons (Sect. 2.1.1). With increasing cluster size a decrease in both temperatures can be seen and converges towards the values for the *Pt* thin film, with Pt_{68}. The observed high temperature for the larger (9 nm) particles (~545 K), does not agree with results from the literature (~443 K) for similar sized particles [48].

Additionally, in Fig. 5.20b the reactivity (ion current signal of the QMS) of the samples as a function of number of atoms per clusters is plotted for three different temperatures. As general trend, an increase in temperature and/or cluster size results in a higher reactivity. Remeasured samples, as well as two samples of the same type are included in this plot and follow this trend. A tendency towards higher performance of Pt_{46} is observed, however further measurements are necessary in order to clarify this particular reactivity. Further, it is noteworthy that the larger clusters exceed the reactivity of the thin film at 433 K, yet a calibration of the QMS signals is needed to validate this result.
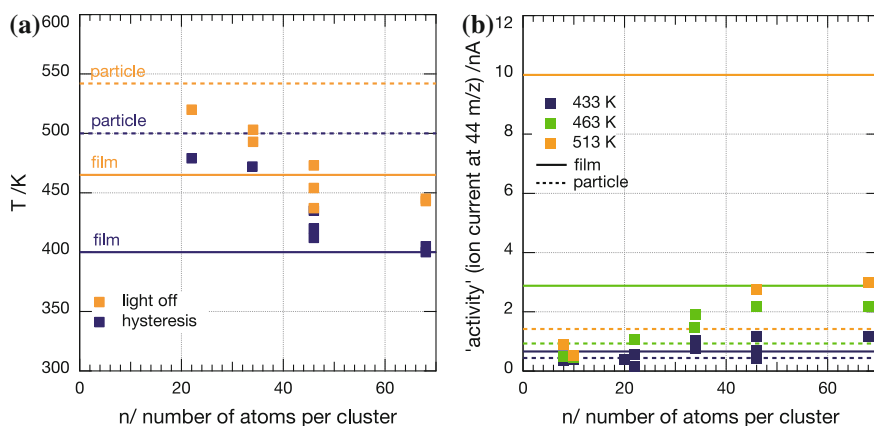
Fig. 5.20 Light off, hysteresis and reactivity for Pt_x, Pt_{9nm} and Pt_{film}. The light off temperature (*blue*) and the corresponding hysteresis temperature (*yellow*) (**a**) and the reactivity for three temperatures (**b**) as a function of size. For comparison the results of the larger particles (*dashed lines*) and the thin film (*drawn trough lines*) are shown

For the graphs in Fig. 5.19 the raw results[7] were plotted in corresponding ***Arrhenius plots***. In Fig. 5.21a different runs show a similar and reproducible Arrhenius behavior over a large temperature regime. Comparing different sizes at their highest temperatures, in Fig. 5.21b different slopes in the Arrhenius plots are apparent and the Arrhenius behavior stretches over a large temperature regime. For the 9 nm sample and Pt_{10} two regions with different slopes can be seen, these are most likely artifacts due to a failure in the temperature read out. Consequently for the determination of the activation energies (see below) these regions were omitted and the Arrhenius fit was performed in the area indicated by the two arrows.

From the slopes of the fits to the Arrhenius plots the **activation energy** was calculated and the results as a function of cluster size is shown in Fig. 5.22b. For larger sizes, the obtained data points reveal a comparable activation energy of 1.0–1.1 eV within the range of the shown error and converge to the value for the thin film with increasing size. For smaller clusters a tendency towards higher activation energies is visible and for Pt_{10} a value of 1.3 eV is reached. This observation is however based on a single data point and further misses data at high temperatures with full conversion, thus needs to be reproduced at higher temperatures for validation. As for the reactivity and the light off values (Fig. 5.20) the activation energy for the 9 nm particles does not fit the overall trend as it is too high, also here additional measurements are necessary.

In Table 5.3 the obtained data is listed with results from *CO* oxidation for comparable systems in the literature. From UHV studies on *Pt*(111), as well as previous μ-reactor measurement on thin films, the value for the activation energy of *Pt*

---

[7] In order to make the results comparable, a background correction is necessary [47], however this is for the presented data omitted. Thus, the obtained raw data is rather discussed for trends.
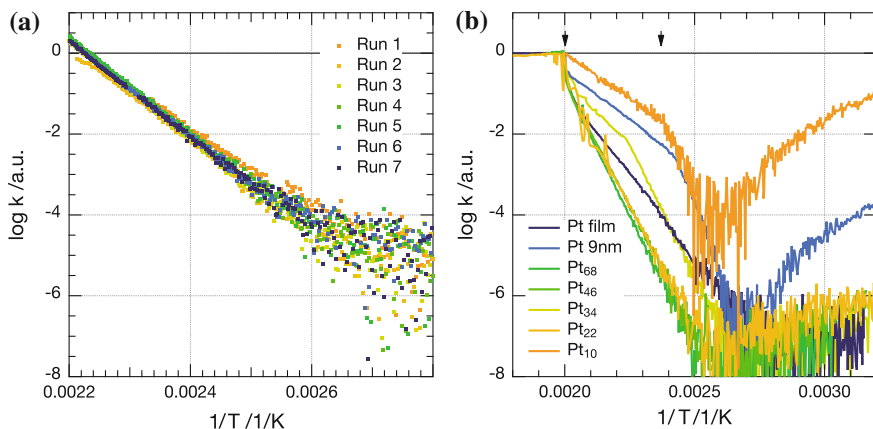
Fig. 5.21 Arrhenius plots for the reactivity measurements shown in Fig. 5.19 for Pt_{46}, Pt_x, Pt_{9nm} and Pt_{film}. Arrhenius plots of different runs with increasing T for Pt_{46} (**a**) and for the highest reactivity of Pt_x, Pt_{9nm} and Pt_{film} (**b**). For better comparability all *curves* have been shifted to the same origin (**a**, **b**) and two *arrows* indicate the region used for the fit (**b**)

Table 5.3 Comparison of activation energies for *CO* oxidation on *Pt* with values from the literature

	Size	Support	Activation energy /eV	/kJ/mol
Campbell et al. [49]	*Pt*(111)	(UHV)	1.0	101
Jensen *PhD Thesis* [47]	Thin film	–	1.2 ± 0.1	115 ± 10
McClure et al. [11, 12]	2.5–4.2 nm	SiO_2	~1.1	~110
Allian et al. [50]	1.2–20 nm	Al_2O_3	0.9 ± 0.1	84 ± 6
Watanabe et al. [9]	Pt_x ($x = 8$–10)	TiO_2	0.7 ± 0.1	65 ± 5
	Pt_x ($x = 4$–7)	TiO_2	0.9 ± 0.1	88 ± 4
This work	Pt_x ($x = 46, 68$)	SiO_2	1.0 ± 0.1	96 ± 8
	Pt_x ($x = 20, 34$)	SiO_2	1.1 ± 0.2	106 ± 14
	Pt_x ($x = 10$)	SiO_2	1.3 ± 0.1	126 ± 9

esurfaces indicate a too small value obtained for the thin film [47, 49]. And, as mentioned, a too high one for the larger particles, independent of the measurement conditions. In light of this observation, the obtained values for the clusters have a tendency towards lower activation energies. This is in agreement when comparing to supported particles, which also show a decrease in activation energy with size, for particles below ~1 nm [11, 12, 50]. Size-selected systems follow this trend until for clusters with less then eight atoms an increase in activation energy can be measured [9]. Considering a different measurement approach and support material, this supports the unexpectedly high value for Pt_{10} in the data set but also the observed decrease for Pt_{20}, Pt_{22} and Pt_{34}. The authors discuss this observation together with XPS data, as results of the transformation from 2 to 3 D clusters.
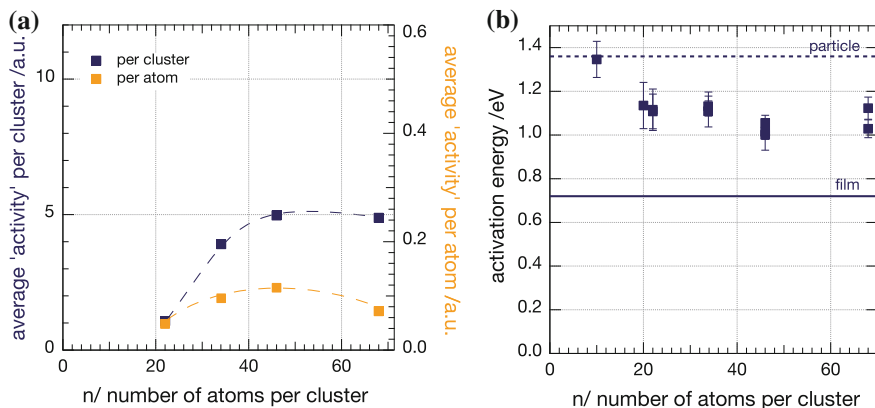
Fig. 5.22 Average reactivity at full conversion (**a**) and activation energies (**b**) for Pt_x as a function of cluster size, for comparison the results of the larger particles (*dashed lines*) and the thin film (*drawn trough lines*) are also shown. An indicated error for the activation energies (**b**) is based on the standard deviation of multiple measurements at the same cluster size; for larger particles and the thin film a similar error holds, is however not explicitly shown. The average reactivity is displayed per cluster (*blue*) and per cluster atom (*orange*); the *dashed lines* serve as a guide to the eye

Summary—The obtained results, the reactivity measurements in μ-reactor, show the feasibility of measuring high surface area model catalyst, consisting of only a few atoms under ambient conditions up to 1 bar. From titration experiments an increasing area after CO oxidation is an indication, that supports stability of such catalysts to temperatures as high as 513 K. However, more measurements, with higher coverages and a consequently larger signals, are necessary to understand the observations made up to date.

Reactivity measurements under steady state conditions as a function of temperature, evidence reactivity of all sizes (except Pt_{10}, due to still missing measurements at higher temperatures). The results obtained show the known light off curves with a hysteresis and are in agreement with the literature. For larger sizes the temperature for full conversion is even lower than for a Pt thin film measured under similar conditions. The average reactivity of multiple measurements for different sizes as a function of cluster and cluster atom is shown in Fig. 5.22a and illustrates the general trend of increasing reactivity with size. However, for Pt_{46} multiple data points show a reactivity comparable to Pt_{68}, revealing a particular high reactivity for this size, this is further illustrated by the reactivity per atom. A slight decrease in the activation energy of Pt_{46} compared to Pt_{68} supports this observation. In order to better understand this, additional measurements are ongoing.

Further, the data of the reactivity was used for Arrhenius plots and extraction of activation energies. The plots show a large temperature range with Arrhenius like behavior and values for activation energy could be extracted (Fig. 5.22b). The obtained activation energies are in the correct order of magnitude when compared to literature values. The data obtained so far suggest a higher activation energy for

very small systems (i.e. Pt_{10}) that might be related to a 2 D structure compared to 3 D structures for larger clusters, a concept previously suggested in the literature [9]. Larger clusters show then a rather structure insensitive behavior, but need further experimental proof, too.

All together the results from the μ-reactors as a platform to test the reactivity of size-selected cluster materials under applied conditions has a high potential to shed light onto the open question of size dependent reactivity. The ongoing measurements of the *CO* oxidation reaction have the potential to contribute to the understanding of the controversial discussion of the structure in/sensitivity of the reaction for small particles.

5.4 Photo Catalysis (Photocat)

In this section the results of the preparation of a hybrid noble metal cluster deco-rated semiconductor photocatalyst material under UHV conditions with independent control of cluster coverage and size are presented. This includes (S)TEM analysis, evaluation and discussion of the *hydrogen* evolution results for different coverages and sizes and concludes with comparison to results from the literature.

5.4.1 (S)TEM Characterization

TEM micrographs taken after the spin coating and deposition procedure are shown in Fig. 5.23. The micrograph in Fig. 5.23a (12k-fold magnification) gives a first impres-sion about the length, diameter and the assembling behavior of the *CdS* NRs. The rods cross randomly in various directions and groups of ordered structures are observed, each consisting of several NRs situated parallel to each other. The structure of the rods appears not to be stiff, since to some extent bent rods are visible.

At higher magnifications of $30k$, as shown in Fig. 5.23b, one can additionally get an impression of the diameter of the NRs which is observed to be in the range of 3–5 nm. Single NRs exhibit only slight changes in diameter along their entire length which could indicate that the rod diameter is mainly determined by the initial size of the growing rod nuclei. In addition *Pt* clusters deposited on the NRs are visible as small dark spots.

Micrographs from **HAADF-STEM** measurements, taken of the as prepared sam-ples are shown in Fig. 5.24 (different coverages) and Fig. 5.25 (different sizes). In Fig. 5.24 the representative $40 \times 40 \, \text{nm}^2$ excerpts show for unselected (a) and size-selected *Pt* clusters (c) the same and in (e) twice the amount of **clusters cover-ages** on the *CdS* NR thin films. This can be observed for the coverage on, as well as adjacent to the NRs. In micrographs with higher magnification (size $10 \times 10 \, \text{nm}^2$), *Pt* clusters with different sizes for the unselected $Pt_{n \geq 36}$ (b) and only one size for both size-selected Pt_{46} (d, f) samples is observed. The overall number of clusters
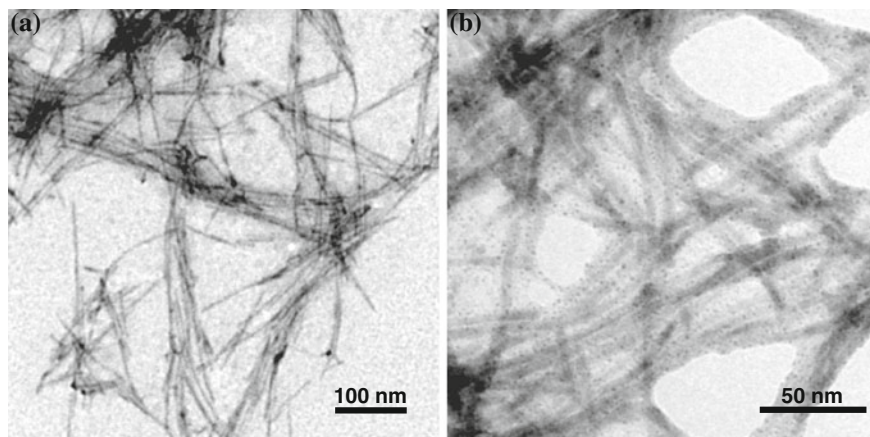
Fig. 5.23 Representative TEM images of the as prepared samples taken at low magnifications. Overview of the structure and assembling behavior of *CdS* NRs (**a**); *CdS* NRs decorated with Pt clusters (**b**)

displayed coincides with the measured cluster coverages ($0.04\,e/nm^2$ and $0.07\,e/nm^2$, respectively) from integrating the neutralization current over time. Sections of single NRs decorated with *Pt* clusters at atomic resolution are also visible on these high resolution images (b, d, f). Individual atomic rows constituting the NRs oriented parallel (b) and perpendicular (f) to the rod length can be resolved; equally, single atoms of *Pt* clusters are visible.

In Fig. 5.25 for the five prepared **cluster sizes** $Pt_x (x = 8, 22, 34, 46, 68)$, all $0.04\,e/nm^2$ coverage, representative $40 \times 40\,nm^2$ and $10 \times 10\,nm^2$ excerpts are shown. All micrographs show similar coverage, corresponding to the expected deposited coverage. Clearly, for different sized clusters the observed size is different and decreases towards smaller clusters, particularly visible in the $10 \times 10\,nm^2$ images. However, different clusters in the same image appear uniform in size, which confirms the mono dispersion of the samples due to size selection and soft-landing. As previously, atomic rows constituting the NRs are partially resolved and single atoms of *Pt* clusters are visible.

For statistics of the rod length seven images with magnifications similar to Fig. 5.23a were taken. The **length distribution** of the NRs in theses images (318 single NRs and $3.3\,\mu m$ total rod length measured) is shown in Fig. 5.26b. The observed distribution is quite broad, ranging from short NRs (about 30 nm) to maximum lengths of 290 nm. The small fraction of 30 nm NRs is likely to be caused by fragmentation from the synthesis procedure. The majority of NRs measured have lengths in the range of 70–170 nm, resulting in an average length, according to this distribution, of 103 nm. This mean value[8] is taken in combination with the cluster count as a basis for the calculation of the cluster coverage in the unit *cluster/NR*.

---

[8] For the calculation of cluster coverage on the NRs the diameter of each single NR included in the statistics is measured and further assumed to be constant along the (average) rod length.
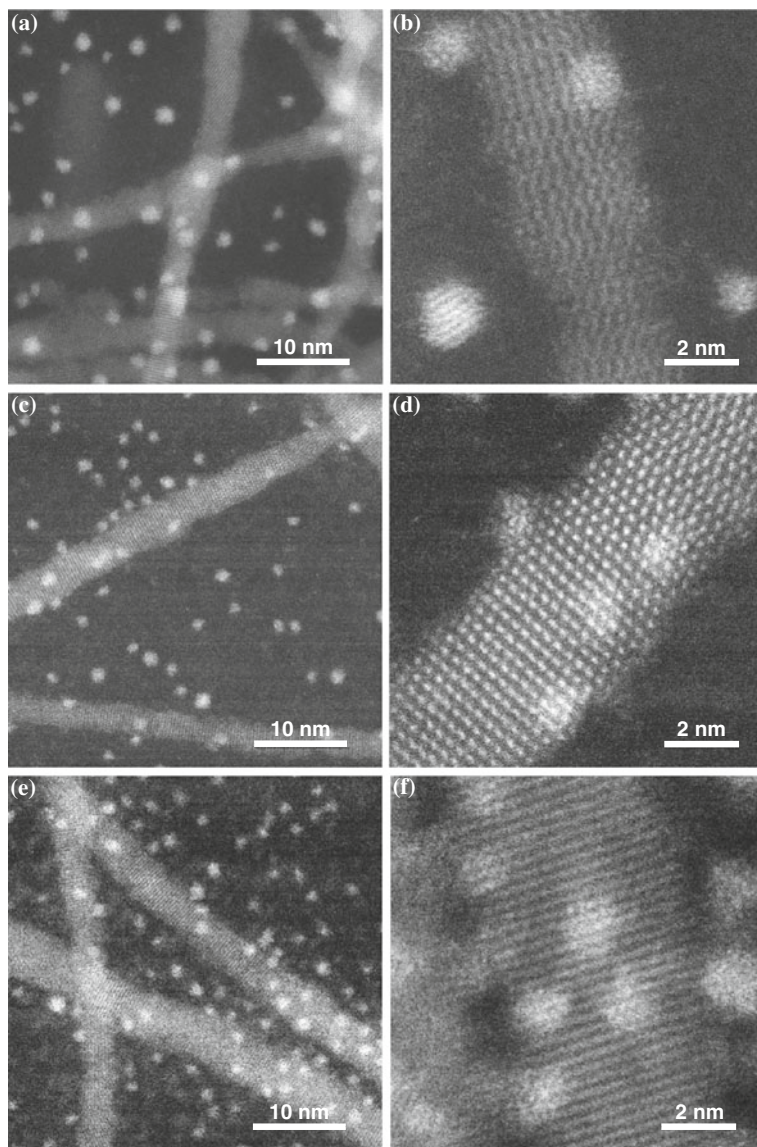
Fig. 5.24 HAADF-STEM micrographs ($40 \times 40\,nm^2$ – a,c,e and $10 \times 10\,nm^2$ – b,d,f) of unselected $Pt_{n \geq 36}$ ($0.04\,e/nm^2$ – a,b) and two different coverages ($0.04\,e/nm^2$ – c,d, $0.07\,e/nm^2$ – e,f) of size-selected Pt_{46} clusters deposited onto CdS NR thin films. For $Pt_{n \geq 36}$ different sizes can be observed, whereas for Pt_{46} the size of the clusters is the same. The amount of clusters fit the expected values. Images at high magnification even allow for resolving atomic structure of rod and Pt clusters. (*Reprinted with permission from* [31]—*Copyright (2012) American Chemical Society*)
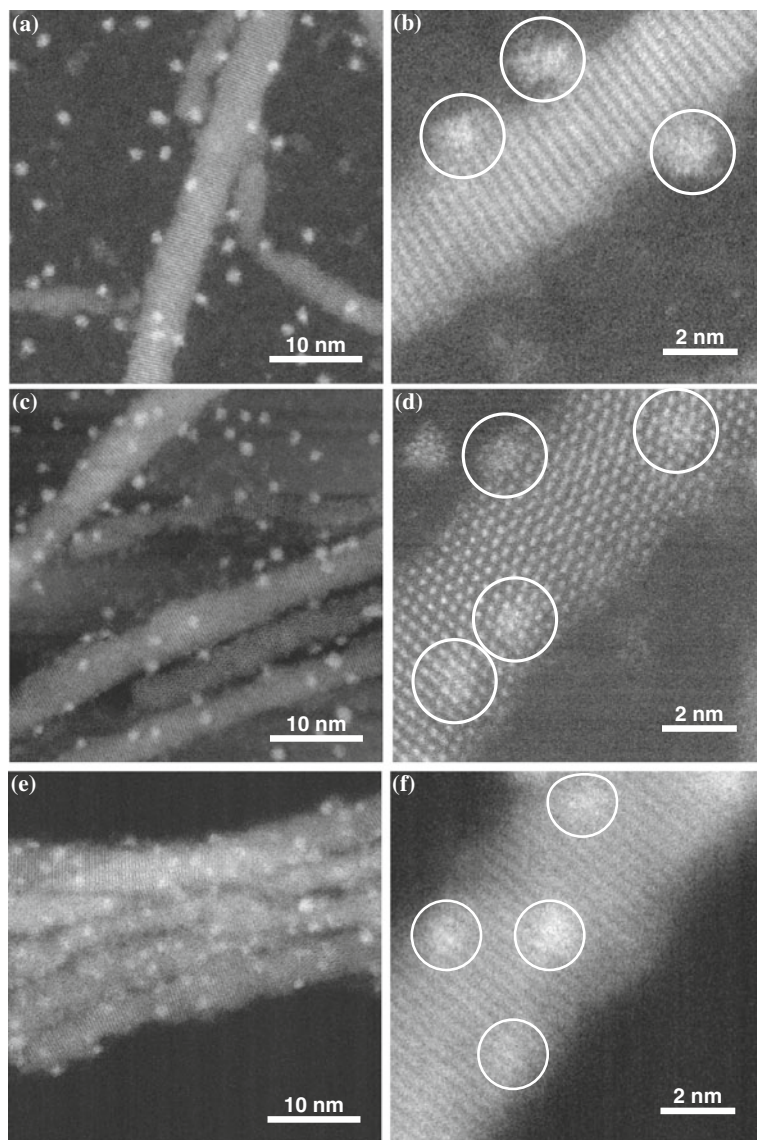
Fig. 5.25 HAADF-STEM micrographs ($40 \times 40\,\text{nm}^2$ — a,c,e,g,i and $10 \times 10\,\text{nm}^2$ — b,d,f,h,j) of size-selected $Pt_x (x = 8 - i, j, 22 - g, h, 34 - e, f, 46 - c, d, 68 - a, b)$ clusters deposited onto CdS NR thin films at a coverage of $0.04\,\text{e/nm}^2$. The amount of clusters fit the expected values and for different sizes the cluster size in the image vary accordingly. Images at high magnification even allow for resolving atomic structure of rod and Pt clusters. For better visibility clusters in the $10 \times 10\,\text{nm}^2$ excerpts are marked by *white circles* [31] *Reprinted with permission from* [31]—*Copyright (2013) American Chemical Society*
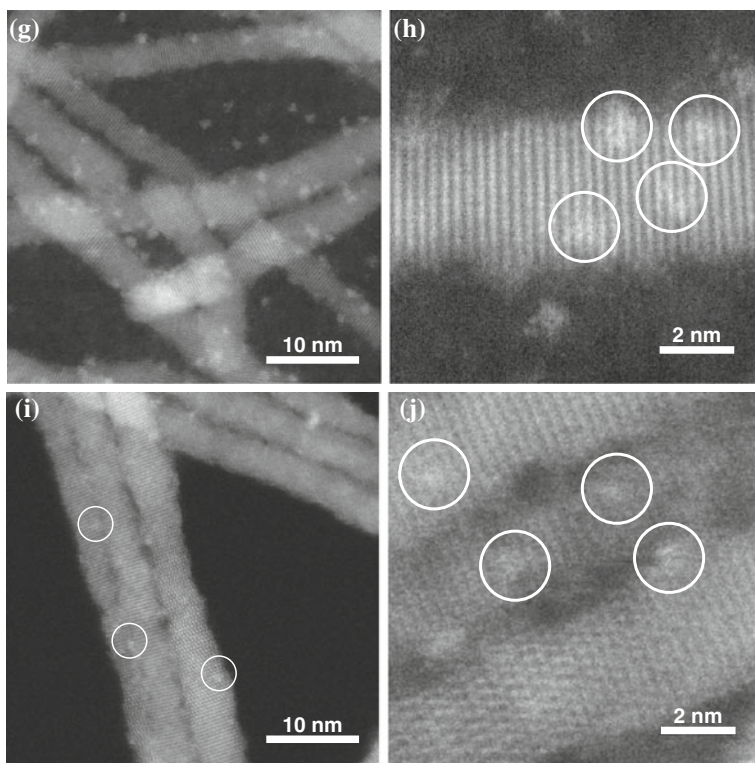
Fig. 5.25 (continued)

The **cluster coverage** on the projected areas of *CdS* NRs is determined for four different samples (0.04 e/nm^2 $Pt_{n \geq 36}$, 0.04 e/nm^2 Pt_{22}, 0.04 e/nm^2 Pt_{46} and 0.07 e/nm^2 Pt_{46}) an the combined results are presented in Fig. 5.26c. The cluster coverage (for clusters of similar size) on pristine carbon support (left axis, blue bars) and the corresponding cluster coverage on CdS NRs (right axis, green bars) are plotted versus the expected cluster coverage from integral measurement of cluster current during deposition. The error bars are based on the variations of cluster coverage met in the evaluation of single (at least five) STEM micrographs used in these measurements.

As denoted earlier (Sect. 5.1.1) the values for the overall cluster coverage on graphite support obtained from particle count agree well with the expectation from cluster current measurements. Similar coverage values for nominally identical Pt_{22} and Pt_{46} samples are obtained, demonstrating independent control over cluster coverage and size. For all four samples the coverage on the NRs is slightly higher than the coverage on the graphite support, however within the error ranges of each other. This observation of higher coverages on NRs can be explained in terms of the fact that the projected NR area is underestimated as adjunct clusters at the edge of the NRs are also included in the coverage measurement on the NRs.
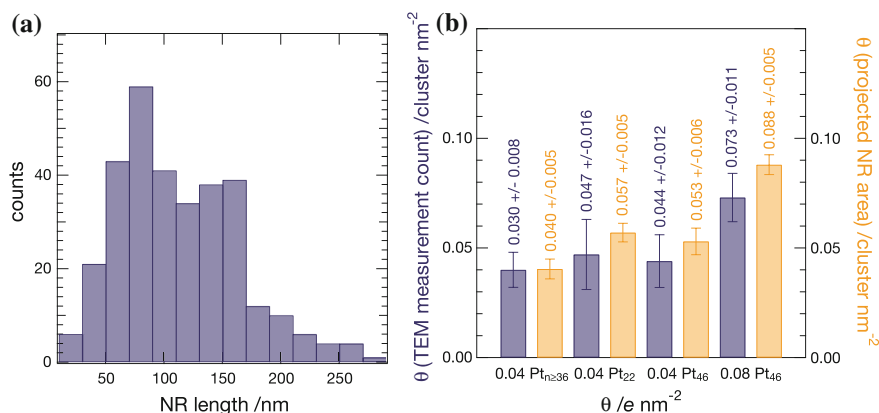
Fig. 5.26 Length (**a**) and coverage (**b**) distribution of the prepared hybrid catalysts. Length distribution of synthesized CdS NRs (**a**). Rod lengths are measured from a series of TEM images with low magnification (similar to Fig. 5.23a). Comparison of cluster coverages on graphite support and on CdS NRs (**b**). For four different samples ($Pt_{\geq 36}$, Pt_{22}, Pt_{46} and Pt_{46}) the number of clusters found on the bare graphite support (*left axis, blue bars*) and their number on the projected NR area (*right axis, yellow bars*) are plotted versus the *bottom axis* showing the amount obtained by integrating cluster current during deposition. The errors result from variation of the counted numbers within the different STEM micrographs used

Cluster coverages on bare graphite support and on CdS NRs are linearly related. Thus, the three values obtained for the two size-selected samples Pt_{22} (0.04 e/nm^2) and Pt_{46} 0.04 e/nm^2 and 0.07 e/nm^2) are used to linearly correlate between the units e/nm^2 and *cluster/NR* in the graphs of the following sections.

5.4.2 Coverage Dependent Reactivity

Time dependent *hydrogen* evolution upon photo-irradiation of some samples with different coverages of unselected $Pt_{n \geq 36}$, and selected Pt_{46} on *CdS* NRs is displayed in Fig. 5.27a. Two **blank samples**, unselected clusters without NRs (open triangles) and NR without clusters (not shown) form negligible amounts of *hydrogen* over time. This shows, that Pt clusters greatly enhance the photocatalytic *hydrogen* evolution from *CdS* NRs, this proves that most of the reactivity steams from the clusters on the NRs and only the hybrid system efficiently produces *hydrogen*.

For the hybrid photocatalyst materials a distinct **linear increase** in catalytic activity with time for all samples is observed. The linear trend over time is preserved in the studied time interval (240 min) and thus suggest that the samples are stable over the course of the experiment. The presented unselected sample (at 0.04 e/nm^2) compared to the corresponding selected sample exhibits a slightly higher *hydrogen* yield at this coverage. For this coverage (0.04 e/nm^2), the *hydrogen* production rate is increased

in comparison to the selected samples. We attribute this to the saturation effect, which is reached earlier for the unselected sample (see below), since for all other coverages the activity of the selected clusters is in general higher. For increasing coverage ($0.07\,e/nm^2$) of Pt_{46}, the *hydrogen* yield is larger, for even higher coverage a similar amount of *hydrogen* is generated after 4 h which is within the typical error range of 8 % within these measurements (compare Fig. 5.27b).

From the obtained values for *hydrogen* **evolution** after four hours the generation **per hour** is calculated and shown in Fig. 5.27b as a function of coverage. Each point represents the average *hydrogen* evolution of one sample of either Pt_{22}, Pt_{46} or $Pt_{n\geq36}$. The cluster coverage is plotted on the top axis as the measured overall cluster coverage from particle count on STEM images (see Sect. 5.1) and correlated on the bottom axis to the coverage in terms of the number of *cluster/NR* (see Sect. 5.4.1).

As only small variations for all sample types for similar samples and within the entire cluster coverage regime can be seen, the measurements prove a **reproducible sample preparation** and *hydrogen* measurement procedure. More over, the data points reveal a smooth trend showing an increasing average *hydrogen* production per hour with increasing cluster coverage. Lower *hydrogen* yields are observed for Pt_{22} samples at all coverages compared to bigger sized clusters.
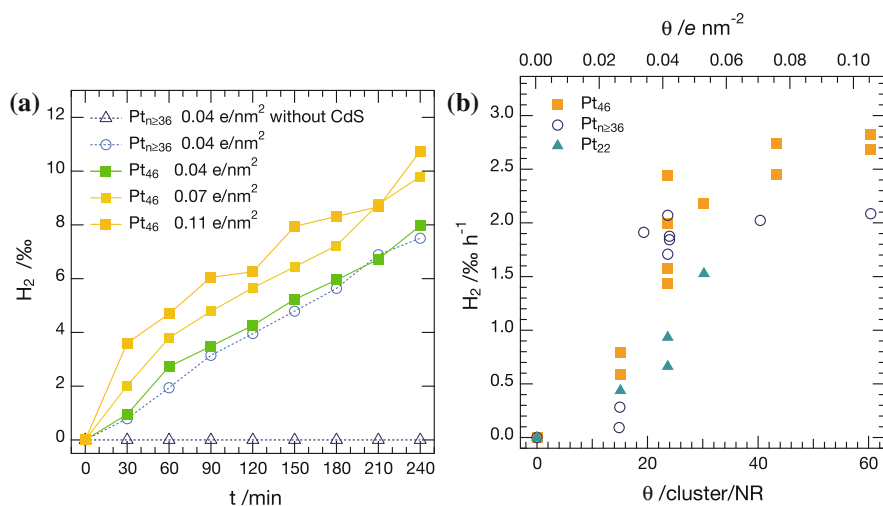

Fig. 5.27 H_2 evolution as a function of time for representative samples (**a**) and for all coverage dependent measurements as H_2 evolution per hour (**b**). In **a** the *hydrogen* generation as function of time for unselected $Pt_{n\geq36}$ (*open circle*) and selected Pt_{46} (*filled squares*) clusters deposited on *CdS* NRs or on blank support (*open triangles*) are shown. Each point represents the total amount of *hydrogen* produced by the sample at that time. The sample without NR shows no photocatalytic activity, whereas all other samples show a linear trend over time. **b** shows the *hydrogen* generation per hour (after 4 h of illumination) for $Pt_{n\geq36}$, Pt_{22} and Pt_{46}. The observed variations demonstrate a highly reproducible measurement and sample preparation procedure. A smooth trend with increasing coverage and reaching of a saturation level (for $Pt_{n\geq36}$ and Pt_{46}) can be seen *Reprinted (adapted) with permission from* [31]—*Copyright (2012) American Chemical Society*

For samples with Pt_{46} and $Pt_{n\geq 36}$ the *hydrogen* evolution eventually reaches a **saturation level** at higher cluster coverages. For the $Pt_{n\geq 36}$ samples this level is reached for coverages higher than $0.04\,e/nm^2$, for Pt_{46} samples above $0.07\,e/nm^2$. The maximum average *hydrogen* production rates are of $2.8 \times 10^{-3}\,H_2/h$ for Pt_{46} and $2.1 \times 10^{-3}\,H_2/h$ for $Pt_{n\geq 36}$. In the investigated coverage regime for Pt_{22} *hydrogen* evolution qualitatively follows the same trend up to a coverage of $0.05\,e/nm^2$. Higher cluster coverages are not investigated, however saturation of *hydrogen* yields upon further increase of cluster coverage as observed for other sample types might be conclusive.

Averaged hydrogen production per hour and the resulting *ML QE*[9] of Pt_{22} and Pt_{46} decorated and $Pt_{n\geq 36}$ as a function of cluster coverage is shown in Fig. 5.28. When considering the *ML QE*, the previous trend is preserved and even more pronounced. Error bars are calculated from standard deviations of multiple measurements on samples with identical coverage (Fig. 5.27b).

The observations can be explained by considering charge-carrier dynamics of such systems [51, 52]. Rapid recombination between photo generated electrons and holes in the absence of *Pt* clusters is assumed since no significant *hydrogen* production over time can be detected over undecorated *CdS* NR samples and is in agreement with colloidal *CdS* NR based system [53]. As the *ML QE*s increase (Fig. 5.28b) with higher cluster coverages for all sample types, a larger number of *Pt* clusters per NR apparently reduces the probability of recombination of photo generated charge carriers. Maximum *ML QE*s of about 4.2 % over the Pt_{46} decorated samples and 3.2 % over unselected samples are apparent.

The presence of a **saturation value**, evidences that a threshold value exists. Thus, additional *Pt* clusters per NR seems to have no effect on the photochemical process any more. This observation is tentatively interpreted by means of photo generated electrons being distributed among more and more *Pt* clusters for increasing coverage.[10] The threshold for saturation is expected for distances between the *Pt* clusters comparable to the spatial extent of the electronic wave functions. In the present case, this allows for estimating this distance to 5 to 8 nm [31].

For even larger coverages, this effect becomes more severe as the indicated maximum *QE* (1.34 %) observed for a colloidal *CdS*/*Pt* NR photocatalyst from the same NR batch under the same experimental conditions with higher catalyst coverage ($\sim 300\,cluster/NR$) shows. For coverages in this range, one expects to observe a decrease in efficiencies. In this context, it should be noted that when comparing the colloidal system to the Pt_{46} samples ($0.04\,e/nm^2$) with the *QE* the overall amount of Pt is reduced by an order of magnitude. Further, since saturation sets in for $Pt_{n\geq 36}$ at $25\,cluster/NR$ compared to Pt_{46} at $40\,cluster/NR$, it can be identified that this

---

[9] The calculation of *QE*s is based on the *ML* model for absorption correction as introduced in Sect. 3.3.6.

[10] The threshold for saturation is expected for distances between the *Pt* clusters comparable to the spatial extent of the electronic wave functions. In the present case, this allows for estimating this distance to 5 to 8 nm [31].
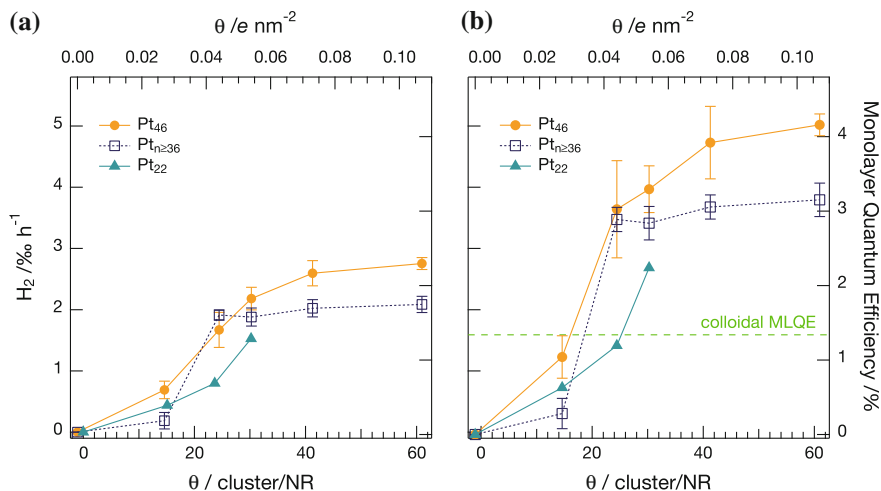
Fig. 5.28 H_2 production per hour (after 4 h of illumination) (**a**) and *ML QE* (**b**) for unselected $Pt_{n \geq 36}$, selected Pt_{22} and Pt_{46} decorated photo catalysts as a function of cluster coverage. The data points represent the averaged multiple measurements, as shown in Fig. 5.27b; error bars are based on the standard deviation of these multiple measurements per coverage. The lines connecting the data points serve as a guide to the eye. The maximum performance of the unselected samples is slightly less than for the Pt_{46} samples and saturation sets in at lower coverages. *Hydrogen* production over Pt_{22} is lower compared to Pt_{46} decorated *CdS* NRs at similar coverage. In the investigated coverage regime *hydrogen* yields and *ML QE*s show qualitatively the same trend with increasing cluster coverage. Corresponding saturation *ML QE*s of all sample series are higher compared to a colloidal *Pt/CdS* NRs (*green dashed line*) photocatalyst system *Reprinted (adapted) with permission from* [31]—*Copyright (2012) American Chemical Society*

process is also related to cluster size.[11] In order to better understand the influence of the size on the reactivity of such systems the reactivity as a function of size is studied in the next section.

5.4.3 Size Dependent Reactivity

For the study of the effect of cluster size, all parameters were kept constant save for the size of the deposited clusters. As a representative coverage 0.04 e/nm^2 was chosen, since for Pt_{46} at this coverage the *hydrogen* evolution has not yet reached saturation, as described in the previous section. As reported above for different coverages, all the different sized samples show a linear increase of the amount of H_2 over time (Fig. 5.29a), which again proves samples are stable over the course of the experiment. Figure 5.29b shows the *hydrogen* **evolution per hour** (H_2/h) for

---

[11] This observation is similar to the finding that the additional presence of larger *Pt* nanoparticles on colloidal *CdS* NRs during extended photo deposition does not lead to an increase in *hydrogen* yield any more [53].
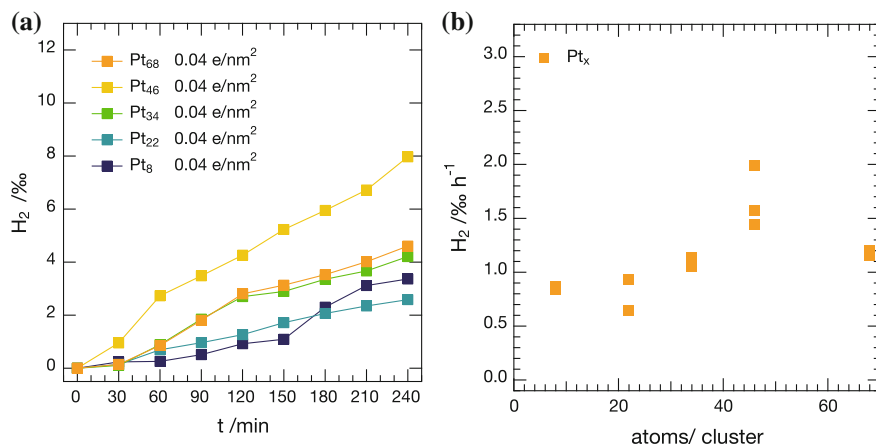
Fig. 5.29 H_2 evolution as a function of time for representative samples of the different sizes (**a**) and the result of all coverage dependent measurements as H_2 evolution per hour (**b**). In **a** the *hydrogen* generation as function of time for representative samples with the sizes $Pt_x (x = 8, 22, 34, 46, 68)$ deposited on *CdS* NRs are shown. Each point represents the total amount of *hydrogen* produced by the sample at that time; all samples reveal a linear trend over time, with a slope dependent on the size. **b** shows the *hydrogen* generation per hour (after 4 h of illumination) for all measured samples and the observed small variations per size demonstrate high reproducibility [54] *Reprinted with permission from* [54]—*Copyright (2013) American Chemical Society*

all measured samples, the data scatter for single *hydrogen* measurements on identical samples demonstrate high **reproducibility**. Different sizes produce different amounts of *hydrogen*.

The averaged *hydrogen* production per hour for different cluster sizes and per *Pt* cluster atom is plotted in Fig. 5.30a; the corresponding resulting *QE* and the corrected *ML QE* as a function of cluster size is shown in Fig. 5.30b. The plotted error bars result from calculation of standard deviations of multiple measurements per cluster size. For both H_2/h production and *(ML) QE* a clear trend is observed: While the smaller clusters Pt_8 and Pt_{22} show little *hydrogen* production, an increase in the production rate is observed for Pt_{34} clusters. The rate further increases for clusters of Pt_{46}, where a maximum[12] of the *hydrogen* production is found; for Pt_{68} the catalytic activity per cluster is again lower. However, when calculating H_2/h for each single *Pt* cluster atom a different image of size-effects is gained. The highest *hydrogen* production per hour and cluster atom of $0.11 \times 10^{-3} H_2$/h is obtained for Pt_8 samples and a continuous decay with increasing cluster coverage is observed—nonetheless a local maximum can still be observed for Pt_{46}.

From the observed size dependent *hydrogen* evolution (Fig. 5.30) two major conclusions can be drawn. First, it is direct evidence that differently sized clusters have different catalytic activity. Second, the reactivity is determined by the precise number

---

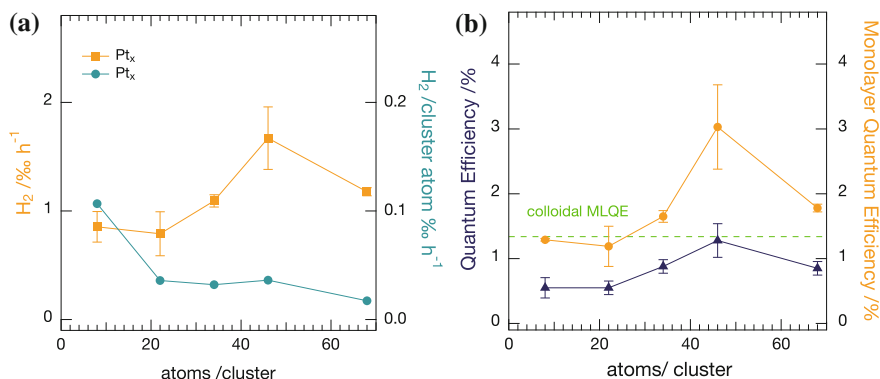[12] Under the assumption of the condition of a scalable regime.

Fig. 5.30 H_2 production per hour (after 4 h of illumination) (**a**) and (*ML*) *QE* (**b**) for selected $Pt_x(x = 8, 22, 34, 46, 68)$ decorated photo catalysts as a function of cluster size at a coverage of 0.04 e/nm². In **a** the data points represent the averaged multiple measurements, as shown in Fig. 5.29b. Error bars shown, are based on the standard deviation of multiple measurements per cluster size—the *lines* connecting the data points serve as a guide to the eye. *Hydrogen* production per hour (*orange squares, left axis*) shows a maximum for Pt_{46}, whereas larger as well as smaller sizes reveal lower *hydrogen* yields. *Hydrogen* production per single cluster atom (*green circles, right axis*) shows a maximum *hydrogen* evolution for Pt_8 decorated samples and decreases with increasing cluster size. A similar trend as for the H_2/h production is displayed for (*ML*) *QE*s (**b**). For comparison, the saturation *ML QE*s for the colloidal *Pt/CdS* NRs (*green dashed line*) photocatalyst system is included [54]. *Reprinted with permission from* [54]—*Copyright (2013) American Chemical Society*

of atoms in the cluster and it thus can be tuned, in the present case for maximum *hydrogen* evolution at a cluster size of Pt_{46}.

In order to obtain a better understanding on how the reactivity of the system is tuned by cluster size a schematic sketch of the energy levels for photocatalytic water splitting with focus on the studied H^+/H_2 partial reaction is presented in Fig. 5.31b. Upon irradiation of light an electron hole pair is formed in the rod's VB, if the photon energy is larger than the band gap of the semiconductor. Thus, an electron is excited from the VB into the CB of the semiconductor. For the H_2 formation, the electron must be transferred to the clusters (more precisely the LUMOs of the clusters). In a next step an electron transfer to the *hydrogen* must be enabled. The transfer of a second electron finally allows the production of molecular *hydrogen* [55–57]. Consequently efficient trapping of the electron by the clusters is important and needs to be dominant over recombination with holes (avoided in the presented case by the scavenger), trapping in surface states and the back reaction. The backward reaction (electron transfer from the cluster to the NR) is still crucial for the reaction rate. After removal of the hole (by the scavenger *TEA*), the electron wave function is mostly delocalized over the NR, if the charge is not trapped by either clusters or surface states. The strength of the cluster to trap an electron, i.e. the location of the cluster LUMO (lowest unoccupied molecular orbitals) is now of paramount importance and determines the reactivity.
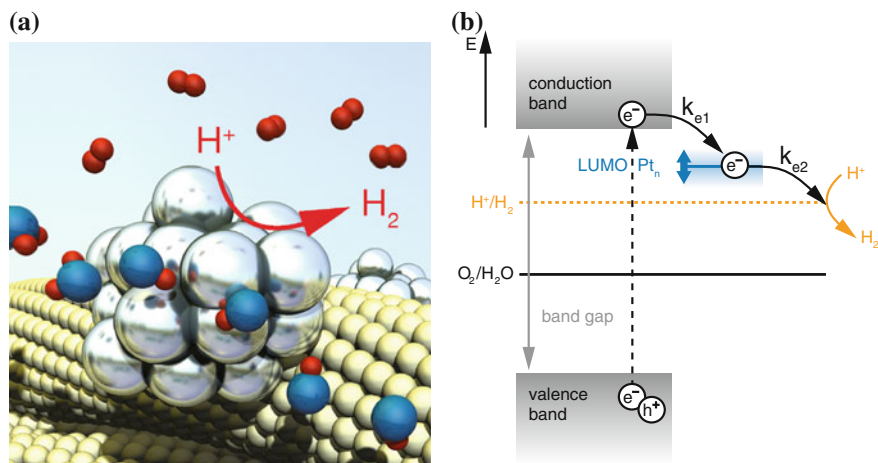
(a)

(b)

Fig. 5.31 Size dependent *water* splitting reaction—schematic sketch of the H^+/H_2 partial reaction (**a**), energy levels involved in the splitting reaction (**b**) [54]

The kinetics of the two electron transfers (k_{e1} and k_{e2}) determine the trapping probability for the electrons. The overall rate of the electron transfer from the NR to the cluster (k_{e1}) is defined by the LUMO states of the clusters with respect to the semiconductor band edge. Clusters with a **low LUMO can trap electrons efficiently** and reduce the back reaction. However, with a too low LUMO the electrons are bound so strong on the clusters that the electron transfer rate from the cluster to the *hydrogen* atoms (k_{e2}) is reduced, resulting in a lower H_2 production.

Therefore, a maximum in *hydrogen* evolution is observed for an optimum position of the cluster LUMO orbitals with respect to the lower edge of the conduction band of the semiconductor and chemical potential of the H^+/H_2 partial reaction. This optimum is defined by a compromise of an efficient trapping of the electron in the cluster (low LUMO) and at the same time a successful electron transfer to the *hydrogen* (high LUMO)—basically applying Sabatier's principle with respect to the bonding strength of the *hydrogen* to the cluster. Varying cluster size, the LUMO of the cluster can be tweaked by varying cluster size [58] and, therefore an optimum is obtained around a size of Pt_{46} resulting in the highest amount of *hydrogen* gas produced.

These considerations are also validated by the observations made for Pt_{22}, where for three different coverages a lower *ML QE* (see Fig. 5.28b) compared to the same coverages of Pt_{46} are observed. Additionally, the unselected clusters and comparable colloidal systems confirm this thesis, as in either case the reactivity is below the selected samples of Pt_{46}, since through heterogeneous size distribution the optimum position cannot be precisely tuned. Thus, by means of using size-selected clusters, through independent control of coverage and size the H_2 evolution can be tuned to maximum efficiency. Testing the performance of different sized clusters around the maximum of Pt_{46} might even further improve the *hydrogen* yield.

5.4.4 Stability

Long-term stability of the prepared *Pt* cluster decorated CdS NR thin film samples is evaluated by measuring *hydrogen* evolution over an extended period of time and imaging a TEM grid after illumination. Fig. 5.32a shows the integral amount of *hydrogen* released over 25 h of a blank sample ($Pt_{n \geq 36}$ without *CdS* NRs) and a Pt_{46} sample, each with a coverage of $0.04\,e/nm^2$. For both samples a linear increase in total amount of *hydrogen* produced can be observed within the first four hours of measurement, upon further illumination of both samples the amount of *hydrogen* evolved decreases rapidly, visible by the strong deviations from the linear relation. A corresponding HAADF-STEM micrograph as shown in Fig. 5.32b was taken after the 25 h measurements in order to elucidate possible reasons for the strong decrease in *hydrogen* production rates encountered. In contrast to the STEM images of the as prepared samples (Sect. 5.4.1) shortened and aggregated NRs are observed. Additionally flocculated NRs are visible as smeared out white spots on the micrograph. *Pt* clusters are displayed as small white spots and are not uniformly distributed any more, however are grouped in ensembles. A closer look reveals that the *Pt* clusters have spatially approached each other, however the ensemble still constitutes of single clusters that have not coalesced.

The decrease in photocatalytic activity can be explained by the dependency on the efficiency of the hole scavenging process. Destabilization of *CdS* NRs by shortening, aggregation and flocculation, encountered also in the colloidal system, is therefore attributed to photooxidation. The long-term stability is determined by the competition between photooxidation and scavenging of photo generated holes. It is reported that a faster consumption of these holes observed with sacrificial agents possessing a more negative potential leads to a higher stability due to domination of the hole scavenging process over photooxidation. Concerning the stability of the *Pt* clusters, the breakup of uniform distribution on the support while no cluster coalescence can be observed, might indicate that this finding is related to a wetting effect. Due to the formation of small droplets, *Pt* cluster ensembles accumulate, while the solvent evaporates. Consequently, after complete solvent evaporation from the TEM support, spatially approached cluster ensembles, that are jammed together, are encountered. This behavior has been observed previously for *Pt* clusters with broader size distribution—TEM images of non touching clusters, appeared in groups [7, 8].

5.4.5 Comparison to Reported Systems

Comparable materials for photocatalytic water splitting have been reported in the literature; in Table 5.4 a summary of characteristics of the prepared catalyst is shown and compared to related systems. *CdS* nano structures decorated with 3–5 nm *Pt* nano crystals for photocatalytic *hydrogen* production were prepared by Bao et al. [59]. The authors measured a stable *hydrogen* yield of 3.1 mmol/h over a 10 wt% *Pt*-
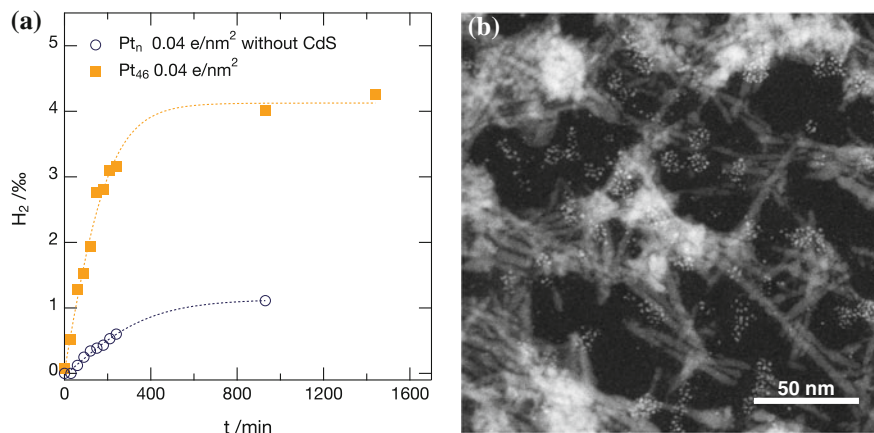
Fig. 5.32 Results of long-term H_2 evolution measurements (**a**) and HAADF-STEM measurement after reaction (**b**). The long term measurement (**a**) on unselected and selected clusters is displayed as a function of time; the interpolation of the raw data points (*dashed lines*) serves as a guide to the eye. Deviations from the linear relation (after first 240 min) indicate catalyst deactivation; after about 400 min of measurement no further *hydrogen* evolution is observed. A corresponding micrograph (**b**) taken of a Pt_{46} sample after illumination and H_2 production over 25 h shows flocculated NRs as big white spots and groups of cluster ensembles in between. Single clusters have spatially approached but are not coalesced

Table 5.4 Comparison of *hydrogen* yields and QEs for reported photocatalyst systems

	Photo catalyst material	H_2 /mmol/h	QE /%	Pt /wt %
Berr et al. [53]	Colloidal Pt/CdS NRs	5 (per g cat.)	3.9	22.5
Bao et al. [59]	Colloidal Pt/CdS NRs	3.10	60.3	10
Yu et al. [60]	Pt/TiO_2	0.14	–	4
This work [31]	Hybrid Pt/CdS NRs	0.1 (Pt_{46})	4.2	2–3

Prepared hybrid photo catalysts show higher photocatalytic efficiency compared to reported colloidal Pt/CdS NRs and Pt/TiO_2 based systems considering the minimized amount of Pt

loaded photocatalyst under visible light irradiation using hole scavengers resulting in a maximum QE of 60.34 %[13] at 420 nm. Considering the influence of Pt nano crystal coverage Bao et al. noticed an increasing *hydrogen* evolution with coverage which reaches a maximum at 13 wt% which upon further increase of coverage quickly decreases. For comparison the Pt-loading of the prepared hybrid cluster photocatalyst sample with a (maximum) coverage of 0.11 e/nm^2 is estimated to be about 2–3 wt% and the corresponding stable *hydrogen* yield at this coverage is about 0.1 mmol/h.

The calculations indicate that the presented method of using size-selected clusters, thus precisely tuning the necessary coverage, achieves a five-fold reduction of noble

---

[13] The extraordinary high QE is related to the high BET surface area of 112.8 cm^2/g of CdS nano structures realizing an efficient separation and fast transport of charge carriers at the high CdS/electrolyte interface [59].

metal loading compared to established photo depositions. Similar savings in noble metal, were previously only elaborated in comparison with the colloidal Pt/CdS NRs system of Berr et al. [53].

Apart from metal sulfide based systems, TiO_2 is an alternative, due to chemical inertness, non-toxicity, low cost, good availability and stability against photo corrosion [61, 62]; however titania suffers from a large band gap, rapid recombination of photo generated electrons and holes and back reaction of produced H_2 and O_2 to H_2O [61]. For example for Pt/TiO_2 nano sheets with (001) facets, using Pt loadings up to 6 wt% and TEA as a hole scavenger the highest observed photocatalytic activity of 140.2 μmol/h was measured for 4 wt% Pt. Again, a further increase of Pt loading caused a reduction of photocatalytic activity, attributed to enhanced light scattering of the samples leading to a decreased irradiation passing through the reaction solution [60].

Summary—The new introduced hybrid cluster photocatalyst with size-selected clusters may not yield in the highest QE or *hydrogen* yields, however allows for determination of the minimum amount of Pt for optimum efficiency. This is of particular importance, since for the presented examples a maximum in *hydrogen* generation activity is met, dependent on noble metal coverage—further a decrease for too high loadings is observed and thus requires precise tuning of the coverage. Additionally the new system has an unprecedented control on the catalyst particle size, which as discussed, through exact adjustment of the cluster LUMO levels allows for optimizing the catalytic reactivity.

References

1. Kunz, S. (2010). Ph.D. thesis, Technische Universität München.
2. Kunz, S., Hartl, K., Nesselberger, M., Schweinberger, F. F., Kwon, G., Hanzlik, M., et al. (2010). *PCCP*, *12*, 10288.
3. Schlögl, K. (2011). Ph.D. thesis, Technische Universität München.
4. Hartl, K., Nesselberger, M., Mayrhofer, K. J., Kunz, S., Schweinberger, F. F., Kwon, G., et al. (2010). *Electrochimica Acta*, *56*, 810.
5. Henry, C. R. (1998). *Surface Science Reports*, *31*, 231.
6. Wang, B., Yoon, B., König, M., Fukamori, Y., Esch, F., heiz, u, et al. (2012). Nano Letters, 12, 5907.
7. Bardotti, L., Tournus, F., Mélinon, P., Pellarin, M., & Broyer, M. (2011). *Physical Review B*, *83*, 035425.
8. Alayan, R., Arnaud, L., Broyer, M., Cottancin, E., Lermé, J., Marhaba, S., et al. (2007). *Physical Review B*, *76*, 075424.
9. Watanabe, Y., Wu, X., Hirata, H., & Isomura, N. (2011). *Catalysis Science and Technology*, *1*, 1490.
10. Watanabe, Y., & Isomura, N. J. (2009). *Vaccum Science and Technology A*, *27*, 1153.
11. McClure, S. M., Lundwall, M., Zhou, Z., Yang, F., & Goodman, D. W. (2009). *Catalysis Letters*, *133*, 298.
12. McClure, S. M., & Goodman, D. W. (2011). *Topics in Catalysis*, *54*, 349.
13. Young, N. P., Li, Z. Y., Chen, Y., Palomba, S., Di Vece, M., & Palmer, R. E. (2008). *Physical Review Letters*, *101*, 246103.

14. Li, Z. Y., Young, N. P., Vece, M. D., Palomba, S., Palmer, R. E., Bleloch, A. L., et al. (2008). *Nature*, *451*, 46.
15. Wang, Z. W., Li, Z. Y., Park, S. J., Abdela, A., Tang, D., & Palmer, R. E. (2011). *Physical Review B*, *84*, 073408.
16. Wang, Z. W., Toikkanen, O., Yin, F., Li, Z. Y., Quinn, B. M., & Palmer, R. E. J. (2010). *Journal of the American Chemical Society*, *132*, 2854.
17. Ernst, F., & Rühle, M. (1997). *Current Opinion in Colloid and Interface Science*, *2*, 469.
18. Batson, P. E. (2008). *Microscopy and Microanalysis*, *14*, 89.
19. Bals, S., Aert, S. V., Romero, C. P., Lauwaet, K., Bael, M. J. V., Schoeters, B., et al. (2012). *Nature Communications*, *3*, 897.
20. Bonanni, S., Aït-Mansour, K., Brune, H., & Harbich, W. (2011). *ACS Catalysis*, *1*, 385.
21. Wepasnick, K. A., Li, X., Mangler, T., Noessner, S., Wolke, C., Grossmann, M., et al. (2011). *Journal of Physical Chemistry C*, *115*, 12299.
22. Gronbeck, H., & Andreoni, W. (2000). *Chemical Physics*, *262*, 1.
23. Nie, A., Wu, J., Zhou, C., Yao, S., Luo, C., Forrey, R. C., et al. (2007). *International Journal of Quantum Chemistry*, *107*, 219.
24. Muller, U., Sattler, K., Xhie, J., Venkateswaran, N., & Raina, G. J. (1991). *Journal of Vacuum Science and Technology B*, *9*, 829.
25. Chorkendorff, I., & Niemantsverdriet, J. W. (2007). *Concepts of modern catalysis and kinetics* (2nd ed.). Weinheim: Wiley-VCH.
26. Williams, D. B., & Carter, C. B. (2009). *Transmission electron microscopy: A textbook for materials science* (2nd ed.). Berlin: Springer.
27. Iwata, S., & Ishizaka, A. J. (1996). *Journal of Applied Physics*, *79*, 6653.
28. Powell, C. J. (2012). *Journal of Electron Spectroscopy and Related Phenomena*, *185*, 1.
29. Eberhardt, W., Fayet, P., Cox, D. M., Fu, Z., Kaldor, A., Sherwood, R., et al. (1990). *Physical Review Letters*, *64*, 780.
30. Rötzer, M. (2012). Internship report.
31. Berr, M. J., Schweinberger, F. F., Döblinger, M., Sanwald, K. E., Wolff, C., Breimeier, J., et al. (2012). *Nano Letters*, *12*, 5903.
32. Matos, J., Ono, L. K., Behafarid, F., Croy, J. R., Mostafa, S., DeLaRiva, A. T., et al. (2012). *Physical Chemistry Chemical Physics*, *14*, 11457.
33. Hansen, T., Wagner, J., Hansen, P., Dahl, S., Topsoe, H., & Jacobsen, C. (2001). *Science*, *294*, 1508.
34. Hansen, T. W., Wagner, J. B., Hansen, P. L., Dahl, S., Topsøe, H., & Jacobsen, C. J. H. (2001). *Science*, *294*, 1508.
35. Hansen, P., Wagner, J., Helveg, S., Rostrup-Nielsen, J., Clausen, B., & Topsøe, H. (2002). *Science*, *295*, 2053.
36. Simonsen, S. B., Chorkendorff, I., Dahl, S., Skoglundh, M., Sehested, J., & Helveg, S. J. (2010). *Journal of the American Chemical Society*, *132*, 7968.
37. Simonsen, S. B., Chorkendorff, I., Dahl, S., Skoglundh, M., Sehested, J., & Helveg, S. (2011). *Journal of Catalysis*, *281*, 147.
38. Datye, A. K., Xu, Q., Kharas, K. C., & McCarty, J. M. (2006). *Catalysis Today*, *111*, 59.
39. Larsson, E. M., Millet, J., Gustafsson, S., Skoglundh, M., Zhdanov, V. P., & Langhammer, C. (2012). *ACS Catalysis*, *2*, 238.
40. Langhammer, C., & Larsson, E. M. (2012). *ACS Catalysis*, *2*, 2036.
41. Langhammer, C., Larsson, E. M., Kasemo, B., & Zorić, I. (2010). *Nano Letters*, *10*, 3529.
42. Kreibig, U., & Vollmer, M. (1995). *Optical properties of metal clusters* (1995th ed.). Berlin: Springer.
43. Tanabe, T., Nagai, Y., Dohmae, K., Sobukawa, H., & Shinjoh, H. (2008). *Journal of Catalysis*, *257*, 117.
44. Simonsen, S. B., Chorkendorff, I., Dahl, S., Skoglundh, M., Meinander, K., Jensen, T. N., et al. (2012). *Journal of Physical Chemistry C*, *116*, 5646.
45. Harris, P., Boyes, E., & Cairns, J. (1983). *Journal of Catalysis*, *82*, 127.
46. Riedel, J. N. (2013). Master's thesis, Danmarks Tekniske Universitet.

47. Jensen, R. (2012). Ph.D. thesis, Danmarks Tekniske Universitet.
48. Santos, V. P., Carabineiro, S. A., Tavares, P. B., Pereira, M. F., Órfão, J. J., & Figueiredo, J. L. (2010). *Applied Catalysis B: Environmental*, *99*, 198.
49. Campbell, C. T., Ertl, G., Kuipers, H., & Segner, J. J. (1980). *Chemical Physics*, *73*, 5862.
50. Allian, A. D., Takanabe, K., Fujdala, K. L., Hao, X., Truex, T. J., Cai, J., et al. (2011). *Journal of the American Chemical Society*, *133*, 4498.
51. Berr, M. J., Vaneski, A., Mauser, C., Fischbach, S., Susha, A. S., Rogach, A. L., et al. (2012). *Small*, *8*(2), 291–297.
52. Wu, K., Zhu, H., Liu, Z., Rodríguez-Córdoba, W., & Lian, T. J. (2012). *Journal of the American Chemical Society*, *134*, 10337.
53. Berr, M., Vaneski, A., Susha, A., Rodrigues-Fernandez, J., Döblinger, M., Jäckel, F., et al. (2010). *Applied Physics Letters*, *97*, 093108.
54. Schweinberger, F. F., Berr, M. J., Döblinger, M., Wolff, C., Sanwald, K. E., Crampton, A. S., et al. (2013). Cluster size effects in the photocatalytic hydrogen evolution reaction. *J. Am. Chem. Soc*, *135*(36), 13262–13265.
55. Maeda, K., & Domen, K. J. (2007). *Journal of Physical Chemistry C*, *111*, 7851.
56. Wang, Y., & Herron, N. (1990). *Physical Review B*, *42*, 7253.
57. El-Sayed, M. (2004). *Accounts of Chemical Research*, *37*, 326.
58. Heiz, U., Sanchez, A., Abbet, S., & Schneider, W.-D. J. (1999). *Journal of the American Chemical Society*, *121*, 3214.
59. Bao, N., Shen, L., Takata, T., & Domen, K. (2008). *Chemistry of Materials*, *20*, 110.
60. Yu, J., Qi, l, & Jaroniec, M. J. (2010). The Journal of Physical Chemistry C, 114, 13118.
61. Zhu, J., & Zäch, M. (2009). *Current Opinion in Colloid and Interface Science*, *14*, 260.
62. Park, H., & Choi, W. J. (2004). *The Journal of Physical Chemistry B*, *108*, 4086.

Part IV
Conclusion and Outlook

Chapter 6
Conclusion and Outlook

6.1 Summary

In the presented work different aspects of supported *Pt* cluster catalysts were studied under well defined UHV and applied ambient conditions. In the following the achieved results and gained insights are summarized.

6.1.1 UHV

The main focus of the UHV experiments was the investigation of the electronic structure as well as the adsorption properties and reactivity of olefins adsorbed on surfaces and supported *Pt* clusters.

In order to discern the feasibility of EES to probe the **electronic structure** of cluster based materials, the **sensitivity of the MIES/UPS setup** was determined. Using adsorbed *TCE* as a probe molecule, and correlating EES with TPD measurements, the results prove a superior submonolayer sensitivity for MIES compared to UPS, and NEXAFS data from the literature. On *Mo*(112) the achieved detection limit was quantified to be as low as $0.02^{\text{TCE}}/\text{SA}$, (13 % of a *ML*).

Based on these results, **EES of supported clusters** (Pt_{11} and Pt_{30}) at low coverages was performed. With MIES no features from the cluster metal could be observed, most likely due to different de-excitation mechanisms on the surface of metals/clusters and the low cluster coverage. UPS results, in contrast, evidence changes for the different coverages and sizes. Electron density at the Fermi edge for Pt_{30} (compared to Pt_{11}) might be an indication for the emergent metallic behavior. In order to verify these observations of a potential metal to insulator transition, the use of local methods is desirable.

CO, as a well known adsorbate, was used as a test molecule. EES results on the *Pt*(111) surface in the submonolayer range are weak, but agree with the literature and show the potential to probe for small changes in the electronic structure.

Using a more systematic study, EES results could contribute to a more complete picture of the *CO* interaction on metal clusters.

By means of TPD and EES, the adsorption properties of **TCE**, a chlorinated olefin and pollutant, were investigated on various surfaces (*Mo*, *Pt* and *MgO*). The results show a physisorption followed by multilayer formation on all surfaces. A weakly interacting *TCE* molecule is evidenced from the analysis of the MO peak positions and intensities as well as WF measurements. For the analysis of EES data, a new data treatment procedure was introduced, allowing one to extract peak features, otherwise obscured by contributions of secondary electrons. The obtained findings of the data analysis suggest flat lying *TCE* molecules on the surface for submonolayer and multilayers, the later being in agreement with the literature.

Based on the results from the surfaces, the *TCE* adsorption on supported *Pt* clusters of different sizes, with prospect to decomposition, was studied. No activation could be observed in TPD and EES measurements for clusters either. However, the analysis of the MO peak energy positions in MIES shows a shift towards lower energy with increasing cluster coverage, likely to be attributed to a relaxation effect. Comparing to surfaces, this shift might be induced by interaction with the clusters, thus represents first results of probing the electronic structure of cluster-adsorbate complexes (in the submonolayer range).

Ethene, as a second olefin, was studied by the same means (TPD and EES) on surfaces in a similar approach. The obtained data agrees well with results from the literature, a weak interaction on *MgO* and strong chemisorption on *Pt*. MIES allowed further to probe the adsorption in the submonolayer range, a previously not reported coverage range. Further, using *ethene* and *hydrogen*, the reactivity on *Pt*(111) with TPR was investigated and findings for the self-/hydrogenation reaction agree with reported data.

The TPR experiments were repeated using unselected *Pt* clusters and reveal a higher reactivity (lower temperature) for clusters compared to the single crystal. Repeated TPR measurements on size-selected *Pt* clusters show a size dependent activation, where a minimum amount of ten atoms is necessary for a reaction to happen. To further elucidate the cluster reactivity, preliminary results from AES and IRRAS are promising towards a better understanding of the reactivity and deactivation on a molecular level.

6.1.2 Ambient

The scope of the ambient experiments was three fold, with an interest in characterization, stability and reactivity of *Pt* clusters under applied reaction conditions, after transfer to ambient conditions. In a highly collaborative approach, the following results were achieved.

For **local characterization**, **STEM** measurements were performed. The obtained micrographs evidence a highly reproducible coverage (average error of 14 %). A specially adapted computer assisted analysis was established and is used for routine

characterization of the STEM images. Results of the analysis show, that unselected and selected clusters reveal expected different PSD (ADF), that reflect the synthesis method. Different selected cluster sizes can be distinguished upon their projected area in the STEM micrographs with a difference as low as at least 12 atoms. A comparison to areas calculated using simple geometric considerations, suggests a sphere like cluster shape, with the exception of very small clusters, that appear as flat 2D structures. On an **integral level**, **XPS** measurements of clusters, evidence a successful deposition also on insulating support materials and a homogenous distribution over the support in the range of the aperture used during deposition. Selected and unselected samples reveal different peak signal shapes and broadness. For selected clusters with different sizes, an observed BE shift for the *Pt* 4*f* signal, converges with increasing number of atoms towards the bulk value. The shift and changes in fit parameters are in good agreement with the literature and can be explained by a final state effect. Comparison to similar systems allows one to estimate the oxidation state of the cluster materials between +*II* and 0, thus are only partially oxidized, giving a potential explanation for the reactivity of such small supported clusters despite transfer to ambient conditions.

The (temperature) **stability** of the cluster catalysts was tested, using **INPS** in combination with **STEM**, as a new approach. A change in plasmon peak position is observed for unselected $Pt_{n \geq 53}$ samples as well as a mixed size Pt_{22+68} sample, whereas the signal of the selected Pt_{68} sample stays stable over the heating at 453 K for 21 h under *Ar* atmosphere. The changes in peak position are corroborated by STEM micrographs and PSD analysis before and after treatment. For $Pt_{n \geq 53}$ and Pt_{22+68} an Ostwald ripening sintering mechanism is suggested, that is however not complete at 453 K; for Pt_{68}, similar sized clusters after the heat treatment show stable particles. Further experiments at higher temperatures, as well as under reactive gas atmosphere (H_2 or CO) and/or oxidative (O_2) are planned to further understand the stability of selected clusters. Also, support effects will be addressed, as samples on Si_3N_4 and SiO_2 were prepared. The stability of the selected samples up to 475 K is supported by first **ETEM** measurements for Pt_{46} on SiO_2 under UHV conditions. Additional measurements, with different cluster sizes and temperatures as high as 600 K are currently in progress as well as imaging cluster samples in situ during the exposure to gases, in particular under a reducing and/or oxidative atmosphere also at elevated temperatures.

First results on the **reactivity** measurements in μ**-reactors**, show the feasibility to measure high surface area model catalyst, in pressures of up to 1 bar. From titration experiments an increasing area after *CO* oxidation is a first indication that supports stability to temperatures as high as 513 K. Reactivity measurements under steady state conditions as a function of temperature, evidence reactivity of all measured sizes. The average reactivity is increasing with size, save for Pt_{46}, where multiple data points show a reactivity comparable to Pt_{68}. For clusters with such 'large' sizes the temperature for full conversion is even lower compared to a *Pt* thin film measured under similar conditions. Arrhenius plots of the measurements show a large temperature range with Arrhenius like behavior. Extracted activation energies are in the correct order of magnitude when compared to literature values and show a higher

activation energy for very small systems (i.e. Pt_{10}) that might be related to a 2D structure and a particularly low energy for Pt_{46}, supporting the reactivity observations. In liquid phase, a new **hybrid cluster photocatalyst material** with size-selected clusters is introduced, allowing for atomic scale insight into photocatalytic processes of precisely defined nanosystems. Supported *CdS* nanorods with *Pt* cluster co-catalysts were used to quantitatively correlate the dependence of the photocatalytic activity for *hydrogen* generation on *Pt* cluster size and coverage. The minimum amount of *Pt* necessary to achieve saturated efficiencies was determined. The results further evidence a cluster size dependence of the catalytic activity. Different cluster sizes show a maximum *hydrogen* production for Pt_{46}, that might be explained by an optimum match of the cluster LUMO in the sense of Sabatier's principle.

Intriguing, is the unexpected **high reactivity of Pt_{46}** clusters in both reactor and photocatalysis experiments, further supported by the deviation of the trend for BE shifts for different sizes in XPS and the low activation energy, determined for *CO* oxidation in the reactors. A systematic study is necessary to shed light on this particular behavior, yet this observation is only possible due to the chosen approach with different techniques.

6.2 Conclusion

In the light of the scope of this work, given in the introduction, and based on the results gained the following conclusion can be drawn.

In terms of UHV studies, the MIES/UPS setup is now characterized and available as an additional tool with a high enough sensitivity in the submonolayer range to probe for the electronic structure of cluster adsorbate complexes. In combination with TPD/TPR, pMBRS and IRRAS a considerably broad and complementary set of techniques is at hand to study supported cluster materials. The results on the well known adsorption of *CO* and the systematic study (incl. the new data treatment procedure) of the adsorption of *TCE* served as a good model system to establish the EES in the existing setup. A solely thermal activation of *TCE* on surfaces and *Pt* clusters is not possible, further activation i.e. using a photocatalytic approach might however be successful. As a new and more complex reaction, the *ethene* hydrogenation was successfully measured on *Pt* clusters for the first time. Both the gained results of the size-selected reactivity and their difference in comparison to the single crystal measurements, as well as the preliminary results with IRRAS and AES, hold a high chance to answer some of the open questions in the mechanism of *ethene* hydrogenation and catalyst deactivation.

With respect to cluster catalysis under ambient and applied conditions, the results and the achieved insights can be benchmarked with the requirements for a successful catalyst material stated in the introduction (Fig. 1.2). A reproducible preparation, with respect to both size and coverage is evidenced on both local and integral level. In particular, the STEM results and the computer assisted analysis are introduced as a tool to monitor the deposition as well as changes after treatments. Using the data

for the *Pt* clusters in this work, the obtained area to size relation might be even able to determine the size/number of atoms for particles synthesized by different means. The thermal stability (i.e. deactivation) of clusters under UHV and (inert) ambient conditions could be shown up to a temperature range with catalytic relevance (i.e. for *Pt* as exhaust catalyst material) with a local and an in–situ integral method. The preliminary findings towards the high stability of selected clusters might help to design more stable catalyst in the future, by understanding the underlying mechanisms for stability better; yet, more systematic studies are necessary. Pressure stability and considerably high activity is supported by the results of the reactivity measurements. The observed reactivity and determined activation energies measured by means of μ-reactors has a high potential to answer open question of size dependent reactivity. Ongoing measurements of the *CO* oxidation reaction might help to understand the controversial discussed structure in/sensitivity of the reaction for small particles. The application of clusters as part of photocatalyst materials, shows the capabilities of those well defined materials, to better understand phenomena in related fields such as photocatalysis. The ability to determine the saturation point for *hydrogen* generation and to tune catalytic performance by optimizing the cluster coverage and size is of also of practical importance for the cost efficient design of photocatalytic nano systems.

All together the examples presented, allow for new insights into the working principles of heterogeneous catalysts and illustrate the high relevance of cluster research in the field of catalysis. In this context UHV experiments provide fundamental information on catalytic reactions, whereas the applied methods ensure that these results are more widely applicable, even under realistic, i.e., technically relevant conditions. The detail and sophistication of the UHV surface science experiments is hereby complementary to the realistic conditions of the ambient experiments on the different platforms. In the future, only a combination of both approaches will help to a more complete comprehension of heterogeneous catalysts. The contributions of this work with respect to *Pt* clusters are only a starting point of this approach and it is still a long way until understanding working mechanisms of an industrial catalyst becomes possible. On the basis of sophisticated model catalyst systems and a variety and combination of different techniques, this goal is however a little less remote.

6.3 Outlook

In the UHV the successful results of the TPR experiments towards *ethene* hydrogenation on different cluster sizes are further investigated. Vibrational information (IRRAS) in combination with the electronic structure (EES) of cluster adsorbates is believed to elucidate the size dependent behavior. In this respect, first isotope experiments with *deuterium* look promising to elucidate the role of the *hydrogen* activation in the hydrogenation reaction. In addition, the application of isothermal pMBRS will help to gain kinetic data which will make the results more widely applicable [1–4].

Last, the carbon formation will be subject to further studies to better understand catalyst deactivation during hydrogenation. In a next step, the activation of *methane*, as future potential energy feedstock [5–10] will be probed on clusters of different metals.

Under ambient conditions, the started collaborations will be continued. More ETEM measurements with different reactant gases are planned possibly allowing to see restructuring mechanisms and learn more about catalyst stability [11, 12]. With respect to INPS, on the basis of the stability measurements, the influence of the support and the size dependent reactivity towards the *hydrogen* oxidation will be investigated in situ [13, 14]. Also, stability and reactivity of *Pt* clusters is probed in an electrochemical cell, to better understand the behavior of electrocatalysts [15–17]. Using μ-reactors will allow, to see if results on the reactivity of the *CO* oxidation under these ambient pressure conditions is different to those in the UHV. For this purpose the support of the UHV experiments is currently being changed to amorphous SiO_2 [18–23], allowing for comparability of the results in the sense of the 'pressure gap'.

To increase the experimental possibilities and flexibility a new UHV chamber for analysis is currently designed. Is will replace the old main chamber and include the additional techniques LEED and XPS, an updated version of the MIES/UPS setup as well as a new crystal holder. Further, sample deposition will be integrated on the chamber in form of a new manipulator with possibilities to heat and prepare the sample upon deposition. The new setup is an important step in order to help to pursuit the joint approach of both UHV and ambient more efficiently.

It will be exciting to see the outcome of the ongoing and planned experiments and leaves one optimistic about the future of cluster science applied to heterogeneous catalysis.

References

1. Olander, D. R., Jones, R. H., Schwarz, J. A., & Siekhaus, W. J. (1972). *Journal of Chemical Physics*, *57*, 421.
2. Olander, D. (1977). *Journal of Colloid and Interface Science*, *58*(1), 169–183.
3. Engel, T., & Ertl, G. (1978). *Journal of Chemical Physics*, *69*, 1267.
4. Campbell, C. T., Ertl, G., Kuipers, H., & Segner, J. (1980). *Journal of Chemical Physics*, *73*, 5862.
5. Lewis, N. S., & Nocera, D. G. (2006). *PNAS*, *103*, 15729.
6. Schwarz, H. (2011). *Angewandte Chemie (International ed. in English)*, *50*, 10096.
7. Lang, S. M., Bernhardt, T. M., Barnett, R. N., & Landman, U. (2011). *Journal of Physical Chemistry C*, *115*, 6788.
8. Löffler, D., Uhlrich, J. J., Baron, M., Yang, B., Yu, X., Lichtenstein, L., et al. (2010). *Physical Review Letters*, *105*, 146104.
9. Heyde, M., Shaikhutdinov, S., & Freund, H.-J. (2012). *Chemical Physical Letters*, *550*, 1.
10. Włodarczyk, R., Sierka, M., Sauer, J., Löffler, D., Uhlrich, J. J., Yu, X., et al. (2012). *Physical Review B*, *85*, 085403.
11. Hansen, T. W., Wagner, J. B., Hansen, P. L., Dahl, S., Topsøe, H., & Jacobsen, C. J. H. (2001). *Science*, *294*, 1508.

12. Simonsen, S. B., Chorkendorff, I., Dahl, S., Skoglundh, M., Sehested, J., & Helveg, S. (2011). *Journal of Catalysis*, *281*, 147.
13. Langhammer, C., & Larsson, E. M. (2012). *ACS Catalysis*, *2*, 2036.
14. Larsson, E. M., Millet, J., Gustafsson, S., Skoglundh, M., Zhdanov, V. P., & Langhammer, C. (2012). *ACS Catalysis*, *2*, 238.
15. Nesselberger, M., Ashton, S., Meier, J. C., Katsounaros, I., Mayrhofer, K. J. J., & Arenz, M. (2011). *Journal of the American Chemical Society*, *133*, 17428.
16. Hartl, K., Nesselberger, M., Mayrhofer, K. J., Kunz, S., Schweinberger, F. F., Kwon, G., et al. (2010). *Electrochimica Acta*, *56*, 810.
17. Nesselberger, M., Roefzaad, M., Fay cal Hamou, R., Ulrich Biedermann, P., Schweinberger, F. F., Kunz, S., Schloegl, K., Wiberg, G. K. H., Ashton, S., Heiz, U., Mayrhofer, K. J. J., & Arenz, M. (2013). The effect of particle proximity on the oxygen reduction rate of size-selected platinum clusters. *Nature Materials*, advance online publication. doi:10.1038/nmat3712.
18. Kim, Y. D., Wei, T., & Goodman, D. W. (2003). *Langmuir*, *19*, 354.
19. Weissenrieder, J., Kaya, S., Lu, J., Gao, H., Shaikhutdinov, S., Freund, H., et al. (2005). *Physical Review Letters*, *95*, 076103.
20. Lu, J., Weissenrieder, J., Kaya, S., Gao, H., Shaikhutdinov, S., & Freund, H. (2007). *Surface Review and Letters*, *14*, 927.
21. Freund, H. J. (2007). *Surface Science*, *601*, 1438.
22. Baron, Stacchiola, D., Ulrich, S., Nilius, N., Shaikhutdinov, S., Freund, H. J., et al. (2008). *Journal of Physical Chemistry*, *112*, 3405–3409.
23. McClure, S. M., Lundwall, M., Zhou, Z., Yang, F., & Goodman, D. W. (2009). *Catalysis Letters*, *133*, 298.

Appendix A

The appendix gives further details on experimental methods and procedures for both UHV and ambient experiments. Further, gas phase photoelectron spectra of the studied molecules are stated along with assignment of the orbitals from theory. In general, the nomenclature of IUPAC with respect to surface science techniques, and names of chemical compounds is followed [1–3] in this thesis.

A.1 UHV Setup and Surface Science

A.1.1 Deposition of Clusters

The conversion for some values in the % ML unit (per cm^2 and per crystal surface area $0.785 \, cm^2$) into e/nm^2 and e/cm^2 is shown in Table A.1. The precise amount

Table A.1 Cluster coverage unit conversion - %ML, %ML per single crystal surface, e/nm^2 and e/cm^2 for selected values

%ML /cm^2	%ML /$0.785 \, cm^2$	Number of clusters /e/nm^2	Number of clusters /e/cm^2
0.005	0.0064	0.0015	0.15×10^{13}
0.010	0.0127	0.0029	0.29×10^{13}
0.050	0.0637	0.0116	1.16×10^{13}
0.060	0.0764	0.0145	1.45×10^{13}
0.075	0.0955	0.0218	2.18×10^{13}
0.100	0.1274	0.0290	2.90×10^{13}
0.150	0.1911	0.0435	4.35×10^{13}
0.200	0.2548	0.0580	5.80×10^{13}
0.300	0.3822	0.0870	8.70×10^{13}
0.500	0.6369	0.1160	11.60×10^{13}

Table A.2 Different values for the amount of atoms per clusters of various Pt_x sizes for a coverage of $0.029\,e/nm^2$

Size /atoms	n atoms /atoms/cm^2	n atoms /atoms/nm^2	Surface atoms /nm^2 (no ccp)	Surface atoms /nm^2 (ccp)
1	0.29×10^{13}	0.03	0.029	0.029
7	2.01×10^{13}	0.20	0.208	0.203
8	2.29×10^{13}	0.23	0.227	0.222
9	2.58×10^{13}	0.26	0.247	0.242
10	2.89×10^{13}	0.29	0.267	0.260
11	3.15×10^{13}	0.32	0.286	0.279
12	3.44×10^{13}	0.34	0.304	0.296
13	3.73×10^{13}	0.37	0.323	0.314
20	5.73×10^{13}	0.57	0.447	0.431
22	6.31×10^{13}	0.63	0.482	0.464
34	9.74×10^{13}	0.97	0.690	0.655
46	13.14×10^{13}	1.32	0.910	0.848
68	19.49×10^{13}	1.95	1.378	1.235
80	22.93×10^{13}	2.29	1.689	2.065

For different sizes the number of atoms in the cluster per cm^2 and nm^2, as well as an approximation of the amount of surface atoms per nm^2 are given. In the later case values taking ccp packing into account are additionally listed

of Pt atoms per cluster size for a coverage of $0.029\,e/nm^2$ ($=0.1\,\%ML$) are listed in Table A.2. Further an approximation for the amount of surface atoms is given.

A.1.2 Temperature Measurement and Control

For temperature measurements on the single crystals a type C (W-5% $Re/Re/W$ 26%) thermocouple (Omega Instruments, UK) is spot welded onto the side of each single crystal. The sketch in Fig. A.1 shows the circuit diagram for temperature control in the nanocat lab. The contact potential of the thermocouples is read out trough a feed-trough at the top of the manipulator and feed into the DatExcel box in mV. The DatExcel converts the mV potential of the thermocouples into a 0–10 V signal in the range of 68–2098 K. Since the C type thermocouple has a nonlinear characteristics curve below 300 K, this is compensated through 26 calibration points programmed into the DataExcel box. The 0–10 V signal is direct feed as monitor into the QMS for TPD measurements (Balzers, QMA 430, BALZERS, Switzerland). The 0–10 V signal is further feed to the PID Controller (Eurotherm 2408, Germany) and converted into values on a K scale. Additionally the Eurotherm controls the heating power on the power supply (Hewlett Packard HP-6032A) with a 0–10 V signal for heating one of the single crystals and has a RS 232 connection for a possible remote control of the heating through the Eurotherm.
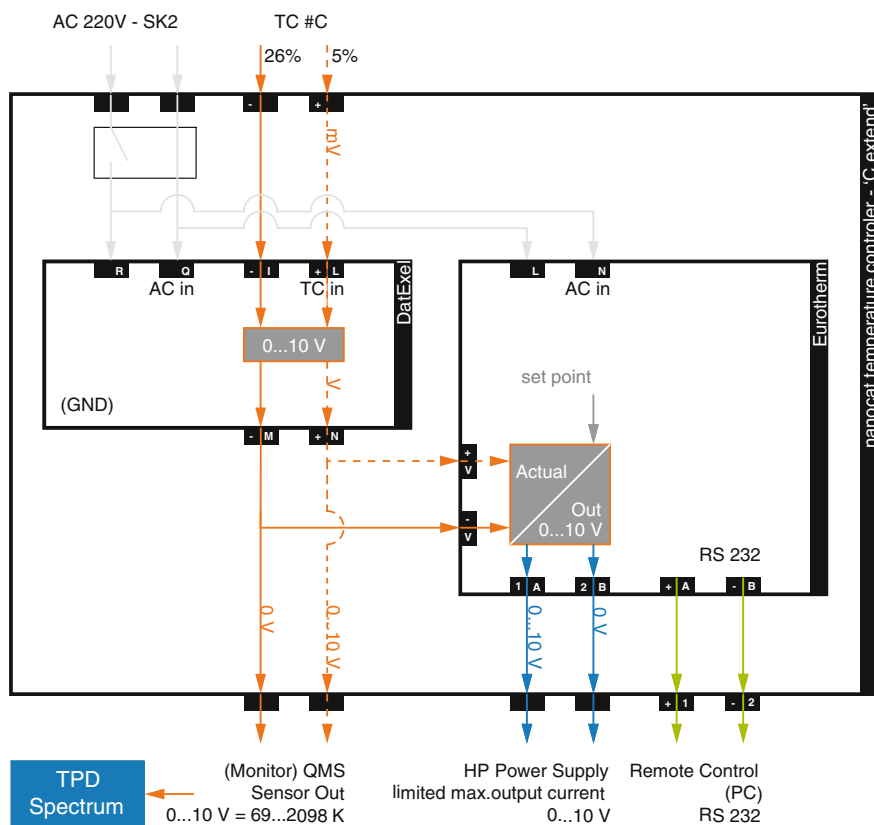
Fig. A.1 Temperature measurement and control

A.1.3 TP Measurements and Data Treatment

The TP measurements were recorded at a dwell time of 0.1 s, because the temperature increase at a heating rate of 2 K/s requires a minimum value of 0.5 s as the signal for the temperature would be convoluted otherwise. The amplifier range was manually set to 10^{-9}, with a resulting optimized SEM range of as low as 10^{-13} A. This avoids unexpected automatic shifts during measurements, when choosing 'AUTO' mode instead. The signals were filtered with a filter time of 40 ms, thus excluding variations below that time. Further, all spectra of *TCE* and *CO* were recorded at a SEM current of 1700 V; spectra related to the ethene hydrogenation were measured with 1800 V. Additionally the resolution for all measurements was 20 [4].

The spectra were recorded using a computer based mass spectrometer software (Balzers, Quadstar 421 Version 2.0), exported as *.asc* files and loaded with a routine of in house design into IGOR Pro 6.22. There the spectra were cut to the right length, to exclude parts with decreasing temperature and integrated automatically between manually set fixed start and end points [5].

A.1.4 Dosage of Molecules

A comparison of the improved precision of the MBD compared to the Langmuir dosage is shown in Fig. A.2. TPDs after dosage of different amounts of *TCE* using the MBD and Langmuir dosage on *Pt*(111) were performed. The resulting TPD peak integrals are plotted as a function of dosage for both methods. From the different slopes an enhancement factor of approximately 25 can be calculated for the MBD. Furthermore, the precision of the doser can be seen from the low deviations in comparison to Langmuir dosage [6–8]. However, the different positions of the various crystals in front of the doser are a cause of error in the absolute value of molecules hitting the surface as theoretical calculations have shown [5].

Representative dosage amounts (in *mTorr*) of the different used molecules on the surfaces $MgO(100)$ and $Pt(111)$ are listed in Table A.3. Surface lattice constants and surface atom densities in cm^2 of the used surfaces in the UHV are stated in Table A.4. Table A.5 summarizes the utilized gases, their mass, purity and supplier.

A.1.5 EES Measurements

Table A.6 states the different EES techniques used along with their probe particle and corresponding excitation energy.
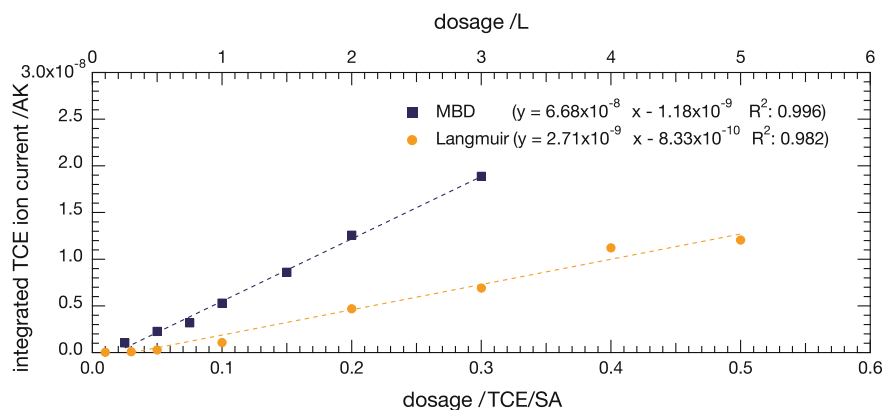
Fig. A.2 Comparison of conventional Langmuir dosage (*L*) and the dosage by means of the molecular beam doser (MBD). Different dosage amounts of TCE on Pt(111) have been performed, followed by subsequent TPDs. The obtained TPD peaks have been integrated and plotted versus the dosed amount. The single data points have been approximated by a linear fit; modified after [8]

Table A.3 Exemplary dosages in the unit *molecules*/*SA* and their corresponding background pressure in mTorr (for $t = 100$ s) for the surfaces $MgO(100)$ and $Pt(111)$ for different utilized when dosing by means of the molecular beam doser [4–6, 9, 10]

Surface	Dosage	Molecule pressure /*mTorr*					
	/atoms/SA	p_{H_2}	p_{D_2}	p_{CO}	p_{O_2}	p_{TCE}	$p_{C_eH_4}$
MgO	0.5	503	711	1876	2005	2590	1877
	1.0	1006	1422	3752	4010	5180	3754
Pt	0.5	335	473	1247	1333	–	1248
	1.0	670	946	2494	2666	–	2496

Table A.4 Lattice constants and surface atom densities of selected surfaces

Surface	Packing	Lattice constant /pm	SA density /atoms/cm^2	Ref.
MgO(100)	fcc	421	2.25×10^{15}	[9, 11]
Mo(100)	bcc	315	1.01×10^{15}	[12]
Mo(112)	bcc	315	0.83×10^{15}	[13]
Pt(111)	fcc	392	1.50×10^{15}	[14]

Table A.5 Detailed information on used organic solvents and gases

Formula	Mass /$\frac{g}{mol}$	Purity /wt.-%	Supplier
H_2	2.01	99.999 (5.0)	Air Liquide
D_2	4.03	99.0 (2.0)	Westfalen AG
He	4.00	99.9999 (6.0)	Air Liquide
Ar	39.95	99.999 (5.7)	Carbagas
CO	28.01	99.999 (5.0)	Carbagas
O_2	32.00	99.999 (5.0)	Westfalen AG
TCE	131.79	99.5	Merck
C_2H_4	82.15	99.95	Westfalen AG

A.1.5.1 MIES/UPS/AES Setup

A schematic sketch of the electronics used for the AES, UPS and MIES experiments is shown in Fig. A.3.

For **AES** electrons from an e-gun are emitted to the sample. After interaction with the surface the emitted electrons are detected after passing through the same hemispherical analyzer by a detector as discussed before. The signal passes then through a preamplifier and a amplifier before reaching the LockIn. The function generator sets a 3 V AC voltage on the sample which pattern is then re-recognized by the LockIn through a reference signal from the function generator. The Lock-In amplified signal is recorded by the computer and together with the signal from the

Table A.6 Comparison of the EES utilized in this work [15–17]

Name of technique	Abbreviation	Probe particle	Excitation energy
Metastable impact electron spectroscopy	MIES (MAES)	Metastable rare gas atom	19.81 eV (He 2^3S_1)
Ultraviolet photoelectron spectroscopy	UPS	Photon	21.21 eV ($He\,I\alpha$)
X-ray photoelectron spectroscopy	XPS (ESCA)	Photon	1253.6 eV ($Mg\,K\alpha$) 1486.6 eV ($Al\,K\alpha$)
Auger electron spectroscopy	AES	Electron (photon)	3000 eV
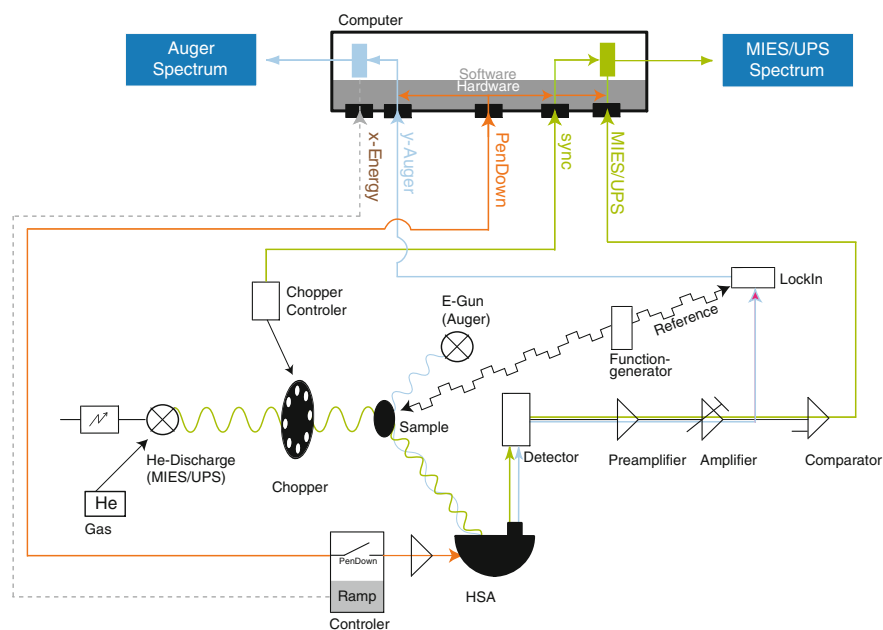
Fig. A.3 Schematic sketch of the utilized electronic setup for the EES (MIES, UPS and AES) data detection

Ramp-Controller and the PenDown, as start signal, the spectrum is recorded via a LabView based software of in-house design.

Using a modified two-stage He discharge source for **MIES/UPS**, based on the design by Kempter et al. [18] UV photons ($He\,I\alpha$, $E_{ex}^{UPS} = h\nu = 21.21$ eV) and metastable helium atoms (He^*, 19.81 eV $= E_{ex}^{MIES}$) are generated simultaneously and directed onto the surface at an angle of 45°. A detailed description of the modified
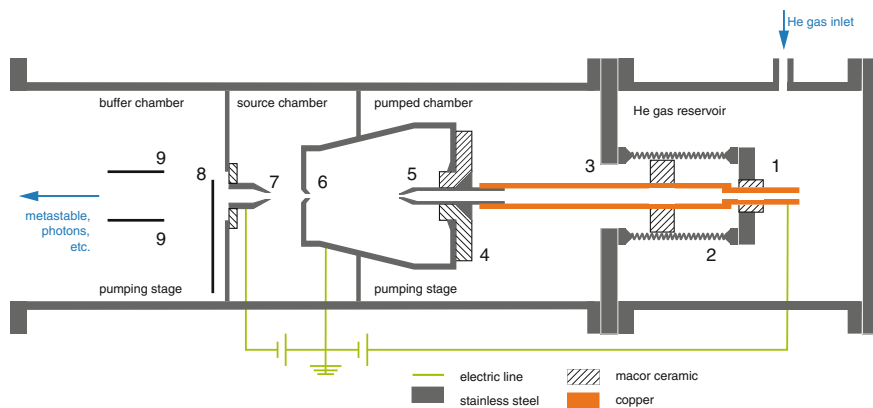
Fig. A.4 Scheme of the utilized MIES/UPS setup: (*1*) Drilled current feedthrough, (*2*) bellow, (*3*) sandwich flange, (*4*) marcor insulator, (*5*) cathode, (*6*) anode plate, (*7*) skimmer, anode for the second discharge, (*8*) chopper, and (*9*) deflector plates [6, 19]. *Reprinted with permission from* [19]*—Copyright 2012, American Institute of Physics*

Table A.7 Representative discharge source parameters

	Pressure /mbar	Discharge	U /V	I /mA
Buffer chamber	7.3×10^{-5}	first	-190	-35.0
Source chamber	4.9×10^{-3}	second	$+296$	$+113.0$
Pre vacuum	6.4×10^{-1}			
He pressure	43.0			

source and the improved signal separation approach (Fig. A.4), can be found in the literature [19].

Briefly, an improved cathode design in the first discharge stage using a *He* gas reservoir allows for higher output of photons and metastable atoms by means of higher voltages, as it compensates for higher temperatures. Table A.7 shows the utilized source conditions in this work. Further, a modified posterior ToF (Time of Flight) separation is applied. Conventionally both MIES and UPS signals are separated by counting electronic events at the analyzer within fixed windows based on the chopper synchronization during measurements. In our approach we record both the kinetic energy of the electronic event and the corresponding time (in sync with the chopper signal) with a LabVIEW based software of in-house design.

Signal separation, originating from photons or metastables is then performed after the measurement. This gives the advantage to check on the signal separation for each data point separately, that means at each measured kinetic energy. This is beneficial, as system parameters (i.e. the chopper frequency) can be adjusted and maximized to the actual measurement conditions and no part of the signal is ignored.

The emitted photoelectrons are detected with a **hemispherical analyzer** which is in line with the surface normal of the sample. For all UPS/MIES measurements the analyzer (VSW Scientific Instruments Ltd. HA150) was used in fixed analyzer transmission (FAT) mode at a pass energy of 10 eV with a scan rate of 0.03 eV/s. The energy resolution was determined to be 0.3 eV by measuring the Fermi-edge of the Mo(100) surface ($T = 90$ K) using a Fermi-function. At the sample, an acceleration potential of -30 V was applied. The spectra were recorded at low sample temperatures ($T \approx 100$ K) from 27–47 eV kinetic energy (KE) scale using a LabView program of in-house design. For AES measurements were performed using the analyzer in fixed retarding ratio (FRR) mode, thus varying the pass energy (constant field in the lens system for keeping the retardation factor $R = E_{kin, A}/E_0 = $ const.).

A.1.5.2 MIES/UPS Post Detection Treatment

At first, the KE of the measured spectra is converted into a binding energy (BE) scale by referencing to the Fermi edge (E_F) of the metal substrates. Further details on this practice can be found in the literature [7, 16, 19, 20]. As this is impossible for the insulating MgO surface the recoded spectra a referenced to E_F of the Mo(100) surface. In the case of TCE the surfaces suffers from charging, thus an alternative energy scale has been chosen (details in Sect. 4.4.1). In order to compare the measured spectra with gas phase PE spectra from the literature, referencing with respect to the vacuum level is required.

Figure A.5 shows this step-wise data treatment exemplary for a MIE/UP spectrum (only the MIE spectra is plotted in A.5) obtained for 0.125 TCE/SA on Mo(112) performed in IGOR Pro 6.22. From the raw spectrum (**step 1**) the WF ($= \phi$) is calculated by subtracting the spectrum width from the corresponding excitation energy E_{ex} ($\phi = E_{ex} - \Delta E + 1/2 \Delta E_{res}$, with $\Delta E = (E_{kin}^{max} - E_{kin}^{min})$ [15, 21, 22] and hereby including the energy resolution of the experiment ΔE_{res} ($= 0.15$ eV in the presented case). E_{kin}^{max} is defined by the position of the E_F (for a metal) while E_{kin}^{min} is related to the energy position of the low energy cut-off of the spectrum. In order to determine the latter, the spectrum is differentiated and the minimum of the first derivative (i.e. $f''(x) = 0$) indicates the point of inflection. The tangent of the spectra at the point of inflection is calculated and its intersection with the x-axis defines the low kinetic energy cut-off of the spectrum. Subtracting the width of the spectrum from the excitation energy yields the **WF**, as seen in **step 2**.

In gas-phase studies the electron BEs are referenced to the vacuum level and plotted on an ionization potential (IP) scale, whereas in the study of solids, E_F provides the experimental reference point on a BE scale (with $E_F = 0$) [22]. To compare gas phase spectra with spectra of adsorbed molecules on a surface, the BE scale of the latter is converted into IP energy scale. In the presented data the WF of the clean metal substrate is added ($IP_{solid} = BE_{solid} + \phi_{clean\,surface}$), thus follow the procedure suggested by Broughton *et al.*; for details see argumentation in Sect. 2.2.3. At high IP energies **secondary electrons** [15, 25] in the spectra suppress features from the adsorbed molecule. In order to reveal features obscured by the secondaries,
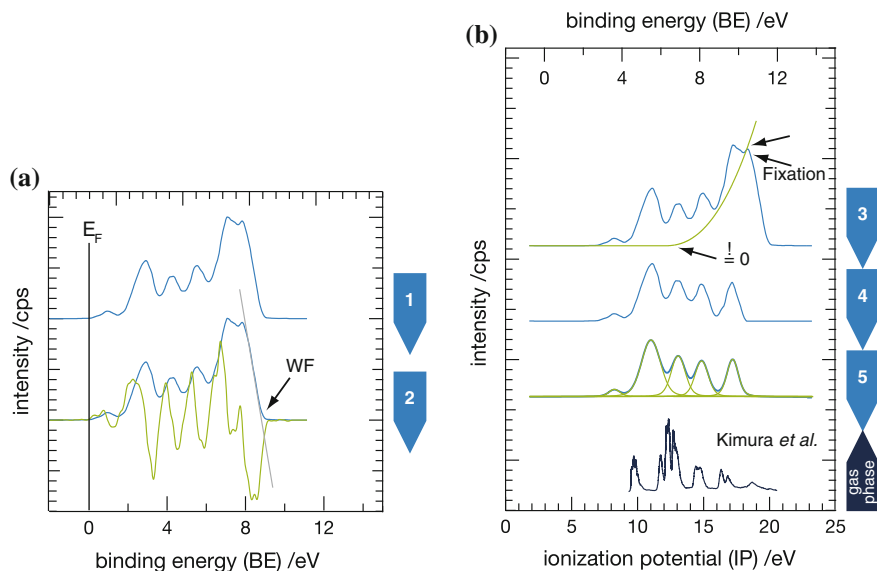
Fig. A.5 Post detection data treatment steps applied for MIE/UP spectra of adsorbed molecules, exemplarily shown for for 0.125 *TCE/SA* on *Mo*(112). Raw spectrum (*1*), WF determination with differentiated spectrum and tangent (*2*). Shift from BE (**a**) to IP (**b**). Secondary electron background correction by subtracting a fitted polynomial function (*3*), background corrected spectrum (*4*), fitted spectrum and sum curve (*5*); gas phase spectrum on the bottom. Roman numerals on top of the bottom spectra assign the peaks of the corresponding gas phase EES spectra [23]. *Reprinted (adapted) with permission from* [24]—*Copyright (2012) Elsevier*

we fit a polynomial function $f(x)$ of degree t (Eq. A.1) at two fixed points on the flank of the secondary peak in the original spectrum (**step 3** in Fig. A.5), with a scaling factor a:

$$f(x) = a(x - x_0)^t \quad for \ x \geq x_0; \ f(x) = 0, \ else \qquad (A.1)$$

By the choice of the curve (in the computer routine), at energies below x_0 the spectrum remains unaffected by the polynomial background subtraction. An eventual remaining background is then accounted for by removing a small linear background. Although the background correction introduces phenomenological parameters only, the above strategy has the advantage of keeping the amount of free parameters low. For all presented *TCE* data the value of x_0 was set to a fixed value of 12 eV, for *ethene* $x_0 = 15$ eV. Thus, eventual errors on peak energy position and intensity introduced by the background correction only enter systematically and do not obscure general trends. Furthermore, the variation of the exponent t in the analysis was restricted to values between 1.4 and 3.2, further reducing the variation of unknown parameters during the background subtraction procedure. For *TCE* the first two peaks/MOs (at $E < x_0$) remain unaffected by the background subtraction; the third and the fourth peak are only affected to a minor degree, due to the restriction of the background

function; a comparable argumentation holds for *ethene*. The peaks in the spectrum of **step 4** are fitted (a common approach as stated in [26, 27]) using a convolution of Lorentzian and Gaussian line shape (Voigt functions) [28]. The resulting fitted peaks of the spectra are shown in **step 5**, from which the peak area and the energy position were extracted; the latter being compared for the presented case to the gas phase data from *TCE* found in the literature [23] (bottom spectrum in Fig. A.5).

A common approach for UP spectra in the literature is the data treatment by subtraction of spectra (particularly the underlying support) in order to make changes in electron density better visible, i.e. [29]. This approach is omitted in this thesis, as this often based on incomparable spectra (due to changing operation conditions of the EES experimental setup) and results in artefact peaks, with no physical meaning [8].

A.1.5.3 XPS Setup

XPS measurement have been performed at a separate UHV setup (Prof. Günther) equipped with a commercial Leybold Heraeus LHS-IO XPS spectrometer. The X-ray tube is operated at an emission current of 20 mA, at a voltage of 12 kV to supply the *Mg Kα* cathode (photon energy of 1253.6 eV) and is kept constant at these conditions for all measurements. In order to to monitor the input voltage for the HV-amplifier an additional digital multimeter (Keithley 191, Keithley Instruments, U.S.A.) is used. The HV-amplifier bipolar by Leybold Heraeus is the set in the detection mode for XPS, the electron energy analyzer power supply is set to a retarding factor $B = 10$ and $E = const$. (biased). Further, the multiplier supply is in the detection mode XPS and a constant multiplier voltage of 3.6 kV was applied for all measurements. The measurements were recorded at a take-off angle of approximately 60°.

Different transmission energies were used for the performed measurements; survey scans were obtained at a pass energy of 100 *PE* (10 scans with step size 1), for the detailed spectra of the characteristic signals 20 *PE* (30 scans with 0.03 step size) were used. To reach the desired quality of the spectra the single scan spectra on one position are recorded several times and averaged afterwards. For the lines scans the number of scans for each position were 90 runs. The detailed spectra for the size-selected *platinum* clusters supported on *silicon* are recorded using at least 150 runs. In order to compensate for fluctuations in intensity, the single measurements of the two detailed *Si2p* and *Pt4f* are switched to one another after 30 scans.

Prior to the measurements, the spectrometer has been calibrated using sputtered samples of the metals *Cu*, *Ag* and *Pt*. Further details with respect to the calibration or the measurement are stated in [30].

A.1.6 Support/Surface Characterization

AE spectra of *MgO*(100)/*Mo*(100), *Mo*(100) and *Pt*(111) excited with an electron energy of 3 kV are shown in Fig. A.6. The following characteristic features are

present: for *Mo*(100) molybdenum at 186 eV (MMN), for *MgO*(100) oxygen at 503 eV (KLL) and magnesium at 1174 eV (KLL) and for *Pt*(111) the platinum at 168 eV (NOO) and 237 eV (NOO). For *Mo*(112) a comparable AES is found as for *Mo*(100), however not explicitly stated here.

MIES/UPS measurements of the clean supports *MgO*(100), *Mo*(100), *Mo*(112) and *Pt*(111) have been recorded at 100 K after applying the cleaning procedures described in Sect. 3.2.2 and are shown in Fig. A.7. The following features in agreement with the literature can be observed.

For **MgO(100)/Mo(100)** the UPS reveal spectral feature with maxima at 6.3 eV and 9.1 eV attributed to emission from the O (2*p*) valence band of MgO. The two peak structure originates from the two types of *p*-orbitals, present in MgO—one oriented parallel and one oriented perpendicular to the surface plane which both get ionized by the ultraviolet radiation. For MIES however only one feature with a maximum at 6 eV is presented, because only MIES only ionized only one type of the aforementioned two types of *p* orbitals, preferably the one oriented perpendicular to the surface [31]. UPS of **Pt(111)** shows the characteristic *d*-band structure, originating from spin-orbit splitting with peaks at 1.5 eV and 4.2 eV. The MIES spectra in contrast does not show any particular features, due to the underlying RT process followed by AN. For both **Mo(100)** and **Mo(112)** the UPS reveals no particular features; MIES is as for *Pt*(111) not straight forward to be interpreted without a deconvolution of the spectra [32, 33], due to the RT/AN process. From the UPS measurements the corresponding work functions (**WF**) of the clean surfaces have been determined. The observed values $\phi_{MgO(100)} = 3.45$ eV, $\phi_{Mo(100)} = 4.56$ eV, $\phi_{Mo(112)} = 4.48$ eV and $\phi_{Pt(111)} = 5.93$ eV with a statistical error of ± 0.05 eV are in excellent agreement with the literature [7, 34, 35].
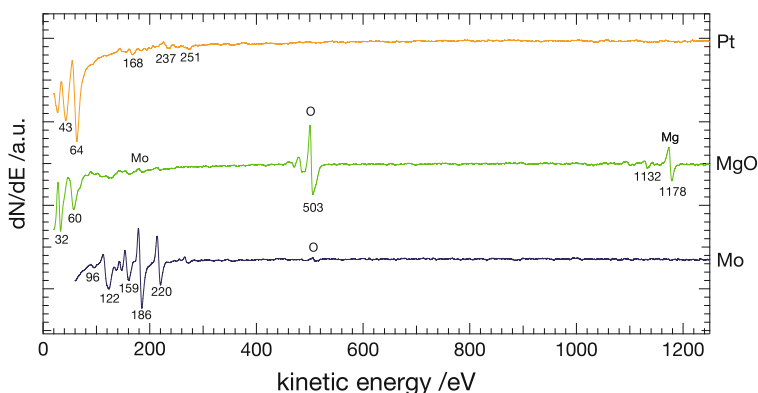
Fig. A.6 AES spectra of *Mo*(100), *MgO*(100)/*Mo*(100) and *Pt*(111), modified after [8]

(a)

(b)

(c)

(d)
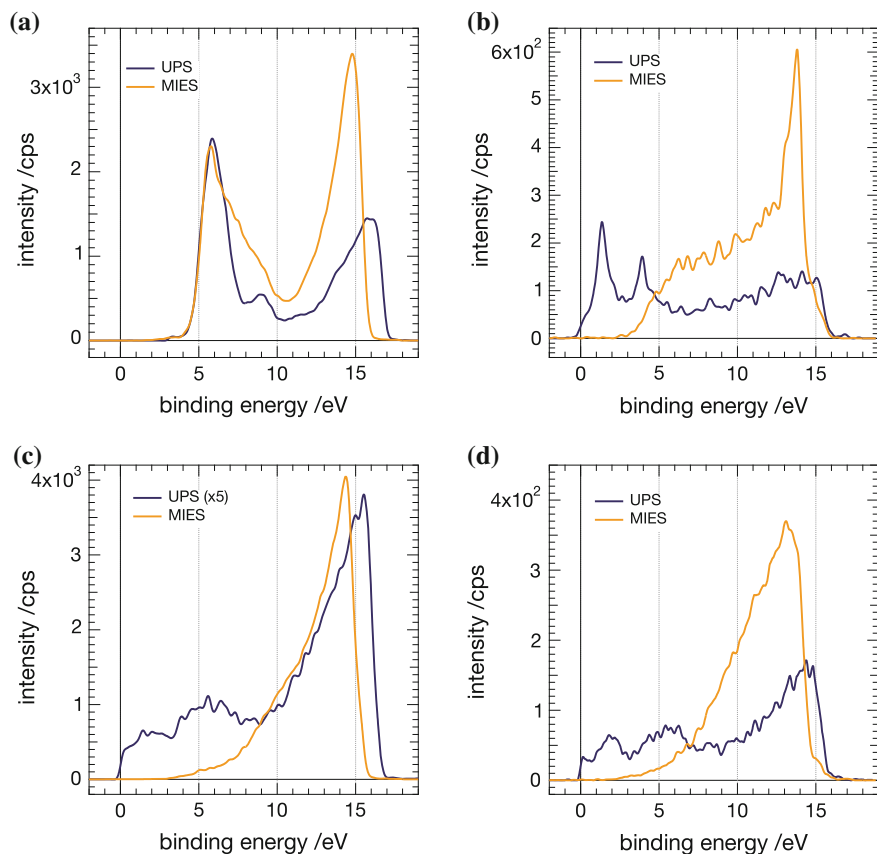
Fig. A.7 EE spectra of the cleaned of $MgO(100)/Mo(100)$–(**a**), $Pt(111)$–(**b**), $Mo(100)$–(**c**) and $Mo(112)$–(**d**) supports; MIES (*blue*) and UPS (*orange*) [6, 8, 24]. *Reprinted with permission from* [19]—*Copyright 2012, American Institute of Physics*

A.2 Ambient Experiments

A.2.1 Sample Preparation and Transfer

A list of samples prepared for ambient experiments is summarized in Table A.8 and states cooperation partners, supports and deposited sizes.

A.2.2 TEM

The **contrast transfer function** (CTF) describes the performance of a TEM and is determined by the electron energy, coherence of the beam as well as focus and

Table A.8 List of samples prepared for ambient experiments. Stated are sample type, cooperation partner, support material (incl. conductivity—yes/no) and deposited sizes

Sample type	Coop partner	Support		Deposited sizes
TEM	LMU	$CdS/Cu/C$	y	8, 22, 34, $n \leqslant 36$, 46, 68
		Cu/C	y	8, 22, 34, $n \leqslant 36$, 46, 68
TEM (E-Chem)	CU/CEN	Au/C	y	8, 22, 34, 46, 68
ETEM	CEN	Cu/SiO_2	n	8, 10, 20, 22, 34, 46, 68
TEM	CHALMERS/	SiO_2	n	8, 22, 34, 46, 68
	CEN	Si_3N_4	n	8, 22, 34, 46, 68
μ-reactor	CINF	SiO_2	y	8, 10, 20, 22, 34, 46, 68
CdS Nanorods	LMU	SiO_2/CdS	y	8, 22, 34, $n \leqslant 36$, 46, 68
INPS	CHALMERS	SiO_2/SiO_2	n	$n \leqslant 53$, 68, 22+68
		SiO_2/Si_3N_4	n	8, 22, 34, $n \leqslant 36$, 46, 68
E-Chem	CU	C	y	8, 22, 34, $n \leqslant 36$, 46, 68

Table A.9 Instrumental specifications for the used TEM microscopes at the different locations

Venue	Manufacturer	Acc. U (kV)	Res. limit (nm)	Camera length
TUM	JEM 2010	120	0.2	
	JEOL, Japan			
LMU	Titan 80-300	300	0.14	196 mm
	FEI, U.S.A.			
DTU	Titan E-Cell 80-300ST	300	0.14	
	FEI, U.S.A.			
DTU	Titan Analytical 80-300ST	300	0.08	
	FEI, U.S.A.			

Table A.10 List of the used TEM grids within this work sorted by the sample type used for the different application, their supplier and grid characteristics

'Sample'	Section	Support		Supplier	Mesh
TEM	5.1.1	Au/C	2 nm	Quantifoil, DE	300
STEM	5.1.1	Cu/C	2 nm	Surface Services, DE	300
ETEM	5.2.1	Si/SiO_2	8 nm	TED PELLA, US	'300'
'INPS'	5.2.2	SiO_2/Si_3N_4	40 nm	Chalmers, SE [38]	'200'
photocat	5.4	$CdS/Cu/C$	(2 nm)	Surface Services, DE	200

spherical aberration (coefficient C_S) of the objective lens. Calculating the function at Scherzer defocus (optimal CTF, with fewest zeros) the point resolution of a particular TEM can be determined [36, 37]—the results of this procedure, e.g. the resolution limits for the used TEM instruments are stated in Table A.9.

Prepared TEM samples and corresponding specifications are listed in Table A.10.

Theoretical cluster sizes used in Fig. 5.1.5 are based on calculation of simple geometrical models; the values used are stated in Table A.11.

Table A.11 Theoretical cluster size, based on simple geometrical models. The clusters are assumed to have a spherical or hemispherical shape and packing space of a *fcc* packing is included or the *Pt* dimer distance in order to find to possible boundary conditions

Cluster size /atoms	Projected surface area /nm^2			
	Sphere		Hemisphere	
	(dimer)	(fcc)	(dimer)	(fcc)
1	–	–	–	–
8	0.232	0.284	0.369	0.451
10	0.270	0.330	0.428	0.523
13	0.321	0.393	0.510	0.623
20	0.428	0.523	0.680	0.831
22	0.456	0.558	0.724	0.885
34	0.610	0.745	0.968	1.183
46	0.746	0.912	1.184	1.448
68	0.968	1.183	1.537	1.878
80	1.079	1.319	1.713	2.093

A.2.3 μ-reactor Measurement Protocol

The complete measurement protocol for the μ-reactor measurements at the CiNF/DTU is based on the procedure file (Lisiting A.1) listed below, stating time, gas flows, temperature, etc.

Listing A.1 Measurement protocol for the combined *CO* oxidation and titration experiment.

```
1   Time;     0   #Initially all flows should be zero
2   Flow1;  0
3   Flow2;  0
4   Flow3;  0
5   Flow4;  0
6   Temp;     0
7   Press;  0
8   Speed;  1
9
10  Time;    20   #Measure area at 30C
11  Temp;    30
12  include;area
13
14  Time;    30   #Run CO-oxidation up to 40C
15  include;start
16  include;light_off_ramp_40
17  include;stop
18
19  Time;    20   #Measure area at 30C
20  Temp;    30
```

```
21  include;area
22
23  Time;    20   #Measure area at 40C
24  Temp;    40
25  include;area
26
27  Time;    30   #Run CO-oxidation up to 60C
28  include;start
29  include;light_off_ramp_60
30  include;stop
31
32  Time;    20   #Measure area at 40C
33  Temp;    40
34  include;area
35
36  Time;    20   #Measure area at 60C
37  Temp;    60
38  include;area
39
40  Time;    30   #Run CO-oxidation up to 80C
41  include;start
42  include;light_off_ramp_80
43  include;stop
44
45  Time;    20   #Measure area at 60C
46  Temp;    60
47  include;area
48
49  Time;    20   #Measure area at 70C
50  Temp;    70
51  include;area
52
53  Time;    30   #Run CO-oxidation up to 100C
54  include;start
55  include;light_off_ramp_100
56  include;stop
57
58  Time;    20   #Measure area at 70C
59  Temp;    70
60  include;area
61
62  Time;    20   #Measure area at 70C
63  Temp;    70
64  include;area
65
66  Time;    30   #Run CO-oxidation up to 120C
67  include;start
68  include;light_off_ramp_120
69  include;stop
70
71  Time;    20   #Measure area at 70C
72  Temp;    70
73  include;area
```

```
74
75   Time;     20   #Measure area at 70C
76   Temp;     70
77   include;area
78
79   Time;     30   #Run CO-oxidation up to 140C
80   include;start
81   include;light_off_ramp_140
82   include;stop
83
84   Time;     20   #Measure area at 70C
85   Temp;     70
86   include;area
87
88   Time;     20   #Measure area at 70C
89   Temp;     70
90   include;area
91
92   Time;     30   #Run CO-oxidation up to 160C
93   include;start
94   include;light_off_ramp_160
95   include;stop
96
97   Time;     20   #Measure area at 70C
98   Temp;     70
99   include;area
100
101  Time;     20   #Measure area at 70C
102  Temp;     70
103  include;area
104
105  Time;     30   #Run CO-oxidation up to 180C
106  include;start
107  include;light_off_ramp_180
108  include;stop
109
110  Time;     20   #Measure area at 70C
111  Temp;     70
112  include;area
113
114  Time;     20   #Measure area at 70C
115  Temp;     70
116  include;area
```

A.3 Gas Phase Spectra and MOs of the Studied Species

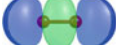### A.3.1 Carbon Monoxide

See Fig. A.8 and Table A.12.
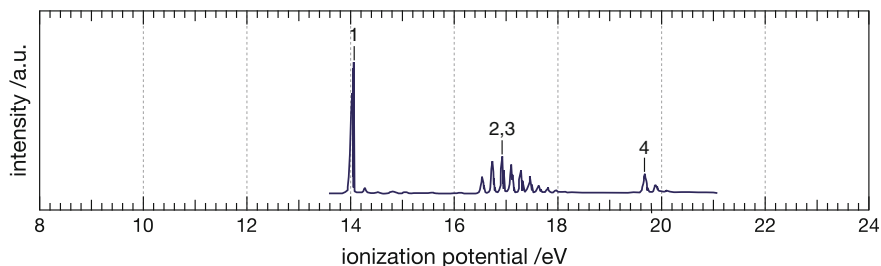
Fig. A.8 Gas phase photo electron spectrum of carbon monoxide adapted from [23]

Table A.12 Experimental [23] and theoretical values from a gas phase measurement of CO with molecular orbital energies, corresponding to the ionization energy (after Koopmans theorem) as well as relative energies of the ionic states corresponding to a final state after a photoelectron transition. Calculated energy values were obtained on CASSCF(6,3) (MOs) and CASSCF(8,7) (Cation) level with a cc-pVDZ basis set

	Peak #	Exp. [23] /eV	Ionic state /eV	$-\varepsilon$ /eV	MO	
I	1	14.01	12.09 ($1\,^2A_1$)	15.00	$5\,a_1\,(\sigma_{C-O})$	
II	2	16.91	15.20 ($1\,^2B_1$)	17.04	$1\,b_1\,(\pi_{C=O})$	
	3	16.91	15.20 ($1\,^2B_2$)	17.04	$1\,b_2\,(\pi_{C=O})$	
III	4	19.72	21.54 ($1\,^2A_2$)	21.78	$4\,a_1\,(n_O)$	

A.3.2 Oxygen

See Fig. A.9 and Table A.13.
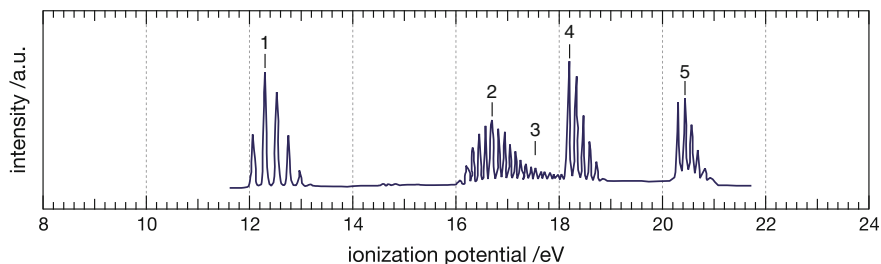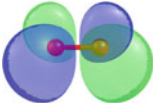
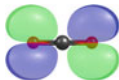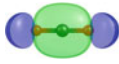**Fig. A.9** Gas phase photo electron spectrum of molecular oxygen adapted from [23]

Table A.13 Experimental [23] and theoretical values from a gas phase measurement of oxygen with molecular orbital energies, corresponding to the ionization energy (after Koopmans theorem) as well as relative energies of the ionic states corresponding to a nal state after a photoelectron transition

Peak #	Exp. [23] /eV	Ionic state /eV	$-\varepsilon$ /eV	MO	
1	12.30	11.89 ($1\,^2B_1$)	6.23	$1\,b_1\;(\pi_{O=O})$	
2	16.62	11.89 ($1\,^2B_2$)	6.24	$1\,b_2\;(\pi_{O=O})$	
3	17.50	16.80 ($2\,^2B_1$)	17.92	$2\,b_1\;(\pi^*_{O=O})$	
4	18.17	16.80 ($2\,^2B_2$)	17.96	$2\,b_2\;(\pi^*_{O=O})$	
5	20.43	19.45 ($1\,^2A_2$)	22.60	$5\,a_1\;(\sigma_{O-O})$	

Calculated energy values were obtained on CASSCF(10,8) (MOs) and CASSCF(10,8) (Cation) level with a cc-pVDZ basis set

A.3.3 Carbon dioxide

See Fig. A.10 and Table A.14.
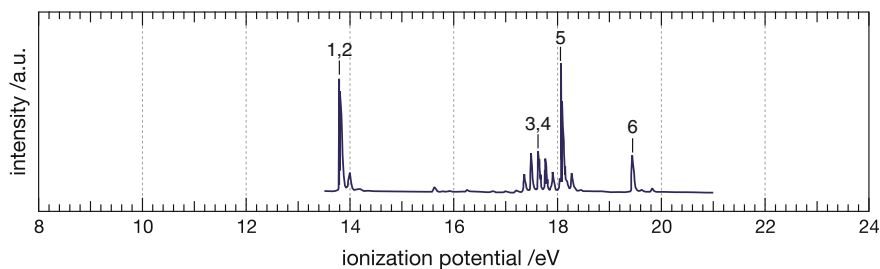
Fig. A.10 Gas phase photo electron spectrum of carbon dioxide adapted from [23]

Table A.14 Experimental [23] and theoretical values from a gas phase measurement of CO_2[5] with molecular orbital energies, corresponding to the ionization energy (after Koopmans theorem) as well as relative energies of the ionic states corresponding to a final state after a photoelectron transition

	Peak #	Exp.[23] /eV	Ionic state /eV	$-\varepsilon$ /eV	MO	
I	1		12.04 $(1\,^2B_1)$			
	2	13.78	12.05 $(1\,^2A_2)$	15.61	$1\,b_2\ (n_O)$	
II	3		15.83 $(1\,^2A_1)$			
	4	17.59	15.84 $(1\,^2B_2)$	18.03	$3\,b_1\ (\pi_{C=O})$	
III	5	18.08	19.15 $(2\,^2B_2)$	20.10	$4\,a_1\ (\sigma_{C-O})$	
IV	6	19.40	21.41 $(2\,^2B_2)$	22.94	$3\,a_1\ (n_O)$	

Calculated energy values were obtained on CASSCF(8,7) (MOs) and CASSCF(8,8) (Cation) level with a cc-pVDZ basis set

A.3.4 Ethene

See Fig. A.11 and Table A.15.
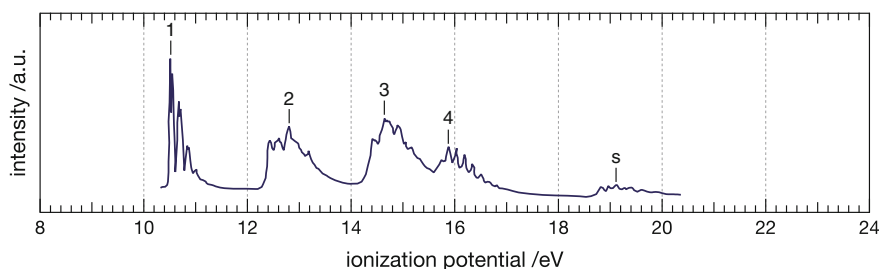
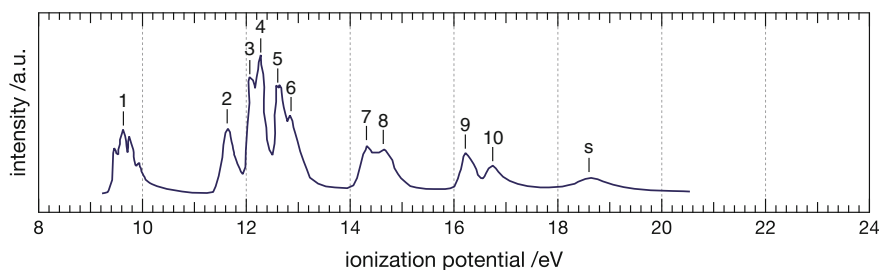**Fig. A.11** Gas phase photo electron spectrum of ethene adapted from [23]

Table A.15 Experimental [23] values from a gas phase measurement of ethene with molecular orbital energies, corresponding to the ionization energy (after Koopmans theorem) as well as relative energies of the ionic states corresponding to a final state after a photoelectron transition

Peak #	Exp.[23] /eV	Ionic state /eV	$-\varepsilon$ /eV	MO
1	10.51	9.79 ($1\,^2B_1$)	9.83	$1\,b_1\,(\pi_{C-C})$
2	12.85	12.53 ($1\,^2B_2$)	15.14	$2\,b_2\,(\sigma_{CH_2})$
3	14.66	14.25 ($1\,^2A_2$)	20.49	$5\,a_1\,(\sigma_{C-C})$
4	15.87	15.62 ($2\,^2B_2$)	15.42	$1\,b_2\,(\sigma_{CH_2})$
5	19.10	17.19 ($2\,^2B_1$)	21.17	$4\,a_1$

Calculated energy values were obtained on CASSCF(10,12) (MOs) and CASSCF(10,10) (Cation) level with a cc-pVDZ basis set
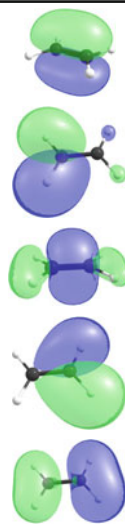
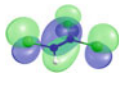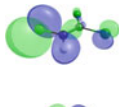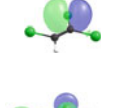## A.3.5 Trichloroethene

See Fig. A.12 and Table A.16.
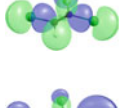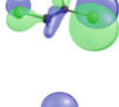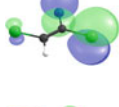
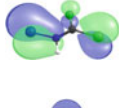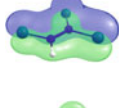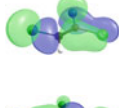**Fig. A.12** Gas phase photo electron spectrum of trichloroethene adapted from [23]

Table A.16 Experimental [23] values from a gas phase measurement of TCE with molecular orbital energies, corresponding to the ionization energy (after Koopmans theorem) as well as relative energies of the ionic states corresponding to a nal state after a photoelectron transition

	Peak #	Exp. [23] /eV	Ionic state /eV	$-\varepsilon$ /eV	MO	
I	1	9.68	8.60 (1 A'')	10.09	7a'' (π_{C-C}, n_{Cl})	
II	2	11.72	10.72 (1 A')	12.91	24 a' (n_{Cl})	
	3	12.17	11.33 (2 A'')	13.62	25 a' (n_{Cl})	
	4	12.33	11.34 (2 A')	15.30	22 a' (n_{Cl})	
	5	12.69	11.85 (3 A')	13.23	23 a' (σ_{C-C}, n_{Cl})	
	6	12.94	12.12 (3 A'')	13.20	6 a'' (n_{Cl})	
III	7	14.35	13.81 (4 A')	13.84	5 a'' (π_{C-Cl}, n_{Cl})	
	8	14.67	14.40 (5 A'')	16.09	4 a'' (π_{C-C}, n_{Cl})	
IV	9	16.25	15.23 (4 A')	17.64	21 a' (σ_{C-Cl}, n_{Cl})	
	10	16.75	15.39 (5 A')	18.34	20 a' (σ_{C-Cl})	
V	s	18.55	–	–	(s)	

Calculated energy values were obtained on CASSCF(2,3) (MOs) and CASSCF(16,10) (Cation) level with a cc-pVDZ basis set. In the last three peaks (8–10) the MOs and the excited cation states are not related directly. It can be assumed that the excitation happens from the according MO but a following relaxation process leads to the final excited cation state

References

1. Schutte, C. J. H., Bertie, J. E., Bunker, P. R., Hougen, J. T., Mills, I. M., Watson, J. K. G., et al. (1997). *Pure and Applied Chemistry*, *69*, 1633.
2. Sheppard, N. (1991). *Pure and Applied Chemistry*, *63*, 887.
3. Porter, H. Q., & Turner, D. W. (1987). *Pure and Applied Chemistry*, *59*, 1343.
4. Crampton, A. (2011). Internship report.
5. Riedel, J. N. (2012). Internship report.
6. Schweinberger, F. F. (2009). Master's thesis, Technische Universität München.
7. Kunz, S., Schweinberger, F. F., Kwon, G., Kiermaier, J., Moal, S. L., Henry, C., et al. (2010). *Surface Science*, *406*, 2184.
8. Zimmermann, T. (2011). Master's thesis, Technische Universität München.
9. Röttgen, M. A. (2007). Ph.D. thesis, Technische Universität München.
10. Heenen, H. (2012). Internship report.
11. Wu, M.-C., Comeille, J. S., Estrada, C. A., He, J.-W., & Goodman, D. (1991). *Chemical Physics Letters*, *182*, 472.
12. Stuckless, J. T., Starr, D. E., Bald, D. J., & Campbell, C. T. (1997). *Physical Review B*, *56*, 13496.
13. Tegenkampa, C., Pfnüra, H., Fedorusb, A., & Naumovetsb, A. (2007). *Surface Science*, *601*, 978.
14. Paulus, U., Wokaun, A., Scherer, G., Schmidt, T., Stamenkovic, V., Markovic, N., et al. (2002). *Electrochimica Acta*, *47*, 3787.
15. Ertl, G., & Küppers, J. (1985). *Low energy electrons and surface chemistry* (2nd ed.). Weinheim: Wiley-VCH.
16. Brundle, C., & Baker, A. (1977). In Brundle, C. & Baker, A. (Eds.), *Electron spectroscopy: Theory, techniques and applications*. London: Academic Press Inc.
17. Brückner, M., Heinz, B., & Morgner, H. (1994). *Surface Science*, *319*, 370.
18. Stracke, P. R. (2000). Ph.D. thesis, TU Clausthal.
19. Spirkl, F. M., Kunz, S., Schweinberger, F. F., Farnbacher, A. N., Schröter, R., & Heiz, U. (2012). *Review of Scientific Instruments*, *83*, 013114.
20. Hüfner, S. (2003). *Photoelectron spectroscopy: Principles and applications* (3rd ed.). Berlin: Springer.
21. Helander, M., Greiner, M., Wang, Z., & Lu, Z. (2010). *Applied Surface Science*, *256*, 2602.
22. Kelemen, S., & Fischer, T. (1981). *Surface Science*, *102*, 45.
23. Kimura, K., Katsumata, S., Achiba, Y., Yamazaki, T., & Iwata, S. (1981). *Handbook of HeI photoelectron spectra of fundamental organic molecules: Ionization energies, ab initio assignments, and valence electronic structure for 200 molecules*. Tokyo/New York: Japan Scientific Societies Press/Halsted Press.

24. Schweinberger, F., Crampton, A., Zimmermann, T., Kwon, G., Ridge, C., Günther, S., et al. (2013). *Surface Science*, *609*, 18.
25. Niemantsverdriet, J. W. (2007). *Spectroscopy in catalysis: An introduction* (3rd ed.). Weinheim: Wiley-VCH.
26. Niemantsverdriet, J. W., & Wandelt, K. J. (1989). *Vacuum Science and Technology A*, *7*, 1742.
27. Joyce, J., del Giudice, M., & Weaver, J. J. (1989). *Electron Spectroscopy and Related Phenomena*, *49*, 31.
28. Doniach, S., & Sunjic, M. J. (1970). *Physics C: Solid State Physics*, *3*, 285.
29. Cassuto, A., Mane, M., Jupille, J., Tourillon, G., & Parent, P. J. (1992). *Physical Chemistry*, *96*, 5987.
30. Rötzer, M. (2012). Internship report.
31. Kantorovich, L., Shluger, A., Günster, J., Stultz, J., Krischok, S., Goodman, D., et al. (1999). *Nuclear Instruments and Methods in Physics Research B*, *157*, 162.
32. Heinz, B., & Morgner, H. J. (1998). *Electron Spectroscopy and Related Phenomena*, *96*, 83.
33. Morgner, H. (2000). In Bederson, B. & Walther, H. (Eds.), *Advances in atomic, molecular, and optical physics* (p. 387). CA: Academic Press.
34. Berge, S., Gartland, P., & Slagsvold, B. (1974). *Surface Science*, *43*, 275.
35. David, R., & Lide, E. (2005). In Lide, D. R. (Ed.), *CRC handbook of chemistry and physics internet version* (85th ed.). FL: CRC Press.
36. Hansen, T. (2006). Ph.D. thesis, Danmarks Tekniske Universitet.
37. Williams, D. B., & Carter, C. B. (2009). *Transmission electron microscopy: A textbook for materials science* (2nd ed.). New York: Springer.
38. Grant, A., & Kasemo, B. (2004). *Nanotechnology*, *15*, 1175.

Curriculum Vitae

Florian F. Schweinberger
  Born: July 10th, 1984 in Garmisch-Partenkirchen, Germany
  Mail to: florian.schweinberger@tum.de

Areas of Interest

Surface Chemistry, Spectroscopy, Heterogenous Catalysis, Cluster Science, Photo-chemistry, Analytical Chemistry and Nanotoxicology.

Education and Training

03/2013
  PhD in Surface Chemistry and Catalysis - 'summa cum laude'
  TUM - Munich, Germany
  Catalysis Research Center / Chair of Physical Chemistry (Prof. Heiz)
  "*Catalysis with supported size-selected Pt clusters,*
  Fundamental UHV and applied ambient experiments"
  'European Graduate School on Sustainable Energy Technology'
  'TUM Graduate School - Faculty Graduate Center Chemistry'
12/2010
  M. Sc. in Chemistry - 'passed with distinction'
  TUM - Munich, Germany
08/2008-07/2010
  Graduate Studies in Physical and Analytical Chemistry
  TUM - Munich, Germany

08/2007-05/2008
> **Graduate exchange studies in Chemistry**
> UQÀM - Montréal, Canada

08/2007
> **B. Sc. in Chemistry**
> TUM - Munich, Germany

06/2003
> **Abitur (A-levels)**
> Werdenfels-Gymnasium - Garmisch-Partenkirchen, Germany

Professional Experiences, Further Training and Research

2008-2009
> **Research assistant**
> TUM - Munich, Germany
> Chair of Physical Chemistry (Prof. Heiz)

09/2008
> **ATHENS intensif course**
> ParisTech - Paris, France

05/2008-08/2008
> **Research assistant**
> Koç University - Istanbul, Turkey
> Surface and Polymer Physical Chemistry Group (Prof. Demirel)

12/2007-05/2008
> **Research assistant**
> UQÀM - Montréal, Canada
> Chaire du recherche du Canada - Chimie Thérapeutique (Prof. Roy)

08/2003-06/2004
> **Civilian Service**
> Sheltered Workshop, Garmisch-Partenkirchen

Publications

Peer Reviewed Journal Articles

1. Schweinberger, F.F.; Crampton, A.S.; Ridge, C.J.; Heiz, U. *2013*, in prep.
2. Wettergren, K.; Schweinberger, F.F.; Deiana, D.; Ridge, C.J.; Crampton, A.S.; Kasemo, B.; Heiz, U.; Langhammer, C. *2013,* in prep.
3. Schweinberger, F.F.; Döblinger, M.; Deiana, D.; Röefzaad, M.; Arenz, M.; Crampton, A.S.; Ridge, C.J.; Esch, F.; Heiz, U. *2013,* in prep.
4. Schweinberger, F.F.; Beer, M.J; Döblinger, M.; Ridge, C.J.; Crampton, A.S.; Wolff, C.; Jäckel, F.; Feldmann, J.; Tschurl, M.; Heiz, U. *2013,*, Journal of the American Chemical Society. 135 (36): 13262. DOI: 10.1021/ja406070q.
5. Nesselberger, M.; Roefzaad, M.; Faycal Hamou, R.; Biedermann, U.; Schweinberger, F.F.; Kunz, S.; Schloegl, K.; Wiberg, G.K.H.; Ashton, S.; Heiz, U.; Mayrhofer, K.J.J.; Arenz M. *2013*, Nature Materials, 12: 919. DOI: 10.1038/nmat3712.
6. Beer, M.J.; Schweinberger, F.F.; Döblinger, M.; Sanwald, K.E.; Wolff, C.; Breimeier, J.; Crampton, A.S.; Ridge, C.J.; Tschurl, M.; Heiz, U.; Jäckel, F.; Feldmann, J. *2012*, *Nano. Lett.* 12 (11): 5903. DOI: 10.1021/nl3033069
7. Schweinberger, F.F.; Crampton, A.S.; Zimmermann, T.; Kwon, G.; Ridge, C.J.; Günther, S.; Heiz, U. *2013*, *Surf. Sci.* 609: 18. DOI: 10.1016/j.susc.2012.09.005
8. Güner, P.T.; Miko, A.; Schweinberger, F.F.; Demirel, A.L. *2012*, *Polym. Chem.* 3, 322. DOI: 10.1039/C1PY00463H
9. Spirkl, F.S.; Kunz, S.; Schweinberger, F.F.; Farnbacher, A.; Schröter, R.; Heiz, U. *2012*, *Rev. Sci. Instr.* 83: 013144.DOI: 10.1063/1.3677648
10. Kunz, S.; Schweinberger, F.F.; Kwon, G.; Kiermaier, J.; Le Moal, S.; Henry, C.; Heiz, U. *2010*, *Surf. Sci.* 604 (23-24): 2184. DOI: 10.1016/j.susc.2010.09.012
11. Hartl, K.; Nesselberger, M.; Mayrhofer, K.J.J.; Kunz, S.; Schweinberger, F.F.; Kwon, G.; Heiz, U.; Hanzlik, M.; Arenz, M. *2010*, *Electrochim. Acta* 56:810. DOI: 10.1016/j.electacta.2010.10.005
12. Kunz, S.; Hartl, K.; Nesselberger, M.; Schweinberger, F.F.; Kwon, G.; Hanzlik, M.; Mayrhofer, K.J.J.; Heiz, U.; Arenz, M. *2010*, *PCCP* 12: 10288. DOI: 10.1039/c0cp00288g

13. Kunz, S.; Schweinberger, F.F.; Habibpour, V.; Röttgen, M.; Harding, C.; Arenz, M.; Heiz, U. *2010*, *J. Phys. Chem. C* 114 (3): 1651. DOI: 10.1021/jp911269z

Conference Proceedings

1. Nesselberger, M.; Kunz, S.; Schweinberger, F.F.; Schlögl, K.; Mayrhofer, K.J.J.; Heiz, U.; Arenz, M. *2012*, *ECS Transaction* 50, 1333. DOI: 10.1149/05002.1333ecst
2. Schweinberger, F.F.; Meyer-Plath, A.A. *2011*, *J. Phys.: Conf. Ser.* 304: 012087. DOI: 10.1088/1742-6596/304/1/012087

Bookchapters

Meyer-Plath, A.A. and Schweinberger, F.F.,
    Chapter "Nanomaterial Characterization and Metrology" in #8144-"Nanotechnology and Human Health", edited by C. Emond and Ineke Malsch - Taylor and Francis and CRC Press Inc, ISBN: 978-0-8493-8144-7

Colophon

This work was created on a Mac using MacOS X (10.8.2-Mountain Lion), LYX (2.0.5.1), BibDesk (1.6.0), Zotero (3.0.10), Adobe CS4 (Photoshop 11.0.1, Illustrator 14.0.0 and Acrobate 9 Pro 9.2.0) and IgorPro (6.22).